A W-band Quasi-optical Mode Converter and Gyro-BWO Experiment

Paul Mcelhinney

SUPA Department of Physics

University of Strathclyde

Thesis submitted for the degree of Ph.D.

2013

This thesis is the result of the author's original research. It has been composed by the author and has not been previously submitted for examination which has led to the award of a degree.

Signed:

Date:

Abstract

High power coherent microwave sources at shorter wavelengths (mm and sub-mm) are in great demand, especially in the fields of plasma physics, remote sensing and imaging and for electron spin resonance spectroscopy. Gyro-devices are by their nature particularly suited to this type of application due to the fast-wave cyclotron resonance maser instability, which is capable of producing high power radiation at frequencies that prove challenging for other sources. A W-band gyro-device based on a cusp electron beam source with a helically corrugated interaction region is currently under development to provide a continuously tuneable source over the range between 90 GHz to 100 GHz with a CW power output of ~10 kW. The work presented herein encompasses the design, construction and measurement of a prototype output launcher for this gyro-device.

A corrugated mode converting horn was designed to act as a quasi-optical mode converter that converts the fundamental operating mode within the gyro-TWA (TE_{11}) to a hybrid mode, which is closely coupled to the fundamental free space Gaussian mode (TEM_{00}). This free space mode allows the possibility for the inclusion of an energy recovery system that can recover a percentage of the energy from the spent electron beam and is predicted to increase overall efficiency by up to 40%. For this scheme the electron beam must be decoupled from the radiation, which can pass through the collector system and vacuum window unperturbed while the electrons are collected at the energy recovery system. This type of corrugated mode converting horn was chosen due to the advantages of a greater bandwidth and the capability to provide a source that is continuously tuneable over this bandwidth.

The results of the design and integration of this corrugated mode converting horn with the gyro-device are presented. The prototype operates over a continuously tuneable bandwidth of 90 to 100 GHz with a return loss better than -35 dB and a Gaussian coupling efficiency of 97.8%. The far field radiation pattern shows a highly symmetrical structure with 99.9% of the power radiated within a cone with a half angle of less than 19° and a cross-polar level less than -40 dB.

Acknowledgements

I would like to thank my supervisors, Dr Wenlong He and Professor Adrian Cross for their help and support during the course of this work. Also, Dr Craig Donaldson and Dr Liang Zhang, who both provided help with the practical and experimental work.

1 Introduction

This chapter contains a basic overview of the history and development of microwave and millimetre sources. The extended interaction klystron (EIKO) oscillator and amplifier (EIKA), the closest competitor in terms of performance to the gyro-devices studied in this thesis, are presented and discussed.

1.1 Project Overview

The PhD project is to develop and construct a key component for a novel gyro-travelling wave amplifier (gyro-TWA) and a gyrotron backward oscillator (gyro-BWO)[1] namely the corrugated output horn. The gyro-TWA had an operating frequency bandwidth between 90 and 100 GHz with a designed operational output power of 5 kW while the gyro-BWO had a frequency tuning range of 84-104 GHz with an output power of up to 12 kW[2]. The Strathclyde W-band gyro-TWA and gyro-BWO, are vacuum electronic devices based on the cyclotron resonance maser (CRM) instability and as such is a sub class of the gyrotron device. These devices use the interaction between a gyrating electron beam and the electromagnetic field of a waveguide mode to transfer part of the electron beam energy to that of microwave field coherently.

1.2 Project Goals

The primary research goal is the development, design, simulation and testing of a suitable device, which would be capable of decoupling a rotating TE_{11} mode from an axis encircling electron beam to a Gaussian output beam. Implementation of this occurs after the electron beam has passed through the interaction region of a W-band gyro device using a helically corrugated waveguide. The motivation for this is to provide a means for inclusion of a depressed collector into the system and increase the overall system efficiency as well as produce a quasi-optical Gaussian beam that is suitable for applications.

1.2.1 Sub goals

- Simulation and design of a corrugated W-band horn
    - The initial stage of this investigation calls for a preliminary design study followed by simulation and optimisation of the corrugated horn using numerical and analytical techniques. The computational simulation is carried out using Mician's Mu-wave wizard and CST microwave studio.

- Simulation and design of an energy recovery system incorporating the horn
    - A further design study and feasibility analysis with particular emphasis on the existing depressed collector system
- Simulation and design of an output window
    - Using the previously discussed design tools a window solution was sought
- Millimetre wave measurements of the components
- The construction and millimetre wave measurements of the components using an Anritsu high frequency vector network analyser to measure the performance and provide any feedback to the design stages.
- Electron beam gyro-device experiments
    - The final stage of the experiment is the fully assembled horn in place within the W-band gyro-TWA experiment.

1.3 Historical Overview

Microwave and millimetre wave sources have become a common if not overly familiar part of the modern world. Since around the time of the 1930's they have provided a reliable source for microwave and mm-wave electromagnetic radiation operating in the range of frequencies between around 300 MHz to 300GHz. The conventional microwave sources, including magnetrons, klystrons, backward wave oscillators and travelling wave tubes are employed in a diverse range of applications such as high-energy particle physics, Radar, television and satellite communication. Even the humble domestic microwave oven owes its existence to the magnetron. Solid-state amplifiers have also made significant progress in recent years in applications such as air traffic control and telecommunications. However, most of the amplifiers still used to power terrestrial and satellite TV broadcasting and RADAR are more likely than not to be based on a reliable vacuum electronic device.

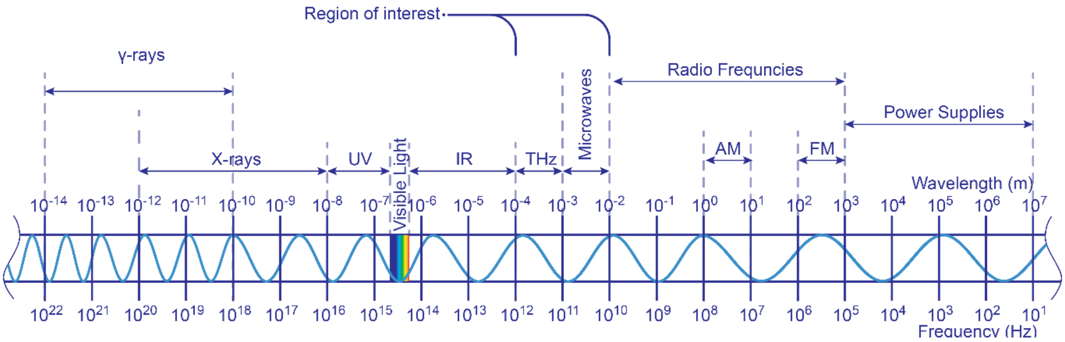

Figure 1.1: Microwave range

Figure 1.1 shows the electromagnetic spectrum and the region that is of interest in the microwave to terahertz frequency band. The region of the spectrum that includes the microwave, mm-wave and terahertz frequencies is commonly referred to by letters, which designate particular bands within the spectrum. Table 1.1 gives a summary of these bands around the region on interest.

X band	8 – 12 GHz	3.8 – 2.5 cm
Ku band	12 – 18 GHz	2.5 – 1.7 cm
K band	18 – 27 GHz	1.7 – 1.1 cm
Ka band	27 – 40 GHz	1.1 – 0.75 cm
V band	40 – 75 GHz	7.5 – 4.0 mm
W band	75 – 110 GHz	4.0 – 2.7 mm
G band	140 – 220 GHz	2.1– 1.4 mm
mm-band	30 – 300GHz	10 – 1 mm
Thz-band	300 – 3000GHz	1 mm – 100 μm

Table 1.1: IEEE microwave frequency bands[3]*.*

1.4 History of mm research

The foundations of microwave and mm-wave technology began in the last two decades of the nineteenth century from the pioneering work carried out into the production and propagation of radio waves by Hienrich Hertz, who from the outset was producing radio waves in the region of 450 MHz[1.4] . He was not however alone in this endeavour and was soon joined by other eminent scientists of the time. Including the likes of Bose and Lebedew; producing radio waves at 5 and 6 mm[5, 6, 7]. This early period can be considered as the first phase of an ongoing evolution in the production of high-powered coherent microwave and mm-sources. The then novel scientific field of electromagnetics first ignited by the fundamental laws lay down by Maxwell[8] was (and still is) a fertile ground for scientific discovery, which saw a massive expansion of the field that still resonates more than a century later. Fundamental discoveries were made during this period in wireless telegraphy[9] and the invention of the first reliable UHF source using the principle of velocity modulation by Barkhausen and Kurz[10]**.** This era also witnessed the first demonstrations of crossed-field devices and the invention of the first low powered Magnetron by Hull[11].

It was however, the Second World War and the surrounding years that produced the second and more comprehensive phase of expansion in the field. In this short decade the range of frequencies attainable and more importantly, the output power at mm and microwave wavelengths was increased. The present phase of research was perhaps began in earnest in the early 1960’s after the invention of the gyrotron and the subsequent move from slow wave devices to the fast wave type device, with the possibility to further increase the power output at shorter wavelengths. A summary of the major milestones in the field of high power microwave sources is given in Appendix 1.

1.5 Overview of mm-devices

There are in general, two distinct and contemporary technologies capable of producing coherent radiation at microwave and mm wavelengths: the vacuum electronics, and the solid-state devices. The solid-state sources rely on similar semiconductor technologies found in conventional lower frequency sources to produce microwave radiation. As such, their capacity to produce both high powers and high frequencies is limited mostly by thermal cooling issues of the semiconductor material. Although the boundaries in this field are ever advancing, the relevance of solid-state research although relevant as a possible input source to the gyrotron travelling wave amplifier is beyond the scope of this project, so further discussion of this technology is not included in this thesis.

Radiation sources based on vacuum electronics, although pre-dating the solid-state devices by almost half a century, are still the paradigm for high power and high frequency operation and reliability. The basic premise for the production of radiation from an electron beam in a vacuum envelope remains relatively unchanged since Thomas Edison first noticed thermionic emission in 1880 and the subsequent developments by Barkhausen and Kurz with the developments in the first decades of the 20th century of power tubes and triodes. However, the ingenuity and complexity of the modern vacuum source is somewhat removed from the early evacuated glass 'valves.'

In essence, conversion of energy from an accelerated electron beam into coherent radiation forms the basis of all vacuum sources. The way in which this energy conversion occurs though varies markedly over the range of modern devices available, but as a rule, there are two main classes of high power vacuum tubes: The fast wave and slow wave source. The distinction between the two is determined with reference to the phase velocity v_{ph} of the electromagnetic wave and that of the speed of light in the medium.

In a slow wave device, the speed of the electromagnetic wave is 'slowed' to match that of the electron beam. In practice, this is can usually be achieved by the means of a periodic structure, which enables coupling between the beam and wave to occur. In the fast wave device the electron beam interacts with an electromagnetic wave with a phase velocity close to or greater than the speed of light. The coupling between the beam and wave usually occurs at a much higher energy and generally in the relativistic regime. The CRM interaction which relies on relativity for its operation can occur for electron beam energies typically greater than 10keV. These devices can further be sub-categorised in a number of ways, such as the signal growth, the operational regime (pulsed or continuous wave), the relationship between magnetic field and electron beam and the direction of the group velocity of the wave relative to the electrons.

1.6 Fast and Slow Wave Millimetre Waves

The slow wave devices were the first to be developed and their sub-classification shares many similarities with that of the fast wave gyro-type devices. Generation of coherent radiation driven from a direct current electron beam is possible only if there is a way to create electron bunching in the beam. This bunching introduces an alternating current component to the beam and if the bunches are synchronous with the RF field then conditions may be favourable for energy exchange to occur. This synchronous bunching is the fundamental basis by which there can exist any generation of radiation from the beam/wave interaction.

The type of microwave device under consideration is determined by the properties of this mechanism. Figure 1.2 demonstrates schematically the typical behaviour of electrons in such a dynamic field, where the electrons bunch around a null point in the field, which is a consequence of the electrodynamic force due to the RF oscillation. In a device, such as a travelling wave tube, the electron velocity is slightly greater than the phase velocity of the waveguide and the bunch will tend to lead the wave and enter into the decelerating phase. Where by the conservation of momentum some energy can be exchanged between the electrons and the field as the electromagnetic field does work on the electrons to decelerate them.

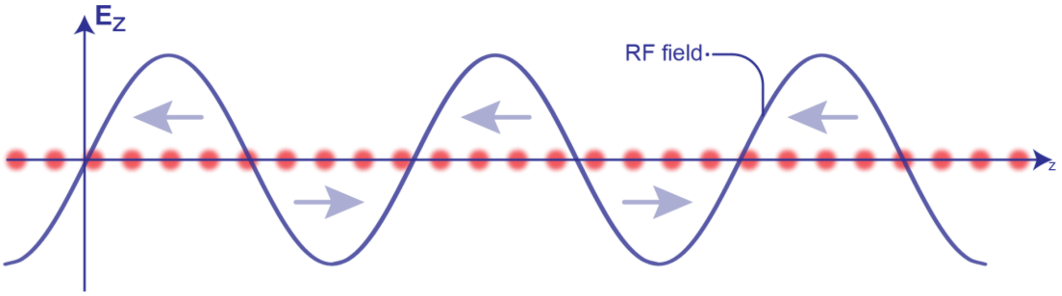

(a) Electrons in a modulated RF field (arrows denote direction of force).

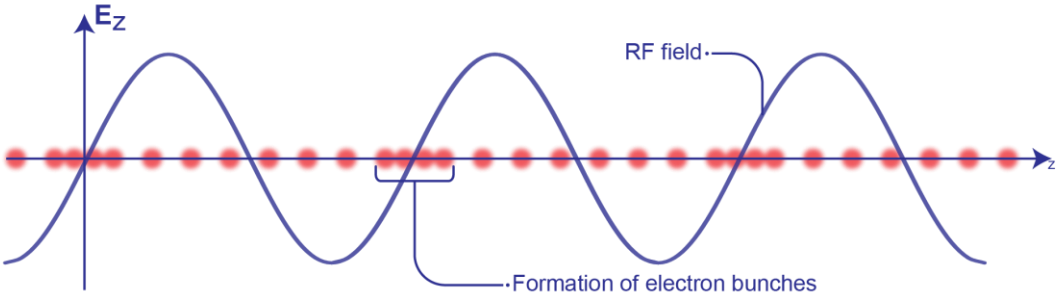

(b) The formation of bunches due to the force of electric field.

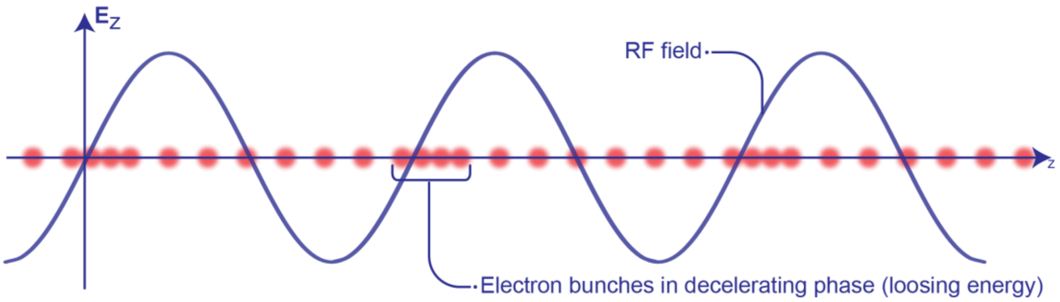

(c) Electrons lead the wave allowing transfer of energy.

Figure 1.2: Formation of electron bunches by AC field.

1.7 Slow Wave Vacuum Devices

Some of the various different slow wave devices such as reflex klystrons, inductive output tube, triodes and magnetrons are summarised in Appendix 2 but for succinctness in this section the klystron, the for-runner of the EIK, the EIK and conventional Travelling Wave tubes and Backward Wave Oscillators are presented.

1.7.1 Klystron

In 1937, brothers Russell and Sigurd Varian developed a prototype device, which was to become known as the klystron, based on the velocity modulation principle at Stanford University in California[12]. This device made use of a resonant cavity to produce bunching of a linear electron beam, which subsequently travels along a drift tube to a second cavity where the electromagnetic energy is extracted. Although, in modern klystrons there are generally multiple cavities to increase the system efficiency and gain.

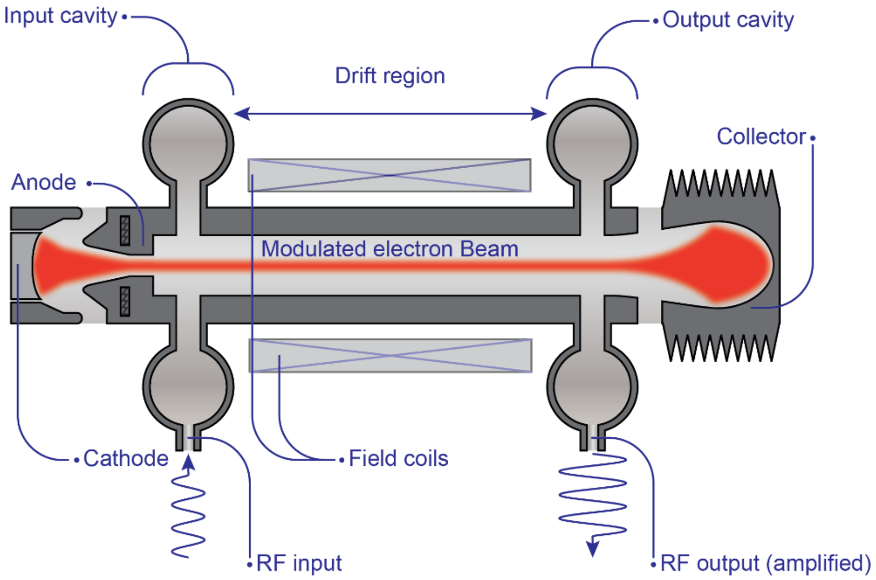

Figure 1.3: klystron tube schematic (two cavity).

The basic principle of the klystron is demonstrated in Figure 1.3. An electron beam is generated, accelerated and confined through a cavity where an external RF signal has been introduced. The alternating field inside this cavity causes the velocity modulation of the electron beam and subsequent bunching, determined by the input frequency. This 'bunched' electron beam then travels down the drift tube and past the output cavity where the modulated charge in the beam excites the cavity modes and subsequently removes energy from the electron beam. This RF power is then removed from the system through a second output coupler before the spent electron beam is dumped at the collector. Klystron tubes, although one of the earliest linear beam sources, have been proven to be extremely reliable and highly efficient (65% efficiency[13]) and are still widely used in many modern applications. They are also capable of very high gain (~60%), with the only limitations on their performance determined by the physical parameters of the system.

To extend the frequency of operation of the klystron into the millimetre and sub-millimetre wavelength range the extended interaction Klystron (EIK) was developed The main difference between an EIK and a Klystron is the inclusion of multiple interaction gaps in each cavity, which raises the impedance of the cavity, in this respect it can be regarded as a combination of the best aspects from the klystron and a coupled-cavity TWT. The EIK is capable of achieving high peak power with excellent efficiency and reliability due to the highly efficient beam modulation and energy exchange between the RF field and beam. There is a high gain over a short period, therefore the EIK can utilize a permanent focussing magnet and this short ladder length also serves to reduce parasitic modes for stability of operation and low noise.

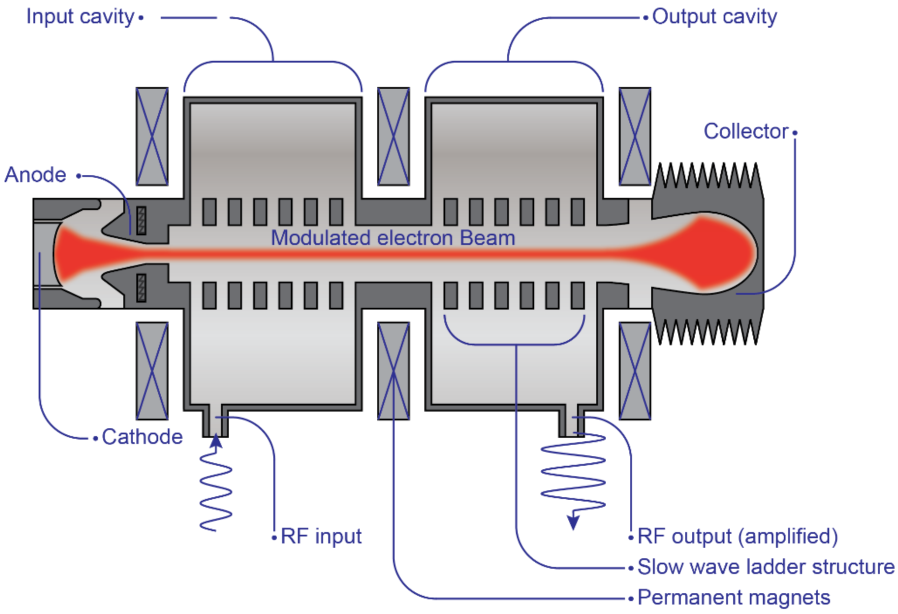

Figure 1.4: Extended interaction klystron schematic.

A schematic showing the EIK is given in Figure 1.4 and Figure 1.5. The electron beam is emitted and accelerated through a focussing aperture in the anode where it is confined by permanent magnets and passes into the beam tunnel. Here it interacts with a series of cavities, which act like a part of a slow wave structure which modulate the beam before energy can be removed in the output cavity.

(a) (b)

Figure 1.5: Schematic showing the comparison between a five gap EIK (a) to a single-gap klystron cavity (b).

The electron beam then leaves the beam tube and is recovered in a collector. The current state of the art is for operation of EIKs is given in Table 1.2[14]. EIKs currently operate at a range of frequencies from 18 —280 GHz but as they are based on resonant coupled cavity structures for electron beam bunching and millimetre wave power extraction they tend to have a bandwidth of <1%.

Frequency (GHz)	**Pulsed Power (W)**	**Average Power (W)**
95	3000	400
140	400	50
183	50	10
220	50	6
280	30	0.3

Table 1.2: State of the art EIK performance.

1.7.2 TWT

The travelling wave tube (TWT) was invented by Rudolf Kompfner in 1942 and first built in 1943[2]

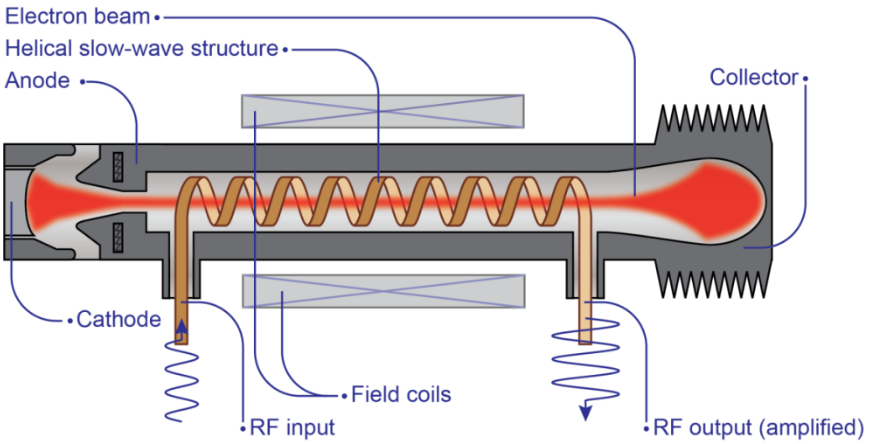

Figure 1.6: travelling wave tube schematic.

The essence of the TWT is a periodical structure that provides the physical geometry for slow wave formation. This is usually either a helix or a coupled cavity structure coupled to an electron beam. In the helix type, an electron beam is generated and confined to an interaction region where there is a helical conductor. The microwave signal is introduced through an input coupler and travels along the helical conductor where there is an exchange of energy with the electron beam due to a bunching of the electrons. Another coupler can then extract this amplified signal before the electron beam is collected. The geometry of the helix or similar structure can be chosen to favour the interaction with the electron beam and thus determine the operational parameters of the device. The helix type TWT can have very impressive power (1kW) and bandwidth (8GHz to 18GHz) performance at microwave frequencies (TMD Ltd) but the performance drops off markedly at W-band frequencies due to the difficulty of manufacturing, supporting and cooling the slow wave helical structure as well as propagating the electron beam through the beam wave interaction region. The amplified signal must also be prevented from returning along the helix, so the inclusion of proper attenuation and severs in the circuit is critical for prevention of this return signal.

1.7.3 Backward wave oscillator

The backward-wave oscillator (BWO) is another velocity-modulated tube operating on a similar principle to the TWT. However, while the TWT is an amplifier in the BWO the microwave signal is created from an internal feedback process. This signal propagates in the interaction region with a negative group velocity, building over time and travels back along the BWO towards the cathode where power is extracted from a coupler.

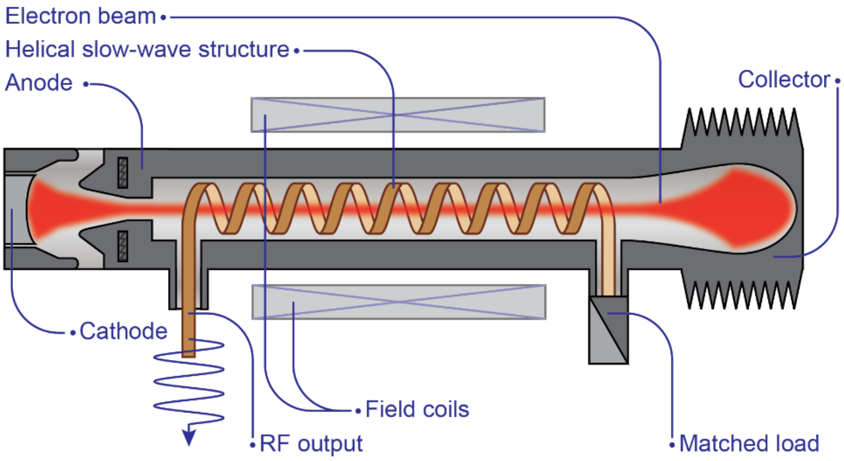

Figure 1.7: A schematic of a BWO using helix as a slow wave structure.

Figure 1.7 depicts the schematic of a drawing of a BWO. A matched load in this case replaces the output cavity. The requirement for inclusion of distributed losses in this case is not critical, as the feedback mechanism is essential to the operation

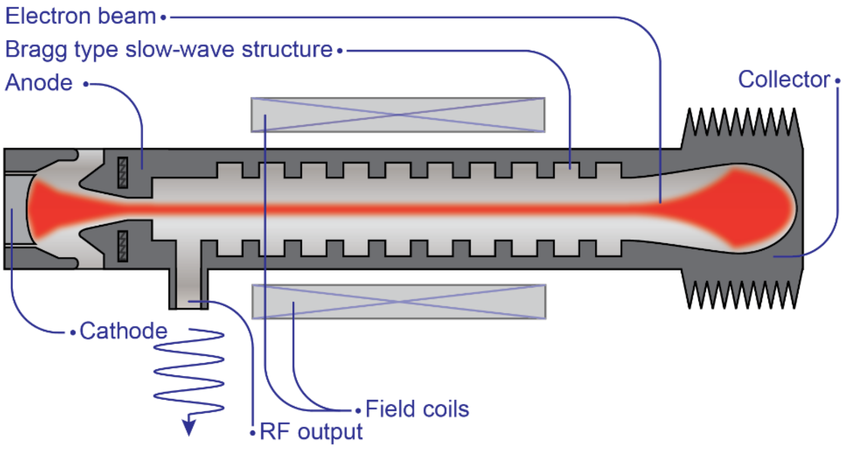

Figure 1.8: A schematic of a BWO using a Bragg structure.

For continuous wave generation, the BWO is suitable for producing high frequency (millimetre and sub-millimetre wave) radiation with high tunability. It can provide 0.5 mW to 40 mW of power at a range of 36GHz to 1.4 THz[15].

Another possible structure that can be used as a slow wave BWO is a periodic Bragg grating (Figure 1.8). This configuration is capable of handling even greater power due to the removal of the slow wave helix, which limits the power output and generation due to the possibility of breakdown within the interaction region. The BWO was the first microwave device driven by a high-current relativistic electron beam to demonstrate efficient, coherent high power microwave (HPM) radiation pioneered by the Institute of Applied Physics (IAP) Nizhny Novgorod, Russia and the Institute of High Current Electronics (Tomsk), Russia. An X-band (8.4GHz to 12GHz) tube generated 0.5 GW of microwave power in single 5-ns pulses from a 500-keV, 10 kA electron beam, with the power dropping to 100 MW per pulse as the pulse repetition frequency was increased to 100 Hz. Later, a 1GW power-level with more than 30% efficiency in 1-2 ns pulses with a repetition frequency of about 10 Hz and 400 MW at 100 Hz repetition was achieved[16].

2 Fast Wave Devices and Gyrotrons

This chapter begins with an overview of the ‘fast wave’ devices before describing the various gyro-devices and their properties and operating regimes. Particular emphasis is placed on the Strathclyde gyro-devices with a helically corrugated interaction region, before a summary of the state of the art in gyro-devices operating at and round 95 GHz is presented.

2.1 Fast Wave Vacuum Devices

Fast wave devices were developed to produce higher power at higher frequencies initially for plasma fusion heating. Higher power high frequency oscillators known as gyrotrons were needed for electron cyclotron resonance heating of plasmas. For the latest generation of high gradient particle accelerators fast wave amplifiers such as gyro-klystrons were developed using the fast wave interaction. In the 1970's the two new class of relativistic microwave sources the gyrotron and the free electron laser were developed. While the conventional tubes discussed previously are eminently capable, there is a fundamental limitation on slow wave structures when attempting to generate high powers at mm wavelengths. It is clear from figure 2.1, that due to the interdependence between the scale of the slow wave structure and the wavelength of the radiation, that as the wavelength becomes smaller, so too must the interaction structure. This not only increases the difficulty for fabrication, but also places an upper limit on the power handling capabilities of the device due to electrical breakdown and the dissipation of heat from the electron beam. As seen in the diagram, where there is a comparison between the dimensions of three structures operating at 30 GHz. The solution lies with removing the complex slow wave structure and moving to a larger diameter smooth interaction region. Therefore, the interaction type must also move to couple between a fast wave and the electron beam, given that there is no longer a structure to slow the wave.

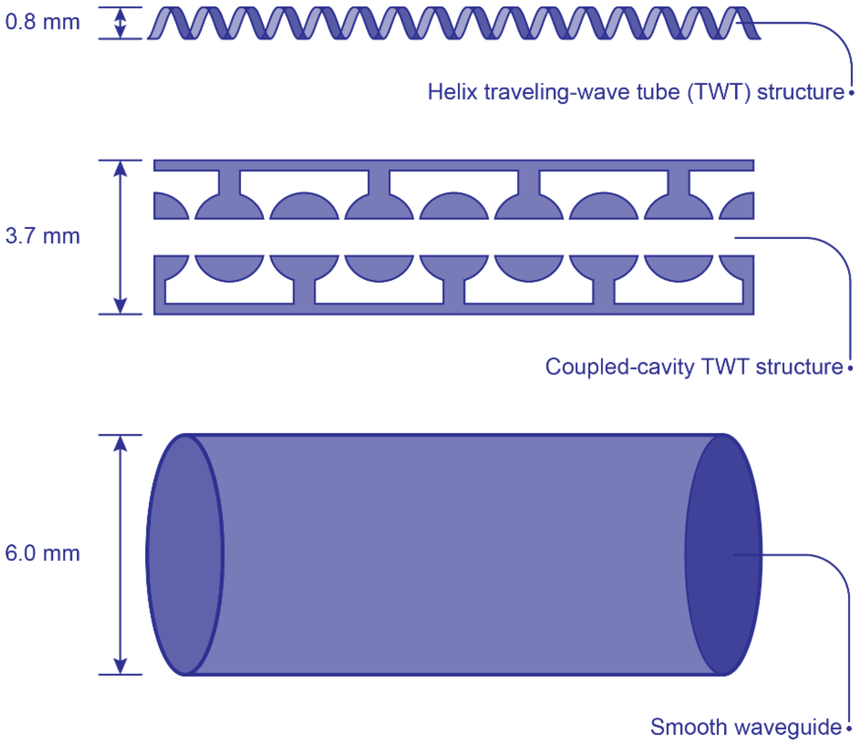

Figure 2.1: Comparison of the shapes and transverse dimensions of three common types of interaction structures at 30 GHz[2]

There are two major classes of fast wave devices, the free electron lasers (FEL) and Gyro-devices. FEL's use a linear electron beam that is accelerated before entering an undulator cavity where their trajectories are modified by a periodic arrangement of magnets causing coherent photon emission. For more information on the FEL please refer to Appendix 3. Gyro-devices exploit the relativistic interaction between a gyrating electron beam in a static magnetic field and a cavity mode to produce a coherent source of radiation. The electrons gyrate in an external longitudinal magnetic field. The frequency has a relativistic mass dependency and when they give or take energy the speed of the particles gyration changes. The gyro-devices amplify or generate microwaves based on the ECM instability.

Both the gyro-device and Free Electron Laser are classified as fast wave microwave sources where the phase velocity v_{ph} of the electromagnetic wave is greater than the velocity of light. For almost every conventional linear beam device there is a gyro counterpart. The class of gyro-devices includes the gyro-monotron, gyro-travelling wave tube, gyro-backward wave oscillator, gyro-klystron, and many others such as the gyro-twystron[17].

2.2 Fundamental Properties of Gyro-devices

The ECM interaction is a relativistic plasma phenomenon, which is capable of coupling the energy of a particle beam radiation. It is this mechanism in a gyro-device that enables the production of coherent emission of radiation from an electron beam. A simple schematic of a gyro-device, which operates under this principle is shown in Figure 2.2.

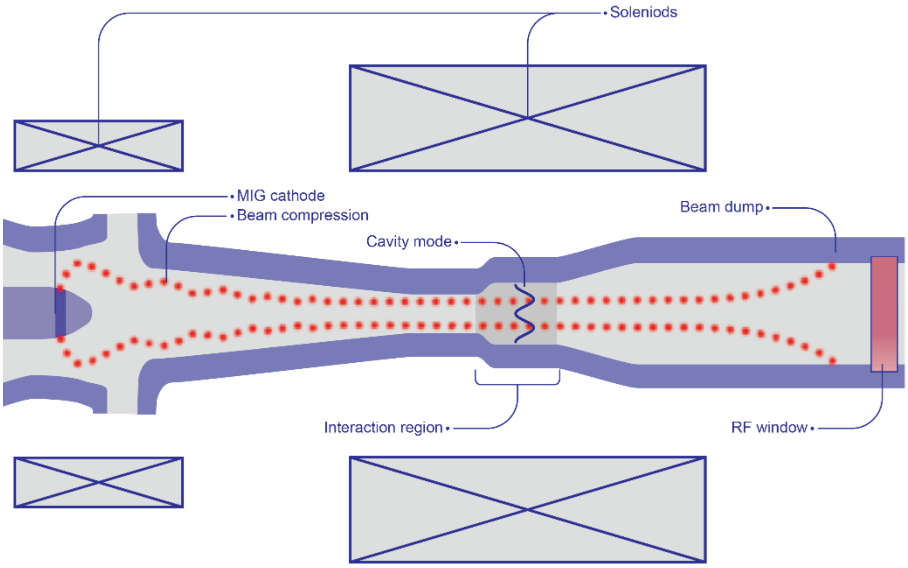

Figure 2.2: Schematic of a typical gyro-device.

Electrons are introduced into a waveguide cavity at high vacuum in the presence of a strong static magnetic field. The magnetic field causes the electrons to gyrate due to the balance between the centripetal and Lorentz forces on the electron. The gyrating electron beam interacts with an electromagnetic mode within the cavity to excite a stimulated emission process resulting in the production of coherent radiation. This takes place because the interaction between the electromagnetic field and the gyrating electrons permits a transfer of energy from the transverse momentum of the electrons and the electromagnetic field.

This resonant exchange of energy between the electrons and the electromagnetic wave occurs where the operating frequency is close to that of the electron cyclotron frequency, as given by equation 2.1.

$$\omega - k_z v_z \approx s\omega_c \qquad 2.1$$

Where ω is the angular frequency of the wave, the axial wavenumber is k_z, the axial velocity of the electrons is $v_{\parallel}$, s is the cyclotron harmonic number, and the relativistic cyclotron frequency is ω_c, e/m is the electron charge to mass ratio and γ is the relativistic factor.

$$\omega_c = \frac{eB_0}{m_e\gamma} \qquad 2.2$$

With careful consideration of the magnetic field strength a frequency can be chosen for the cyclotron orbit that is closely matched with the cavity mode allowing energy to be transferred between the electrons and the radiation field at that frequency. The electron beam is then free to exit the cavity having undergone energy exchange with the electromagnetic field and is collected at a beam dump where the remaining energy is removed. The coherent radiation is transmitted out of the system through a vacuum window.

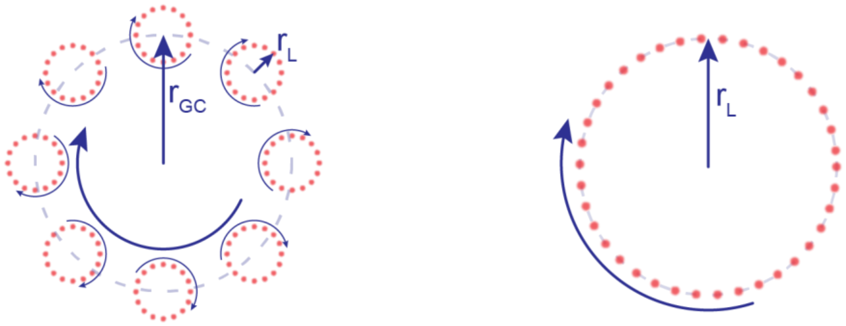

(a) MIG type gyrotron electron beam *(b) Axis encircling electron beam*

Figure 2.3: Electron beam configurations.

The type of electron source used in gyrotrons is usually a magnetron electron gun, which is used to produce an annular electron beam with the required physical properties for the gyrotron interaction. The electrons inside this annular region have an orbit defined by the radius of the emitter, as well as the individual contribution of the electron cyclotron orbit at the operational cyclotron resonance frequency of the gyrotron. This leads to a hollow beam where the electrons orbit around a common guiding centre with a series of sub-groups following a smaller orbit determined by their Larmour radius (Figure 2.3 a). The Strathclyde W-band gyro-TWA/BWO has a slightly different beam configuration. The electron beam for this device is designed to be axis encircling and therefore has only a rotation component around the axis of propagation.

In both of these cases the electron beam has a velocity v_z, in the axial direction along the length of the gyrotron and a velocity $v_\perp$, which produces a rotation of the electrons around the axis of the gyrotron. The ratio of the transverse to the longitudinal velocity is usually denoted by $\alpha = v_\perp / v_z$, and in the interaction region of a gyrotron this is usually between 1 and 2. Because the main mechanism for extracting energy relies on the transverse velocity of the electron it is important to maximise this velocity for the highest efficiency of the interaction and for this reason it is also important to minimise the spread in both the axial and perpendicular velocity. This factor will clearly limit the overall system efficiency since a large fraction of the energy in the electron beam will remain in the axial component.

A basic understanding of the energy transfer process is achieved by considering the simple case of a single electron beam or ensemble, which has a common guiding centre, propagating with a velocity perpendicular to a constant magnetic field. In this case, the effects of space charge can be neglected although the presence of this effect produces a minor perturbation in the general case. This is analogous to a single group of electrons in a MIG-type beam and also describes the axis encircling beam.

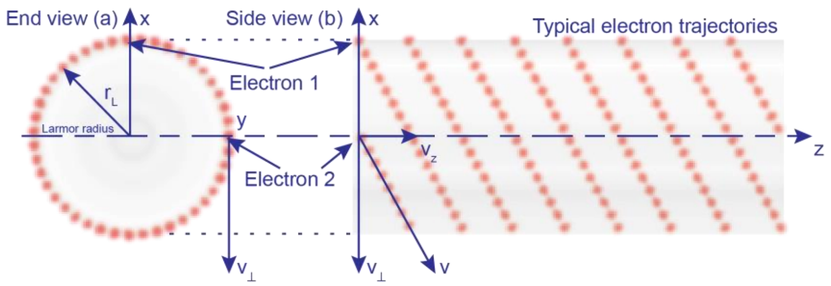

Figure 2.4: Idealised electron trajectories in a CRM interaction.

If the guiding centre of the electrons is coincident with the z-axis of a coordinate system then the electrons execute a circular orbit with the locus on the z-axis and a constant radius r_L .This is the Larmor radius given by:

$$r_L = \frac{v_\perp}{\omega_c} \quad 2.3$$

Here $v_\perp$is the transverse electron velocity and ω_c is the relativistic cyclotron frequency. The physical evolution of the CRM mechanism may be described phenomenology by consideration of Figure 2.5, which depicts a schematic view of electrons gyrating in a constant magnetic field perpendicular to the plane of the page.

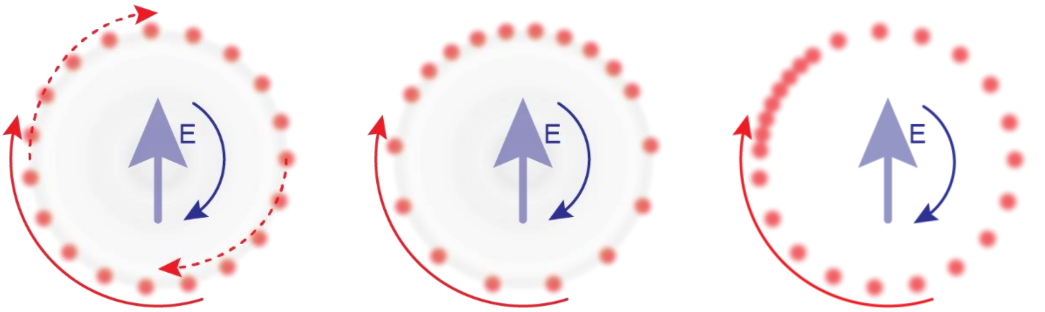

(a) Electrons change in momentum due to action of Electric field

(b) Electron bunch begins to form.

(c) Electron bunch lags the electric field and energy is transferred to the field

Figure 2.5: Electron bunching mechanism in the CRM interaction. The red arrow shows the motion of the electrons and the dotted red arrow shows the relative acceleration and deceleration of the electron. The light blue arrow is the rotating electric field and the dark blue arrow is the direction of the field rotation.

In part (a) the electrons are evenly distributed around an orbit described by the Larmor radius $\mathrm{r_L}$. If there is an electric field present rotating with a similar angular frequency as the electrons then there can be an interaction between the gyrating electrons and the co-rotating field. In a simplified approach, where the frame of reference is assumed to be stationary in terms of the electrons then the interaction may be described by considering the result of the electric field on the electrons. The relativistic dependence of the electron gyro-frequency ω_c provides a bunching mechanism for the gyrating electrons due to the relativistic dependence on their mass. Electrons that experience acceleration due to the action of the electric field increase in mass and therefore undergo a reduction in their angular frequency, whereas electrons that are decelerated undergo an increase in angular frequency. Depending on the relative position of the electrons within the orbit the electrons in opposite phases are affected in different ways, those that lead the electric field by $\pi/2$ have a net gain in energy and electrons that lag by $\pi/2$ loose energy. This has the overall effect of producing electrons, which are either advanced in phase in the case decreased gyro-frequency or phase retardation in the case of increased gyro-frequency.

When a phase bunch occurs the action of the space charge effect becomes important, but far from inhibiting the formation of the electron bunches, the space charge actually enhances formation of the phase bunch. This is because the electrons that are repelled away from the bunch are accelerated and thus in the process and consequently a reduction in the gyro-frequency, whereas those electrons that are decelerated away from the bunch undergo a decrease in relativistic mass gaining energy and an increase in gyro-frequency. Therefore, the net consequence of the space charge is to produce an enhanced electron bunch.

This physical process may be exploited to provide energy extraction from the electron beam. At this point, there is both an acceleration and deceleration of the electrons due to the electric field. If the conditions in the field are altered slightly, so that the angular frequency of the field is slightly greater than the gyro-frequency (so called detuning) then the electron bunches will be formed in the decelerating phase. This allows the exchange of energy to the electric field from the electron beam and hence from the system as emitted radiation. The efficiency of a practical device is around 40%; with the limit defined by an effect known as ‘phase trapping' where after there has been energy extraction from the electron beam the gyro-frequency begins to increase above the RF frequency causing the electrons to move into the accelerating phase and thus extract energy from the field.

The operational range of frequencies that can be achieved using gyrotrons and gyro-devices is typically in the range between 10 GHz to 1000 GHz, with average power ranging from a few megawatts to tens of kilowatts[18]. The theoretical foundation for gyro devices was laid in the 1950’s, with the development of the first gyrotron oscillators[19, 20, 21]. Since then there has been a great deal of research and development to produce gyrotron devices for applications covering a wide range of scientific disciplines and technological applications. The range of frequencies and potential power output capabilities of gyro-devices make their research and manufacture an attractive prospect given that alternative devices that are presently capable of producing radiation in this frequency range are either incapable of producing the high power outputs of which the gyrotron is capable, or they are simply not able to operate at these frequencies at all. This is especially true at present with the so called ‘terahertz gap’; the range of the EM spectrum between 100 GHz and 3 THz[22, 23] where there is a failure in the present generation of electronic and laser devices to provide radiation in this range (Figure 2.6).

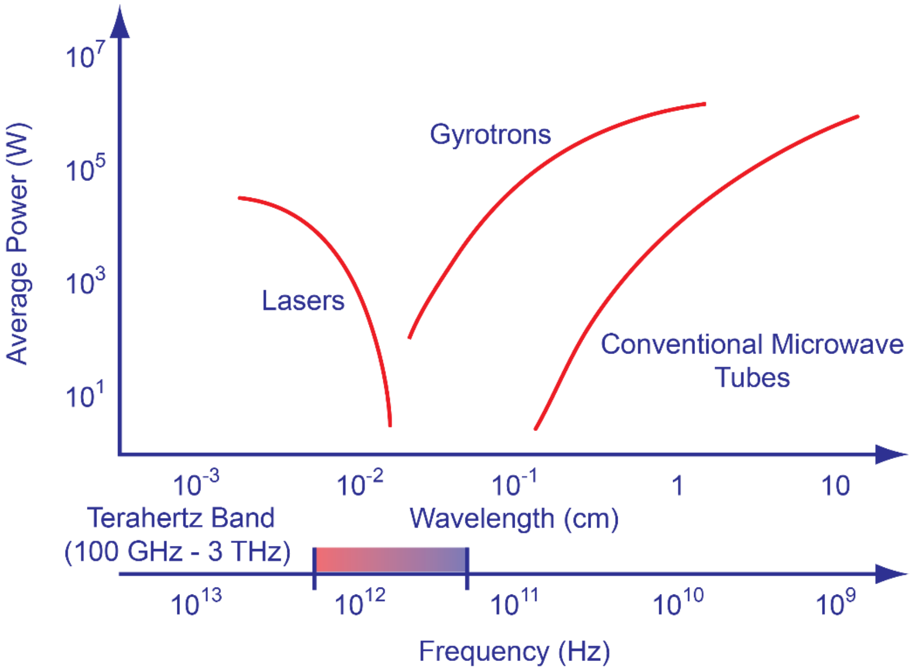

Figure 2.6 Operational regime of gyrotron microwave devices (average power)[2]*.*

The powers of microwave sources have rapidly increased over the 8 decades since around the time of the Second World War. Figure 2.7 provides a concise overview of this evolution[24]. At higher frequencies the output power that can be achieved is lower and since the power of these devices scales as function of the square of the frequency (f^2), the graph shows the parameter, Pf^2, as a function of time. Also shown in this graph is the large difference in powers between vacuum and solid state devices.

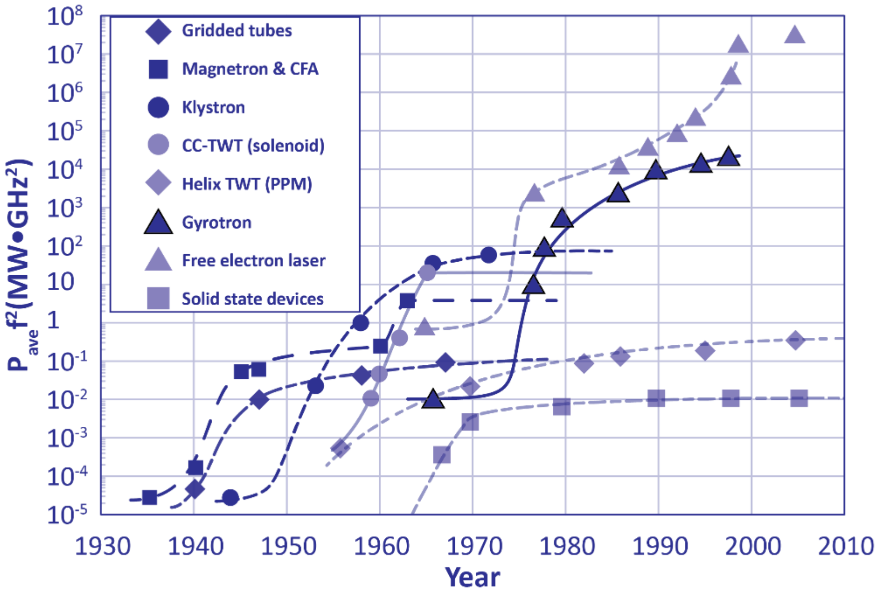

Figure 2.7: The variation in performance of vacuum and solid state microwave sources since the 1930's.

2.3 Review of Gyro type Microwave devices

A wide range of gyro-device exists, which utilize the ECM instability to produce coherent radiation. These devices are characterised a similar way to the slow wave microwave tubes although the physical mechanism responsible for microwave generation is much different. The Gyro-monotron (gyrotron) has been well established for some time now and is capable of very high >50% efficiency with energy recovery systems. These devices are also capable of high powers but suffer slightly at higher frequency due to the reduction in size of the interaction region and the inherent reduction of the waveguides power handling. As the frequency increases and the power falls other methods must be sought to improve the performance. While gyrotrons have a better overall efficiency, their tuned cavities are much less flexible and their bandwidth suffers as a result. One approach is to develop novel cavities, such as that discussed in this thesis, which can provide an excellent power over a broad bandwith at sub-THz to THz frequencies.

2.4 Gyro-monotron

After the work of experimentalists such as Chow and Pantell[25], Bott[26] and Feinstein[27] in the sixties the first devices that went on to utilize the ECM interaction were the gyrotron oscillators (gyrotrons), which were the first to show promise as high power microwave operation during the 1970's when Soviet/Russian scientists[28, 29, 30, 31, 32] made advances in the output power, through the development of magnetron injection guns and large diameter tapered waveguide cavities.

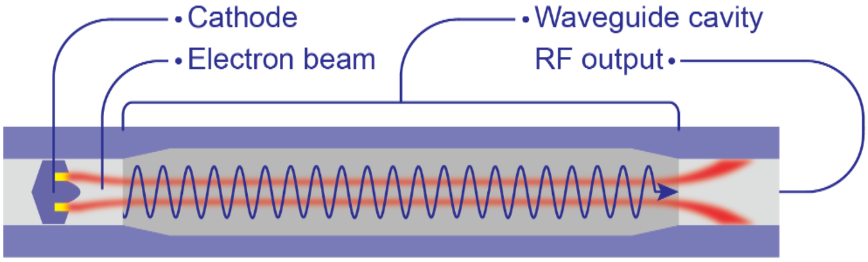

Figure 2.8 Schematic diagram of a Gyrotron Oscillator.

The gyro-monotron, which is the alternative name for the gyrotron typically only exploits a weakly relativistic electron beams where the beam voltage is less than 100 kV and the value of gamma is less than 1.2. They also operate with a high pitch angle $\alpha = v_{\perp}/v_z > 1$, with an operational mode close to the cut off mode of the waveguide. A typical dispersion plot for a gyro-monitron is given in Figure 2.9.

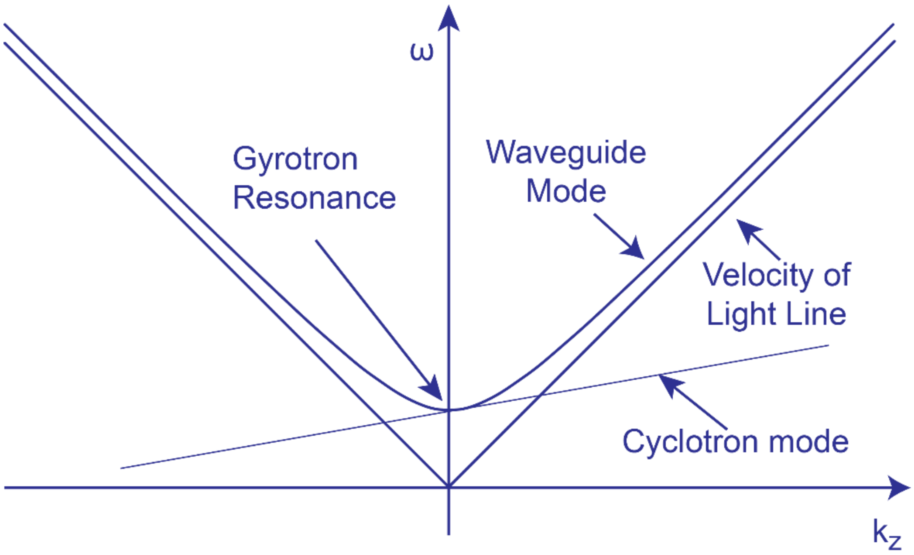

Figure 2.9 Typical dispersion plot for a Gyrotron.

The Doppler shift is small, which results in a relationship producing radiation close to the cyclotron frequency or at a harmonic.

$$\omega \cong s\omega_c \quad s = 1,2 \ldots \tag{2.4}$$

$$v_{ph} = \frac{\omega}{k_z} \gg c \qquad 2.5$$

The frequency mismatch in a gyro-monotron is kept small and positive $\omega - s\omega_c$ to produce the correct phase bunching (electrons should be in the retarded phase).

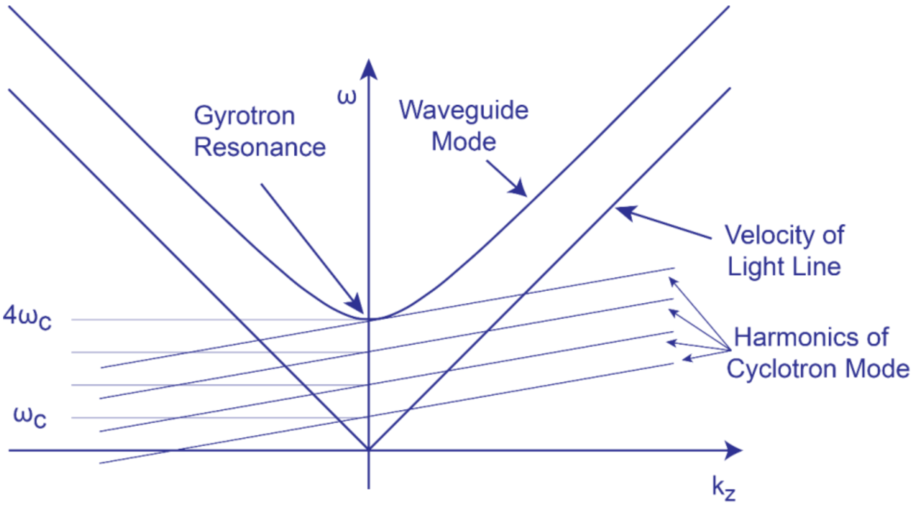

Figure 2.10 Dispersion for a harmonic gyrotron

Gyro-monotrons may be operated at harmonics of the cyclotron frequency; reducing the required magnetic field for that particular frequency by a factor given by the harmonic number *s*. This reduces the overall efficiency of the device.

2.5 Gyro-klystron

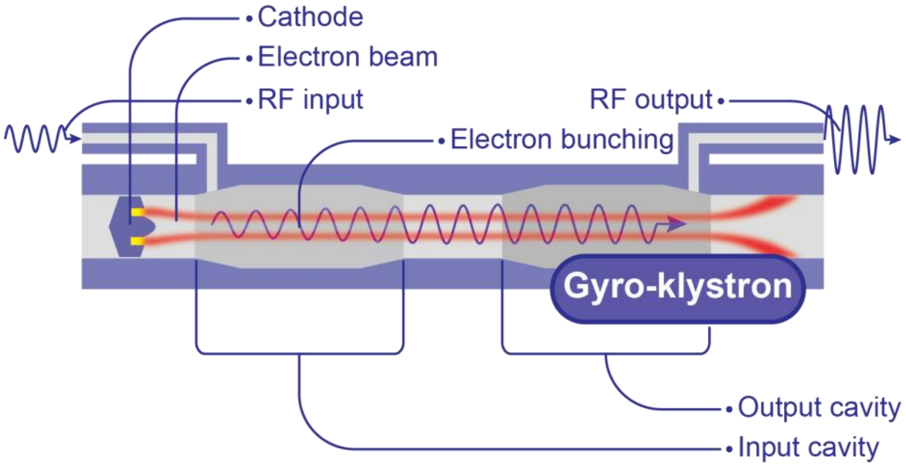

Figure 2.11: A schematic diagram of a Gyro-klystron.

Gyroklystrons employ ballistic bunching of electrons over a distributed interaction region in a regime that is roughly analogous to the operation of a conventional klyston tube, using weakly relativistic electron beams with the same parameters as gyrotron oscillators. Figure 2.11 shows a schematic of a two-cavity gyro-klystron. The energy of the electron beam is modulated due to the interaction with the input signal in the first cavity, but they are also azimuthally bunched by the cyclotron interaction. As the beam propagated along the drift tube the ac current grows, before reaching the second cavity where the beam then drives a large RF signal from which there can be energy extraction. They are narrow band devices with some similarities to the slow wave klystron, employing several cavities to maximise the possible overall gain. They were originally invented for radar applications, for example two phase-matched Ka-band gyroklystrons powering a megawatt radar that tracks objects orbiting the earth[33]. The state of the art gyro-klystrons in W-band are produced by the Institute of Applied Physics, Nizhny Novgorod, Russia that can generate up to 0.4MW at 95GHz for a gain up to 30dB and an electronic efficiency of up to 30% within a band of up to 0.5%[34].

2.6 Cyclotron Auto-resonance Maser (CARM)

A Gyrotron can be operated with a more highly relativistic beam $\geq 1MeV$. The condition in which such a highly relativistic beam is synchronous is met in an interaction region where the phase velocity of the electromagnetic radiation is closely matched to the speed of light and the Doppler shift term in this case is large.

$$\omega \cong k_z v_z + s\omega_c \qquad 2.6$$

If $c \cong v_z$ then the increase in the cyclotron frequency caused by the extraction of beam energy is almost equal to the Doppler term and so if the resonance conditions are met initially then they will be continued throughout the interaction.

+

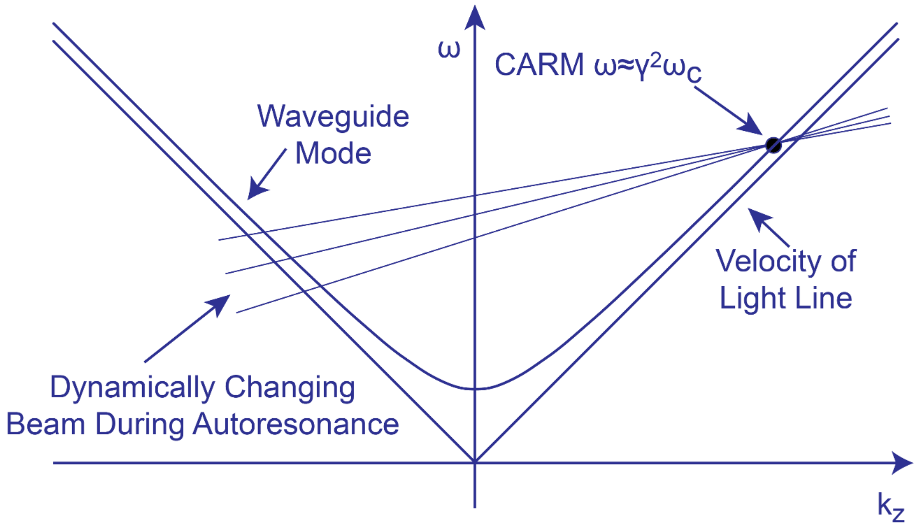

Figure 2.12: Dispersion plot for CARM.

This continuous compensation of the resonance conditions is the so-called auto resonance phenomenon. Figure 2.12 demonstrates that during auto resonance the fast cyclotron wave changes to ensure that the working frequency is constant even though the phase velocity and Cyclotron frequency are changing. Cyclotron resonance devices operated in this regime are called Cyclotron auto resonance MASERs (CARMs). Other lower frequency interactions on the dispersion curve need to be avoided; this can be done by choosing suitable operational conditions.

The large Doppler up shift used in the CARMs allows for a reduction in the magnetic field requirements. The instability in a CARM is convective. Feedback is a necessary condition of operation therefore a Bragg resonator may be used to facilitate the process. The electron beam employed in a CARM has a relatively low velocity ratio ($\alpha \approx 0.7$). The efficiency of a CARM is highly sensitive to the spread in the beam velocity $\Delta v_z/v_z$, which must be smaller than 1% to achieve the theoretically optimal efficiency of 40%[35].

2.7 Gyro-BWO

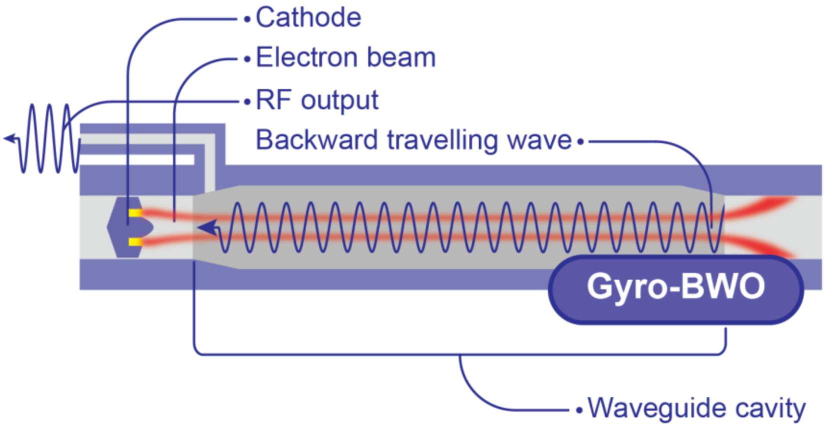

Figure 2.13 Schematic diagram of a Gyro-BWO

The gyro-BWO is an efficient source of high-power frequency-tuneable coherent radiation. If the design of the gyro-device is such that the electron beam or the magnetic field enable the fast wave beam line on the dispersion diagram to cross on the negative side of the waveguide mode with a negative phase velocity as demonstrated in Figure 2.14 then there will be generation of a “backward wave.” This is absolute instability (internal feedback) where the waves grow in time at the same position.

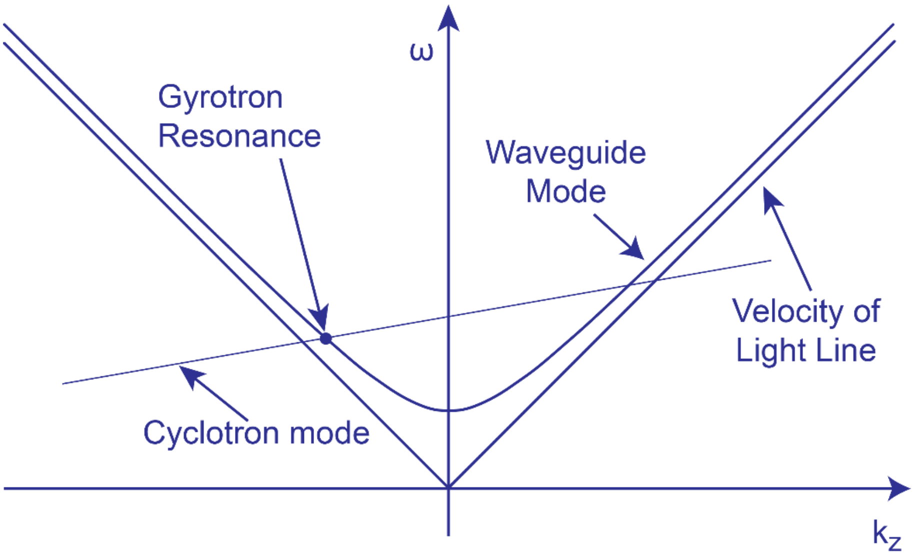

Figure 2.14 Dispersion plot for Gyro-BWO.

The operational frequency is determined by the slope of the beam line on the dispersion diagram, which is a function of the electrons velocity v_z. The velocity v_z is a function of the acceleration voltage V_0, so the operational frequency may be changed over a broad range by changing the acceleration voltage as well as the magnetic field. Relatively high magnetic fields are required for high frequency operation due to a Doppler down shift in frequency $\omega_c/2 < \omega < \omega_c$. For oscillation at the fundamental of the electron cyclotron, the output frequency scales as 28GHz/Tesla for a mildly (70keV) relativistic electron beam.

The early studies into gyro-BWO's were conducted in the 1960's in Russia. As the electron beam travels down the interaction region in an applied magnetic field its cyclotron mode couples with a waveguide mode of a backward propagating wave. This results in the growth of a microwave from the inherent noise in the system. The gyro-BWO is an oscillator and has been extensively studied[36,37,38,39,40].

2.8 Gyro-TWT

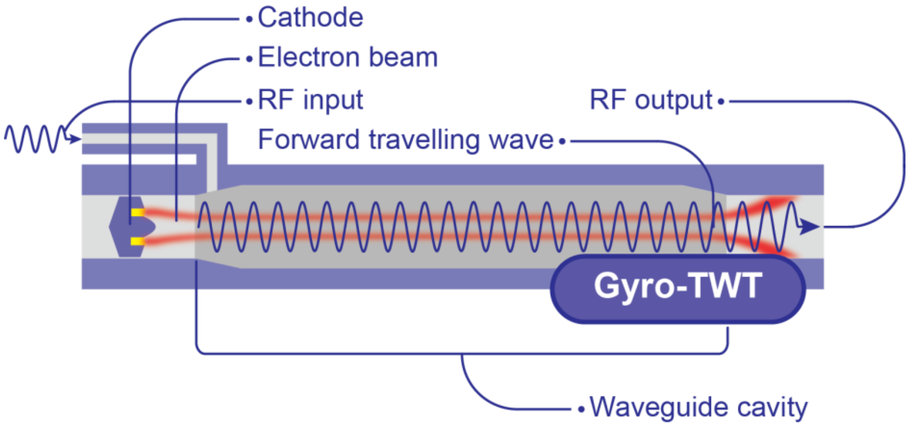

Figure 2.15 Schematic diagram of a gyro-TWT.

In the gyro-TWT, a tenuous electron beam is emitted into a cylindrical waveguide cavity in order to drive the ECM instability in conjunction with a 'seed' RF signal from an input coupler. Since there is no output signal without the input in a gyro-TWT the system can be assigned a gain, which is given by:

$$G = 10\, log_{10}(P_{out}/P_{in}) dB \qquad 2.7$$

The Gyro-TWT is capable of a high gain and efficiency using a moderately relativistic electron beam to interact with a fast waveguide mode at a grazing intersection between the fast cyclotron mode and the waveguide mode as seen in figure 2.16.

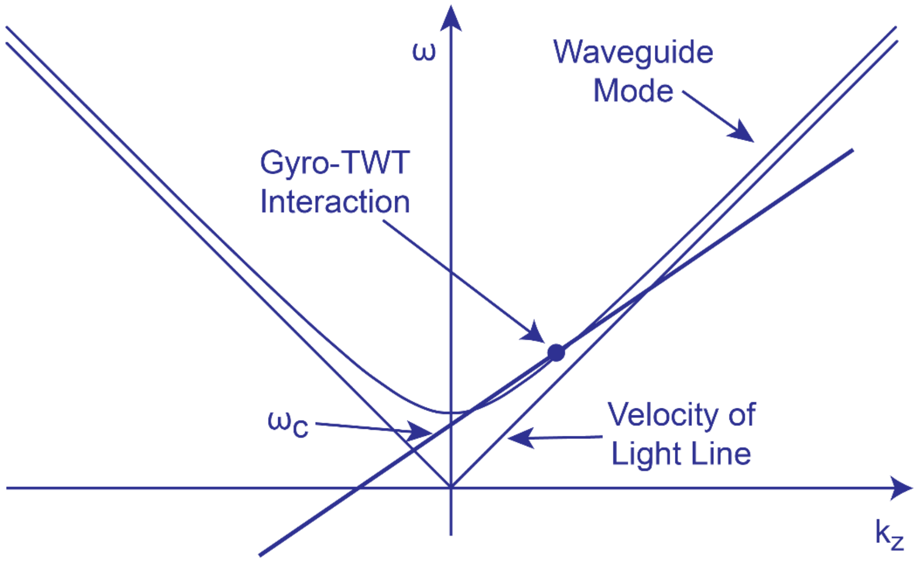

Figure 2.16 Dispersion plot for Gyro-TWT.

The high gain and efficiency of the gyro-TWT is due to the close matching of the phase velocities of the modes and the fact that the phase velocity of the waveguide mode is almost equal to v_z. The axial bunching mechanism is relatively weak in a gyro-TWT $\omega/k_z \gg c$. The gyro-TWT uses an unloaded waveguide as a resonant circuit, which allows the gyro-TWT to operate with a much larger potential bandwidth than other gyro-devices. The typical performance of gyro-TWT devices at ~95 GHz is shown later in Table 2.1.

The gyro-TWA exploits a convective instability near the cut-off frequency that, at sufficiently high beam current, may turn into an absolute instability when the unstable spectrum extends into the backward wave region. Oscillation is also possible even at low current levels, due to the possibility of feedback from reflection. Such reflections occur when sections of the interaction circuit are mismatched. The feedback loop can be effectively eliminated through the incorporation of a sever into the device. However, the absolute instability is quite different from the reflective instability in that the associated backward wave is internally generated by the AC electron beam current and, hence, even when sections of the interaction structure are separated by a sever, they remain coupled by the beam. One solution is the introduction of either lumped or distributed wall loss. These losses are distributed over much of the interaction length and, like the sever, cut off the reflective feedback loop. Unlike the sever, however, it forms an integral part of the amplification stage whilst functioning as an energy sink to the predominantly backward power flow of the absolute instability.

Whereas all of the energy in a pure electromagnetic mode is in the electromagnetic fields, when the mode exists in the presence of energy from the beam, the generated mode not only resides in the electromagnetic fields, but also in the kinetic energy of the oscillatory electron motion. Wall losses absorb only energy from the electromagnetic fields and so attenuate the reflected wave significantly more than they reduce the forward gain of the amplifying wave. This effect can be exploited to achieve both high gain and reflective stability. Reflective oscillations of a global nature start when the total amplifier gain exceeds reflection plus any internal attenuation losses.

It was also shown theoretically that the danger of oscillation through an absolute instability (in the absence of any reflection) could be reduced if there were a small wall resistivity. There are, however, a number of problems associated with wall resistivity. Firstly, it reduces both the gain and the bandwidth of the device. Additionally, it introduces the possibility of a resistive instability.

2.9 The Strathclyde W-band Gyro-device

In most gyrotrons this interaction region usually consists of a smooth cylindrical waveguide with dimensions carefully chosen to meet the conditions for stable emission of radiation. The Strathclyde W-band device does not use a smooth waveguide; the interaction region in this case is a helically corrugated waveguide as shown in Figure 2.17.

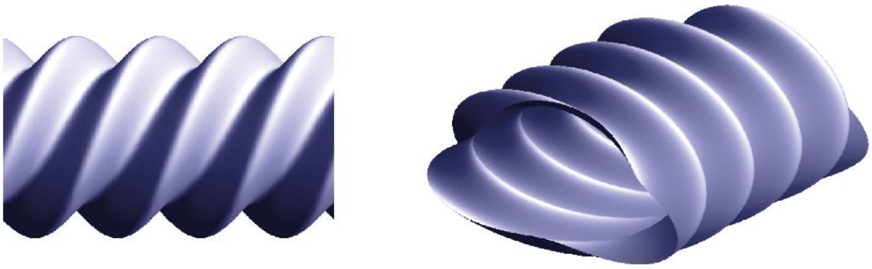

Figure 2.17: Helically corrugated structure.

Using this structure as the basis for both the gyro-TWA and BWO (Figure 2.18) provides a number of advantages over the conventional smooth waveguide. Operational bandwidth is increased and the required magnetic field reduced by operating at the 2nd cyclotron harmonic, while the power handling is increased due to the oversized waveguide. This allows for higher frequency operation at reduced costs.

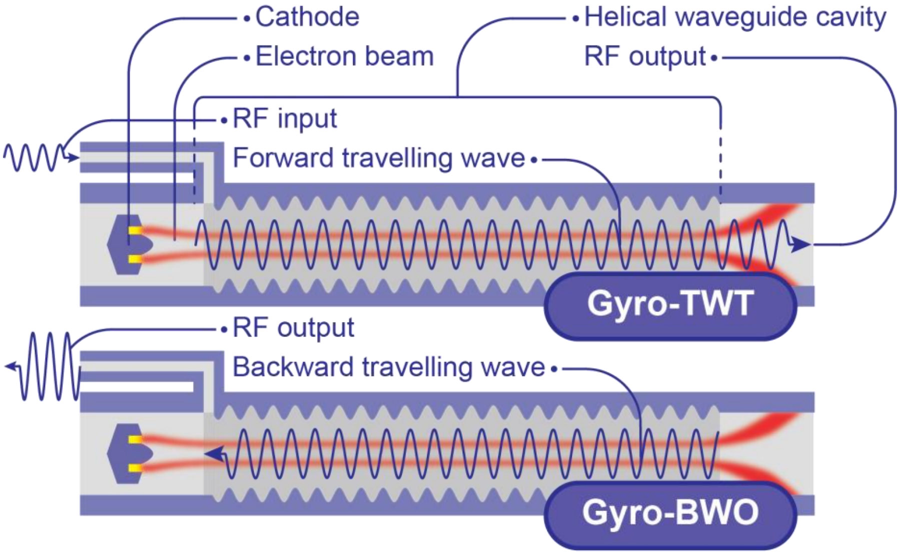

Figure 2.18: Schematic showing the Strathclyde gyro-devices based on helically corrugated interaction region.

Until the late 1990s, only the gyrotron and gyro-klystron had been developed sufficiently to achieve high operating efficiency. Whilst the gyro-TWA offered attractive broadband amplification, there are a number of problems associated with interaction in a circular waveguide. The most attractive operating regime is when the axial electron velocity is close to the group velocity of the wave. On a dispersion diagram, this would appear as a grazing incidence of the wave and beam dispersion characteristics. Consequently, gyro-TWA's employing weakly relativistic electron beams are designed to operate in the region of $k_z = 0$. Subsequently, when operating close to zero axial wavenumber, the beam-wave synchronism line intersects with the waveguide mode only over a narrow bandwidth (Figure 2.16).

Additionally, operation close to $k_z = 0$ increases the possibility of a parasitic gyrotron self-excitation, making operation susceptible to absolute instability even when the circuit is perfectly matched so that there is a complete absence of feedback. In the case of a resonant cavity, ω and $k_z$assume discrete values, hence restricting cyclotron resonance to a narrow range of magnetic field strength for each mode. The waveguide structure of the gyro-TWA, by contrast, has no such restrictions and, consequently, the electrons can resonate simultaneously with a multitude of forward and backward waves both at the fundamental and higher cyclotron harmonics.

This can be shown in Figure 2.19, where the dispersion of the first four cyclotron harmonic beam-wave synchronism lines along with lowest order waveguide mode are plotted. The interaction between the waveguide and electron beam can occur at the points where there is an intersection.

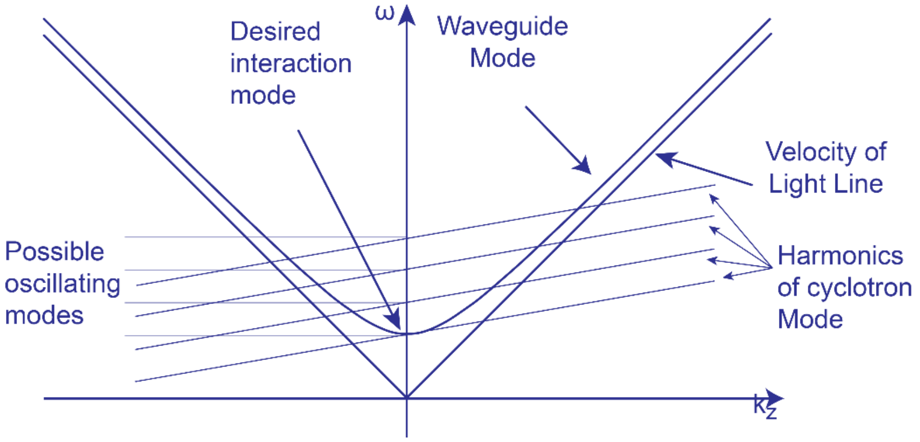

Figure 2.19: Dispersion diagram illustrating possible instabilities for operation close to $k_z = 0$ in a circular waveguide.

Intersections in the backward-wave region ($k_z < 0$) are potential absolute instabilities, whilst those in the forward-wave region ($k_z > 0$) are normally convective instabilities. When operating close to $k_z = 0$, the condition for a mode to become absolutely unstable is when the instability bandwidth of the forward mode extends into the backward-wave region. The result is a threshold current, above which the desired convective instability transitions into an absolute instability.

In the case of gyro-TWAs driven by electron beams with relativistic axial velocities, bandwidth and stability may be improved by selecting an operating wave with a relatively large axial wavenumber, such as is employed in the CARM (Figure 2.12). However, by considering again (2.6), it can be seen that waves having large axial wavenumber, k_z, will be more susceptible to degradation of phase-matching of the interaction due to the varying Doppler shifts associated with any spread in axial electron velocities, v_z. This will reduce both the gain and the efficiency of the device.

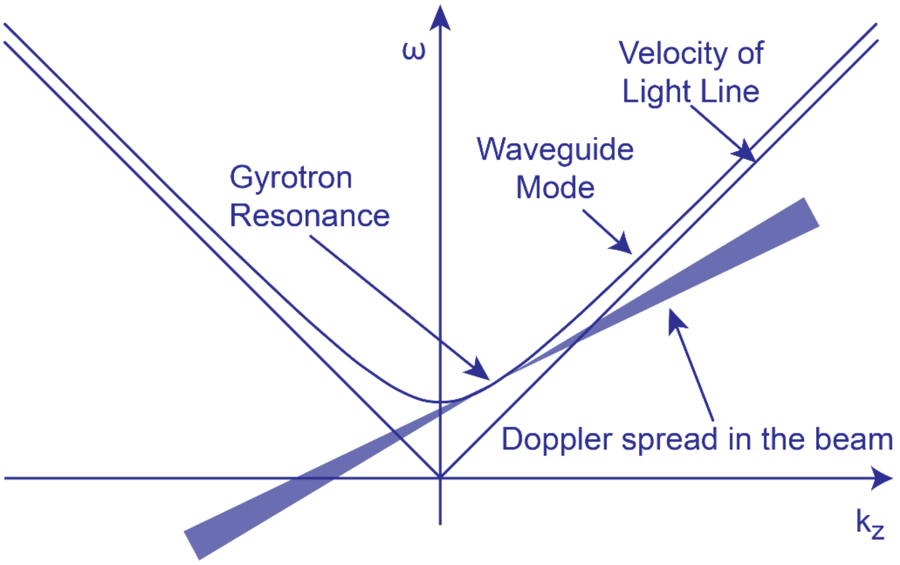

Figure 2.20: Dispersion diagram illustrating beam-wave interaction in a circular waveguide operating at $k_z >> 0$.

To overcome these problems associated with interaction in a circular waveguide, it is possible to radically alter the dispersion of the waveguide in the region close to the zero axial wavenumber so as to significantly increase the group velocity of the eigenwave and the width of the resonant electron-wave interaction band. This can be achieved through the introduction of a helical corrugation on the inner wall of the circular waveguide.

2.10 Synthesis of Ideal Waveguide Dispersion

The geometry of a threefold helical waveguide is illustrated in Figure 2.21. The helical profile of the waveguide's inner surface can be represented in cylindrical coordinates as:

$$r(\phi, z) = r_0 + l\cos\left(\bar{m}_B\phi - \bar{k}_B z\right) \qquad 2.8$$

Where r_0 is the mean radius, l is the corrugation amplitude, $\bar{m}_B$ and $\bar{k}_B = \frac{2\pi}{d}$ respectively define the azimuthal number and axial component of the Bragg periodicity vector and d is the period of the corrugation.

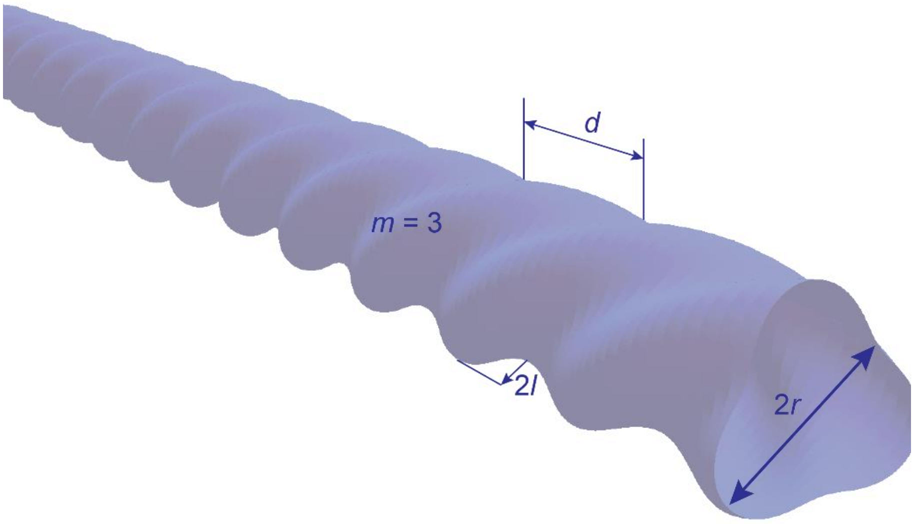

Figure 2.21: Geometry of a three-fold helical waveguide.

In the case of a corrugated waveguide, it is possible to represent the electromagnetic field as the superposition of spatial harmonics. Assuming that the corrugation is amplitude is small ($l \approx 0$) these spatial harmonics possess dispersion characteristics approximately equal to those of the smooth waveguide modes transposed in axial wavenumber by an integer number of the Bragg periodicity vector, k_B. Resonant coupling occurs between the modes for nonzero corrugation amplitudes in the case when their axial and azimuthal wavenumbers satisfy the Bragg conditions:

$$\bar{m} = m_A + m_B$$

$$k_{z_1} - k_{z_2} = k_B \qquad 2.9$$

Where m_1 and m_2 are the azimuthal numbers of the modes 1 and 2 respectively (positive m for right-handed modes) and k_{z1} and k_{z2} are the axial wavenumbers. The result is the formation of eigenwaves, the dispersion of which can be represented as a splitting of the partial mode dispersions close to the frequencies of intersection with the dispersions of the spatial harmonics.

Let k_{z1} and k_{z2} now be tied to the specific values of axial wavenumber taken at the wave vector k_0 of exact Bragg resonance. Should coupling occur in the frequency region close to the cut-off of mode 2, one of the eigenwaves (the fundamental spatial harmonic) can exhibit dispersion with positive group velocity at zero wavenumber – a property that is ideal for gyro-devices. The dispersion splitting may be increased by increasing the corrugation amplitude and a value $k_{z2} \geq 0$ is achieved through careful selection of the corrugation period so as to create a larger eigenwave group velocity that is almost constant over a broad frequency band. Additionally, this results in an upshift in the cut-off frequency of the undesirable upper eigenmode.

Such an eigenwave, with non-zero group velocity near zero axial wavenumber, is ideal for broadband, stable gyro-TWA operation with the specific value of group velocity for the eigenwave tuned to the longitudinal electron beam velocity through the correct setting of the geometrical parameters of the corrugation.

The design of the helical interaction region was undertaken with the assistance of three computer codes, namely the mathematical packages MatLab and the numerical particle in cell (PIC) code MAGIC, which uses a Finite-difference time domain Maxwell solver based on a discrete formulation of the conventional equations over a so called "Yee Cell" formulation is that the full-grid and half-grid placement of field elements[41].

Four key parameters need to be determined in order to design the corrugation for a given set of gyro-TWA operating parameters. These are the mean radius of the waveguide, the corrugation depth, the axial period of the helical corrugation and the total length of helical waveguide gain section. The first three parameters are determined by through the use of perturbation theory in the absence of an electron beam. The resultant normalised equation is:

$$(\mathrm{k}_z^2 - 2\delta)\left(k_z + \varDelta_g - \frac{\delta}{k_0}\right) = \frac{2\sigma^2}{k_0} \qquad 2.10$$

Where δ is the frequency mismatch, Δ_g the geometric mismatch, σ the coupling coefficient of the two eigenmodes, k_0 the axial wavenumber for the TE_{21} mode and k_{z0} the axial wavenumber for the TE_{11} mode corresponding to k_0.

A good approximation to the operating eigenwave of the gyro-TWA was obtained using MatLab. These purpose written codes provided considerably shorter solution times than more general numerical codes such as MAGIC and, hence, a far greater range of parameter space could be explored. By matching this operating eigenwave with an electron beam line it was possible to determine the desired mean waveguide diameter, corrugation depth and axial period. The dispersion of the operating eigenwave was then confirmed using MAGIC to directly model the performance of the helical waveguide. In this way the helix parameters are more accurately determined.

The frequency band over which the dispersion of the eigenwave is approximately linear determines the mean diameter of the helical interaction region. For a frequency band of 90 – 100 GHz a mean diameter of 1.3 mm was chosen. The dispersion of the operating eigenwave is shown in Figure 2.22.

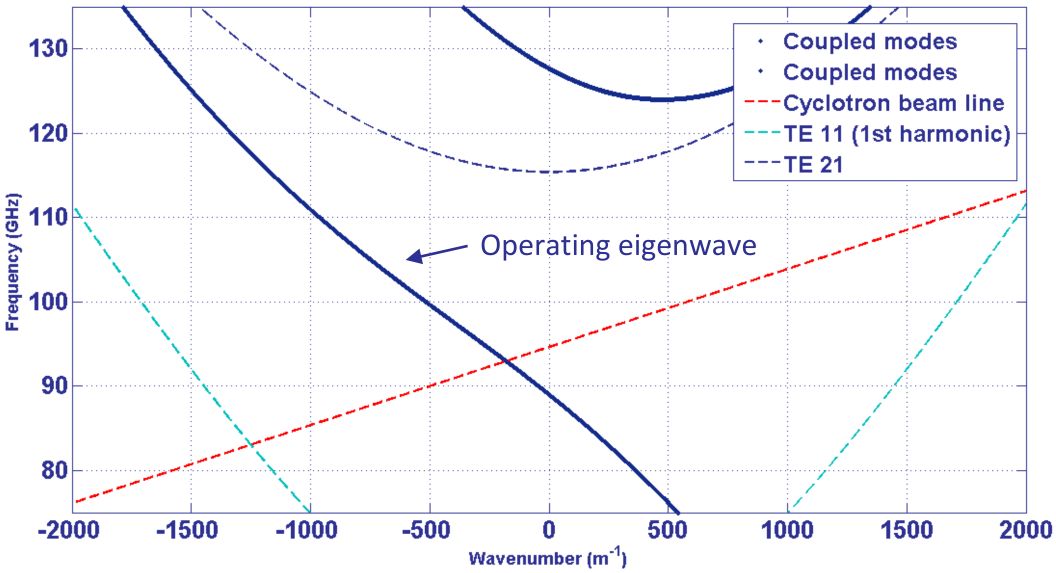

Figure 2.22: The dispersion of the operating eigenwave as determined by perturbation theory (Matlab). The solid dark blue line represents the coupled modes, with the operational mode denoted by an arrow. The first spatial harmonic of the TE_{11} *is shown in light blue (dashed) and the* TE_{21} *is shown in dark blue (dashed). A typical electron beam dispersion profile is shown in red (dashed).*

2.11 Beam and Wave Decoupling

The main focus of this project was to develop a decoupling method by which the electron beam and the EM-wave are separated after the interaction region. The spent electron beam is then collected and its energy recovered, while the radiation is conditioned for extraction from the system for external applications. As the electron beam in question is typically high energy, the question of its disposition is not trivial and as such any unwanted encroachment of the beam may cause excessive heating of components and even undesired emission of x-ray radiation. This is especially true if the RF radiation is extracted by means of a dielectric window, which would undergo significant damage, should the electron beam be allowed to impact upon it.

2.11.1 Energy recovery systems

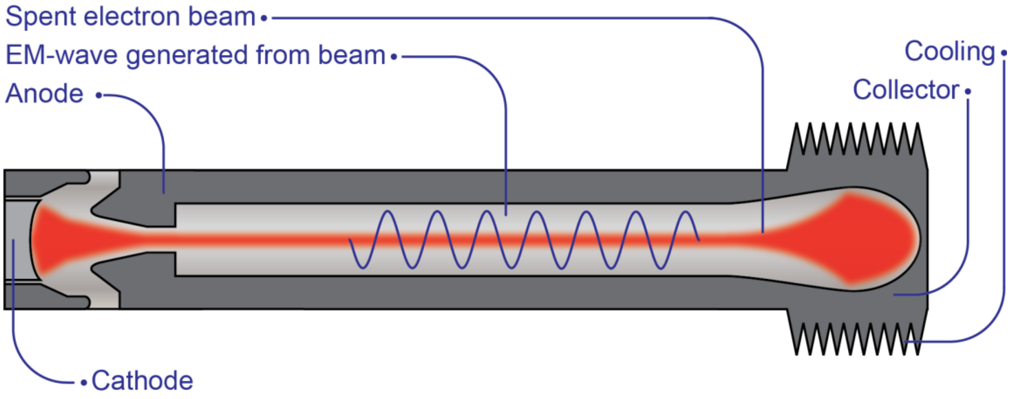

Figure 2.23: Simple electron beam tube and collector

In a simple microwave tube, the electron beam is emitted at a cathode and transported through some interaction system, where there is an exchange of energy between the electron beam and an electromagnetic wave. The spent electron beam is then dumped onto a collector that is at the same potential to the anode (ground potential). This results in energy lost to the surroundings in the form of heating by the electrons bombarding the metallic collector as well as generation of x-rays when the electron beam has a high energy, which is always the case in relativistic devices. This is a problem that may be overcome by providing cooling and shielding around the collector, but the real issue for operation of high power devices is the overall system efficiency. If the radiation is generated with a 40 kW electron beam and the system losses are neglected, then if the output power is ~10 kW there will be 30 kW of wasted energy in the electron beam and a maximum system efficiency of 25%. This is a fundamental barrier to the efficiency of any device but it may be overcome by using a depressed collector system, where the potential of the collector is ‘depressed’ in relation to that of the anode (below ground) and closer to the potential of the cathode. A portion of the electron energy is recovered as they are decelerated by the electric field.

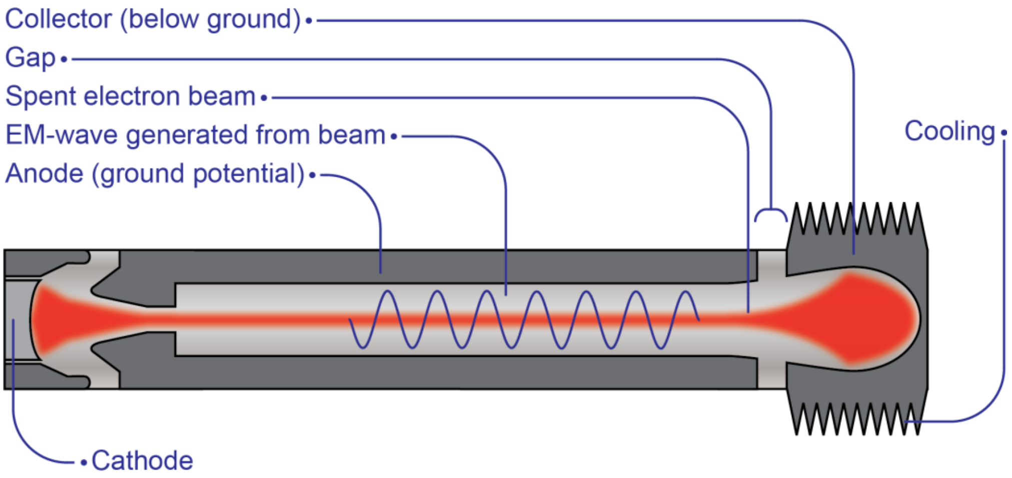

Figure 2.24: Simple electron beam tube and with single stage collector

This idea has been around since the earliest developments of high power microwave devices in the 1940's[42], and was advanced by adding an additional stage to the collector; improving the collector efficiency further. Early efforts to produce tubes with higher efficiencies using multiple stages were however unsuccessful, due to problems with back-streaming of electrons. In the 1960's there was a re-evaluation of this problem in light of the need for extremely highly efficient devices, particularly TWT's, for operation in the challenging environment of space. Where there is a particular need for energy efficiency and proper heat management.

The inclusion of these energy recovery systems is almost trivial in the more conventional types of vacuum tube, where the beam dynamics are simple. In TWT's, BWO's, Klystrons and IOT's the electron beam is non-relativistic and linear, having all the momentum in the longitudinal direction. Gyrotrons, by their very nature, provide a much more complicated environment for the operation of depressed collector systems. There is a far higher percentage of electron momentum carried in the transverse direction by the gyrating electron beam. This has however, not stopped the development of depressed collectors for gyrotrons. The highest power gyro-devices are used in applications where it is unacceptable to 'throw away' many kilowatts of beam power, therefore the design of reliable collectors is critical to modern high power gyro devices and has been facilitated through the use of computational simulation and optimized design.

2.11.2 Quasi-optical mode converters and gyrotrons

There are a number of methods by which RF power may be extracted from a gyro-device. In the simplest case the power is transmitted axially through a microwave window directly adjacent with the gyrotron cavity. In this case, provision must be made for the inclusion of tapers after the cavity and adequate provision for dumping the electron beam before the window. This arrangement is generally only found in experimental gyro-devices where efficiency and beam recovery are not critical. A typical arrangement for such a structure is shown in Figure 2.25.

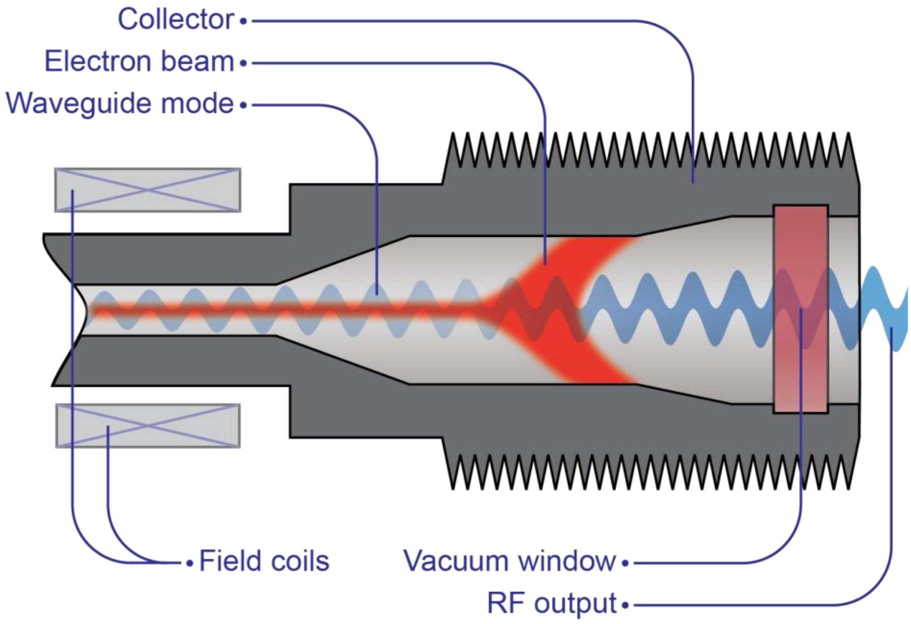

Figure 2.25: longitudinal gyro-output schematic.

The quasi-optical output coupler or Vlasov launcher[43] is another method commonly used to extract the RF power radially from the system. This type of system usually consists of a waveguide launcher in conjunction with a set of fixed mirrors that correct the radiated beam and form a Gaussian mode. This free space mode is then suitable for transmission through a window.

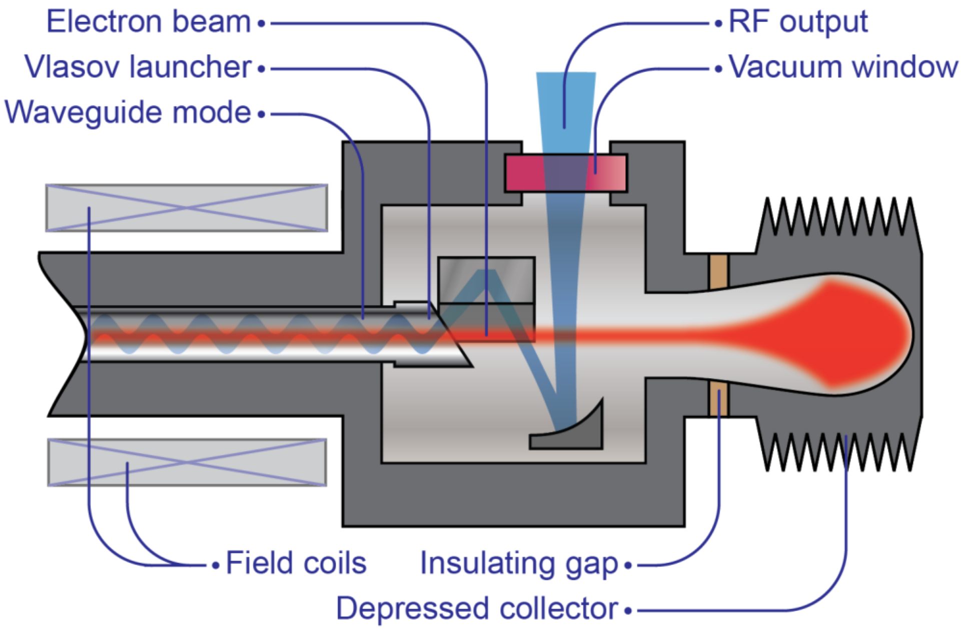

Figure 2.26: Vlasov type gyro-output schematic.

The major advantage of the Vlasov launcher (Figure 2.26) is that with the RF radiation absent from the system the electron beam can be freely manipulated to recover a portion of the beams energy. This has the benefit of increasing the overall efficiency of the system as well as reducing the energy in the beam at the interface with the collector thus reducing the levels of hazardous x-ray production, as well as reducing the complexity and cost of the cooling system for the collector. The disadvantage of this method however, is that by introducing a spiral cut into the waveguide a geometrical factor arises, which places a physical limit on the operational bandwidth of the system. This means that any gyrotron that uses a Vaslov launcher will be a narrow band device, or at best will be step tuneable over a range of discrete operating frequencies. As the Strathclyde gyro-TWA and gyro-BWO are designed to be constantly tuneable over the range between 90 to 100 GHz another method was sought to provide the beam and wave decoupling.

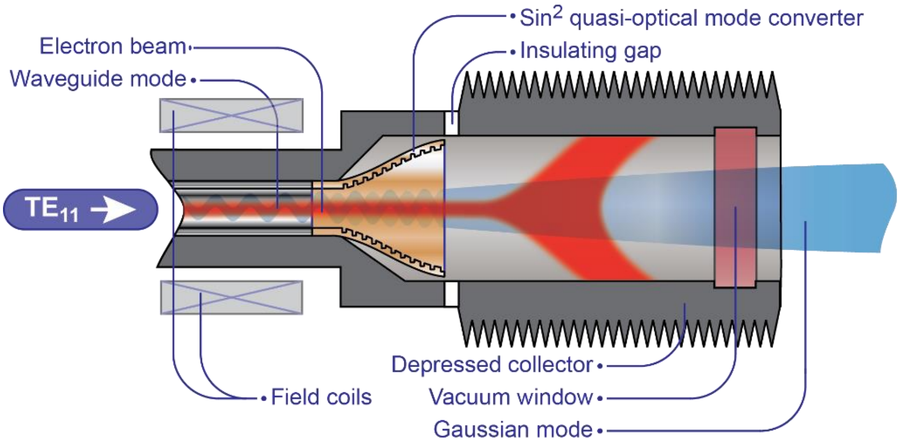

Figure 2.27: Proposed design schematic for quasi-optical beam/wave decoupling system in gyro-TWT

The approach that seemed to best fit the design of the Strathclyde W-band gyro-TWA was to dispense with the axial output and complex mirror arrangement of the Vlasov launcher in favour of a corrugated mode converting horn-launcher. This could bridge the insulating gap of a depressed collector by launching a free-space mode and out-couple the wave axially once the electron beam has been intercepted by the collector. A schematic demonstrating the premise is given in Figure 2.27.

This has the advantage of a proven ability to operate over a large bandwidth with a very small reflection coefficient. This low reflection is of crucial importance in applying this method to an amplifier design, where the reflection places a limit on the overall gain of any amplifier. In this case, a reflection of less than -35 dB is deemed to be acceptable and within the known operational limits of such a corrugated horn. The main disadvantage of this method is that the beam and wave remain coaxial thereby introducing a complication by placing the output window on the axis of the electron beam. This would be a critical obstacle for conventional electron beams, but our system uses a large orbit axis encircling electron beam and as such may be collected safely before reaching the output window.

2.12 Applications of Gyro-devices

The current development of high power gyro-devices is driven in part by the need for powerful sources of microwave and sub-microwave radiation across a wide range of applications and fields. Figure 2.28 provides a representative outline of the current applications for devices in this range of wavelengths[18].

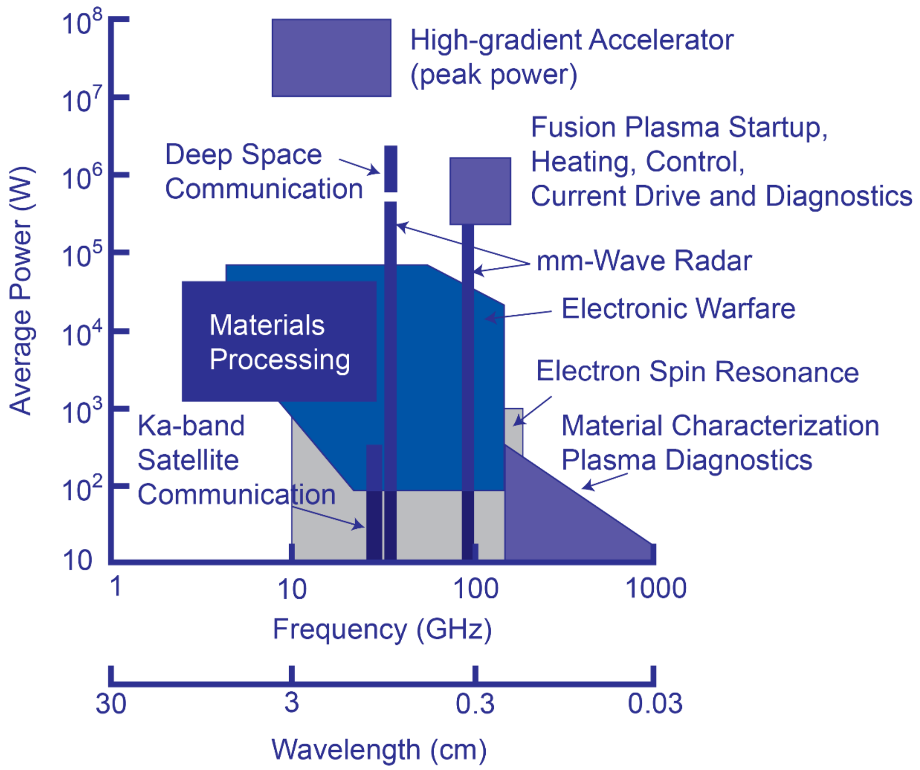

Figure 2.28 Applications of high power mm and sub-mm waves[18]

The gyro-TWT has been demonstrated to be an attractive source for RADAR and communications applications due its high bandwidth capabilities. Such millimetre wavelength sources can provide very high resolution RADAR imaging as well as the ability to accurately profile clouds and fog[44]. This ability to penetrate this atmospheric window also makes for an excellent source for deep space communications. One of the main applications of the gyro-TWA is in high frequency spectroscopy, which can hugely benefit from this new technologies ability to provide high power amplification over high bandwidths and at high frequencies, resulting in improved absolute and concentration sensitivity, higher electron polarisation, improved spectral resolution and orientational selectivity. High frequency pulse EPR is also key to next generation DNP techniques that have recently dramatically improved the sensitivity of NMR (by orders of magnitude) for many types of sample. There is therefore a strong requirement for the development of high peak power pulse sources at modest average power, bandwidth at high frequency (e.g. 10 GHz at 95 GHz, 20 GHz at 260 GHz and 40GHz at 395 GHz) for pulse DNP.

Radiation sources for high field EPR, whether pulsed or CW, must be in the millimetre or sub-millimetre wave regions to enable the technique to deliver its unique promise of dramatic improvements in sensitivity and resolution. Here, cutting edge international EPR research is dominated by the application of multi-dimensional pulse techniques, double resonance and CW multi-frequency EPR, especially at high fields. Leaders in this field are Dr. Graham Smith's High Field EPR group at the University of St. Andrews[45,46].

The gyro-klystron is also an excellent candidate for a millimetre wavelength source with applications in communications and RADAR, but research into gyro-klystron has also returned novel non-military RADAR applications such as the detection and tracking of space debris, an application which is becoming increasingly important as the commercialisation of space and subsequent increase in the number of satellites in low earth orbit increases. Gyro-klystrons have also found uses in the field of particle accelerator physics: At CERN there has been development of a 50 MW 30 GHz W-band gyro-klystron for testing and conditioning of RF structures in the Compact Linear Collider[47].

Gyro-BWOs have proven to be suitable for applications where a broad range of frequencies are desirable; due to the capability of the gyro-BWO to be continuously tuneable over a broad frequency range by altering either the magnetic field or the accelerating voltage[48,49]. These devices would be suitable for military use in electronic counter measures, where the ability to tune over a wide frequency range is necessary. They are also of use in plasma heating and spectroscopy and as drivers for high power amplifiers.

Gyro-monitrons or oscillators are by far the most mature technology of all the gyro-devices having found a role in the heating of fusion plasmas in the early 1970's, when the Institute of Applied Physics (IAP), Nizhny Novgorod, Russia produced gyrotrons capable of 1.5 kW at 326 GHz and 10 kW at 34 GHz[50, 51]. Since then the development of these devices has been carried forward by both industry and the scientific community, and gyrotrons have now become available that can provide megawatts of power[52] and are used in plasma start-up, plasma heating, current drive, instability control and in plasma diagnostics[53]. Gyrotrons at lower powers have also found uses in the processing and characterisation of materials.

2.13 Current Status in Gyro-TWT development

At this time, a number of institutions are actively researching W-band gyro-TWT devices for various applications. The main technical problems include, but are not limited to, the optimisation of a device that can produce a high output power while retaining a reasonable operational bandwidth. The University of California has produced a gyro-TWA employing distributed wall loss, which is capable of an output power of 140 kW (CW) with a bandwidth of 5%. Whereas the higher power device developed in Taiwan has achieved a peak output of 215 kW but with a more limited bandwidth of 0.7%. A summary of these devices is given in Table 2.1.

Out of all of the devices listed only one, the W-Band TE_{01} Mode Gyrotron-TWA from UC Davis, was shown to be capable of operating with high power with a continuous wave output. Table 2.1 should be compared to Table 2.2, which details the operating parameters of the EIKA at 94GHz[54]

Device	Operating Frequency (GHz)	Output (kW)	Gain (dB)	Efficiency (%)	Bandwidth (%)
University of California gyro-TWT[55]	93.5	75 (peak[1])	45	22.5	3.7
University of California ultra-high gain gyro-TWT[56]	93.5	110 (peak)	71		5
University of California 94GHz[57]	92.2	59	42	26	1.3
W-band second-harmonic gyrotron traveling wave amplifier with distributed-loss and severed structures[58]	89.9	215 (peak)	60	14.3	1.8
Broadband W-Band Gyro-TWT Amplifier[59]	96	1.5 (peak)			8.3
Novel quasi-optical W-band gyro-TWT[60]	94				
High-average power W-band gyro-amplifiers[61]	93.8	10.2 (peak)	33	31	0.7
W-Band TE01 Mode Gyrotron[62]	92	140 (CW[2])	50	28	5

Table 2.1 Current gyro-TWT developments

94 GHz EIK	
Peak Power	2000 W
Bandwidth	250 MHz
Duty Cycle	3-10%
Gain	55 dB
Efficiency	33%

Table 2.2: CPI 94 GHz EIKA.

---

[1] Peak power output for pulsed operation

[2] Continuous wave power output

3 Electromagnetic Theory of Guided Waves

In this chapter, an overview of the fundamental physical processes relevant to the current investigation will be presented. Included in this discussion will be consideration of basic electromagnetic theory, boundary conditions, impedance, and wave propagation within guided and corrugated structures, modes and waveguide dispersion.

3.1 Maxwell Equations

James Clerk Maxwell laid the theoretical foundations for understanding all electromagnetic phenomena with his fundamental laws of electromanetism.[63] These can be summarised in the following four partial differential equations derived by Oliver Heaviside[64]. These laws are given by equations (2.3 – 3.4), below[65].

Faraday's Induction Law

$$\nabla \times \overline{\boldsymbol{E}} = -\frac{\partial \overline{\boldsymbol{B}}}{\partial t} - \overline{\boldsymbol{M}} \tag{3.1}$$

Ampère's Circuital Law

$$\nabla \times \overline{\boldsymbol{H}} = \frac{\partial \overline{\boldsymbol{D}}}{\partial t} + \overline{\boldsymbol{J}} \tag{3.2}$$

Gauss's Law

$$\nabla \cdot \overline{\boldsymbol{D}} = \rho \tag{3.3}$$

Gauss's Law for Magnetism

$$\nabla \cdot \overline{\boldsymbol{B}} = 0 \tag{3.4}$$

Faraday's law of induction relates the circulation of an electric field ($\boldsymbol{E}$) to the rate of change of a magnetic flux ($\boldsymbol{B}$) enclosed by the field minus the magnetisation of the media ($\boldsymbol{M}$). Ampère's law is the corollary of this relating the circulation of a magnetic field ($\boldsymbol{H}$) to the rate of change of the electric displacement ($\boldsymbol{D}$) and the charge ($\boldsymbol{J}$).

3.1.1 Constitutive relationships

The relationships between the magnetic flux and the magnetic field and the electric displacement and electric field can be expressed in the constitutive relationships 3.5 and 3.6.

$$\overline{\boldsymbol{B}} = \mu_0 \mu_r \overline{\boldsymbol{H}} = \mu \overline{\boldsymbol{H}} \tag{3.5}$$

$$\overline{\boldsymbol{D}} = \epsilon_0 \epsilon_r \overline{\boldsymbol{E}} = \epsilon \overline{\boldsymbol{E}} \tag{3.6}$$

For a linear material, the individual electric and magnetic field terms can be linked through the form of two constitutive relations, given by equations 3.5 and 3.6. Here, ε_r and μ_r represent the relative permittivity and permeability, respectively, of the media in question, while ε_0 and μ_0 are the permittivity and permeability of free space, respectively. For convenience, the products of $\varepsilon_0\varepsilon_r$ and $\mu_0\mu_r$ will be referred to as the permittivity and permeability, ε and μ, respectively, of the media. A third constitutive relation is often used for the case of a good metallic conductor. In such a case, the current density is linked to the electric field, through the conductivity of the metal (σ), as given by equation 3.7.

$$\bar{\boldsymbol{J}} = \sigma\overline{\boldsymbol{E}} \qquad 3.7$$

3.2 Wave equation and plane wave solutions

The wave nature of electromagnetic fields can be derived completely from Maxwell's equations. Assuming a harmonic time dependence the time derivatives in equations 2.3 and 3.2 can be replaced by $j\omega$ then for a source free, linear, isotropic, and homogeneous region Maxwell's equations are:

$$\nabla \times \overline{\boldsymbol{E}} = -j\omega\mu\overline{\boldsymbol{H}} \qquad 3.8$$

$$\nabla \times \overline{\boldsymbol{H}} = j\omega\epsilon\overline{\boldsymbol{E}} \qquad 3.9$$

$$\nabla \cdot \overline{\boldsymbol{D}} = \rho \qquad 3.10$$

$$\nabla \cdot \overline{\boldsymbol{B}} = 0 \qquad 3.11$$

From Maxwell's equations, equations can be obtained for the electric and magnetic fields which describe their propagation. These inhomogeneous wave equations are given below by equations 3.12 and 3.13, for the electric and magnetic fields, respectively[66, 67]. For the case of a medium with no free sources, the right hand sides of both equations can be set equal to zero, leaving equations which hold for homogenous media.

$$\nabla^2\overline{\boldsymbol{E}} - \frac{\boldsymbol{1}}{\boldsymbol{c}^2}\frac{\boldsymbol{\partial}^2\overline{\boldsymbol{E}}}{\boldsymbol{\partial t}^2} = \boldsymbol{\nabla\rho} + \mu\epsilon\frac{\boldsymbol{\partial}\bar{\boldsymbol{J}}}{\boldsymbol{\partial t}} \qquad 3.12$$

$$\nabla^2\bar{\boldsymbol{H}} - \frac{\mathbf{1}}{\boldsymbol{c}^2}\frac{\boldsymbol{\partial}^2\bar{\boldsymbol{H}}}{\boldsymbol{\partial t}^2} = -(\boldsymbol{\nabla}\times\bar{\mathbf{J}}) \qquad 3.13$$

The solutions to these wave equations take a general form as shown by equation 3.14 which depicts the solution for the electric field in a Cartesian geometry. Such equations assume that both the magnetic and electric fields are time harmonic, and propagate along the z-axis, in the positive direction. The transverse and axial components of the electric field are given by E_{trans} and E_z, respectively, where ω is the angular frequency of the signal, and is equivalent to $2\pi f$, where f is its frequency. Additionally, k represents the wave-number of the wave.

$$\bar{\boldsymbol{E}}(x,y,z) = \bar{E}_{trans}(x,y) + \hat{z}\bar{E}_z(x,y)e^{i(\omega t-kz)} \qquad 3.14$$

For an unbounded medium, the frequency and wave-number are related through equation 3.15.

$$k = \omega\sqrt{\mu\epsilon} = \frac{2\pi}{\lambda} \qquad 3.15$$

Equations 3.16 and 3.17 represent the case for a wave travelling in a free, linear, isotropic, and homogeneous region, media with no free sources.

$$\nabla^2\bar{\boldsymbol{E}} + \omega^2\mu\epsilon\bar{\boldsymbol{E}} = 0 \qquad 3.16$$

$$\nabla^2\bar{\mathbf{H}} + \omega^2\mu\epsilon\bar{\mathbf{H}} = 0 \qquad 3.17$$

A simple solution for these differential equations, which represents a *plane*, *linearly polarised wave* may be expressed in 3.18 and 3.20 for both electric and magnetic fields.

$$\bar{\boldsymbol{E}} = \bar{\boldsymbol{E}}_0 e^{j(\omega t-kz)} \qquad 3.18$$

$$\bar{\boldsymbol{H}} = \bar{\boldsymbol{H}}_0 e^{j(\omega t-kz)} \qquad 3.19$$

3.3 Waveguide Theory

The previously derived equations describe the propagation of electromagnetic waves in free space or a homogenous and isotropic region of space, having the same material properties and characteristics over all space. When boundaries or discontinuities arise, there are an entirely different set of phenomena, which become evident on consideration of the conditions imposed by these boundaries. In the simplest case, a boundary may be as a simple change in material properties, such as a travelling wave may encounter passing from the free space of vacuum into a medium with a lower or higher dielectric constant. Here the change in the impedance can affect the incident and reflected wave, changing the propagation vectors as well as the phase. This is a simple example of which there are many others that may be considered, but the metallic waveguide is the most relevant for application to gyro devices.

A fundamental property of waves inside a guided structure is the cut-off frequency or wavelength. There exists in a bounded medium a limit on the maximum wavelength of the electromagnetic wave and there will be a point where the wavelength exceeds the limits imposed by the boundaries and is cut off. The boundaries imposed on an electromagnetic wave determines the fundamental frequency or the allowed mode. In both cases, there are no limits on the existence of higher harmonic frequencies, but nothing with a wavelength greater than this limiting dimension can propagate. This cut off wavelength, $\lambda_c$leads to the definition of a cut off wave number (equation 3.20)[68].This wavenumber determines the lowest possible propagating mode, which can be supported by the waveguide and is due to the physical dimension of the waveguide, either the longest side for a rectangular waveguide or the diameter for a cylindrical waveguide. Any mode with a wavelength larger than the cut off wavelength will not propagate and will decay evanescently.

$$k_c = \frac{2\pi}{\lambda_c} \tag{3.20}$$

Therefore the dispersion equation for the waveguide is:

$$\omega^2 = \frac{k^2}{\mu\epsilon} = k^2 {v_{ph}}^2 , v_{ph} = \frac{\omega}{k} = \frac{1}{\sqrt{\mu\epsilon}} , v_{gr} = \frac{d\omega}{dk} \tag{3.21}$$

Where $v_{ph}$is the phase velocity and $k = \sqrt{{k_c}^2 + \beta^2}$ is the magnitude of the magnetic wave vector and β is the propagation vector. It is worth noting that where, $\frac{1}{\sqrt{\mu_0 \epsilon_0}}$ is the velocity of light in a vacuum and as either μ_r or ϵ_r may be greater than unity, then there exists the possibility for the phase velocity within a bounded medium to be greater than the velocity of light in a vacuum. This does not violate the principle of relativity because the group velocity (which carries information) is always less than c.

3.3.1 Modes

There are three general classifications that can be applied to electromagnetic waves determined by the transverse amplitude profile of the electromagnetic wave. The general forms of these modes are characterised by the components of the electric and magnetic fields in the direction of propagation. If there are no $\boldsymbol{E}_z$ field components, then the electric field will exist only in the transverse plane. Therefore, the modes that exhibit this property are designated transverse electric modes (TE). As is the case, when there are no $\boldsymbol{B}_z$field components and the modes are transverse magnetic (TM). If the electric and magnetic field components are both defined in the transverse plane and both the $\boldsymbol{E}_z$ and $\boldsymbol{B}_z$ components are zero, then the wave is a transverse electric and magnetic wave (TEM). TEM cannot propagate in a hollow waveguide due to the absence of a central conductor. In free space the TEM wave the electric and magnetic field vectors are orthogonal to each other and in the plane normal to the direction of propagation.

3.3.2 Cut off

Figure 3.1 shows the first and second TE modes alongside the free space TEM mode. The lowest point in the plot is the cut off value for the waveguide, with all higher propagating modes existing above this line.

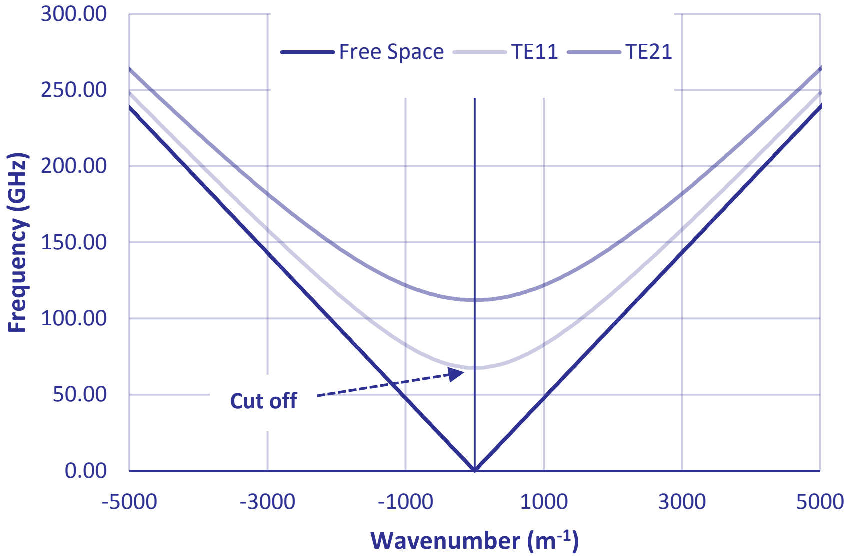

Figure 3.1 dispersion diagram of some waveguide modes.

The TM and TE modes are therefore infinite above the cut off and can be designated by the inclusion of mode indices to classify the successive modes. The indices are given here as $TM_{m,n}$ and $TE_{m,n}$. However, some texts may represent the indices in a different order, so the convention used herein is summarized in Table 3.1.

Waveguide Type	m	n	Fundamental Mode
Rectangular waveguide	Number of half wavelengths present across the longest transverse co-ordinate	Number of half wavelengths present across the shortest transverse co-ordinate	$TE_{1,0}$
Circular waveguide	Number of full wavelengths present across the azimuth co-ordinate	Number of half wavelengths present across the radial co-ordinate	$TE_{1,1}$
Co-axial waveguide	Number of full wavelengths present across the azimuth co-ordinate	Number of half wavelengths present across the radial co-ordinate	TEM
Corrugated circular waveguide	Number of full wavelengths present across the azimuth co-ordinate	Number of half wavelengths present across the radial co-ordinate	$HE_{1,1}$

Table 3.1: Mode designations in waveguides.

3.3.3 Impedance

The electrical concept of impedance can be useful in the analysis of electromagnetic waves, especially when considering the propagation of waves within a metallic waveguide. In circuit theory, the definition of impedance is the complex ratio of the voltage and current within an A/C circuit (equation 3.22).

$$Z = \frac{\mathrm{V}}{I} = \frac{|\mathrm{V}|e^{j(\omega t - \phi_V)}}{|I|e^{j(\omega t - \phi_I)}} \tag{3.22}$$

This extension of this concept to the analysis of electromagnetic fields provides three fundamental relationships, which are useful for characterisation and analysis of problems involving waveguides and radiated fields[69].

$$\eta = \sqrt{\frac{\mu}{\varepsilon}} \tag{3.23}$$

Equation 3.23 represents the *intrinsic* impedance of the medium. This is entirely dependent on the properties of the medium. In free space, the intrinsic impedance is constant in any direction. However, the permittivity and permeability for other materials can be a function of space and frequency; therefore, the intrinsic impedance may be more complicated for these cases.

$$Z_w = \frac{\mathrm{E}_t}{H_t} \tag{3.24}$$

The second type of impedance (3.24) that can be used to characterize EM fields is the *wave* impedance. This is a general property of the wave and may be different for TEM, TE and TM waves, depending on the medium or the frequency of the wave. The wave impedance is a ratio of the transverse components of the electric and magnetic fields. Another possible definition for the impedance of an electromagnetic field is the *characteristic* impedance (3.25). This property is defined for a transmission line, as the ratio between the voltage and current for a travelling wave in the line. The concept is extremely useful for representing waves in a waveguide when the waveguide is modelled as a transmission line circuit.

$$Z_0 = \sqrt{\frac{\mathrm{L}}{C}} \qquad 3.25$$

3.4 Boundary conditions

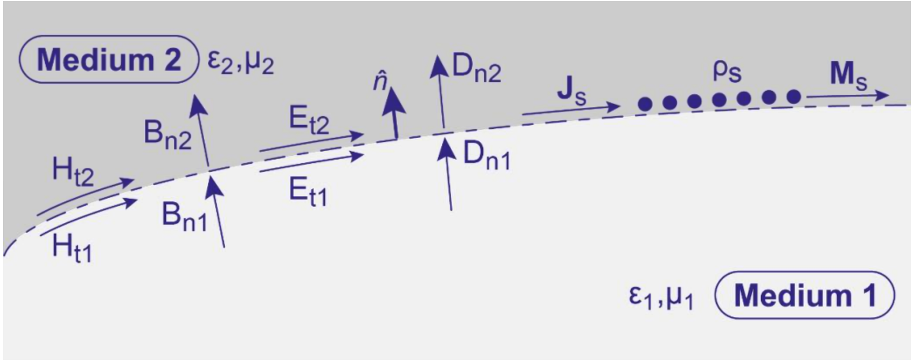

Figure 3.2: Geometry of a general material interface.

Maxwell’s equations are the basis for characterisation of any electromagnetic phenomenon, but their particular solution requires that a set of boundary conditions need to be applied. This is particularly true in the case of guided electromagnetic waves. Figure 3.2 describes the general case for electric and magnetic fields at a boundary between two different media.

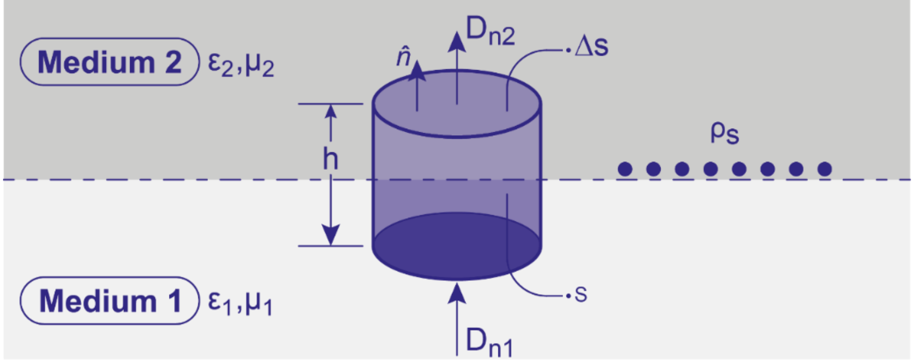

(a) Closed surface

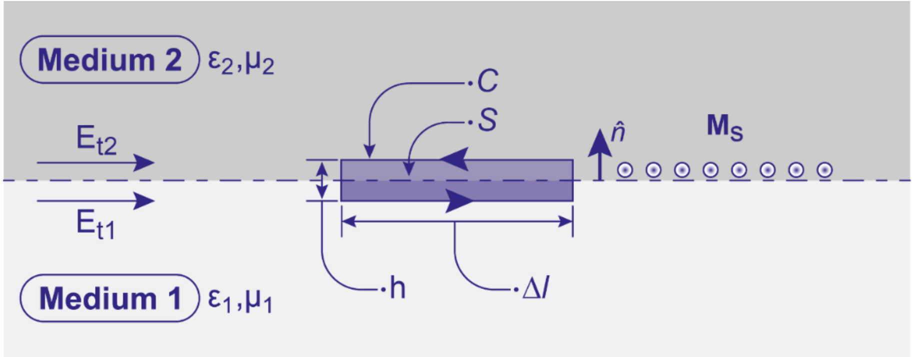

(b) Closed contour

Figure 3.3: Boundary geometry for arbitrary field distributions.

Considering Maxwell's equations over the geometries and field distributions expressed in Figure 3.3a and Figure 3.3b it is possible to derive a set of relationships for the field components at a material interface for the general case as well as the boundaries at a dielectric and conducting interface[70]. These boundary conditions are expressed in vector form by equations 3.26 —3.37.

Fields at a General Interface

$$\hat{\boldsymbol{n}} \cdot (\bar{\boldsymbol{D}}_2 - \bar{\boldsymbol{D}}_1) = \rho_s \cdot \tag{3.26}$$

$$\hat{\boldsymbol{n}} \cdot \bar{\boldsymbol{B}}_2 = \hat{\boldsymbol{n}} \cdot \bar{\boldsymbol{B}}_1 \tag{3.27}$$

$$(\bar{\boldsymbol{E}}_2 - \bar{\boldsymbol{E}}_1) \times \hat{\boldsymbol{n}} = \bar{\boldsymbol{M}}_s \tag{3.28}$$

$$\hat{\boldsymbol{n}} \times (\bar{\boldsymbol{H}}_2 - \bar{\boldsymbol{H}}_1) = \bar{\boldsymbol{J}}_s \tag{3.29}$$

At the boundary between two lossless dielectrics, there will be no surface current or charge densities therefore the normal components of $\bar{\boldsymbol{D}}$ and $\bar{\boldsymbol{B}}$ and the tangential components of $\bar{\boldsymbol{E}}$ and $\bar{\boldsymbol{H}}$ must be continuous across the interface between the media.

Fields at a Dielectric Interface

$$\hat{\boldsymbol{n}} \cdot \bar{\boldsymbol{D}}_2 = \hat{\boldsymbol{n}} \cdot \bar{\boldsymbol{D}}_1 \tag{3.30}$$

$$\hat{\boldsymbol{n}} \cdot \bar{\boldsymbol{B}}_2 = \hat{\boldsymbol{n}} \cdot \bar{\boldsymbol{B}}_1 \tag{3.31}$$

$$\hat{\boldsymbol{n}} \times \bar{\boldsymbol{E}}_2 = \hat{\boldsymbol{n}} \times \bar{\boldsymbol{E}}_1 \tag{3.32}$$

$$\hat{\boldsymbol{n}} \times \bar{\boldsymbol{H}}_2 = \hat{\boldsymbol{n}} \times \bar{\boldsymbol{H}}_1 \tag{3.33}$$

In a case where one of the materials is a perfect and lossless conductor, which is a reasonable approximation for most problems involving metals, the field components must reduce to zero. The above relations may be simplified to the forms expressed in equations 3.34 — 3.37.

Fields at an Interface with a Perfect Conductor

$$\hat{\boldsymbol{n}} \cdot \overline{\boldsymbol{D}} = \rho_s \tag{3.34}$$

$$\hat{\boldsymbol{n}} \cdot \overline{\boldsymbol{B}} = 0 \tag{3.35}$$

$$\hat{\boldsymbol{n}} \times \overline{\boldsymbol{E}} = 0 \tag{3.36}$$

$$\hat{\boldsymbol{n}} \times \overline{\boldsymbol{H}} = \overline{\boldsymbol{J}}_s \tag{3.37}$$

3.5 General solutions for guided waves

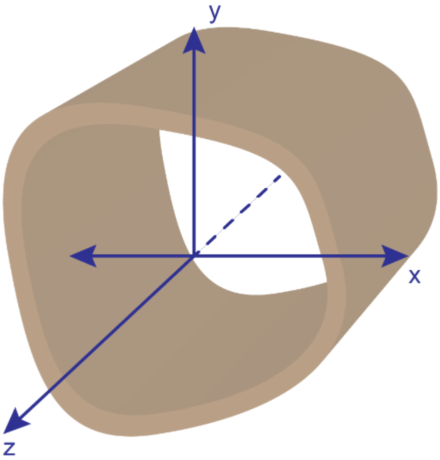

Figure 3.4 General waveguide

In the general case, assuming harmonic time variance, a waveguide having boundaries parallel with the z-axis that are uniform, perfectly conducting and of infinite length as in Figure 3.4 the electric and magnetic fields can be expressed as follows:

$$\overline{\boldsymbol{E}}(x,y,z) = [\overline{\boldsymbol{e}}(x,y) + \hat{\boldsymbol{z}}\overline{\boldsymbol{e}}_{\boldsymbol{z}}(x,y)]e^{-j\beta z} \tag{3.38}$$

$$\overline{\boldsymbol{H}}(x,y,z) = \left[\overline{\boldsymbol{h}}(x,y) + \hat{\boldsymbol{z}}\overline{\boldsymbol{h}}_{\boldsymbol{z}}(x,y)\right]e^{-j\beta z} \tag{3.39}$$

Where the waves propagate along the z-axis in the direction of +z and where there is assumed to be no attenuation losses and $\overline{\boldsymbol{e}}(x,y)$ and $\overline{\boldsymbol{h}}(x,y)$represent the transverse components, while $\overline{\boldsymbol{e}}_{\boldsymbol{z}}(x,y)$and $\overline{\boldsymbol{h}}_{\boldsymbol{z}}(x,y)$represent the longitudinal components. Using the harmonic form of Maxwell's equations it is possible to derive a set of equations (3.40 - 3.45) for the components of the transverse and longitudinal fields.

Faraday's Law *Ampère's Law*

$$\frac{\partial E_z}{\partial y} + j\beta E_y = -j\omega\mu H_x \tag{3.40}$$

$$\frac{\partial H_z}{\partial y} + j\beta H_y = -j\omega\epsilon E_x \tag{3.41}$$

$$-j\beta E_x - \frac{\partial E_z}{\partial x} = -j\omega\mu H_y \tag{3.42}$$

$$-j\beta H_x - \frac{\partial H_z}{\partial x} = j\omega\epsilon E_y \tag{3.43}$$

$$\frac{\partial E_y}{\partial x} - \frac{\partial E_x}{\partial y} = -j\omega\mu H_y \tag{3.44}$$

$$\frac{\partial H_y}{\partial x} - \frac{\partial H_x}{\partial y} = j\omega\epsilon E_z \tag{3.45}$$

A further modification can be sought from these equations, which expresses the transverse field componentsH_x,H_y, E_x and $E_y$in terms of the longitudinal components E_z and H_z**[3.8]**.

$$H_x = \frac{j}{k_c^2}\left(\omega\epsilon\frac{\partial E_z}{\partial y} - \beta\frac{\partial H_z}{\partial x}\right) \tag{3.46}$$

$$E_x = \frac{-j}{k_c^2}\left(\beta\frac{\partial E_z}{\partial x} + \omega\mu\frac{\partial H_z}{\partial y}\right) \tag{3.47}$$

$$H_y = \frac{-j}{k_c^2}\left(\omega\epsilon\frac{\partial E_z}{\partial x} + \beta\frac{\partial H_z}{\partial y}\right) \tag{3.48}$$

$$E_y = \frac{j}{k_c^2}\left(-\beta\frac{\partial E_z}{\partial y} + \omega\mu\frac{\partial H_z}{\partial y}\right) \tag{3.49}$$

3.5.1 TM and TE Modes

Equations 3.46 to 3.49 may be used to derive expressions for the TE and TM modes within a waveguide. In this case, only the TM modes are considered, but the TE derivation is almost identical. For the transverse magnetic waves $H_z = 0$ and $E_z \neq 0$ equations 3.46 to 3.49 reduce to the following:

$$H_x = \frac{j}{k_c^2}\left(\omega\epsilon\frac{\partial E_x}{\partial y}\right) \tag{3.50}$$

$$E_x = \frac{-j}{k_c^2}\left(\beta\frac{\partial E_z}{\partial x}\right) \tag{3.51}$$

$$H_y = \frac{-j}{k_c^2}\left(\omega\epsilon\frac{\partial E_z}{\partial x}\right) \tag{3.52}$$

$$E_y = \frac{j}{k_c^2}\left(-\beta\frac{\partial E_z}{\partial y}\right) \tag{3.53}$$

In this case $k_c \neq 0$ and $\mathrm{E_z}$ may be found from the Helmholtz equation

$$\nabla^2\mathrm{E_z} + \mathrm{k}^2\mathrm{E_z} = 0 \tag{3.54}$$

This can be reduced to the two dimensional wave equation:

$$\left(\frac{\partial^2}{\partial x^2} + \frac{\partial^2}{\partial y^2} + k_c^2\right)e_z = 0 \tag{3.55}$$

A similar result can be shown for TE waves:

$$\left(\frac{\partial^2}{\partial x^2}+\frac{\partial^2}{\partial y^2}+k_c^2\right)h_z=0 \qquad 3.56$$

3.5.2 Cylindrical waveguide theory

If a waveguide, constructed with a circular cross section as is shown in the figure below. Then the following derivation gives the electromagnetic fields allowed within the guide. This cylindrical waveguide has an inner radius *a*, and a point may be represented in cylindrical coordinates by its position along the z-axis and its radius *p* and angle from the x-axis *phi*.

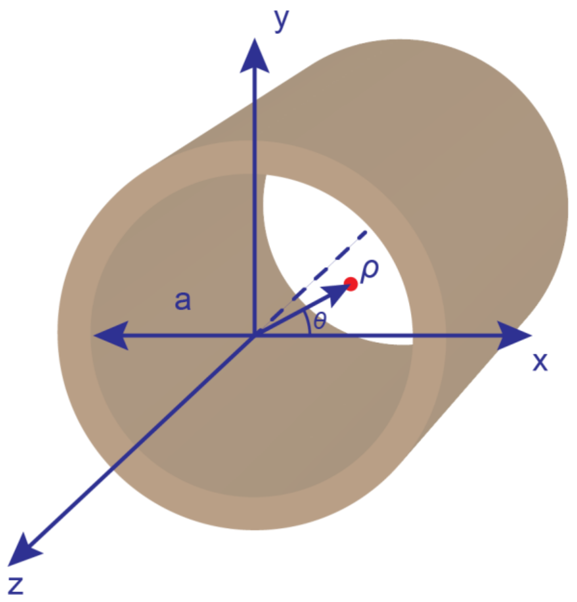

Figure 3.5: Geometry describing a cylidrical waveguide.

Using this reference frame the cylindrical components of the transverse fields may expressed as:

$$E_\rho=-\frac{j}{k_c^2}\left(\beta\frac{\partial E_z}{\partial\rho}+\frac{\omega\mu}{\rho}\frac{\partial H_z}{\partial\phi}\right) \qquad 3.57$$

$$E_\phi=\frac{-j}{k_c^2}\left(\frac{\beta}{\rho}\frac{\partial E_z}{\partial\phi}-\omega\mu\frac{\partial H_z}{\partial\rho}\right) \qquad 3.58$$

$$H_\rho=\frac{j}{k_c^2}\left(\frac{\omega\epsilon}{\rho}\frac{\partial E_z}{\partial\phi}-\beta\frac{\partial H_z}{\partial\rho}\right) \qquad 3.59$$

$$H_\phi = \frac{-j}{k_c^2}\left(\omega\epsilon\frac{\partial E_z}{\partial\rho} + \frac{\beta}{\rho}\frac{\partial H_z}{\partial\phi}\right) \qquad 3.60$$

For TM modes $H_z = 0$ and $E_z \neq 0$ and E_z can be found by solving:

$$\nabla_{\mathrm{trans}}^2 \mathrm{e_z} + k_c^2 \mathrm{e_z} = 0 \qquad 3.61$$

If $\mathrm{e_z}(\rho, \phi, \mathrm{z}) = \mathrm{e_z}(\rho, \phi)e^{-j\beta z}$ then this may be written as:

$$\frac{\partial^2 \mathrm{e_z}}{\partial r^2} + \frac{1}{r}\frac{\partial^2 \mathrm{e_z}}{\partial r} + \frac{1}{r^2}\frac{\partial^2 \mathrm{e_z}}{\partial \phi^2} + k_c^2 \mathrm{e_z} = 0 \qquad 3.62$$

Equation 3.62 can be solved using a separation of variables and can be shown**70** to be separable into the general solutions 3.63 and 3.64.

$$P(\phi) = \mathrm{A}\sin \mathrm{k_\phi}\phi + \mathrm{B}\cos \mathrm{k_\phi}\phi \qquad 3.63$$

$$\mathrm{R}(\rho) = CJ_n k_c \rho + CY_n k_c \rho \qquad 3.64$$

Where $J_n$and Y_n are Bessel functions of the first and second kind. Since Y_n becomes infinite at $\rho = r$ the Y_n term can be neglected, so the solution for $\mathrm{e_z}$ may be written as:

$$E_z = (A_c\sin(n\phi) + B_c\cos(n\phi))Jn(n, k_c\rho)e^{-\iota\beta z} \qquad 3.65$$

In this case, the transverse structure and the value of the cut off frequency is determined by the Bessel function (Figure 3.6).

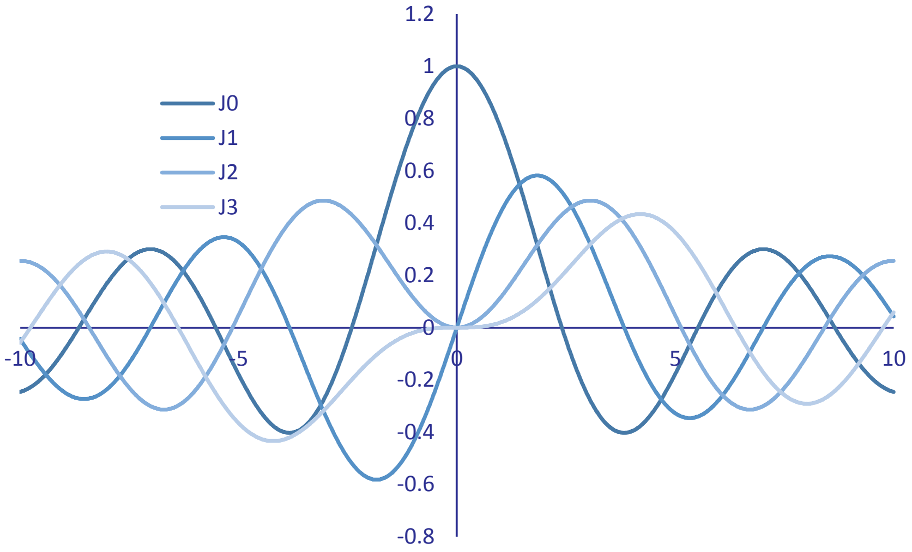

Figure 3.6: Bessel functions.

Remembering that H$_z$ = 0 the TM field components for a cylindrical waveguide are:

$$E_\rho = -\frac{i\beta}{k_c}(A_c\sin(n\phi) + B_c\cos(n\phi))\frac{d}{d\rho}Jn(n, k_c\rho)e^{-i\beta z} \tag{3.66}$$

$$E_\phi = -\frac{i\beta n}{k_c^2\rho}(A_c\sin(n\phi) + B_c\cos(n\phi))Jn(n, k_c\rho)e^{-i\beta z} \tag{3.67}$$

$$H_\phi = -\frac{i\omega\varepsilon}{k_c}(A_c\sin(n\phi) + B_c\cos(n\phi))\frac{d}{d\rho}Jn(n, k_c\rho)e^{-i\beta z} \tag{3.68}$$

$$H_\rho = \frac{i\omega\varepsilon n}{k_c^2\rho}(A_c\sin(n\phi) + B_c\cos(n\phi))Jn(n, k_c\rho)e^{-i\beta z} \tag{3.69}$$

This approach may also be used to derive a complementary set of equations describing the TE field components.

The cut-off wave-number of a cylindrical waveguide mode becomes more subtle due to the use of cylindrical co-ordinates. The general form is given by equation (3.70), below, where $p_{m,n}$ refers to a specific value for a given mode. For a TM mode, $p_{m,n}$ is the nth root of the Bessel function of the first kind, *J$_m$ (x)*. Similarly, $p_{m,n}$ for a TE mode is the nth root of the derivative of such a Bessel function, *J'$_m$* (x), and is usually written as $p'_{m,n}$. As a result, TE and TM modes with the same indices are not degenerate.

$$k_c = \frac{p_{m,n}}{r_w} \tag{3.70}$$

3.6 Hybrid mode theory

If Maxwell’s equations are expressed using a general coordinate system where the z coordinate lies along the axial direction then the phasor form of Faraday's law and Ampère's law may be decomposed into the following:

$$(\nabla_t - i\beta\hat{z}) \times (E_t + E_z\hat{z}) = \mathrm{i}\omega\mu(H_t + H_z\hat{z}) \tag{3.71}$$

$$(\nabla_t - i\beta\hat{z}) \times (H_t + H_z\hat{z}) = \mathrm{i}\omega\varepsilon(E_t + E_z\hat{z}) \tag{3.72}$$

This applies to any given system of coordinates that used to describe the fields within a cylindrical waveguide, where, the assumption is that the material properties remain constant along the z direction. Using this method and looking for solutions describing the TE modes where $E_z = 0$, the transverse and longitudinal components may be separated to obtain the following set of equations[71]:

$$\nabla_t \times E_t = \mathrm{i}\omega\mu H_t\hat{z} \tag{3.73}$$

$$-i\beta\hat{z} \times E_t = \mathrm{i}\omega\mu H_z \tag{3.74}$$

The following relations may be derived for the transverse components of TM fields within a cylindrical waveguide, where $H_z = 0$ and $k_t = \sqrt{k^2 - \beta^2}$.

Transverse components of TE fields

$$E_t = \frac{-i\omega\mu}{k_t^2}\nabla_t H_z \times \hat{z} \tag{3.75}$$

$$H_t = \frac{-\mathrm{i}\beta}{k_t^2}\nabla_t H_z \tag{3.77}$$

Transverse components of TM fields

$$E_t = \frac{-\mathrm{i}\beta}{k_t^2}\nabla_t E_z \tag{3.76}$$

$$H_t = \frac{-i\omega\varepsilon}{k_t^2}\hat{z} \times \nabla_t E_z \tag{3.78}$$

Hybrid modes are a superposition of the TM and TE basis modes and using the preceding generalized description of these modes a concise representation of the hybrid modes may be explicitly derived.

$$E_t = \frac{-i\omega\mu}{k_t^2}\left[\nabla_t H_z \times \hat{z} + \frac{\beta}{\omega\mu}\nabla_t E_z\right] \tag{3.79}$$

$$H_t = \frac{-i\omega\varepsilon}{k_t^2}\left[\hat{z} \times \nabla_t E_z \times \hat{z} + \frac{\beta}{\omega\varepsilon}\nabla_t H_z\right] \qquad 3.80$$

These relationships are valid for any coordinate system and may readily be expanded as required.

At this point, it is worthwhile to consider the physical interpretation of hybrid modes and how they are excited within a cylindrical waveguide. From the previous descriptions of the TE and TM modes within a waveguide, where the transverse boundaries are perfectly conducting it is evident that only the TE and TM modes may be excited (co-axial structures excluded). It is therefore necessary to consider a system in which the waveguide boundaries are not perfectly conducting.

$$Z = \frac{E_\phi}{H_z} \qquad 3.81$$

$$Y = \frac{-H_\phi}{E_z} = i\sqrt{\frac{\varepsilon}{\mu}}B \qquad 3.82$$

If there is a constant and finite surface impedance or admittance as defined by equations 3.81 and 3.82, then the modes supported by this waveguide can be hybrid.

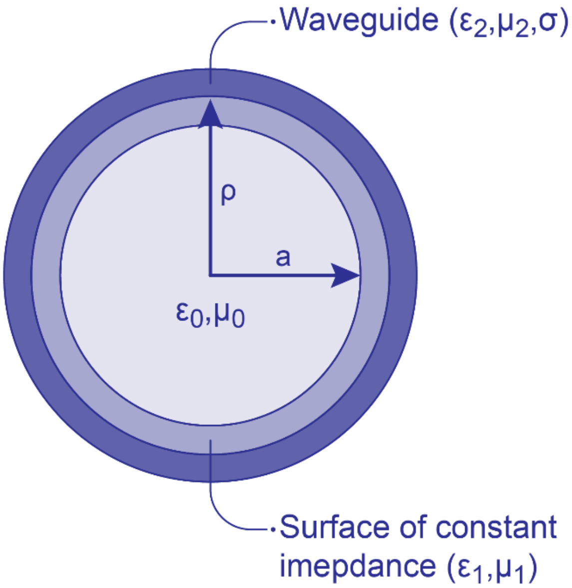

Figure 3.7: A surface of constant impedance.

For a structure with the geometry depicted in Figure 3.7, where the surface of constant impedance is located at $\rho = a$, the longitudinal components of the electric and magnetic fields between the origin and the boundary at the surface of constant impedance may be described as follows:

$$E_z = iJ_m\ (u\rho/a)\ \ cos(m\phi) \tag{3.83}$$

$$H_z = \frac{i\Lambda}{\eta_0} J_m\left(\frac{u\rho}{a}\right)\sin(m\phi) \tag{3.84}$$

Where:

$$\left(\frac{u}{a}\right)^2 + \beta^2 = k^2 = \omega^2\mu_0 a_0 \tag{3.85}$$

The transverse field components are then obtained directly from the longitudinal components using 3.75 to 3.78.

$$E_\phi = -\frac{v}{u}\left[\frac{m\beta}{k_0}\left(J_m\left(\frac{u\rho}{a}\right)\Big/\left(\frac{u\rho}{a}\right)\right) + \Lambda J'_m\left(\frac{u\rho}{a}\right)\right]\sin(m\phi) \tag{3.86}$$

$$E_\rho = \frac{v}{u}\left[\frac{m\beta}{k_0}J'_m\left(\frac{u\rho}{a}\right) + m\Lambda\left(J_m\left(\frac{u\rho}{a}\right)\Big/\left(\frac{u\rho}{a}\right)\right)\right]\cos(m\phi) \tag{3.87}$$

$$H_\phi = \frac{v}{u\eta_0}\left[J'_m\left(\frac{u\rho}{a}\right) + \frac{m\beta\Lambda}{k_0}\left(J_m\left(\frac{u\rho}{a}\right)\Big/\left(\frac{u\rho}{a}\right)\right)\right]\cos(m\phi) \tag{3.88}$$

$$H_\rho = \frac{v}{u\eta_0}\left[m\left(J_m\left(\frac{u\rho}{a}\right)\Big/\left(\frac{u\rho}{a}\right)\right) + \frac{\beta\Lambda}{k_0}J'_m\left(\frac{u\rho}{a}\right)\right]\sin(m\phi) \tag{3.89}$$

By imposing the boundary conditions from 3.79 and 3.80 at $\rho = a$ an equation can be derived for the waveguide mode (u) and the hybrid mode factor (Λ)[72].

$$\Lambda = \frac{(B-X)u^2}{2m\beta a} \pm \sqrt{1 + \left(\frac{(B-X)u^2}{2m\beta a}\right)^2} \tag{3.90}$$

This expression gives a value for the hybrid mode factor in terms of both the susceptance and reactance as well as the modal eigenvalue u. The two possible solutions to this equation correspond to the two types of hybrid modes HE and EH, where the ordering of the letters designate the dominant longitudinal field component. HE modes have the transverse components dominated by the H_z field, whereas the EH modes have the transverse components dominated by the E_z field.

3.7 Corrugated Waveguides

One possible method for generating hybrid modes within the waveguide is the introduction of a corrugation along the inner surface of the waveguide. This corrugation can act like the surface of constant impedance previously discussed when defining the hybrid modes. This surface impedance analysis provides a convenient and accurate method characterise the fields within a corrugated waveguide.

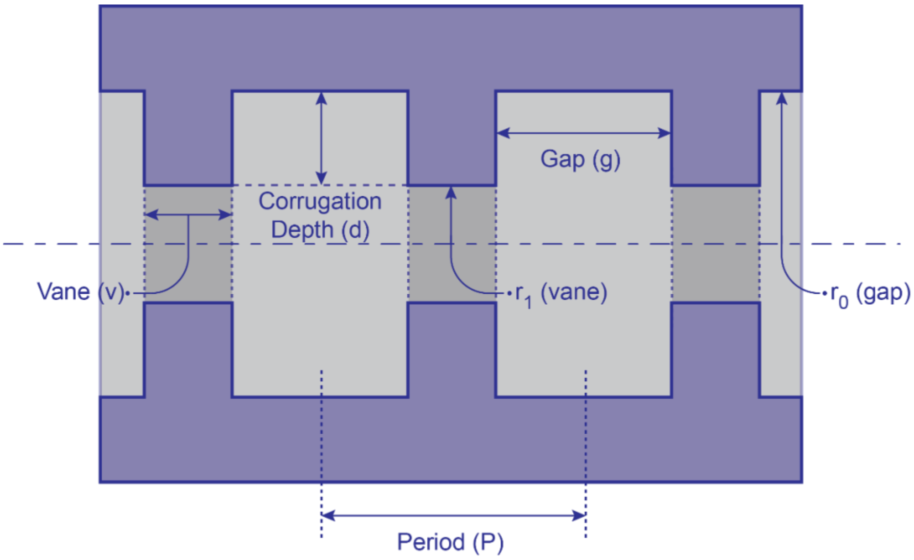

Figure 3.8: Corrugated waveguide geometry.

Within a corrugated waveguide, the dominant mode is the hybrid HE_{11}, which has the following transverse E-fields in Cartesian space[73,74]:

$$E_x = \frac{(X-Y)}{kr_1} A_2 J_2(k_c r)\sin(2\phi) \tag{3.91}$$

$$E_y = A_1 J_0(k_c r) - \frac{(X-Y)}{kr_1} A_2 J_1(k_c r)\cos(2\phi) \tag{3.92}$$

X and Y are the impedance and admittance at the boundary $r_0 = r_1$ and Z_0 is the free space impedance. This mode has practical applications due its relatively low attenuation and linear field structure. The HE_{11} mode is stimulated by excitation of a combination of TM and TE modes within a waveguide. The electric fields for these modes are shown in Figure 3.9. This mixture is (generally accepted) to be composed of 85% TE_{11} and 15% TM_{11} with the correct polarization and phase shift between them.

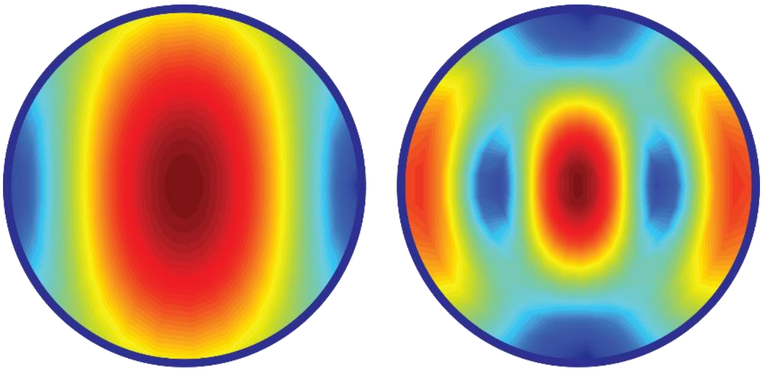

TE_{11} TM_{11}

Figure 3.9: Electric field contours for a TE_{11} and a TM_{11} mode.

From equations 3.91 and 3.92, it can be seen that there exists a condition when (X-Y) = 0, then the impedance and admittance at the boundary are either equal or both zero when the field in the waveguide is dependant only on the axial component of the field. This is the ***balanced hybrid condition***. When the field has no *phi* component there will be no cross-polarization in the aperture field, which is an ideal condition for a feed. The HE_{11} hybrid mode that is produced by the ideal mixture of both the TE_{11} and TM_{11} modes is demonstrated in Figure 3.10.

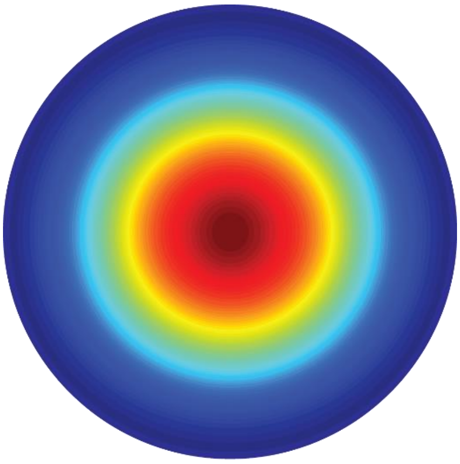

HE_{11}

Figure 3.10: HE_{11} E-field in circular waveguide

This balanced hybrid condition is achieved in practice by the construction of a corrugated waveguide with the desired properties. When there is the correct number of corrugations per wavelength the azimuthal electric field will be equal to zero at $r_0 = r_1$ so $X = 0$. If the vane length (t) and gap length (b) are optimized and the corrugation depth (s) is one quarter of a wavelength then the corrugations can act as transmission lines where the short circuit at r_0 is transferred to an open circuit at r_1, so no axial currents will be generated by *the* azimuthal magnetic field so $Y = 0$.

This balanced hybrid condition is frequency dependant due to the corrugation and will only occur at a single frequency, so zero cross-polarization will also only be achieved at this frequency

4 Antenna Theory

The decoupling of the electron beam from the electromagnetic wave in the gyro-TWA may be carried out through the inclusion of an antenna system on to the waveguide after the interaction region. In the gyro-BWO the same result is achieved by placing an antenna on the waveguide immediately after the output window. In either case, the launcher is a waveguide antenna system designed to emit a quasi-optical radiation mode. Chapter 4 provides the theoretical overview of the antenna and quasi-optical theory required to design such a system.

4.1 Gaussian beams and Quasi-optics

4.1.1 Quasi-optics

The Quasi-optic approximation describes the propagation of radiation within a system with transverse dimensions that are relatively large when compared to the wavelength of the radiation. Usually the radiation in question will be a reasonably well collimated beam with a wavelength within the microwave to sub-millimetre range. This is in contrast to the geometrical optics case where the transverse dimensions of the system are far greater than the wavelength; such that the diffractive effects of the system on the radiation may be neglected and the propagation can be considered to conform to a ray coincident with the propagation vector of the radiation. At the other extreme is diffractive optics, which is concerned with the case where the radiation wavelength is of comparable size with the system dimensions. An example would be the diffraction grating, or more applicably to the field of mm and sub-mm waves, the near field regions at an antenna boundary. In the latter case a full description of the propagating fields must rely on the Fresnel treatment of radiation. The three optical regimes and their relations to the system size are summarized in Table 4.1.

Diffractive Optics	$D \approx \lambda$
Quasi-optics	$D > \lambda$
Geometrical Optics	$D >> \lambda$

Table 4.1: Optical Regimes.

The field of quasi-optics describes the case between diffractive and geometrical optics when there is a beam of radiation with a diameter that is only slightly smaller than the overall size of the system. In such a situation the beam may be described by Gaussian beam modes and Gaussian beam propagation, which also takes into account the effects of diffraction given that the beam exists within some reasonable constraints.

Quasi-optics and Gaussian beam analysis are particularly effective for microwave and millimetre wave feed horn characterization and design, where the radiated fields are very close to a Gaussian distribution. Radiation that is emitted from these devices can be treated like a Gaussian beam with a distinct beam waist and divergence as shown in Figure 4.1.

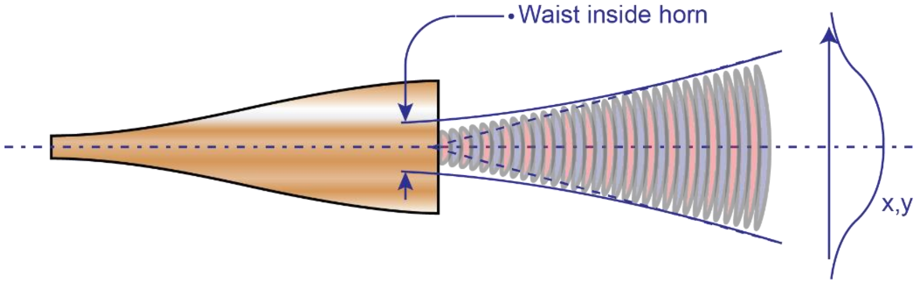

Figure 4.1: Gaussian beam produced by a mode converting horn.

Such a representation also lends itself readily to the inclusion of other quasi-optical elements such as mirrors and lenses as shown in Figure 4.2, where the quasi-optical Gaussian approach allows for a simple and accurate mathematical description.

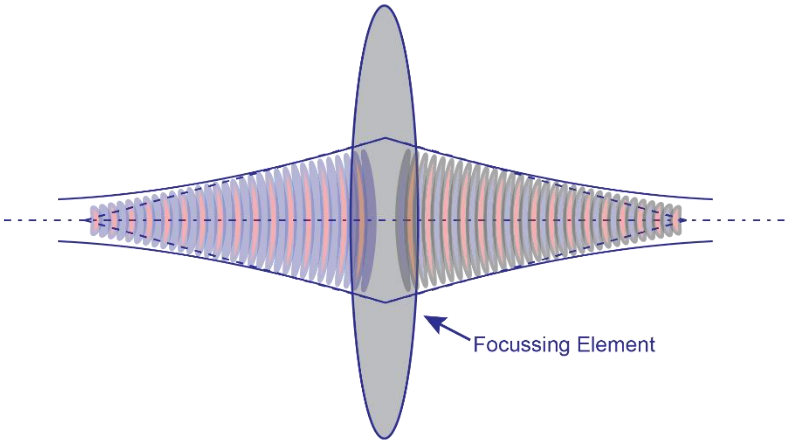

Figure 4.2: Gaussian beam transformation by a quasi-optical focusing element.

4.1.2 Application of Quasi-optics

The controlled transmission of electromagnetic waves is carried out by a number of ways dependent on the wavelength of the radiation. The radio waves used in telecommunication are most commonly transmitted along coaxial cables as well as being quite readily propagated in the atmosphere, whereas optical wavelengths are generally transmitted along fibres. Of course all electromagnetic waves may be freely transmitted in free space

At the frequencies of interest for mm and sub mm waves the means of propagation are most commonly single mode waveguide components rather than the conventional coaxial cable used at lower radio frequencies. Other means are also available including the micro-strip, the strip-line, and the slot-line, however these methods do not lend themselves well to high power applications. These types of system by their very nature are metallic conductors and dielectrics; as such, both of these materials exhibit losses that increase with frequency. In the general case loss per unit length of dielectric materials increases at a rate proportional to frequency, but at the mm and sub-mm wavelengths this loss can be proportional to the square of frequency[75,76].

Polyethylene for example, which is a low-loss material has an absorption coefficient of 0.65 dB/cm at a frequency of 500 GHz[77]. Even the relatively low loss waveguide is not immune to loss due to the conductivity of the metal from which it is constructed. A W-band copper rectangular waveguide will have a loss per unit length of 2.53 dB/m at around 95 GHz. It is therefore clear that for very high frequency and high power applications the use of standard components is constrained by their inherent loss.

To overcome this problem it is advantageous to consider transmission of the radiation in free space, which is effectively lossless apart from certain frequencies where resonant molecular transitions occur where absorption coefficients can be as large as a few tens of decibels per meter; there are however windows of transmission as shown in Figure 4.3. that are used for cloud profiling cloud profiling radar and Electron Paramagnetic Spectroscopy and Dynamic Nuclear Polarisation applications.

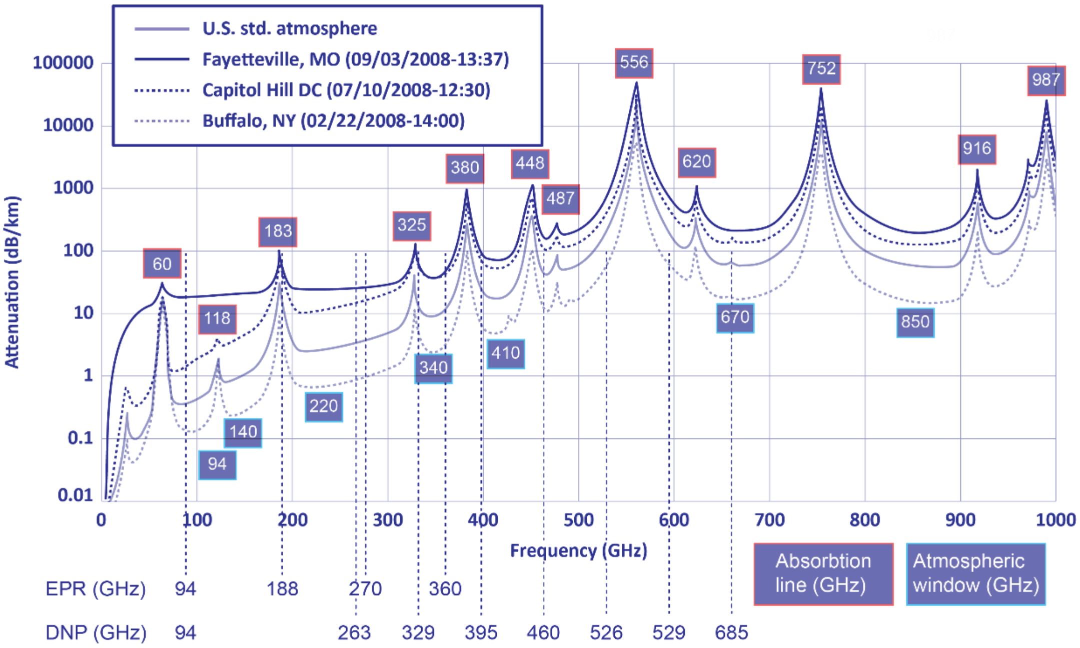

Figure 4.3: Graph of mmw/sub-mmw atmospheric attenuation (4 cases) showing absorption lines and "windows" with EPR and DNP frequencies overlaid. From Wallace & Rosker, SPIE vol. 7485, 74850E, 2009.

To classify a system as optical, the wavelength of the radiation must be very much smaller than the smallest dimension of any aperture or element of the system. This imposes some challenging constraints over the design of any system working in the mm and sub-mm range. Especially when the beam spread from a collimated source is taken into account; as the beam diameter is approximately doubled in size on a scale roughly equal to $D^2/2\lambda$. Therefore, a source of radiation with a wavelength of a few mm will experience a dramatic increase in the lateral dimension after only a few centimetres of propagation. It is clear therefore, that in order to use free space as a propagation medium for mm waves the diverging beams will have to be refocused at some point, and this focussing will be carried out in the near field. The Rayleigh region is effectively the near field and is a subset of the Fresnel region and ends at the Fraunhofer distance of $D^2/2\lambda$, where D is the aperture diameter and λ is the free-space wavelength of the radiation[78]**.**

At the aperture of a section of cylindrical waveguide, the electric field of the escaping radiation expands into free space[79]. At sufficient distance from the aperture, the field behaves in a certain manner, according to the mode in which it is polarised. Once in this far field regime i.e. beyond Fraunhofer distance the angular distribution of the field no longer changes as a function of distance.

4.1.3 Gaussian Modes and Beam Propagation

The use of Gaussian beams via a quasi-optical method overcomes the problem of accurately calculating the behaviour of radiation within the system as well as providing a number of other advantages that make it suitable method for low loss transmission of mm-waves.

One of the advantages is the elimination of the metallic or dielectric transmission lines and their inherent loss; the inclusion of focussing elements does produce some loss in the quasi-optical system, but the distance between the focussing elements and mirrors is such that the loss is relatively small in comparison with waveguide systems. This also means that the power handling abilities is far better as the absence of metallic and dielectric waveguide components decreases the likelihood of breakdown.

Another advantage due to the absence of boundary conditions and the subsequent dispersion of conventional waveguides is the ability for quasi-optical systems to handle multiple polarizations and can operate over very large bandwidths. This fact also improves the overall power handling as the overall power may be distributed over a broader range of frequencies compared to the single mode waveguide.

The formalism for Gaussian modes may be derived from various starting points, including diffraction from apertures and resonator reflectors[80], and solution of the paraxial wave equation. Beginning with the latter the free space solution to Helmholtz equation may be found in the following form:

$$\bar{\mathbf{E}}(\mathrm{r},\mathrm{t}) = \mathrm{E}_0 \mathrm{e}^{\mathrm{j}(\mathrm{x}\mathrm{k}_\mathrm{x}+\mathrm{y}\mathrm{k}_\mathrm{y}+\mathrm{z}\mathrm{k}_\mathrm{z}-\omega\mathrm{t})} = \mathrm{E}_0 \mathrm{e}^{\mathrm{j}(\mathbf{k}\cdot\mathbf{r}-\omega\mathrm{t})} \qquad 4.1$$

$$\bar{\mathbf{E}}(\mathrm{r},\theta,\phi,\mathrm{t}) = \frac{\mathrm{E}_0(\theta,\phi)}{r}\mathrm{e}^{\mathrm{j}(\mathrm{k}\cdot\mathrm{r}-\omega\mathrm{t})} \tag{4.2}$$

This solution represents the electromagnetic wave as a plane wave; equation 4.2 is also a solution of the wave equation, which provides a more physical description of the propagation of a spherical wave-front.

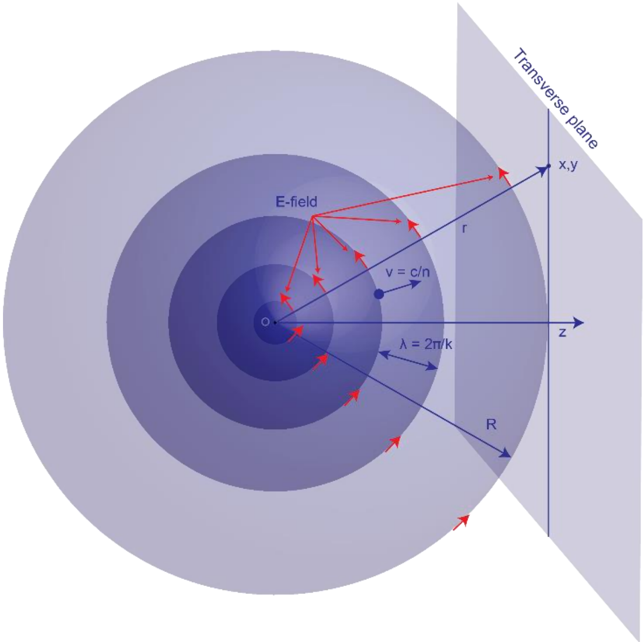

Figure 4.4: Spherical Waves - surfaces of constant phase radiating from a point source at O.

Figure 4.4 provides an idealized representation of the propagation of a spherical wave from a point source. If the source is an aperture and the diameter of the aperture is small compared to the wavelength and the distance from the source then this model may be used to approximate an aperture source. Once the distance from the source becomes great enough the curvature of the wave fronts may be small enough that they can be represented as a plane wave. Equation 4.2 may be then solved by looking at the problem in terms of a plane wave where the function $\mathrm{U}(\mathrm{x},\mathrm{y},\mathrm{z})$ specifies the phase and irradiance of the wave.

$$\bar{\mathbf{E}}(\mathrm{r},\mathrm{t}) = \mathrm{U}(\mathrm{x},\mathrm{y},\mathrm{z})\mathrm{e}^{\mathrm{j}(\mathrm{k}\cdot\mathrm{z}-\omega\mathrm{t})} \tag{4.3}$$

This solution may be derived from the following wave equation, which is the paraxial approximation of the Helmholtz equation:

$$\frac{\partial^2 U}{\partial \mathrm{x}^2} + \frac{\partial^2 U}{\partial \mathrm{y}^2} = -2jk\frac{\partial U}{\partial z} = 0 \tag{4.4}$$

This may be solved to provide an equation for the E-field in a Gaussian beam.

$$\bar{\mathbf{E}}(\mathrm{r},\mathrm{t}) = \mathrm{e}^{\mathrm{j}\frac{(x^2+y^2)}{2R(z)}}\mathrm{e}^{-\mathrm{j}\frac{(x^2+y^2)}{2w^2(z)}}\mathrm{e}^{\mathrm{j}(\mathrm{k}\cdot\mathrm{z}+\mathrm{p}(\mathrm{z})-\omega\mathrm{t})} \tag{4.5}$$

$$x^2 + y^2 = r^2 \tag{4.6}$$

In general the solutions to this equation are the Gauss-Hermite polynomials for rectangular coordinates; but if the problem is cylindrically symmetric it may be expressed in cylindrical coordinates using Gauss-Laguerre polynomials[81, 82]. These modes are required for a full treatment of any field distribution, but are not essential or even desired when considering the efficient operation of a Gaussian beam system. It is therefore only worth considering the fundamental mode that is axially symmetric so it will only be necessary to deal with a transverse radial c-ordinate and an axial distance along the direction of propagation to describe the behaviour of the beam.

.

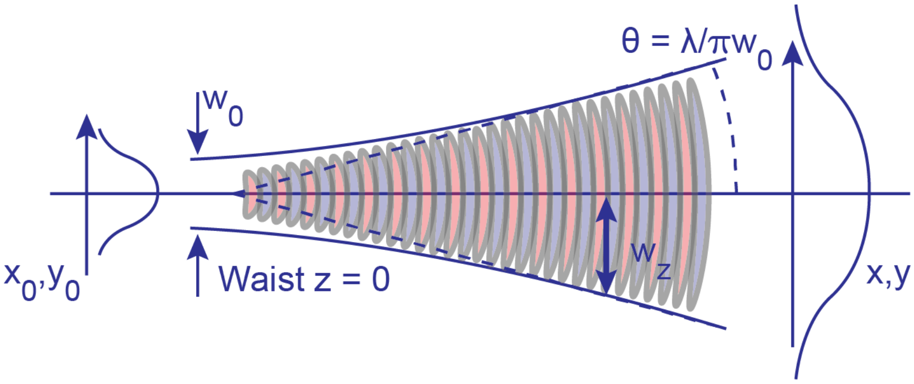

Figure 4.5: Gaussian beam propagation.

The spherical propagation of a Gaussian beam in the z direction is demonstrated schematically in Figure 4.5.

$$\mathrm{R(z)} = \mathrm{z}\left[1 + \left(\frac{\pi w_0^2}{\lambda z}\right)^2\right] \tag{4.7}$$

Equation 4.7 defines the radius of curvature of the beam wave-front and equation 4.8 defines the beam waist as functions of the z component.

$$w^2(\mathrm{z}) = \omega_0^2\left[1 + \left(\frac{\lambda z}{\pi w_0^2}\right)^2\right] \qquad 4.8$$

The divergence profile of a Gaussian beam is unlike that of a conventional beam in that it does not diverge linearly in the region close to the beam waist; within this region the divergence angle is relatively small. As the beam propagates this angle increases until it reaches the asymptotic limit where it is described by a cone with the angular radius

$$\theta = \frac{\lambda}{\pi w_0} \qquad 4.9$$

4.1.4 Gaussian Beam Transformation

So far the treatment of a Gaussian beam considers only the ideal growth of a beam of radiation away from a given beam waist, with an amplitude distribution concentrated perpendicular to the direction of propagation and which has a planar phase front. This may be achieved in practice using a feed horn to excite the fundamental mode Gaussian beam, or a combination of several different modes.

The characteristics of the electric field as a function of a distance from this beam waist may then be calculated in principle from the above equations. This is fine as long as the beam remains within the confocal distance $z_c = w_0^2/\lambda$, where the beam grows laterally as is the described by the above Gaussian functions. But when the distance is greater than z_c where the beam size grows linearly as z increases and the beam can be considered to be in the far field, then the system can no longer be described as quasi-optical and steps must be taken to correct this problem.

The beam must therefore be constrained from spreading laterally and growing beyond the bounds of a Gaussian beam. This can be done in a similar way to that used in conventional optics. Using lenses or mirrors the radius of curvature may be altered to produce a converging beam and this beam will then propagate to another beam waist where it will once again begin to expand.

While this process is analogous to the focusing of a beam in geometrical optics, the alteration of a Gaussian beam is more correctly a transformation due to the fact that in quasi-optics there is not a corresponding focus as the radiation is not concentrated to a point. It is therefore better to consider the operation as a transformation of one beam waist onto another.

When considering the mathematical treatment of such transformations it is far simpler to use only the fundamental Gaussian mode. This is justified because the fundamental beam mode provides a robust representation of the radiation from most types of antenna and feed horns. In addition, the radius of curvature R and beam waist ω_0 remains the same for all Gaussian beam modes so the formulas describing the propagation of a Gaussian beam apply in all cases equally. Except when the phase shift φ needs to be considered, which is dependent on the mode and must be accounted for in certain cases.

The transformation may therefore be described quite adequately, in an analogous way to the representation of ray transformations in geometrical optics through the application of ray matrices and the inclusion of the complex beam parameter q, which is defined in equation 4.10. Where $R(z)$ is the radius of curvature and λ_0 is the wavelength in free space and n is the index of refraction of the medium.

$$\frac{1}{q(z)} = \frac{1}{R(z)} - \frac{i\lambda_0}{n\pi w(z)^2} \tag{4.10}$$

This method assumes that the location and the slope of the ray at the output are linear functions of the input ray. It describes a system that is capable of both representing the basic as well as more complex multi element optical systems.

If the position along a ray is denoted r and the slope as r' then a set of the following equations describing the transformation of the beam may be defined, where the parameters A, B, C and D represent the properties of an arbitrary optical system.

$$r_{out} = Ar_{in} + Br'_{in} \tag{4.11}$$

$$r'_{out} = Cr_{in} + Dr'_{in} \tag{4.12}$$

The ray position and slope can be written as a column matrix then the system of linear equations may then be written in the form of an ABCD Matrix.

$$\begin{bmatrix} r_{out} \\ r'_{out} \end{bmatrix} = \begin{bmatrix} A & B \\ C & D \end{bmatrix} \cdot \begin{bmatrix} r_{in} \\ r'_{in} \end{bmatrix} \tag{4.13}$$

This is a more convenient form, which allows multiple optical elements to be cascaded together to find an overall system matrix through the multiplication of the successive 2x2 matrices. The radius of curvature of the beam is defined as the ratio of the position to the slope:

$$R = \frac{r}{r'} \tag{4.14}$$

Therefore, the matrix equation may be used to find a relationship for the radius of curvature.

$$R_{out} = \frac{AR_{in} + B}{CR_{in} + D} \tag{4.15}$$

Since the radius of curvature for a Gaussian beam can be expressed in terms of the complex q parameter this can be rewritten in the following form:

$$q_{out} = \frac{Aq_{in} + B}{Cq_{in} + D} \tag{4.16}$$

This relationship between the two values q_{out} and q_{in}provides all that is needed to describe the propagation of a Gaussian beam through an optical system, given the initial values of q_{in} and the ABCD matrix that characterizes the system.

Using the ABCD propagation law allows us to obtain the complex beam parameter at any point within the system and if the wavelength of the radiation is known the beam waist and radius of curvature may be found from the following equations:

$$w = \sqrt{\frac{\lambda}{\pi \, Im(-1/q)}} \tag{4.17}$$

$$R = \left[Re\left(\frac{1}{q}\right)\right]^{-1} \tag{4.18}$$

The ABCD matrix can be derived for a simple case by considering the distance L that a ray travels in a uniform medium with a constant refractive index.

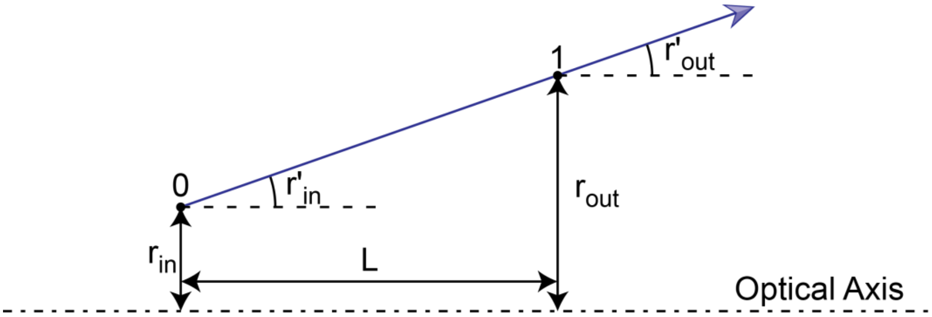

Figure 4.6: Simple ray transformation geometry.

It is clear that the ray slope r' is unchanged and that the translation of the ray in the direction perpendicular to the axis is a function of the tangent of the slope.

$$r'_{out} = r'_{in} \text{ and } r_{out} = r_{out} + L\tan(r'_{in}) \qquad 4.19$$

If the paraxial approximation is used then we can formulate a set of equations similar to equations 4.11 and 4.12, where the coefficients are replaced by constants derived from the assumptions of equation 4.18.

$$r_{out} = 1r_{in} + Lr'_{in} \qquad 4.20$$

$$r'_{out} = 0r_{in} + 1r'_{in} \qquad 4.21$$

From these equations, the matrix form can be discerned as follows:

$$\begin{bmatrix} r_{out} \\ r'_{out} \end{bmatrix} = \begin{bmatrix} 1 & L \\ 0 & 1 \end{bmatrix} \cdot \begin{bmatrix} r_{in} \\ r'_{in} \end{bmatrix} \qquad 4.22$$

A similar method may be used to find any arbitrary ABCD matrix for a given optical element. Table 2 contains some of the most common ABCD matrices used in optics. Further discussion of ABCD matrices as applicable to quasi-optics can be found in Pedrotti[80] and Goldsmith[83].

Optical Element	Matrix
Distance L in uniform medium	$\begin{bmatrix}1 & L\\0 & 1\end{bmatrix}$
Curved interface from refractive index n_1 to n_2; R > 0 if concave to left; for flat interface take limit R ~ ∞	$\begin{bmatrix}1 & 0\\ \frac{n_1 - n_2}{Rn_2} & \frac{n_1}{n_2}\end{bmatrix}$
Thin lens of focal length f	$\begin{bmatrix}1 & 0\\ \frac{1}{f} & 1\end{bmatrix}$
Reflection from a curved mirror	$\begin{bmatrix}1 & L\\ \frac{-2}{R} & 1\end{bmatrix}$
Reflection from a flat mirror	$\begin{bmatrix}1 & 0\\0 & 1\end{bmatrix}$

Table 4.2 Common ABCD matrices for optical transformations.

4.2 Launching and Coupling of Gaussian Beams

4.2.1 Gaussian Beams from Feed Horns and Radiating Systems

Microwave and millimetre wave feed horns can produce an aperture field that is very close to a Gaussian distribution and are therefore ideal when coupling between free space and guided wave devices such as mixers and detectors, or in the case of high power mm-waves between a source and free space. The hybrid modes, which are present within these corrugated waveguides can upon transformation into free space be seen to be coupled with the free space Gaussian modes. The Gauss-Hermite or Gauss-Laguerre functions may then be employed in the evaluation of the coupling between the radiated fields and the aperture fields.

In the general case, it would be likely that more than one mode would be required to provide the ideal aperture distribution, but it is likely that most of the power will be present in the fundamental mode and so the Gaussian mode treatment provides quite a robust model.

4.2.2 Corrugated antennas

Corrugated feed horns have an idealized aperture field distribution that is derived from the field distributions inside a cylindrical waveguide and is of the form:

$$E_r(r) = J_0\left(\frac{\propto r}{a}\right) \tag{4.23}$$

Where in the case of the fundamental mode $\propto$ is equal to 2.405 and a is the radius of the aperture. This Bessel function is very close to the Gaussian function that describes the field amplitude distribution in a Gaussian beam and is therefore an excellent approximation to that function. Indeed, when the ratio of the beam waist to the radius of the aperture is equal to approximately 0.64 it is found that the 98% of the power is in the fundamental mode**[84]**. The aperture field of a HE_{11} mode can be seen alongside the fundamental Gaussian mode in Figure 4.7.

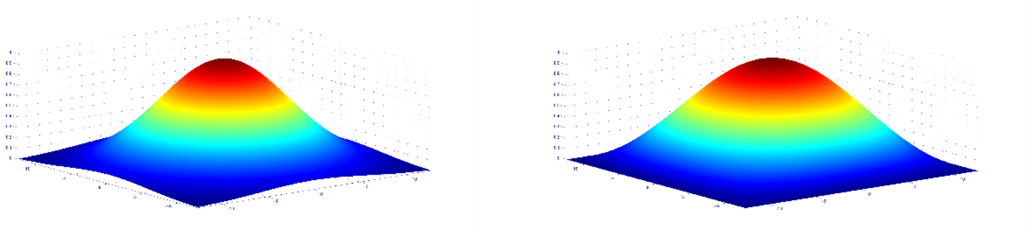

(a) Gaussian distribution

(b) HE_{11} aperture distribution

Figure 4.7: The normalised Gaussian distribution and the aperture field distribution of the HE_{11} mode.

4.2.3 Hybrid mode theory

A more precise representation of the electric field for the dominant hybrid mode that is present at the aperture of a corrugated waveguide is given in equation 4.24.

$$\begin{aligned} \mathrm{E} = {} & \mathrm{AJ_0(k \cdot r)\hat{\imath}_x} \\ & - \left(\frac{\mathrm{X-Y}}{4}\right)\frac{\mathrm{U_0^2}}{\mathrm{kr_1}}\mathrm{J_2(k \cdot r)}\big(\cos 2\phi\hat{\imath}_{\mathrm{x}} \\ & + \sin 2\phi\hat{\imath}_{\mathrm{y}}\big) \end{aligned} \tag{4.24}$$

Where r_1 is the radius of the corrugated waveguide, k is the free space wavenumber, $\mathrm{J_n}$ is a Bessel function of the first kind, U_0 is a normalized transverse wavenumber and X and Y are the normalized reactance and admittance of the boundary. When $r = r_1$ it can be seen from this equation that the field at the aperture has only a component in the x direction; it is free from the angular term ϕ and there is no cross-polarization. This is the balanced hybrid condition when (X-Y) = 0 and is the case when either X =

Y, or both are equal to zero. This condition may never be achieved inside a conventional waveguide, but in a corrugated waveguide the surface reactance is approximately zero if the number of corrugations per wavelength is large (this approximation improves as this number gets larger) and if the corrugations are constructed to be a quarter wavelength deep then they will behave like a short transmission line with a short at the conducting wall and an open circuit at the corrugation boundary $r = r_1$. With this condition applied there will be no axial currents generated by H_ϕ, therefore the admittance at the boundary will also be zero (Y = 0). It is clear that this balanced hybrid condition will only be met at certain specific frequencies due to the dependence on the depth of the corrugations, which is usually taken to be λ/4 at the center of the operational band. But from equation 4.24 it can be seen that there is also a dependence on kr_1 for the ϕ terms, which means that the performance may be improved by increasing the size of the waveguide aperture (r_1). So it is possible to produce a hybrid mode that is very close to the ideal HE_{11} over a relatively large frequency range.

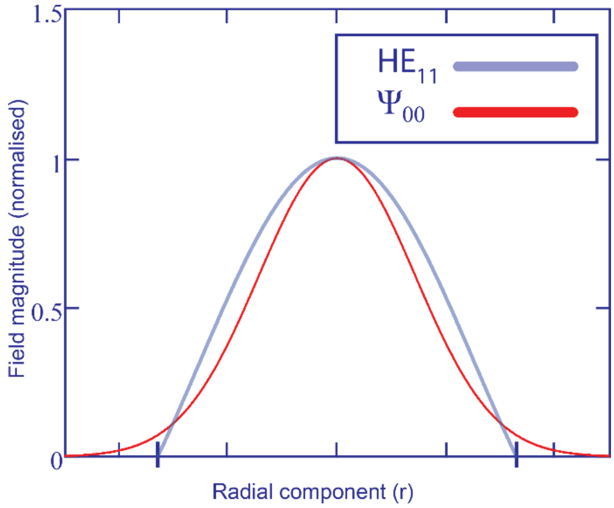

Figure 4.8: Correlation between HE11 mode and fundamental free space Gaussian mode.

Figure 4.8 demonstrates the analytically derived comparison between the HE_{11} field at the aperture of a waveguide and a Gaussian field of a TEM wave in free space. It is generally accepted that the HE_{11} mode is capable of providing an extremely high conversion efficiency to the Gaussian free space mode given the appropriate mixture of TM/TE modes. It has been demonstrated that for the perfect mode mixture the following combination of modes are desirable[85].

TE$_{11}$	84.496%	**TE$_{12}$**	0.082%	**TE$_{13}$**	3.58×10^{-3}%	**TE$_{14}$**	4.94×10^{-4}%
	0°		180°		180°		180°
TM$_{11}$	14.606%	**TM$_{12}$**	0.613%	**TM$_{13}$**	0.121%	**TM$_{14}$**	0.039%
	0°		0°		0°		0°

Table 4.3: Ideal phase and amplitude for coupling to free space TEM Gaussian mode, showing the normalised power and .phase difference.

For extremely high (>98%) coupling the fundamental HE$_{11}$ mode is not sufficient. It has been demonstrated that with the inclusion of higher order modes in the feed that the coupling between the Gaussian free space modes and the waveguide modes may be improved to reach efficiencies as great as 99.8% and above[86,87]. This approach must include the coupling and matching of the phase and amplitudes over a range of modes within the waveguide therefore the complexity of the design must be increased to compensate. However, if this approach is employed the coupling into free space and the reflection into the input of the horn can be reduced, greatly increasing the gain and efficiency of the system.

5 Simulation and Design of a W-band Corrugated Horn

This chapter details the design process for the inclusion of a corrugated horn antenna to be used as a Gaussian beam launcher with the Strathclyde W-band gyro-TWA/BWO system. The first part of the chapter lays out the principal objectives for this design before the simulation and optimisation of the finalised prototype, which is discussed in the second half of the chapter.

5.1 Design Brief

The design of a 2nd harmonic W-band gyro-TWA operating over the 90 – 100 GHz frequency band with a output power of 5 kW and greater than 10% efficiency calls for the development of a means to decouple the electron beam and radiation. This system is an evolution of a previous gyro-BWO, which has been constructed with an operational bandwidth of 84 – 104 GHz and an output power of greater than 10 kW (Figure 5.1).

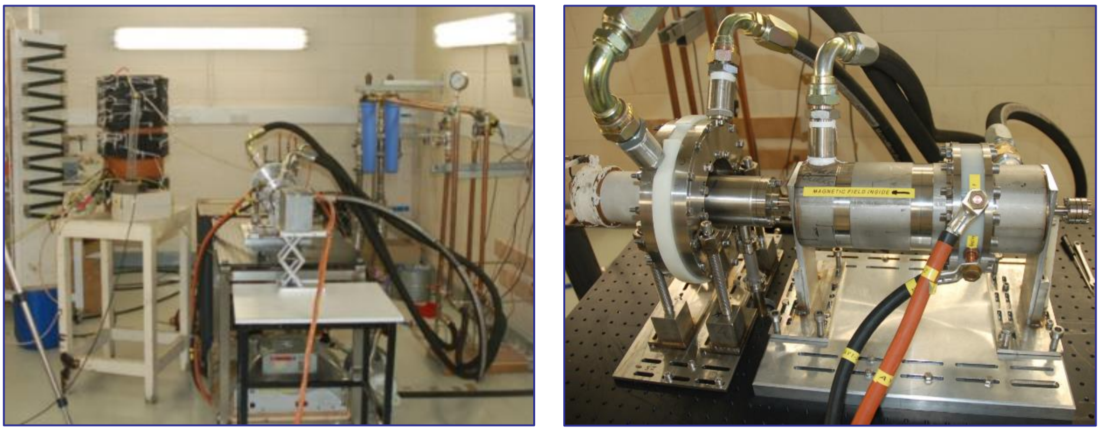

(a) Experimental bay with power supply and cooling. *(b) Gyro-BWO, showing reverse coil and main coil.*

Figure 5.1: Experimental apparatus (Gyro-BWO)

The operational efficiency of this system can be greatly improved by introducing an energy recovery system[88, 89]. This type of 'depressed collector' works on the principle that the electrons give up a portion of their kinetic energy while traversing a potential that is held below that of the main body of the tube and on doing so they strike the surface of the collector setting up a current that can be fed back into the system therefore reducing the power needed and increasing the system "wall plug" efficiency. For such a system to be incorporated into the gyro-TWA it is essential that there is a break in the waveguide to allow for this change in potential. In the gyro-BWO this is not important since the beam and wave are travelling in opposite directions so the wave can be extracted at the output coupler at the Cusp gun end of the device and the electron beam is free to enter the collector. The schematic for this system is shown in Figure 5.2 where the horn can also be seen fulfilling its second requirement to produce a quasi-optical output that is suitable for applications. However, the gyro-BWO radiation can be coupled output at the downstream position as shown in Figure 5.2 or if the power is very high a step down or step up Bragg reflector can be used to reflect the radiation forward in the same direction as in the case of the gyro-TWA Figure 5.3.

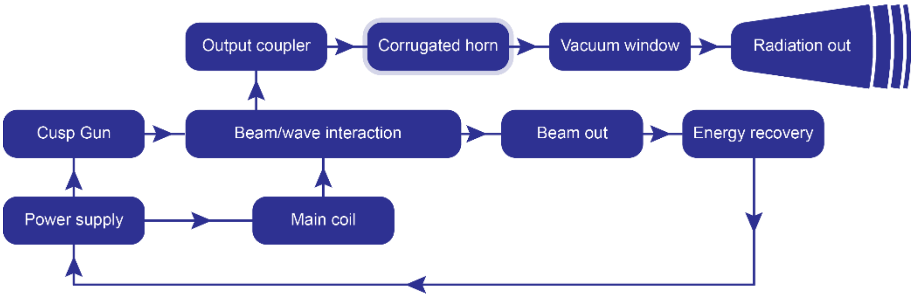

Figure 5.2: Gyro-BWO schematic

Figure 5.3 shows the alternate design where the horn is expected to be used in a gyro-TWA in order to launch a Gaussian millimetre wave beam as the input to a transmission line system and is very different from the oscillator. In the gyro-TWA the beam and wave both travel in the same direction and there is now a need to decouple them before the energy recovery system can be implemented. This is the proposed scheme for the design of the horn.

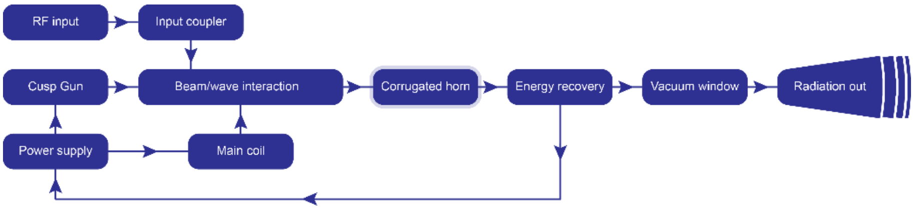

Figure 5.3: Gyro-TWA schematic

It should be noted that the gyro-BWO and gyro-TWA share many similarities in operation and design and only differ in the direction the electromagnetic wave is propagating in the beam-wave interaction region i.e. a forward wave for the gyro-TWA and a backward wave for the gyro-BWO. Therefore it is important that the horn is capable of integration with either system.

5.2 Define System Requirements and State System Objectives

The first step in the design process is a clear definition of the of system objectives, which is succinctly given by a statement of the main system goals:

Develop a quasi-optical output for a gyro-TWA that is to be continuously tuneable over the range between 90 and 100 GHz, which should be compatible with an energy recovery system.

This statement provides the fundamental motivation for any subsequent work and is a clear communication of intent for all future design iterations.

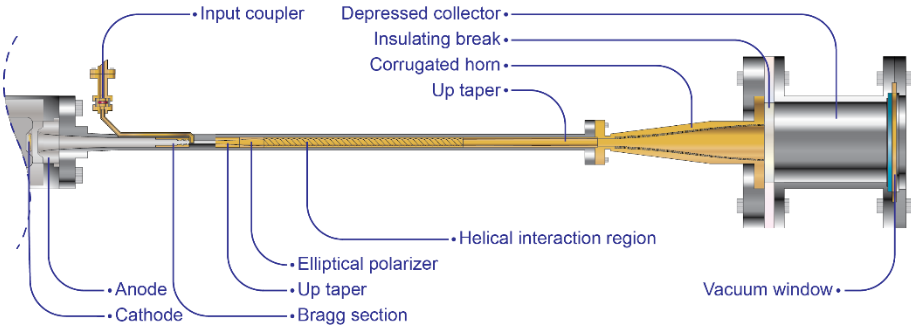

Figure 5.4: Gyro-TWA beam tube schematic with corrugated horn, proposed collector and window.

The basic schematic of the gyro-TWA system is shown in Figure 5.4, where the component can be seen in context as part of the system under development.

5.3 Overall System Context

The Gyro-TWA is to be a continuation of the work, which I was involved in, on a W-band gyro-BWO[90, 91, 92]. As such the design must take into account the existing systems and specifications. Although the conversion to an amplifier will result in considerable renovation of the existing prototype, the fundamental properties and operational principles are expected to remain unchanged. It is therefore reasonable to consider the design of any component in terms of the design of the gyro-BWO.

5.4 Develop Criteria for Evaluating and Selecting Components

5.4.1 Feasibility/Acceptability Criteria

The basis for an acceptable design of a component that meets the design requirements is dependent on the system requirements and design constraints. These determine the baseline from where any design must originate, but real world conditions and non-system requirements must also be factored into the design process. The most significant of these is the cost of manufacture closely followed, and related to the ease of manufacture. For the purpose of this project the initial cost of any component was an important factor and the manufacture was to be done by the most expedient method; using 'in-house' manufacturing as much as was practicable given the design and 'in-house' capabilities.

5.4.2 Quantitative Figures of Merit

- Operational bandwidth should span 90 to 100 GHz continuously.
  - The first consideration is the operational frequency range over which the optimal performance of the horn should be maintained. This is specified by the design of the gyro-TWA and should be between 90 to 100 GHz. This is the primary design goal, but the secondary goal calls for compatibility with the gyro-BWO over the bandwidth between 84 to 104 GHz. This secondary goal is far less important and is only to be considered once the primary goal has been achieved.
- Less than -35 dB return loss over the 90 to 100 GHz bandwidth.
  - The second consideration, which is strongly coupled to the first is the reflection or the S_{11} performance of the horn. Integration into the traveling wave amplifier brings a constraint on the amount of power that can be returned into the interaction region. This is due to the possibility of the occurrence of spurious and unwanted oscillations within the interaction region. Such oscillations would limit the overall amplification factor and efficiency of the gyro-TWA.

- At aperture 85% of the power should be in the TE_{11} mode and 15% in the TM_{11} mode to produce the closest approximation of the HE_{11}.
    - To generate a hybrid mode with the correct HE_{11} mode the power and phase in the TE/TM modes should be distributed as stated. It is not essential to have the power fractioned in this ratio however this is the generally accepted ratio to produce the desired HE_{11} mode.
- The HE_{11} mode, or more correctly the aperture field should be closely correlated with the fundamental Gaussian mode
    - The coupling between the aperture and the free space fundamental Gaussian mode relies on the generation of the 'ideal' HE_{11} mode in the aperture. The best aperture field need not be derived from the HE_{11} mode alone and the inclusion of higher order modes may improve the coupling efficiency by advantageous selection of power and phase. It is therefore better to consider the coupling between the aperture field and free space including all modes present.

5.4.3 Qualitative Figures of Merit

- 99.9 % of the power should be contained within a solid angle which subtends no more than 0.379 steradians, or theta about 20 degrees.

$$\Omega = 2\pi(1 - \cos\theta) \qquad 5.1$$

- Radiation primary lobe (beam width) must be well defined with a narrow beam waist at the window.

5.5 Trade-offs

As there is a large number of system and component requirements, which need to be carefully considered during the design and optimization process it is imperative to have a well-defined set of trade-offs from the outset. Given these considerations any subsequent design considerations can be implemented swiftly and with a greater level of confidence. In this case there are a number of conflicting output parameters, such as the reflection and the operational bandwidth. Therefore, it is necessary to define these from the outset with a weight that defines how these parameters will be used later in the design process. These parameters are given a ‘weight’ and are listed in Table 5.1.

Rank	Design parameter
1	Reflection (S_{11}) should be less than -35 dB
2	Operational bandwidth between 90 and 100 GHz
3	Component should not perturb the electron beam
4	Allow for the incorporation of a depressed collector
5	Produce a quasi-optical output mode
6	Component to allow the design and construction of a gyro-TWA
7	Input diameter should be no less than 2.6 mm (the mean diameter of the output section from the helically corrugated waveguide)

Table 5.1: Design parameter weights

In first and most important trade-off careful consideration must be given to an overall system and component design, which minimizes the reflected signal (S_{11}) to less than -35 dB at most. Second to the primary consideration is that the design should allow for operation of the device over a continuous and instantaneously variable bandwidth between 90 GHz and 100 GHz. This feeds back into the first consideration as the reflection must also be considered over this frequency range. The component must be capable of integration into the gyro-TWA system and therefore must not cause any interference with the primary CRM mechanism. As such there should be a minimal perturbation of the electron beam by the component. This includes disallowing for both modification of the electrons trajectory as well as any further parasitic CRM interactions at the component stage.

Another highly desired outcome is that the component should allow for the inclusion of a depressed collector system. Such a system can provide an increase in the overall system efficiency. This outcome is however combined with the need to produce a quasi-optical output mode so that the free space radiation mode would be capable of propagation through the depressed collector.

Finally the component should allow the design and construction of the gyro-TWA. This simply requires that the component should be incorporated with relative ease into the design for the system which is already in place. The primary incarnation of this outcome is that the diameter of the input section should be at least 3.6 mm, as this is the dimension of the output beam tube of the original gyro system.

5.6 Develop alternate system concepts

At this point in the system design it is sensible to investigate and develop alternate system concepts and to assess any past solutions, which may have existed to solve this problem.

Generally, gyrotrons are produced with depressed collection systems by incorporating a Vlasov type mode converter[93], which is used in applications requiring the decoupling of the beam and wave. But Vlasov mode converters, while practical and widely deployed in this area are not continuously tuneable over our operational frequency range. So this solution is not acceptable according to the secondary design trade-off.

Another possible solution is the simple mode converting horn, either a Potter horn[94] or a dielectric loaded horn can be used in this role. The Potter horn is however a narrow band device and the dielectric loaded horn is not compatible with a high power electron beam. Therefore, both of these solutions also fail the trade-off selection process.

The majority of the design trade-offs can be achieved using a corrugated inner structure. This type of corrugated horn may be constructed to be broadband and continuously tuneable over our range of operational parameters. It can also be used to generate a quasi-optical mode with a large diameter output, meeting the needs of the collector and the electron beam. It was therefore decided that the system was best served by incorporation of a suitably designed and optimized corrugated horn.

5.7 Simulation tools

5.7.1 Matlab, and MathCAD and Excel

The initial profiles and data analysis were calculated using mathematical models constructed for the most part using MathCAD, from initial equations describing the optimal size and characteristics of standard horns[95, 96, 97, 98, 99]. This provided a fast and transparent method by which a new profile could be created and tested. The depth of the corrugations their width and the function controlling their depth could all be altered and the results of any changes quickly plotted.

Once the shape of the profile was determined in this way the variables defining the corrugated structure were exported into excel where the data was formatted and conditioned for import into the mode matching software where the optimization of the design was carried out.

5.7.2 Mu-wave

The mode matching optimization was conducted using an integrated software package provided by Mician. This package primarily consists of a core mode matching solver and a design and analysis front end, collectively known as Mu-wave Wizard. Using this method allows for an extremely rapid optimization and design procedure, wherein the initial parameters describing the components may be imported from a text file by means of a custom dialogue, or directly input using the software design tool. An optimisation may then be run on the component parameters using the built in optimizer. The parameters for the optimization may be the system s-parameters, electric field at the aperture or the far field properties. The design may be optimized using many variables at once, although a large number of optimization variables cause a reduction in the speed and accuracy of the optimizer.

5.7.3 CST

Once the optimized design has been finalised using Mican Mu-wave the model may be verified on Computer Simulation Technology’s Studio Suite. CST is complete set of 3D electromagnetic simulation tools that can be used to calculate the properties of an electromagnetic problem in a CAD environment. Using a time domain solver the detailed evolution of the field patterns may be resolved, which is not possible using the mode matching method. CST can also produce a full set of s-parameters and a detailed far field plot in 3 dimensions.

5.8 Design Study

After the decision was taken to use an axial mode converter in favour of the radial Vlasov type typically seen in gyrotron oscillators a number of design choices were remaining ranging from a simple waveguide to much more complicated nonlinear structures. In each case the design called for the use of a corrugated inner surface to allow for the generation of a hybrid mode with the desired HE_{11} properties.

5.9 Computational simulations

There are essentially three different types of corrugated horn: The corrugated waveguide feed[100 101, 102], the corrugated linear horn[103, 104] and the corrugated profiled horn[105] (Figure 5.5). Computational analysis of each type was conducted using CST Microwave Studio and Mican Mu-wave.

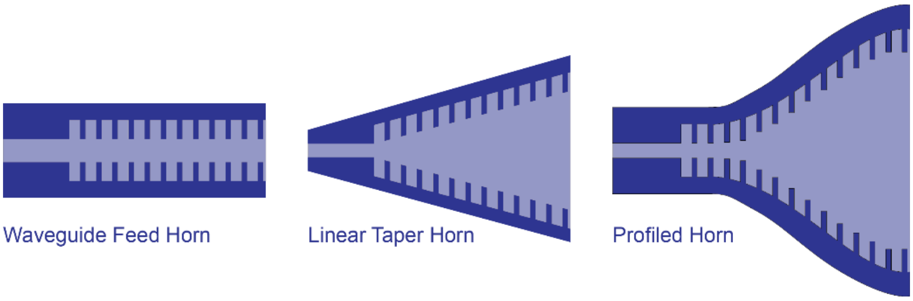

Figure 5.5: Types of Corrugated horn

The most important parameters for optimisation are the corrugation depth, the gap and vane length, the horn taper angle and input and output radius. These parameters should be investigated to produce the desired radiation characteristics in the far field. In this case the goals of the simulation are to produce a device that has less than -35 dB reflection with a far field radiation pattern having low side lobes and low cross-polarization. The horn should convert efficiently from the fundamental waveguide mode in the waveguide to the free space fundamental mode for propagation across a break in the waveguide and eventual transmission through a microwave window.

The beam width at the window should also be less than twice the diameter of the window for optimal transmission (>99.9%).

The mode matching method**[106, 107]** (Mician µ-Wave) is especially suited to this type of corrugated horn simulation, where the structure is essentially constructed by the summation of a series of stepped elements. The structure and frequency of the simulation limit the effectiveness of other types of software such as CST Studio due to the number of simulation cells that are required. It is possible to produce useful and insightful models on CST, but the time taken for each simulation eliminates CST as a viable method for optimization.

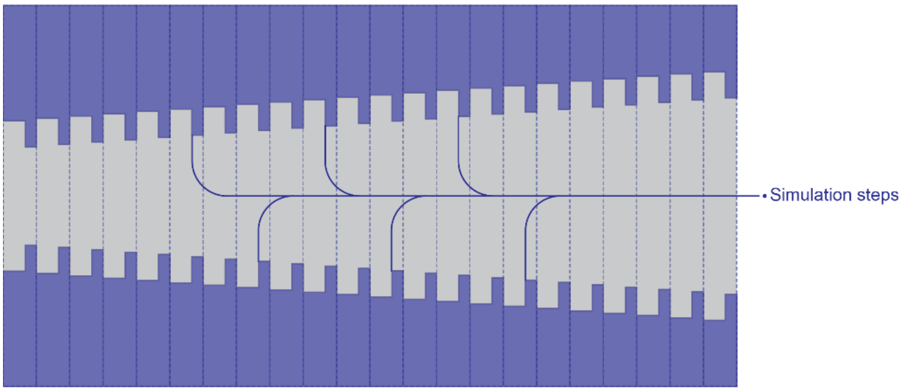

Figure 5.6: Mode matching geometry

Figure 5.6 demonstrates schematically the simulation geometry of µ-Wave. Each individual step in the model is evaluated separately as a waveguide discontinuity and the results are cascaded to produce a scattering matrix for the entire model. This produces a fast and accurate result that is readily optimized. Simulations of an X-band corrugated horn using µ-Wave were also compared with experimental data gathered from a horn already constructed by the group to validate the computational model.

Several different types of profile and corrugation geometry were simulated using the mode matching software before the final choice of a corrugated horn with a Sin^2 profile was chosen. This design was simulated and studied with consideration of the system criteria as laid out in section 4, whereupon after careful consideration of the electron beam profile the input radius was increased to facilitate passage of the beam. The design process for this prototype is laid out in the following sections.

5.10 Sin^2 Profiled Horn

A good possibility for the profile shape would be to use a Sin^2 function to derive a nonlinear profile for the horn. Equation 5.2 defines the profile, where L is the overall length, r_{in} is the input radius and r_{out} is the output radius. The value of A determines the characteristics of the profile, when A = 0 this reduces to the linear case and when A = 1 the profile is sin^2. In this case A was set to 0.7.

$$r(z) = r_{in} + (r_{out} - r_{in})\left[\frac{z}{L}(1-A) + A\sin\left(\frac{\pi z}{2L}\right)^2\right] \qquad 5.2$$

This type of profile has some similarities to the Gaussian profile however the sin^2 profile offers a longer length for a given output diameter.

5.10.1 Sin^2 Profiled Horn – Type 1

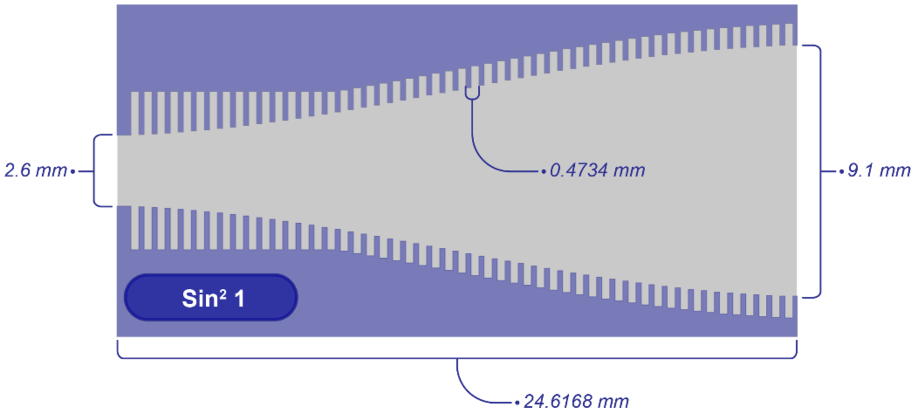

Figure 5.7: Sin^2 profiled horn – Type 1

The parameters for the simulation of the Sin^2 profile are similar to those used in the previous simulations (see appendix 4). The impedance matching section was once again changed from $\lambda_c/2$ at the input to $\lambda_c/4$ at over the first 16 steps, keeping the outer radius constant and altering the inner radius to match the profile. The input diameter and the gap and vane parameters are the same as the previous profile types and the output diameter is 9.1 mm. This profile is shown in Figure 5.7.

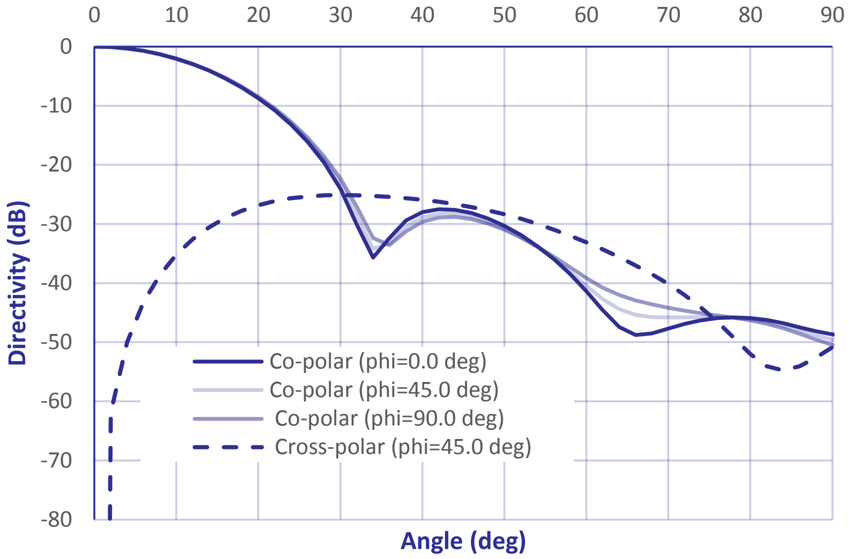

Figure 5.8: Sin^2 profiled horn – Type 1 far field pattern

This profile type has the best far-field performance as can be seen in Figure 5.8. The cross polar pattern has a maximum at -25 dB and the main lobe of the co-polar pattern is now at -25 dB at 30 degrees.

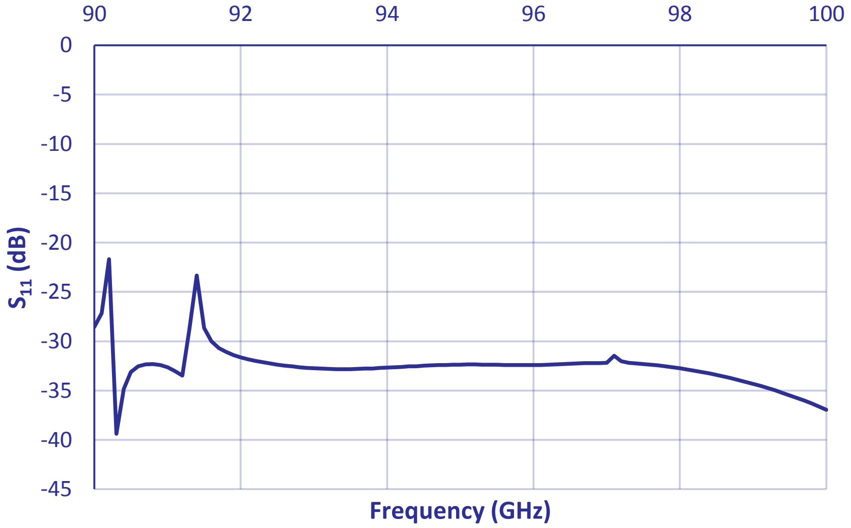

Figure 5.9: Sin^2 profiled horn – Type 1 S_{11}

Unfortunately, this type of profile has not performed as well over the bandwidth. The reflection between 90 and 92 GHz shows some unwanted spikes (Figure 5.9).

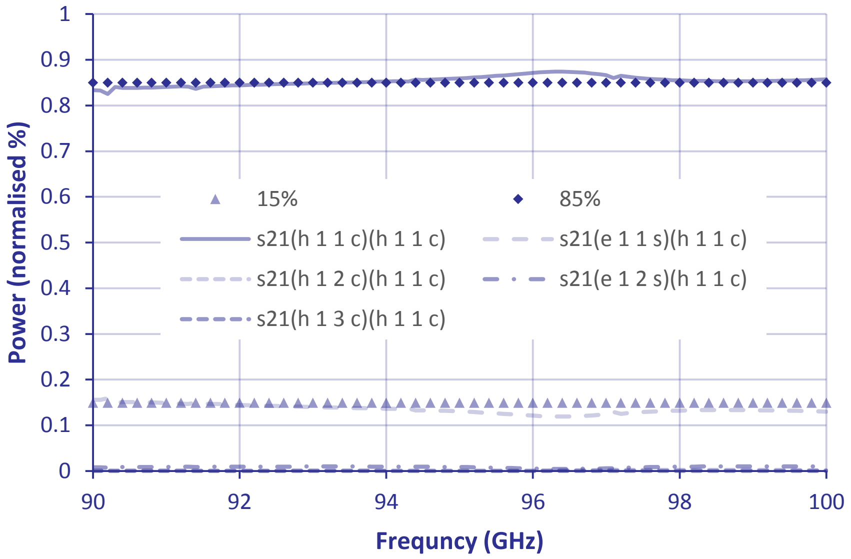

Figure 5.10: Sin^2 profiled horn – Type 1 S$_{21}$

The transmission characteristics of this profile are clearly on a par, if not better than those of the third linear profile (Figure 5.10). The TE$_{11}$ and TM$_{11}$ modes remain at the 85% and 15% transmitted power mixture over the entire bandwidth.

5.10.2 Sin^2 Profiled Horn – Type 2

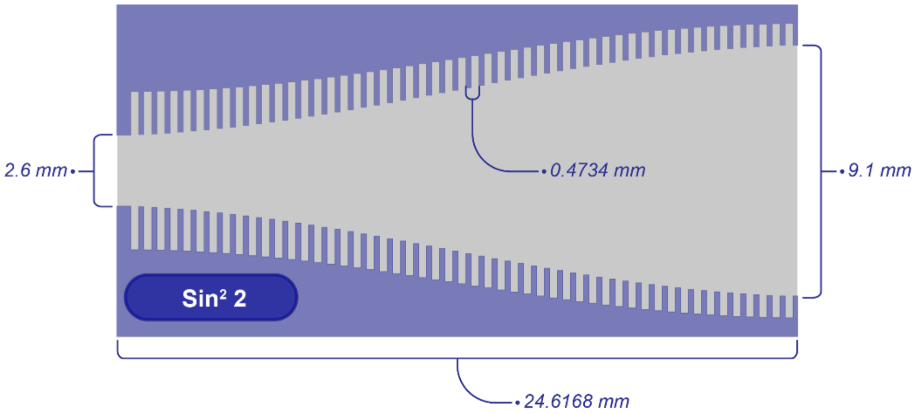

Figure 5.11: Sin^2 profiled horn – Type 2

The second type of Sin^2 profile used the impedance matching section where the depth of the corrugations were changed from $\lambda_c/2$ at the input to $\lambda_c/4$ at the output of the horn. Apart from this all the other parameters are the same as the first sin^2 profile. A schematic of this design is shown in Figure 5.11.

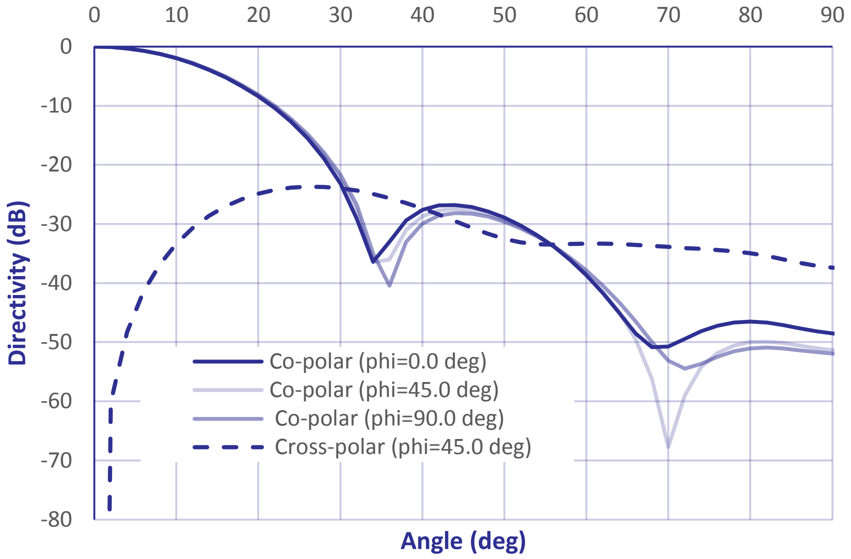

Figure 5.12: Sin^2 profiled horn – Type 2 far field pattern

Figure 5.12 displays the far-field performance of the second type of Sin^2 profile. Here there is once again a slight difference between the cross-polar plots of this and type 1 and 2. There is a slight difference in the cross-polar and the second lobe of the co-polar patterns.

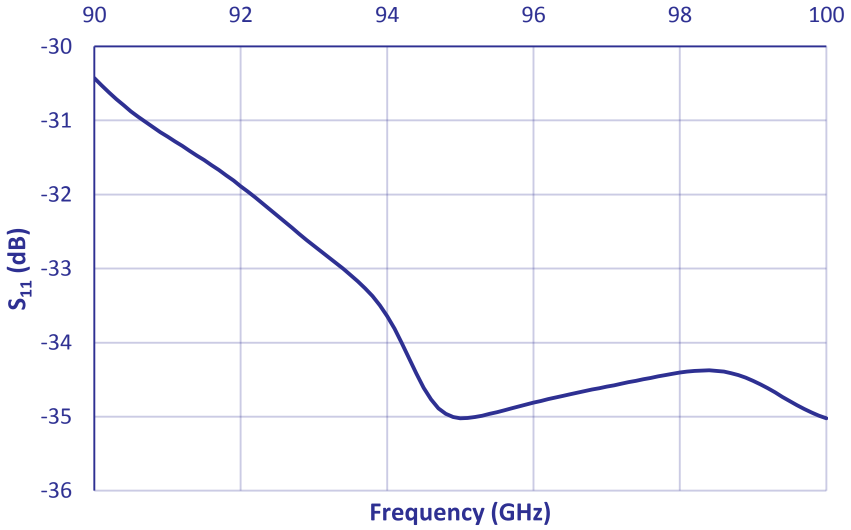

Figure 5.13: Sin^2 profiled horn – Type 2 S_{11}

This design is also very close to the target for reflection (Figure 5.13). The S_{11} at 95 GHz meets this target of-35 dB and the rest of the bandwidth falls below -30 dB.

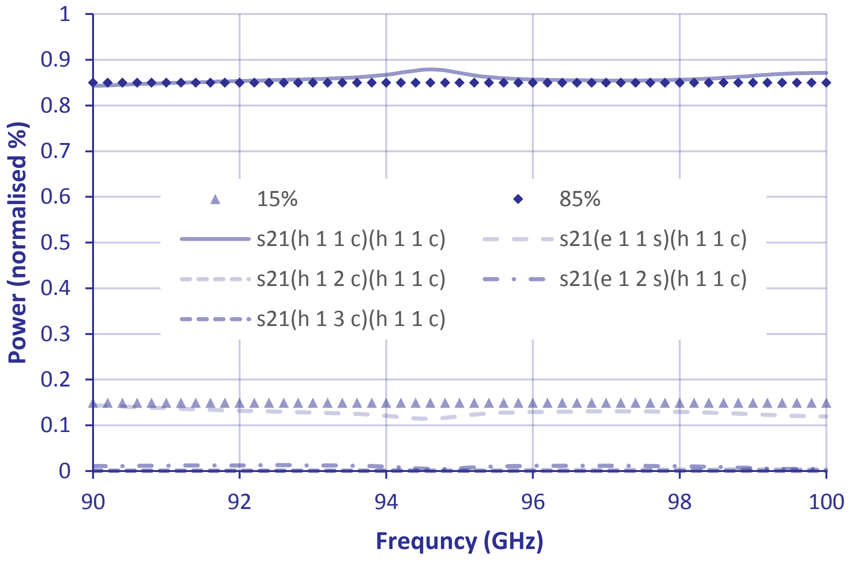

Figure 5.14: Sin^2 profiled horn – Type 2 S_{21}

Once again the transmission characteristics of the second sin^2 profile are as good as those of the previous design type (Figure 5.10).

5.11 Profile Comparisons

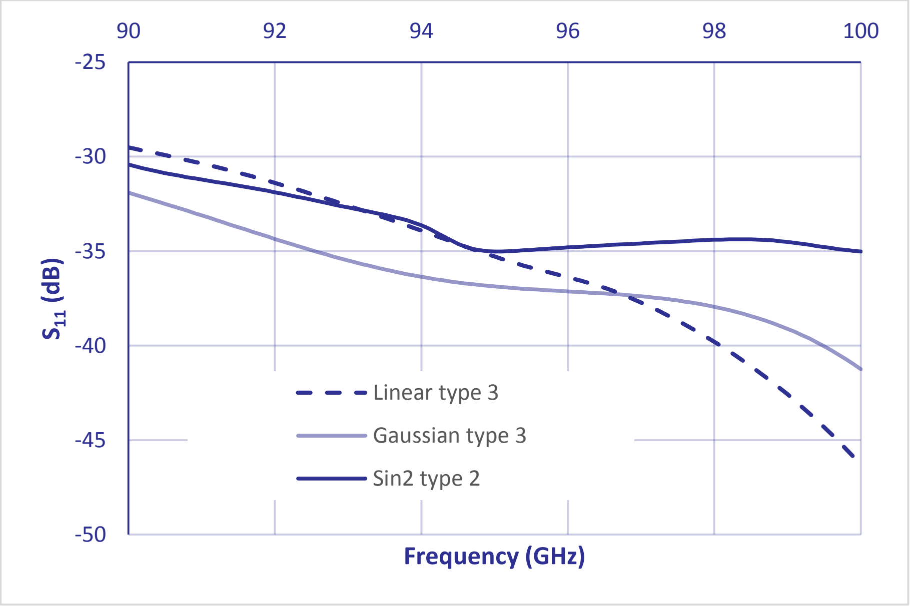

Figure 5.15: S_{11} comparison (best 3 designs).

In Figure 5.15 a clear demonstration of the refection generated by the best three profile types. While both the linear and Gaussian profiles do produce a reflection of less than -35 dB, the linear horn does not perform as well over the entire bandwidth.

The sin^2 profile does produce a greater reflection than the Gaussian profile, but the performance of the sin^2 profile is better than -35 dB over from 95 to 100 GHz and with further optimisation this performance can be improved.

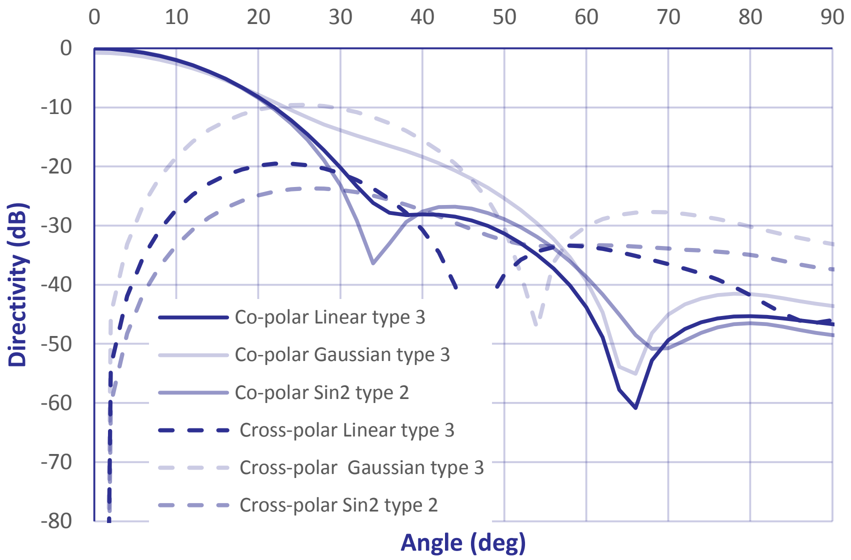

Figure 5.16: Far-field comparison (best 3 designs).

When the far-field patterns from these three types are compared (Figure 5.16) it is clear that the sin^2 profile is the superior choice. Both the co-polar and cross-polar radiation patterns of this profile are better and in comparison with the Gaussian profile the sin^2

On returning to the original considerations laid out in Table 5.1, a choice can be made on the best horn profile for our needs. It is evident that all three designs operate well at the centre frequency of 95 GHz, with the Gaussian producing the best performance over the remainder of the bandwidth and the sin^2 and linear closely matched. The Gaussian far-field profile is however not acceptable and the transmission (s_{21}) from this profile is also outside the boundaries of our goals. This profile is the better choice when we consider the electron beam due to its shorter length, but the problems with the far-field and the transmission remove this profile from further considerations.

The sin^2 profile and the linear profile compare well in transmission (s_{21}), but the sin^2 profile has a better far-field pattern and this type of profile has a faster increase in the inside diameter over the length. This is better for the electron beam, allowing for a greater clearance between the waveguide wall and the beam.

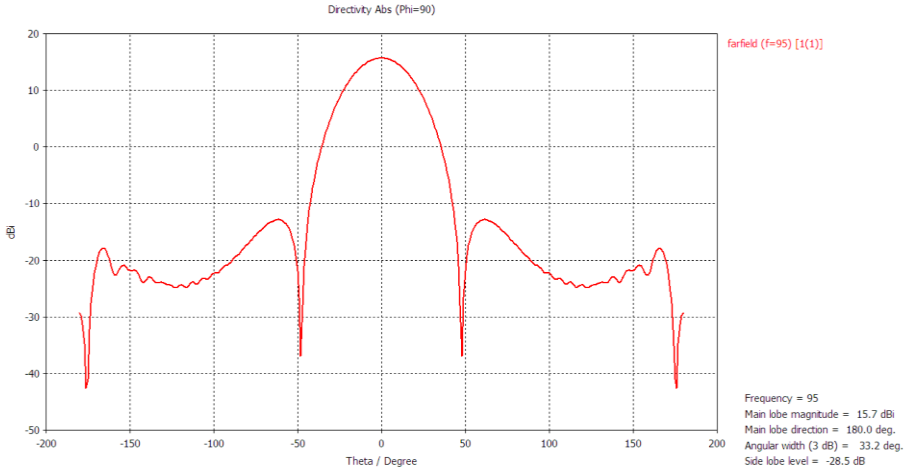

Figure 5.17: CST far-field (Sin^2 profiled horn – Type 2)

All of these types can be incorporated into our current system and are capable of producing a quasi-optical output. However, the far-field performance of the sin^2 profile makes this the best choice for further design and optimisation. A preliminary CST simulation of the sin^2 profile was carried out and the results showing the far-field and the magnitude of electric field in the y-z plane are shown in Figure 5.17 and Figure 5.18.

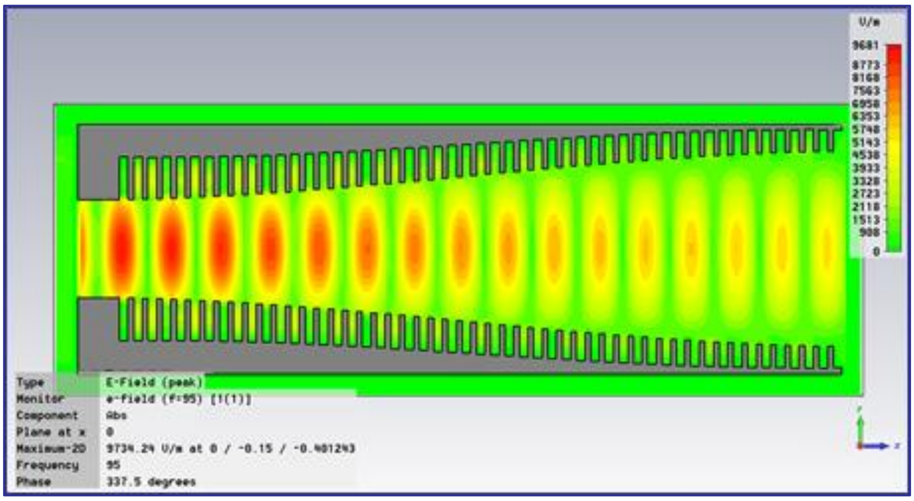

Type	E-Field (peak)
Monitor	e-field (f=95) [1(1)]
Component	Abs
Plane at x	0
Maximum-2D	9734.24 V/m at 0 / -0.15 / -0.401243
Frequency	95
Phase	337.5 degrees

Figure 5.18: CST Absolute magnitude of electric field (Sin^2 profiled horn – Type 2)

5.12 Optimization and Design of Sin^2 Horn

After the initial tests had determined that the best design for our application was a non-linear taper using a profile determined by the sin^2 function a simulation was carried out using the mode matching software. The model was constructed first analytically using equation 5.2 to derive the non-linear profile. Then the corrugation depths were calculated and the corresponding variables containing the sin^2 profile with the linear depth taper were exported to a text file for import into the simulation software. At this point the initial parameters were as shown in Table 5.2.

Simulation Parameters	**Initial Value**
Input diameter	3.6 mm
Output diameter	7.2 mm
Gap length	**0.1λ**
Vane length	**~2/3 Gap**
Corrugation depth (input)	1.5 mm
Corrugation depth (output)	0.75 mm

Table 5.2: Horn design parameters.

These are the same parameters which were successfully implemented in the design study to determine the optimum profile type. At this point the design was optimized using the following optimization goals (Table 5.3). The weights for each goal was kept equal and only the TE_{11}, TM_{11} and S_{11} parameters were considered.

Goal function	Constraint	Weight
TE_{11}	= 85% (power)	1
TM_{11}	= 15% (power)	1
S_{11}	< -35 dB	1

Table 5.3: Optimization goals for the corrugated horn

The software allows for the possibility of optimization over all the design parameters. Each individual step and gap length could be optimized and altered with great speed, but initial investigations found that for this case there were too many variables (> 100) for this type of optimization scenario to be practicable. Therefore the optimization variables were limited to the width of the gaps and vanes.

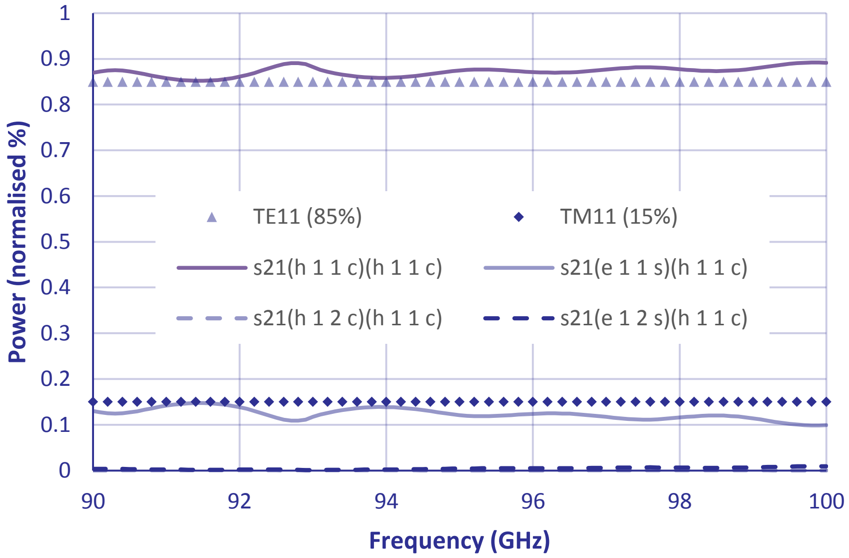

Figure 5.19: Optimisation of Sin^2 profiled horn (S_{21}).

The results from the simulation and optimization using the mode matching method can be seen in Figure 5.19. The dotted lines represent the ideal values of 85% and 15% for transmission of the TE_{11} and TM_{11} modes respectively, which are given to produce the desired HE_{11} mode at the aperture. This figure also alludes to the fact that there are higher modes present, although they are not readily discernible in this plot. However, the TE_{12} and TM_{12} modes have much less than 1% of the power.

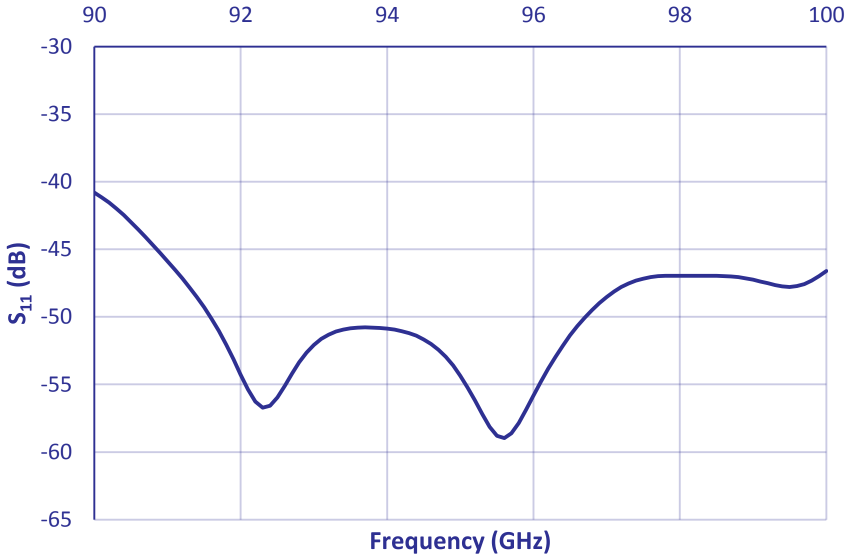

Figure 5.20: Sin^2 profiled horn – initial optimisation S_{11}.

The reflected power is very much less than -40 dB (Figure 5.20) using this design and well below our goal of -35 dB.

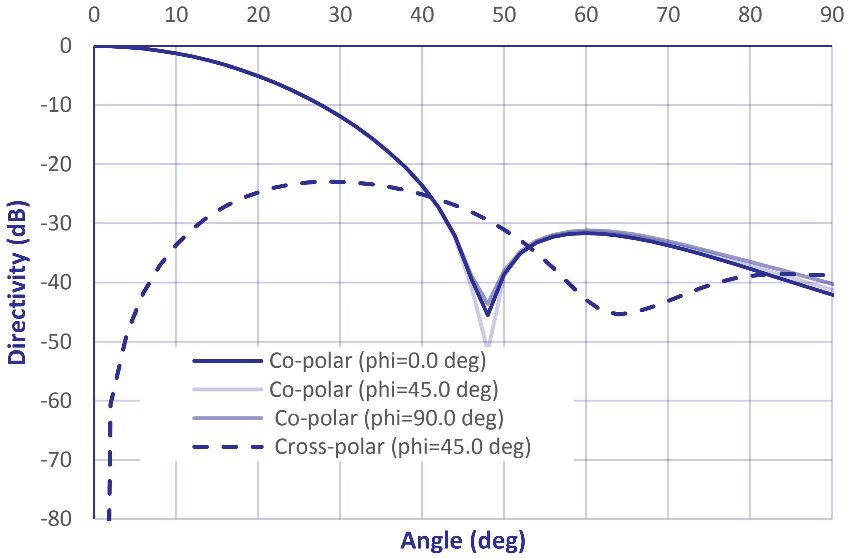

Figure 5.21: Sin2 profiled horn – initial optimisation far-field pattern.

The far field profile is wider than what we would desire (Figure 5.21). The first null in the co-polar pattern is at 48 degrees, which would produce an angular spread that may not be suitable for the design. The cross-polar pattern is very good at less than -47 dB (absolute value).

5.12.1 Final optimisations

During this time, the parameters for the design were modified taking into account a new electron beam spread that was derived from a PIC simulation; showing the electron beam to have an azimuthal orbit at the point of the horn greater than what was deemed tolerable for the previous design. The results are shown in Figure 5.22.

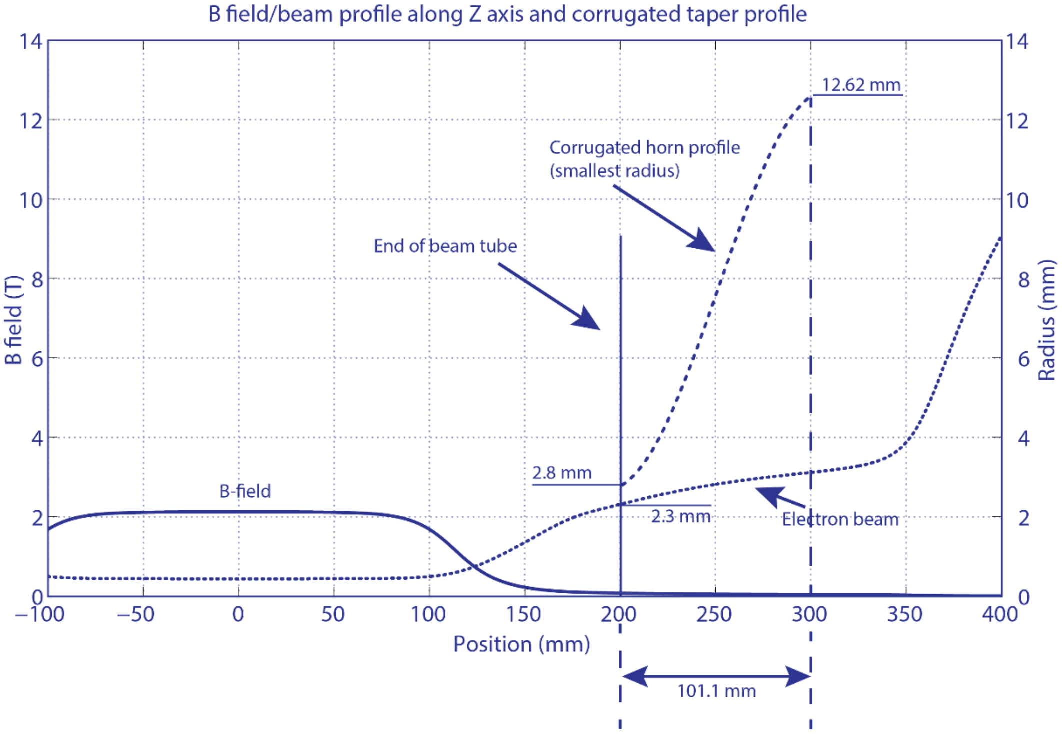

Figure 5.22: Simulation results showing electron beam radius along z-axis[108].

With this new design parameter in mind the decision was made to increase the diameter of the input section from 3.6 mm to 6 mm to allow for the electron beam. The widths of the gaps and vanes were also determined to be problematic due to the difficulties in manufacture that would be caused for such small structures with high ratios of length to width. A study was conducted to find out just what the impact of increasing the width and length of the gaps and vanes using the parameters from the first $\sin^2$ profiled horn and changing only the width. Table 5.4 lists the updated parameters for this study, with the swept parameters underlined.

Simulation Parameters	**Initial Value**
Output diameter	7.2 mm
Gap length	**0.1mm -0.7 mm**
Vane length	**~2/3 Gap**
Corrugation depth (input)	1.5 mm
Corrugation depth (output)	0.75 mm

Table 5.4: Changing the width of the gaps and vanes.

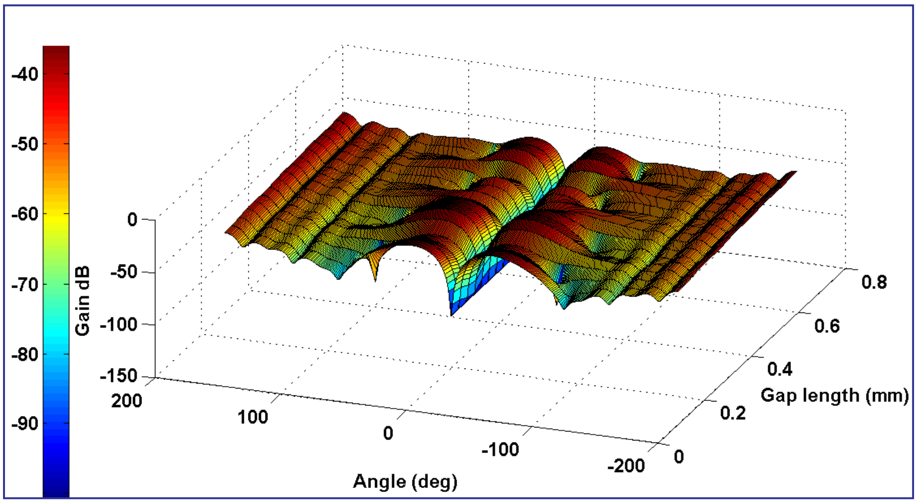

(a) Evolution of cross-polar pattern.

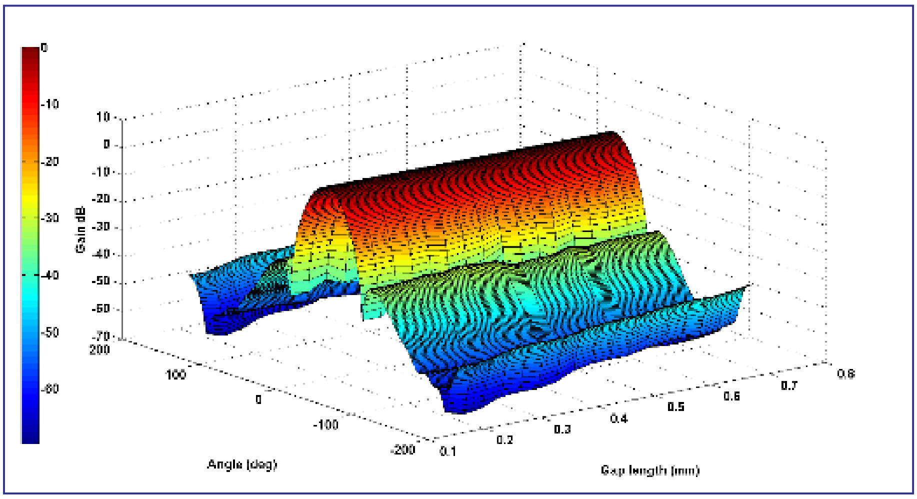

(b) Evolution of co-polar pattern.

Figure 5.23: Parameter sweep of gap and vane lengths.

The results from this parameter sweep are shown in two contour plots (Figure 5.23 a & Figure 5.23 b), which demonstrates that alteration of the gap and vane lengths is not overly detrimental to the radiated far-field and although there is some degree of variation seen in the cross-polar pattern it is within the level that is acceptable in our application.

The effect of altering the input diameter was also studied and the results show that there is an acceptable level of variations between an input diameter of 3.6 mm and that of 6 mm. The far field does show an increased cross-polar level but this is not a problem for our design. The transmitted power lies very close to the ideal values and those of the original input diameter horn. There are higher order modes that were not seen in the simulation of the smaller diameter, but these are at a negligible level compared with the TE_{11} and TM_{11} modes.

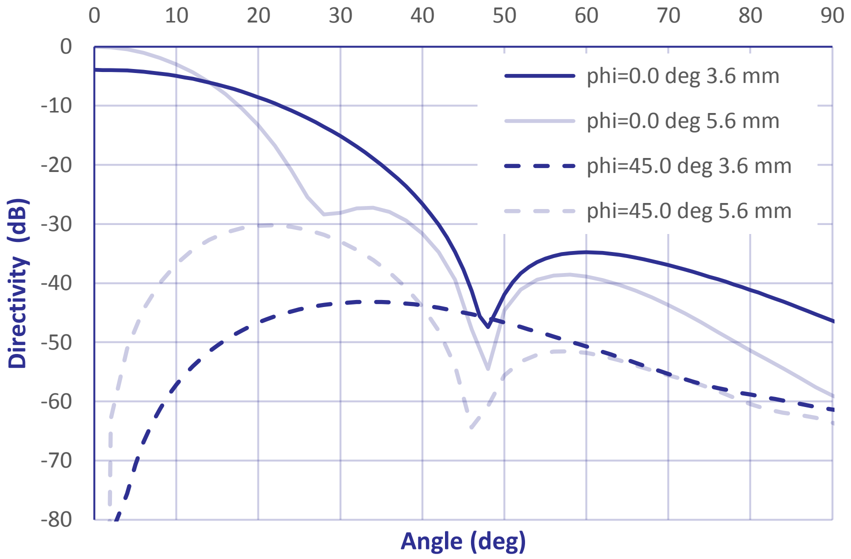

Figure 5.24: Sin2 profiled horn – comparison between input radii far-field patterns.

Figure 5.24 and Figure 5.25 demonstrate the changes between the differing input diameters. The reflection remains almost unchanged when the input is increased and is still well within our design goals. The far-field however does exhibit some substantial changes, especially in the cross-polar pattern. The pattern is almost 12 dB higher because there are higher order modes now present in the throat of the horn. The cross-polar pattern is also very different, but this is an improvement over the smaller diameter input. The directivity is now better and the main lobe has narrowed.

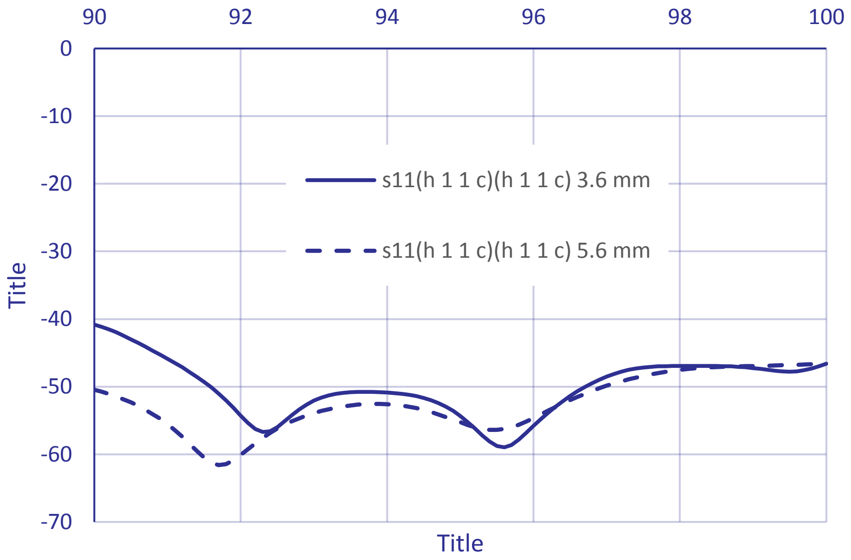

Figure 5.25: Sin^2 profiled horn – comparison between input radii s_{11}.

The transmission has also changed very slightly, with the inclusion of the higher order modes, but these are still very small in percentage power compared to the TE_{11} and TM_{11} modes and therefore are omitted from Figure 5.26. Both the TE_{11} and TM_{11} modes show a similar percentage power in the higher diameter design to the previous smaller diameter and are considerably smother over the bandwidth.

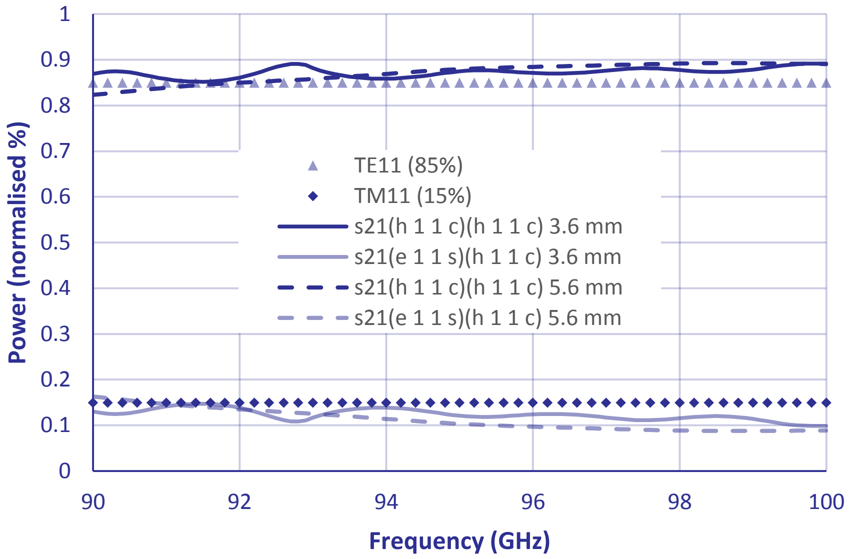

Figure 5.26: Sin^2 profiled horn – comparison between input radii s_{21}.

From this study it is evident that the input diameter and the lengths of both the gaps and vanes may be increased without greatly altering the overall performance if the horn.

5.12.2 New Goal function

Goal function	**Constraint**	**Weight**
TE_{11}	= 85% (power)	1
TM_{11}	= 15% (power)	1
S_{11}	< -35 dB	2

Table 5.5: Improved goal functions.

With these parameter sweeps in mind, a new design using a 6 mm input diameter section was created. Once again, the sin^2 profile with the linear taper was used and the number of corrugations set at 50. The optimisation was carried out on the gaps and vanes allowing for a larger gap and vane width. For this set of optimizations a new goal function was used (Table 5.5) that gave more weight to the reflection as this is a critical system requirement. The second change was to add a goal function for a narrow beam width as well as optimizing for the HE_{11} mix. By reducing the weight factor for the transmitted TM_{11} and TE_{11} powers and including this new goal function a faster convergence was achieved.

Sin^2 Simulation Parameters (MK II)	
Input diameter	6 mm
Output diameter	2 x Din to 56x Din
Gap length	**0.1 mm to 0.7 mm**
Vane length	**0.1 mm to 0.7 mm**
Corrugation depth (input)	1.5 mm
Corrugation depth (output)	0.75 mm

Table 5.6: MK II simulation parameters

This method produced results that were satisfactory, but further optimization was possible by manually tuning some of the parameters. This was required because the alteration of certain parameters, such as the number of corrugations and the taper angle, were outside the capability of the software. After the initial optimisation was conducted on the horn with 50 periods, the derived parameters were used to generate a number of different simulations that had a greater number of periods and a larger diameter aperture. The factor governing the optimal design at this point was the co-polar pattern, which gave the beam width and the beam symmetry. From these final manual simulations, a design having 100 corrugations with an output diameter of 224 mm was chosen. After the optimisation the gap and vane width were 0.6 and 0.5 mm respectively.

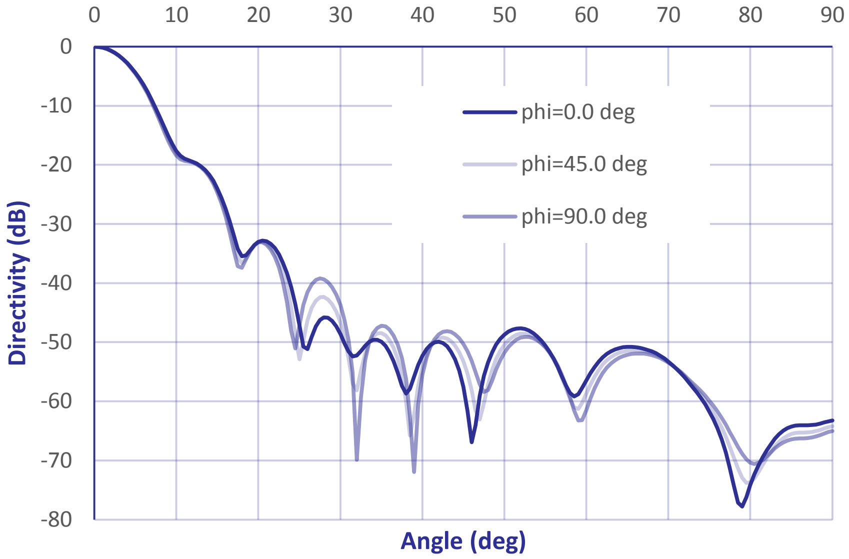

Figure 5.27: Sin^2 profiled horn – final prototype far-field

Figure 5.27 demonstrates the highly symmetric radiation pattern produced by the 100 period (Mk II) horn. 99.9 % of the radiated power is contained within a half angle of 17 degrees.

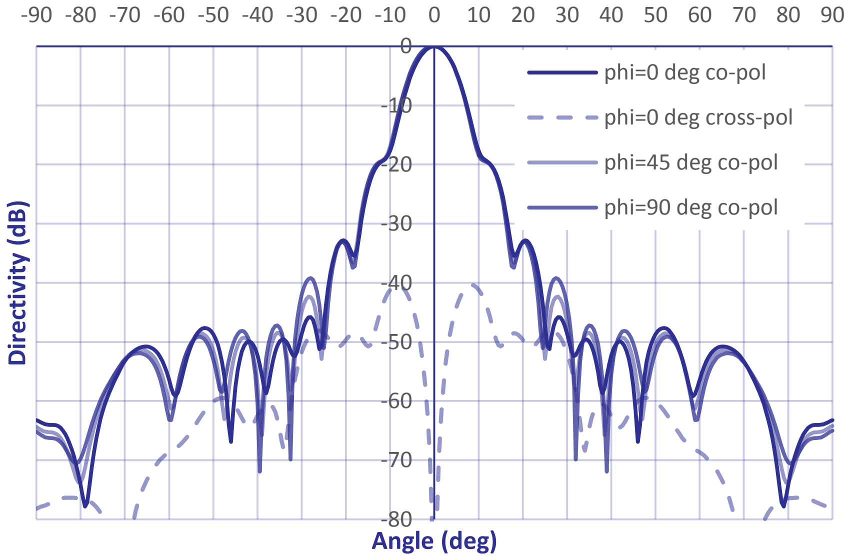

Figure 5.28: Sin^2 profiled horn – final prototype combined far-field

The full radiation profile, shown in Figure 5.28, shows a cross-polar component less than -40 dB.

5.13 CST Simulation

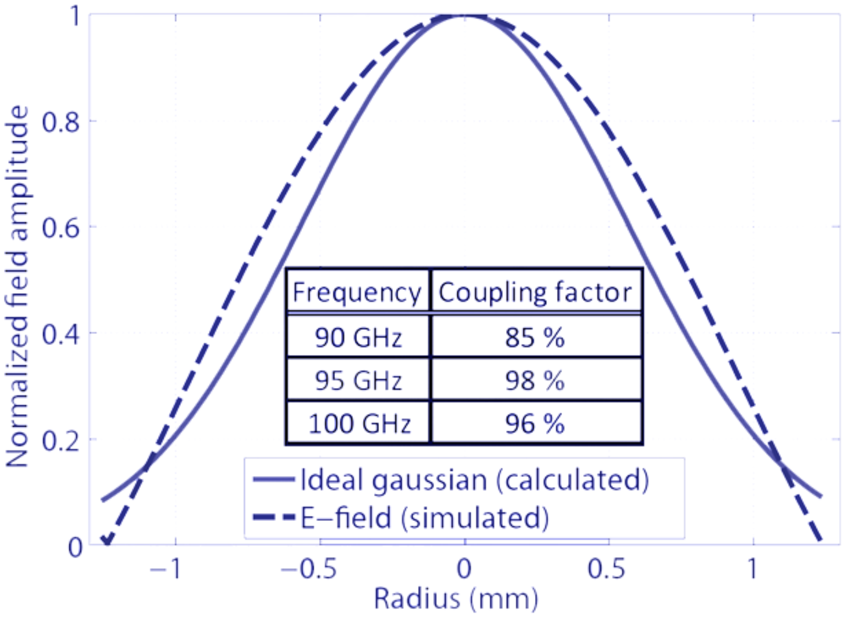

Frequency	Coupling factor
90 GHz	85 %
95 GHz	98 %
100 GHz	96 %

Figure 5.29: Sin^2 profiled horn – final prototype calculated coupling integral (Matlab).

The parameters for the Mk II horn were imported into CST Microwave Studio where an investigation could be conducted into the field patterns within the horn as well as the far fields. From this simulation, a graph can be generated showing the electric field at the horn aperture. This compares well with the ideal Gaussian field profile derived from numerical calculation and is shown in Figure 5.29. For more information on CST MW please refer to Appendix 5

The far-field was also investigated using CST, which determined that the directivity of the prototype horn is greater than 26 dB. This simulation was further modified by increasing the free space to allow for 200 mm of space in the positive z direction. The results of this simulation were then analysed using Matlab, where Figure 5.30 is derived, showing both the ideal Gaussian beam radius as it propagated in the z direction and the simulated Gaussian beam generated from the MK II horn. A further trace shows the radius of any aperture that would be required to provide a transmission of 99.9%.

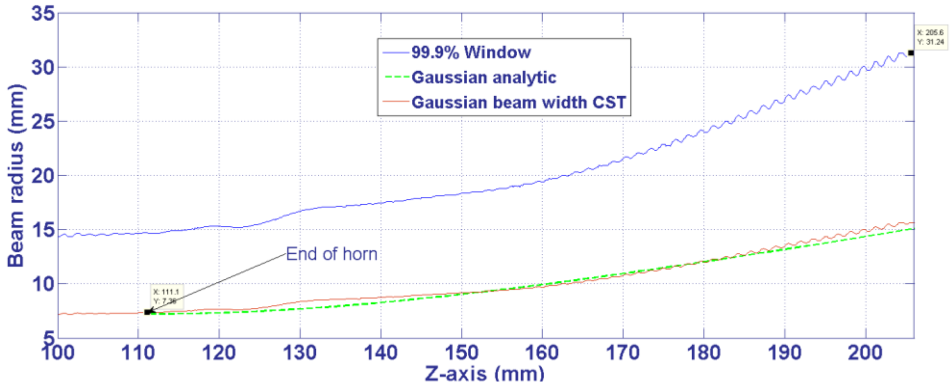

Figure 5.30: Gaussian beam simulated in CST.

This is a useful plot for determining the parameters of the collector system and output window. From this, it is clear that at a distance from the aperture of around 50 mm any window must be at least 17 mm in radius.

From these simulations, an optimized design in the form of a $\sin^2$ profiled horn with 100 corrugations and an output diameter of 224 mm is the best choice for the first prototype, which is to be constructed for integration with the gyro-TWA system.

6 Horn Construction and Millimetre Wave Measurements

Chapter 6 describes the methodology behind the construction, experimental measurement and validation of the corrugated horn design. The construction of the first prototype is described in detail, giving an insight into the in-house manufacture and design. The millimetre wave measurement validation process is then detailed. Here the finished prototype was subject to far-field measurements using a vector network analyser.

6.1 Acceptance of Prototype Design

Once an optimal design had been developed and finalized the construction of the horn was commenced. Two working prototypes were initially commissioned each made of oxygen-free high conductivity (OFHC) copper. They were constructed by first machining a mandrel from HE 30 aluminium (Figure 6.1 a-c), then by electroforming copper on the mandrel (Figure 6.1 d), and finally by eroding away the aluminium mandrel using a chemical etching process (Figure 6.1 e). The whole process produces the corrugated internal structure of the prototype horn.

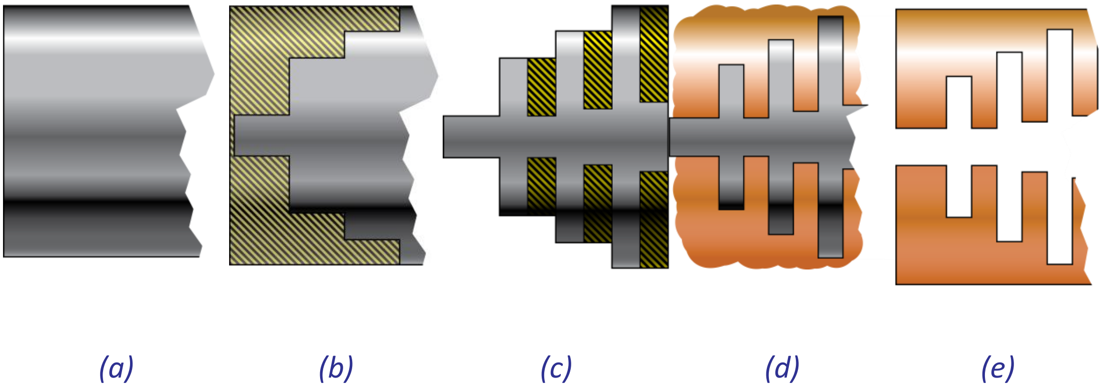

Figure 6.1 Stages in the construction of the corrugated horn

6.2 Aluminium Mandrel Construction

6.2.1 Tolerance Testing

The first stage in manufacturing a prototype was to consider the effect of machine tolerances on the performance. This is important in determining the feasibility of the design given the chosen method of fabrication and is clearly essential before further progress can be made. The tolerance is not only determined by the tools used in the manufacture of the aluminium former but also the copper growth process. In the first case, machining tolerances are well understood and can be accounted for with relative ease for a simple design. This was one of the key reasons for choosing to keep the width of the gaps and vanes constant over the length of the horn, but in fact the performance of the horn remained stable over any alterations in the width of the gaps and vanes that could possibly be induced due to physical manufacturing.

A greater threat to the performance was considered to be from the copper growth. The copper is ‘grown’ onto the aluminium substrate and therefore subject to a degree of anisotropy as it is deposited. This is especially true when there is a large aspect ratio to the length and depth of any cavity that is to be filled by the copper, such as is found in the horn design and may lead to incomplete or irregular growth of the horn.

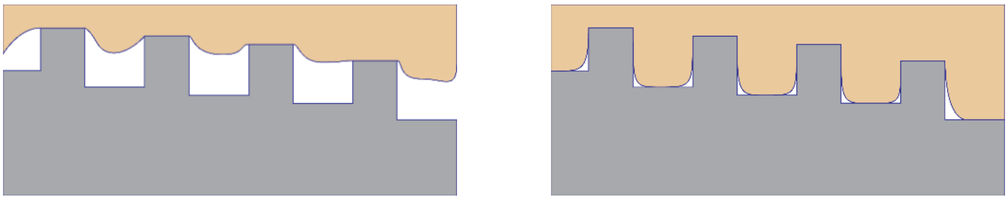

(a) Incomplete formation

(b) Rounding of the copper vanes

Figure 6.2 Inhomogeneous copper growth (temp picture)

Figure 6.2 demonstrates the two most likely scenarios where irregular growth may occur, where either the copper grows radially from the tips of the aluminium vanes and closes over before filling up the gaps. This would result in the incomplete formation of the copper vanes in the completed horn. The second likely scenario could be caused by inhomogeneous growth of the copper between the aluminium vanes, resulting in an uneven ‘rounding’ of the copper vanes in the finished horn. Both of these situations are difficult to simulate and predict and there must be a certain level of confidence placed in the skill of the contractors who will undertake the electroforming process.

To investigate the risk of manufacture a set of tolerance simulations were conducted to evaluate the effects of errors in the sizes of the vanes during the manufacturing process on the performance of the horn. Figure 6.3 and Figure 6.4 demonstrates the effect that changes in the inner diameter might have given the tolerance of ± 0.025 mm.

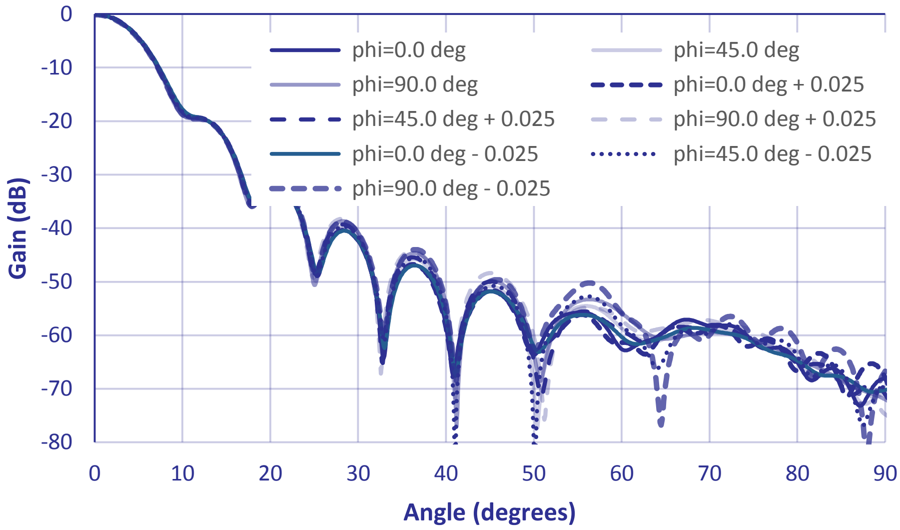

Figure 6.3 Tolerance tests of co-polar far-field pattern (changing r ± 0.025 mm)

In both the cross-polar and co-polar graphs it is evident that a small difference in the diameter of ~50 μm does not pose a series problem with the overall performance. The only more noticeable difference in the far field due to such a manufacturing error is alteration of the far-field pattern at higher angles where the power is extremely low.

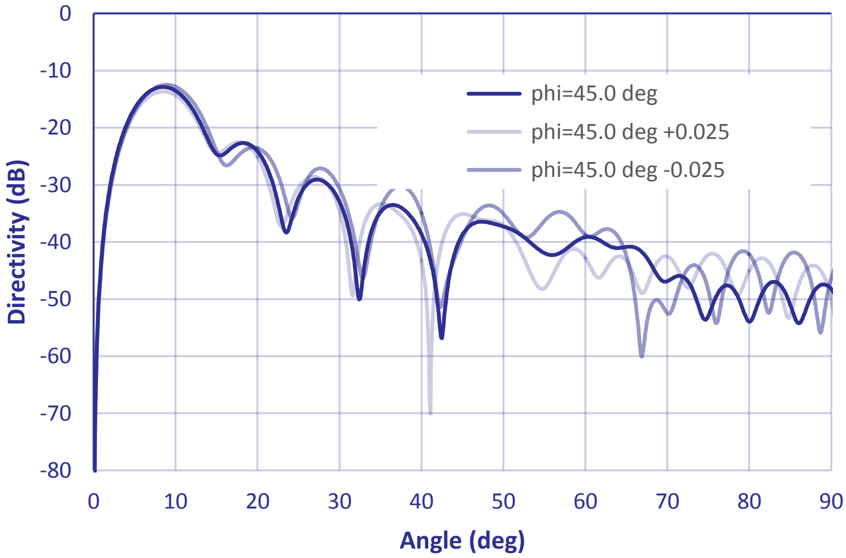

Figure 6.4 Tolerance tests of cross-polar far-field pattern (changing r ± 0.025 mm)

In the second set of tolerance tests the effect that a change in the width of the vanes is simulated, such as may be caused by an improper growth of the copper. Figure 6.5 contains the result of a far-field simulation for the worst case scenario and demonstrates that the horn design is quite robust to a change in the spacing of 100 µm. However, it should be noted that the aperture field and coupling performance would be compromised by such an error.

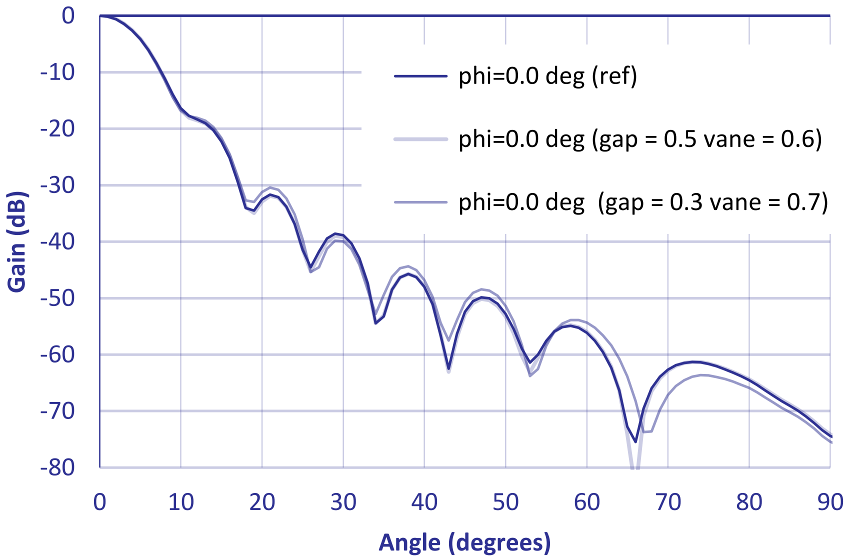

Figure 6.5 Tolerance tests of co-polar far-field pattern (changing gap and vanes ± 0.2 mm)

Another consideration, which can affect the performance of the horn, is the size of the aperture flange after the last vane. In this design the flange at the aperture will span the inner diameter at the last vane to the outside diameter of the horn. The initial simulations and optimizations were conducted without consideration of this discrete variable, but for construction of the final prototype its dimensions should be quantified. µ-wave was used to produce a set of far-field radiation patterns where the simulated variable was the aperture flange.

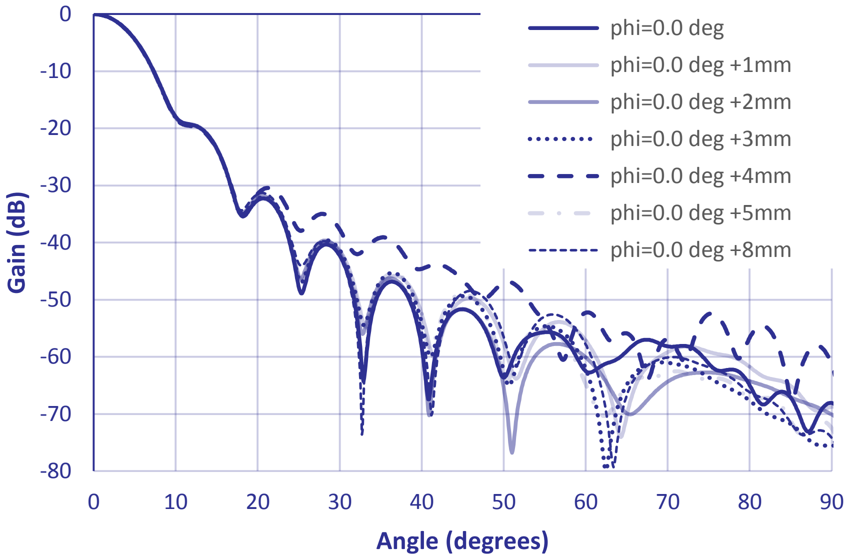

Figure 6.6 Effect of output flange on co-polar radiation pattern

This was done from 0 mm to 8 mm in steps of 1 mm. Figure 6 and Figure 7 show the effect on the patterns due to the change in aperture flange size. From these results a flange size of 3 mm at the aperture was selected as the best performing.

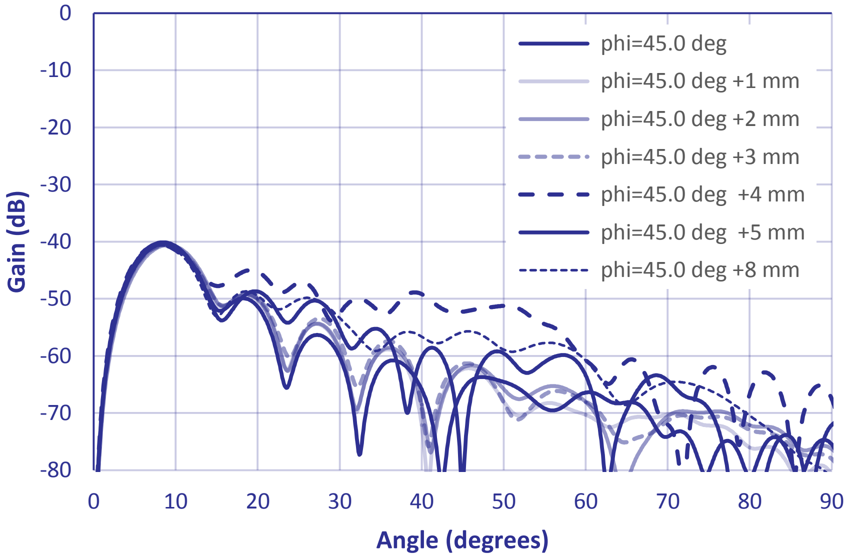

Figure 6.7 Effect of output flange on cross-polar radiation pattern

6.2.2 CAD Model and Mandrel Machining

The aluminium formers were constructed using a computer controlled high precision lathe. The model was obtained by importing a step file from CST Microwave Studio.

This 1-dimensional profile is shown in Figure 6.8, along with the CAD rendering of the drawing.

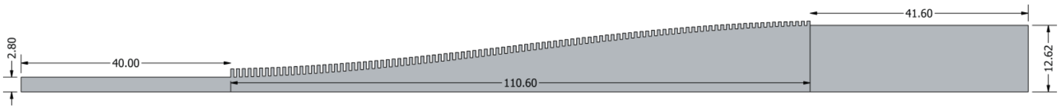

(a)Horn profile

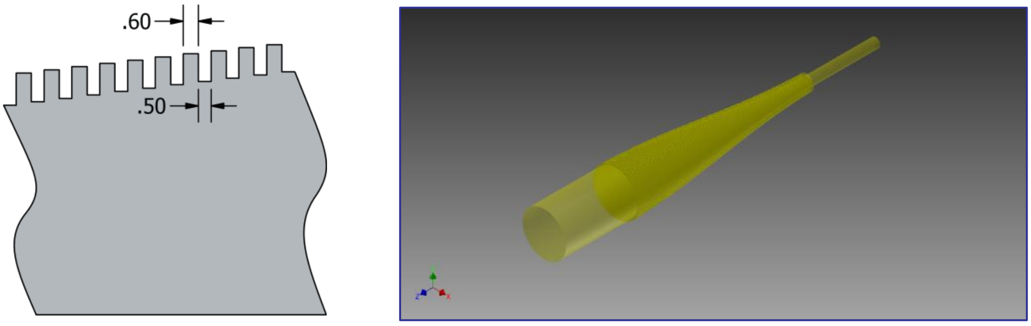

(b)Typical corrugations

(c)3D CAD rendering (One CNC)

Figure 6.8: Profile of the former.

The profile model was used to produce the two prototype formers with a tolerance of 50 microns in diameter and ~10 microns in the axial direction. These prototypes were named “prototype-1” and “prototype-2.” Initial examination of the formers under a CCD microscope at ~20x magnification showed that there was a very small burr around the inside of each vane (Figure 6.9).

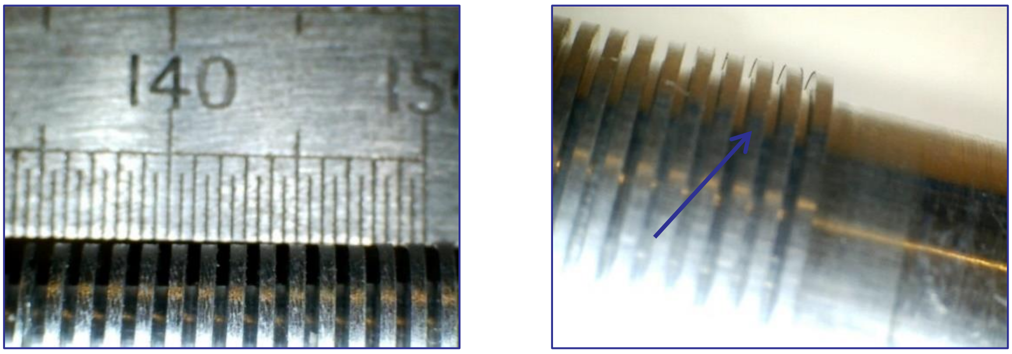

(a)Typical vane (gap) dimensions

(b) Burr on inside of aluminium vanes (gaps)

Figure 6.9 Photo of former taken with CCD microscope

This was a cause for concern due to the method of fabrication: It was possible that the copper would be grown unevenly around this feature, which could cause the vane to close up prematurely, stunting the growth in the deepest of the vanes. A remedy for this problem was the careful polishing of the inside of the vanes using Scotchbrite®.

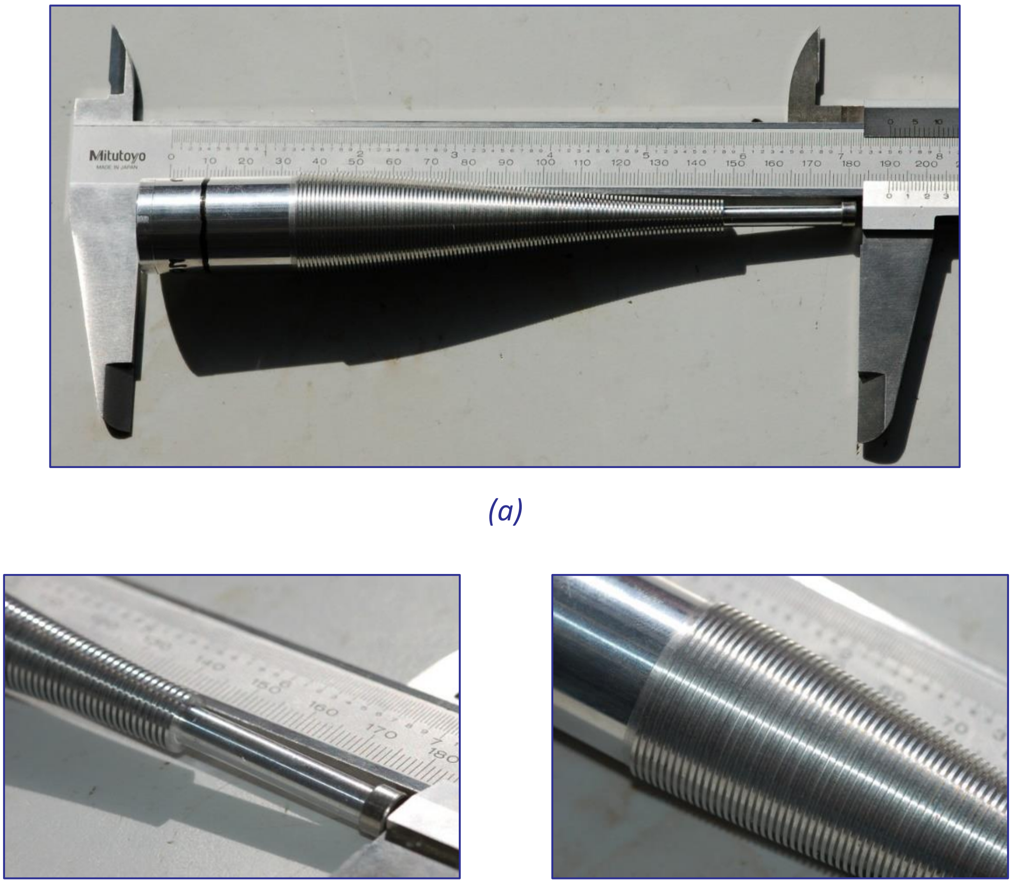

(a)

(b) (c)

Figure 6.10 Photographs of an Aluminium former

The dimensions of formers were measured and compared with the designed values and if the machining errors were in the acceptable range then the mandrels were prepared for the copper growth by cleaning in isopropyl alcohol and drilling an M4 threaded hole at the throat end of the former. One of the prepared aluminium formers is shown in Figure 6.10

6.3 Copper Grown onto Formers

The copper was grown onto the formers by electroforming to a thickness of 6 mm on each and 20 mm was left free at each end of the former to facilitate trueing of the parts. This process was undertaken by contractors at Waveform, now Thomas Keating Ltd, who are world leaders in the fabrication of components of this type[109]. The resultant part can be seen in Figure 6.11.

Figure 6.11 Twin formers showing copper growth

Two identical parts were grown to allow for testing, while keeping a second part in reserve for future integration into the vacuum system.

6.4 Former 1 machined with flange for VNA

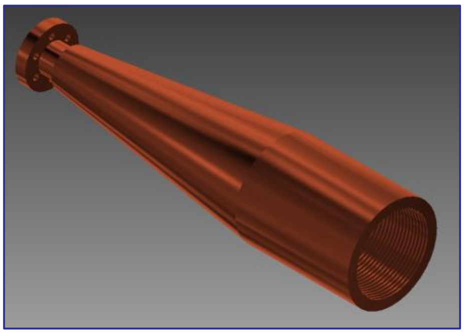

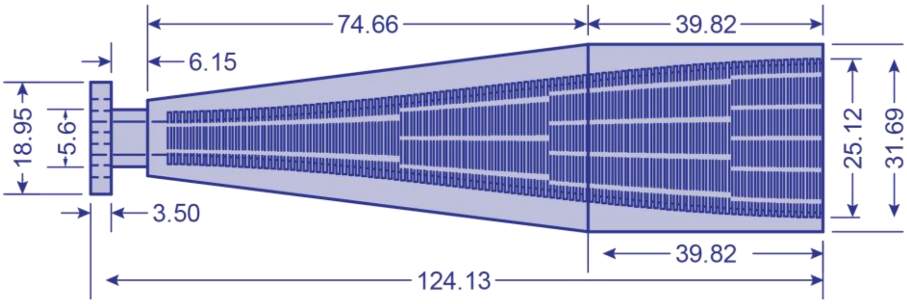

Figure 6.12 Drawing of flange for horn

At this stage one of the formers was machined to produce a prototype horn (prototype one) that was suitable for testing using a vector network analyser (VNA). A flange was machined at the throat of the horn to enable the connection between the horn and the VNA. Figure 6.12 shows the specifications for the flange for prototype one as well as the finishing for the outside of the horn. This work was carried out in house and left the horn with an inside aperture diameter of 212 mm as shown in Figure 6.12, as determined in the simulations.

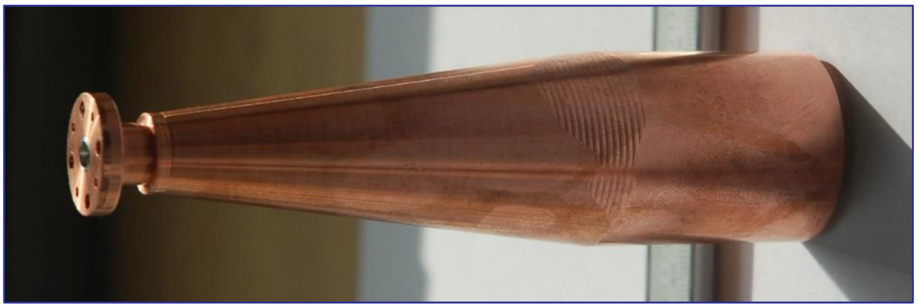

(a) Machined copper on aluminium former

(b) Aperture output end of the grown former

(c) Throat end showing flange for VNA measurements

Figure 6.13 Aluminium former with copper after machining.

Figure 6.13 shows the machined prototype still containing the aluminium former after the grown copper is machined to the final outside specifications and before the aluminium former is dissolved.

6.5 Machined former sent for Etching

(a) Final horn

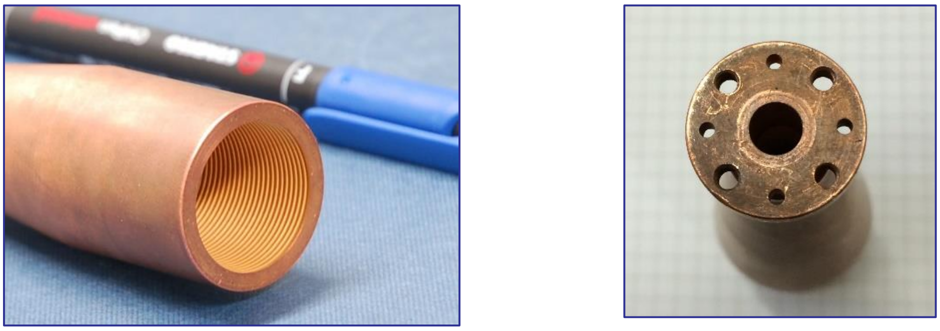

(b) Aperture output end of the finished horn.

(c) Throat end of finished horn.

Figure 6.14 Finished copper horn after etching.

The aluminium was removed from the inside of prototype one using an etching process, which typically involves immersion of the part in a mixture of HNO_3, H_3PO_4 and CH_3COOH that is suitably diluted with H20 to control the reaction rate for a given temperature. This reaction is highly endothermic and produces large amounts of H_2 gas and was therefore carried out once again by Waveform (Thomas Keating Ltd). The horn was returned to Strathclyde and the finished result is shown in Figure 6.14.

6.6 Horn Performance Testing

On return of the prototype from the aluminium etching procedure, measurements of the performance were taken using a high frequency vector network analyser (VNA). The reflection and transmission, as well as the far-field characteristics were investigated using the VNA. The model used was an Anritsu ME7808B with W-band

OML heads, which is capable of measuring over a very broad frequency range (75 – 110 GHz) with 1601 data points. For more details about the VNA used please refer to Appendix 6. The measurements can be carried out relatively quickly and the data stored on an internal hard drive or saved to a removable medium for future data analysis.

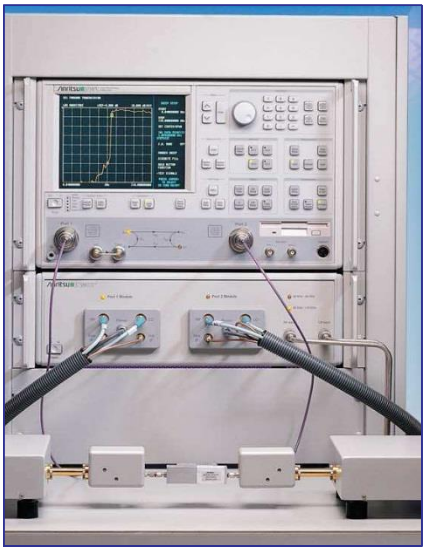

Figure 6.15 Anritsu ME7808B broadband VNA

The system is controlled using an Anritsu 3738A VNA (Lightning) mainframe. This is a high performance VNA that provides the user interface as well as controlling the two synthesizers (MG3692B), which are used for the LO and RF drive to the mm-wave (75GHz to 110GHz) OML modules, and is capable of performing the standard two-port s-parameter measurements, as well as the time domain and swept power gain compression measurements. Only the s-parameter measurements were required for testing the horn prototype.

The VNA was calibrated with the standard Anritsu WR-10 waveguide calibration kit (3655W) using an offset short method. This method eliminates all the sources of errors using a twelve term error correction algorithm. This places the reference plane for the device under test (DUT) between the waveguides at port 1 and 2. In this case the DUT is the horn prototype including a taper and a rectangular to cylindrical mode converter. This is not ideal as the inclusion of these components will introduce spurious signals to the measurement. However, the reflection from the taper and rectangular to cylindrical mode converter were measured and found to be less than -0.5 dB on average over the measured frequency range. This calibration method was used for both the measurement of the reflection as well as the measurement of the far field pattern.

It should be noted that the far field s-parameters may only be assumed to be a relative indication of the trend and not an absolute representation of the transmission properties of the horn. A more comprehensive calibration would be required in order to properly evaluate the full transmission and reflection of the horn on the VNA, which need to take into account the free space between the transmitting and receiving antennas. For this investigation this custom calibration was deemed unnecessary.

6.6.1 Reflection Measurements

Using the W-band VNA the microwave properties of the horn prototype were measured. The reflection was determined by one port measurement where microwaves were radiated into a microwave absorbent material (echosorb). The experimental apparatus for this measurement is shown in Figure 6.16. Only one of the VNA head units is required. This is connected to the prototype horn by means of a rectangular to cylindrical converter, which is a standard 2.540 x 1.270 mm to 2.39 mm waveguide. This is followed by an up-taper that increases the diameter from 2.39 mm to the 6 mm diameter of the horn input. The horn once connected to a suitably calibrated VNA may have the refection measured by monitoring the S_{11} response of the VNA.

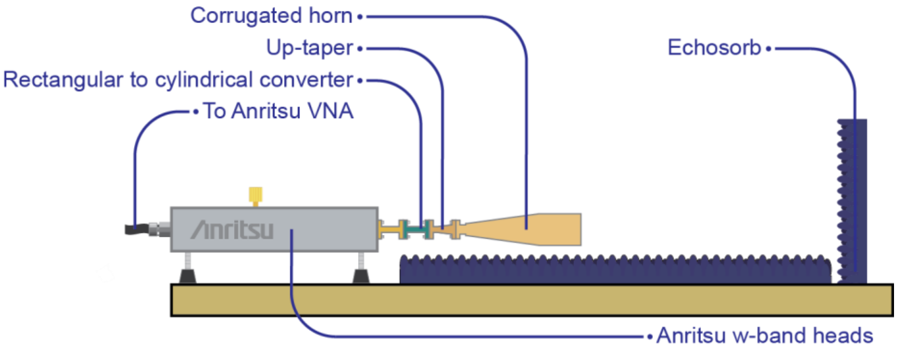

Figure 6.16 Schematic for one port reflection measurements

Figure 6.17 shows the S_{11} performance of the horn as measured by the one port VNA experiment. The overall performance is good showing an average reflection of less than 30 dB over the bandwidth of 90 GHz to 100 GHz. The measured result is much noisier due to the connections to the VNA.

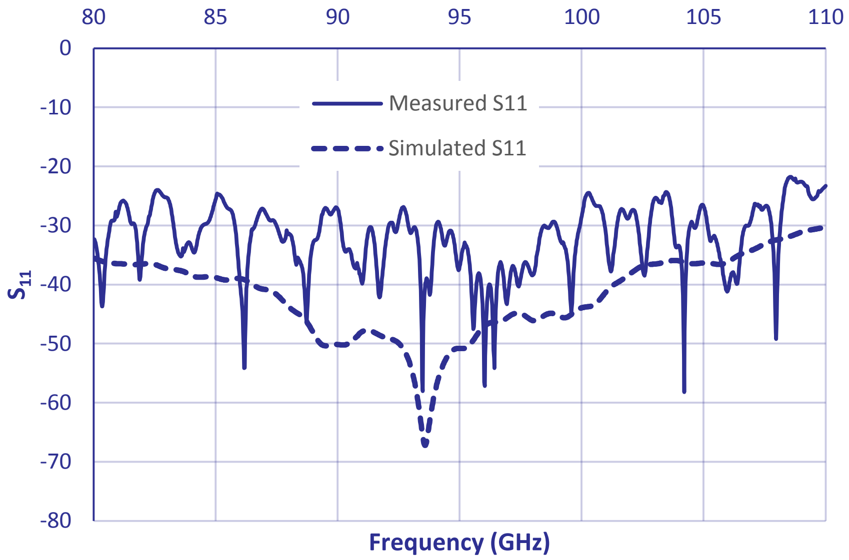

Figure 6.17 Measured and simulated microwave reflection from the corrugated horn

6.6.2 Far-field Measurements

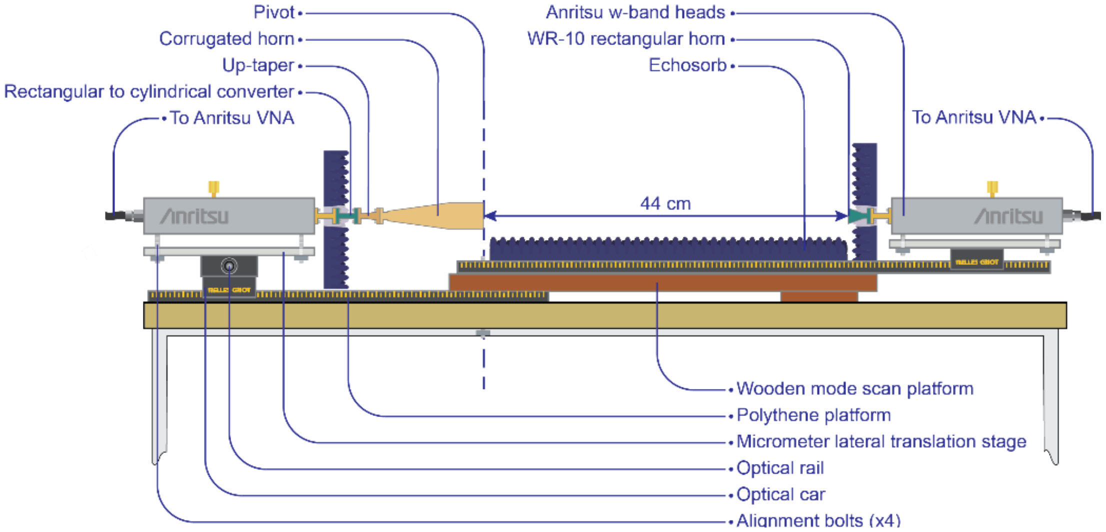

Figure 6.18 Profile view of far-field rig.

An experiment was devised to measure the far-field radiation pattern using the VNA. This allowed the performance of the horn to be evaluated over the entire frequency range. Once again the prototype horn was connected to the (calibrated) W-band VNA head via the rectangular to cylindrical waveguide converter and the cylindrical up-taper. For this measurement a far-field scanning rig was constructed to ensure an accurate angular sweep of the receiving horn was possible, while ensuring that the proper alignment of the receiving (RX) and transmitting horns (TX) is maintained.

The TX head was mounted by way of a set of four independently adjustable bolts to a rectangular polythene platform, which was itself firmly affixed to a micrometer lateral translation stage. The translation stage was fixed to an optical rail by means of a car, allowing the whole TX stage to move over every axis with a good degree of confidence. This entire assembly was bolted to the lab bench as is shown in Figure 6.18.

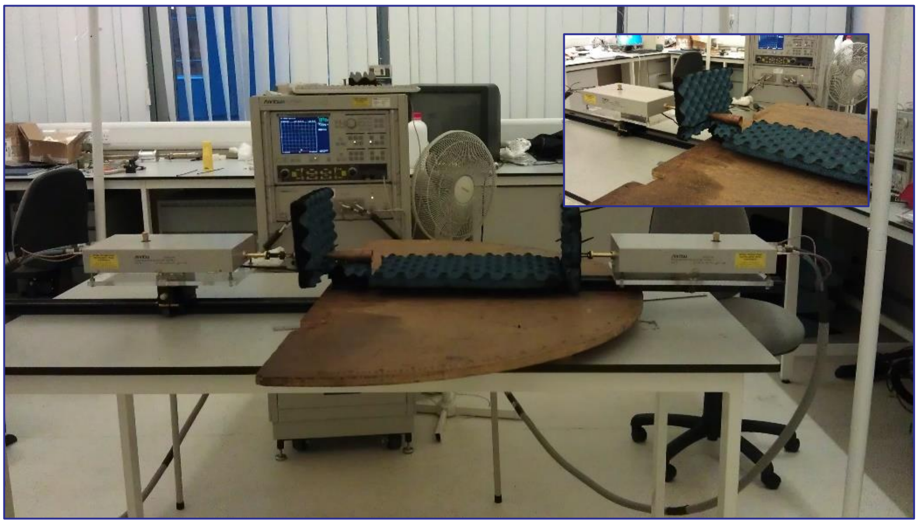

(a) E-plane scan (Insert: Transmission horn).

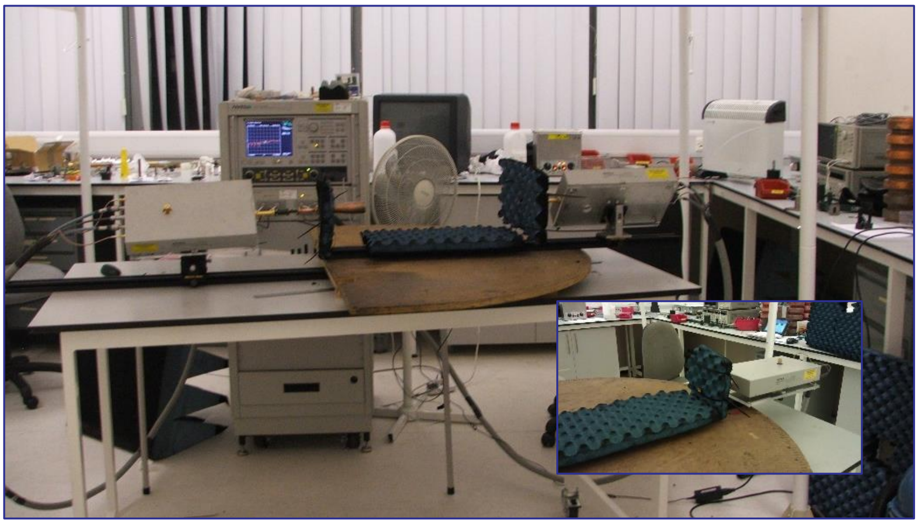

(b) H-plane scan (Insert: Receiver horn).

Figure 6.19: Photograph of Far-field scan.

The RX stage was constructed in a similar way, with the exception that the optical rail was mounted around a pivot and sits on a calibrated angular scale where it is free to move through 180 degrees. The receiving horn was a standard WR-10 rectangular horn, connected to the second port of the VNA. Both the TX and RX stages are enclosed in microwave absorbent material to prevent unwanted reflections from the metal of the VNA equipment, as well as from the surface of the table. Photographs of the typical setup are shown in Figure 6.19.

After the setup was properly aligned and used to calibrate the W-band receiving horn when swept over the 180 degree range in one degree increments, while measuring the transmission and reflection properties over the frequency range of 84-104 GHz. This method is clearly demonstrated by the schematic diagram of Figure 6.20.

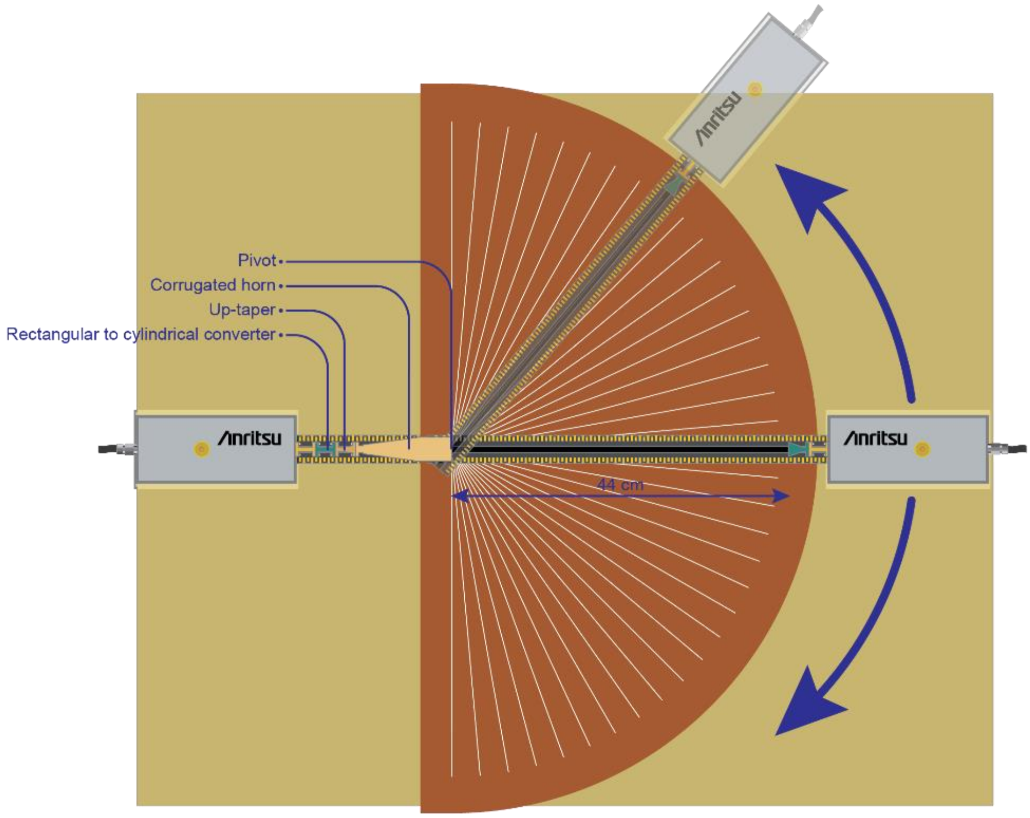

Figure 6.20: Top view of far-field rig.

This measurement was carried out for the E-plane component, the H-plane component and for the 45° cross-polar component of the far-field radiation pattern using a 90 degree and 45 degree bracket that was attached to the optical rail. This allows the VNA heads to be orientated so the TX and RX horns are in a relative position shown in Figure 6.21. The oriented the system could be re-aligned using a laser level and the angular scan measurements carried out.

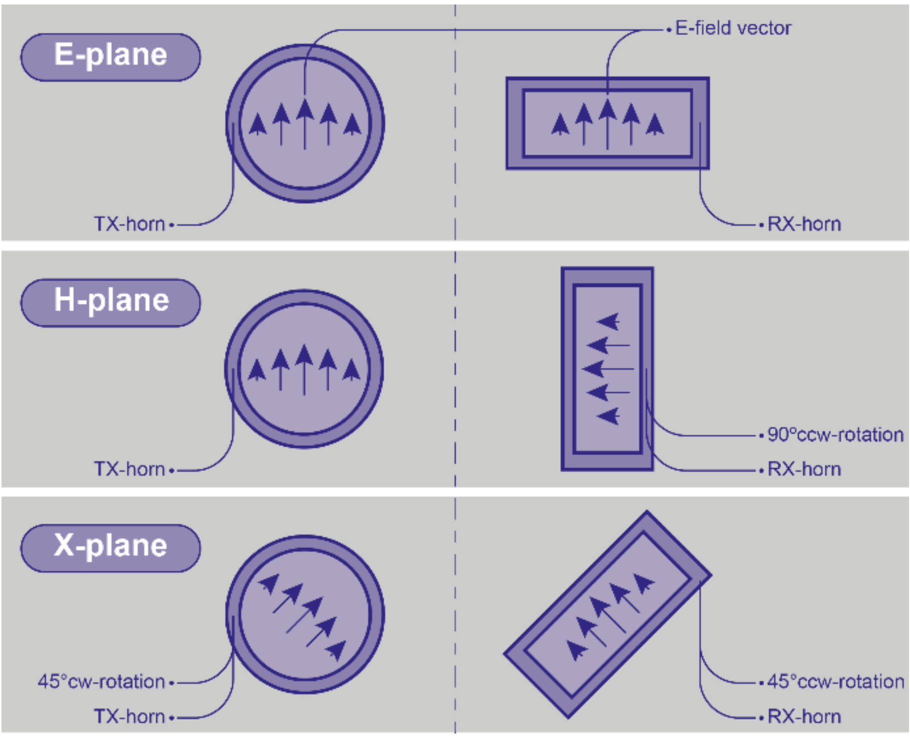

Figure 6.21: TX/RX orientations.

Figure 6.22 shows the measured far-field pattern at 95 GHz compared with numerical simulation. The -30 dB edge is within a half angle of 12 degrees and the pattern shows more than 99% of the output power is within 30 degrees.

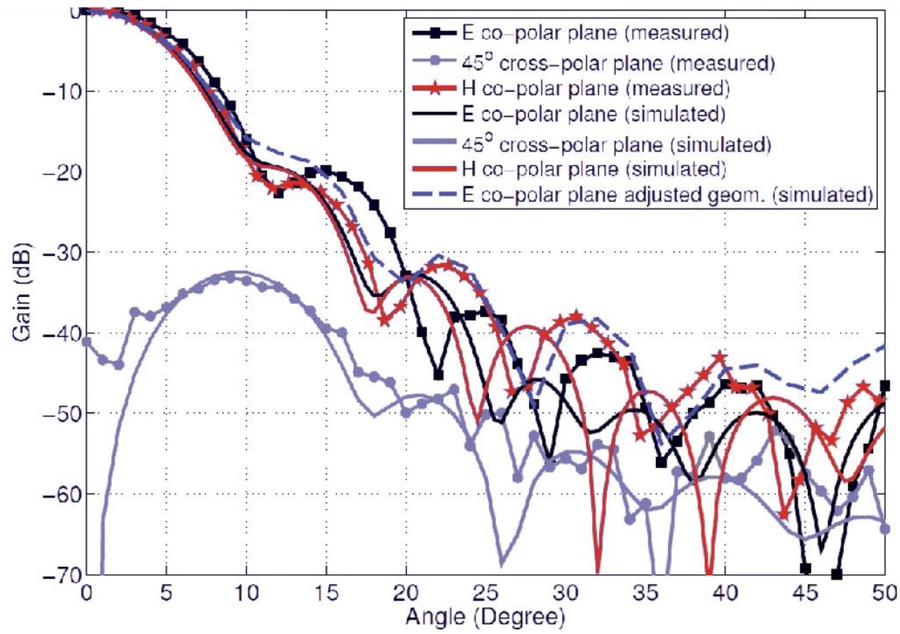

Figure 6.22 Measured and simulated far-field performance from the corrugated horn

An offset between the simulated and measured nulls as well as a broadening of the second lobe in the E-plane scan can be seen in Figure 6.22. This is possibly due to the manufacturing error in the range of +-25 µm. This effect can be demonstrated in simulation and is shown in Figure 6.22 (dotted line). Another possible reason for this difference may be due to the beam pattern of the receiving horn. The measured far-field shows a rotationally symmetric radiation pattern that is consistent with a Gaussian profile.

6.6.3 Simulated and measured co-polar plane radiation pattern.

The broadband performance of the horn can be seen in the following series of figures where the measured and simulated radiation patterns have been collated into a series of contour plots showing the evolutions of the far field patterns over the 84 to 104 GHz range, with the scale normalized in dB). The E and H-plane compare well to the simulated far-fields, a similar result is found for the 45 plane.

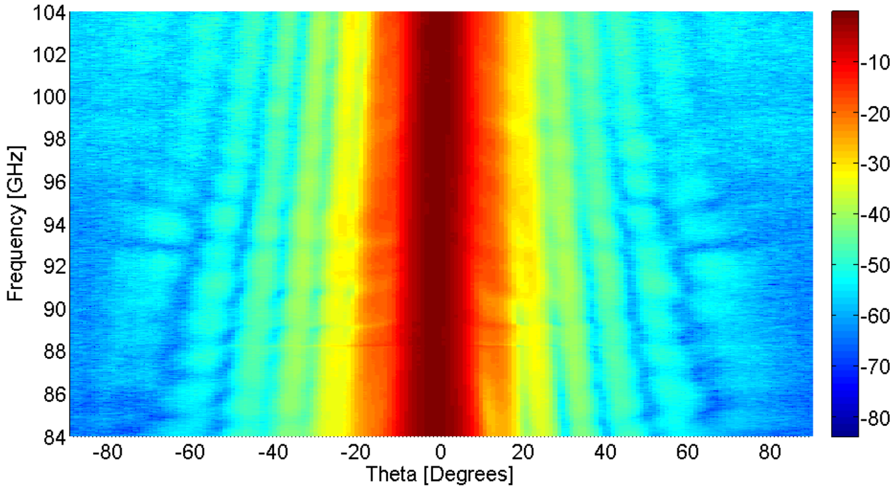

Figure 6.23 E-plane co-polar (measured)

Figure 6.23 and Figure 6.24 are the measured and simulated far-field E-plane over the measured frequency range.

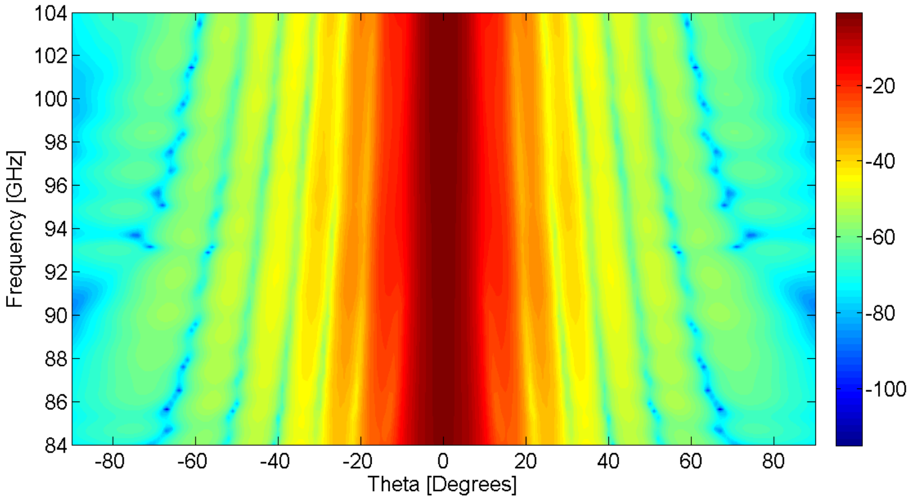

Figure 6.24 E-plane co-polar (simulated – μ-wave)

Both of these figures show a progressive narrowing of the main lobe and side-lobes as the wavelength decreases as would be expected. Both the simulated and measured values are in good agreement down to -50 dB where the signal to noise ratio of the VNA becomes apparent.

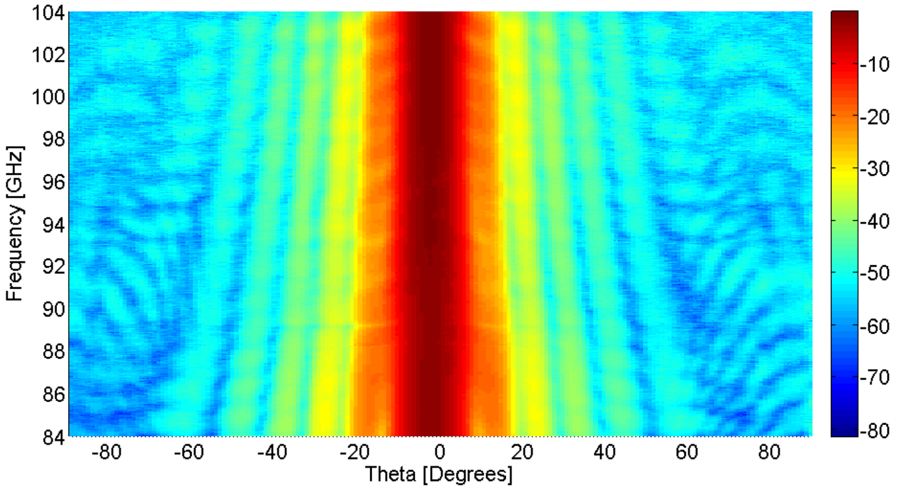

Figure 6.25 H-plane co-polar (measured)

Figure 6.25 and Figure 6.26 are the corresponding measured and simulated H-plane far-field results.

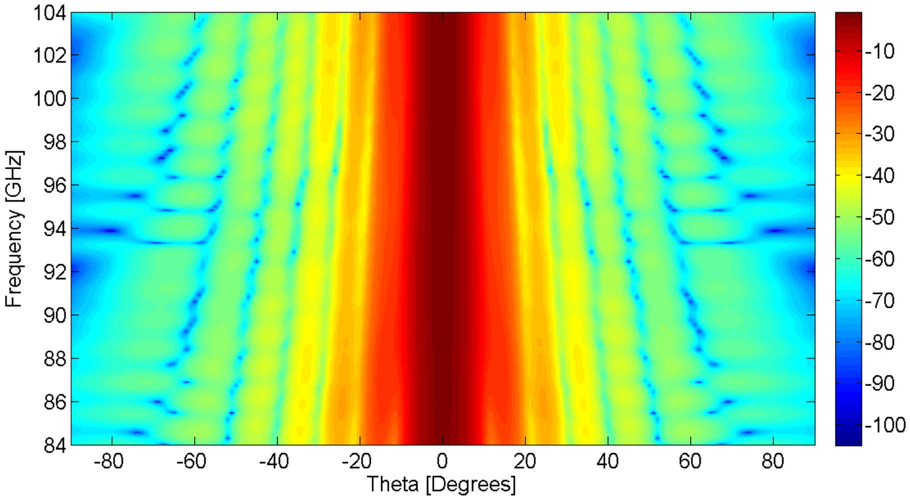

Figure 6.26 H-plane co-polar (simulated – μ-wave)

These plots show is a narrowing of the beam with increasing frequency as predicted by simulations and as shown in other corrugated horns[110, 111], but the primary lobe in both the E and H-plane measurements remains stable over the entire range. These results agree very well with the simulations over the measured frequency band, which demonstrates that the designed and manufactured horn has a very well defined primary lobe with low side-lobes and low cross-polarization. The viability of the corrugated horn design for implementation in a continuously tuneable and broadband gyro-device has therefore been demonstrated.

This design has been demonstrated to be a viable quasi-optical mode converter to launch a Gaussian beam through a depressed collector system meeting the design specifications. The low reflection (-30 dB), high directivity (27 dB), the high purity Gaussian content (98%) and broadband capability (90--100 GHz) fall within the design criteria. Therefore the prototype corrugated horn is suitable for inclusion into the gyro-TWA/BWO experiment.

6.7 Aperture Testing

One of the principal reasons for the design and fabrication of this horn was its incorporation into the gyro-TWA system for use with a depressed collector system. Such a system consists of an insulating break in the waveguide followed by a number of vanes or apertures, which the electron beam will pass through before striking the surface of the collector. The purpose of these vanes is to capture any back streaming electrons, or those produced from secondary emission. The typical geometry of a depressed collector system is shown in Figure 6.27 (a).

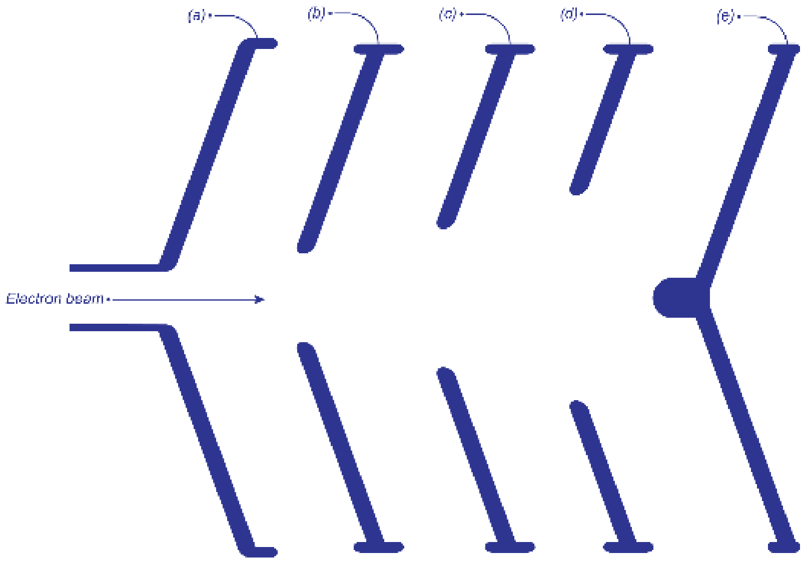

(a) Typical multi-stage depressed collector.

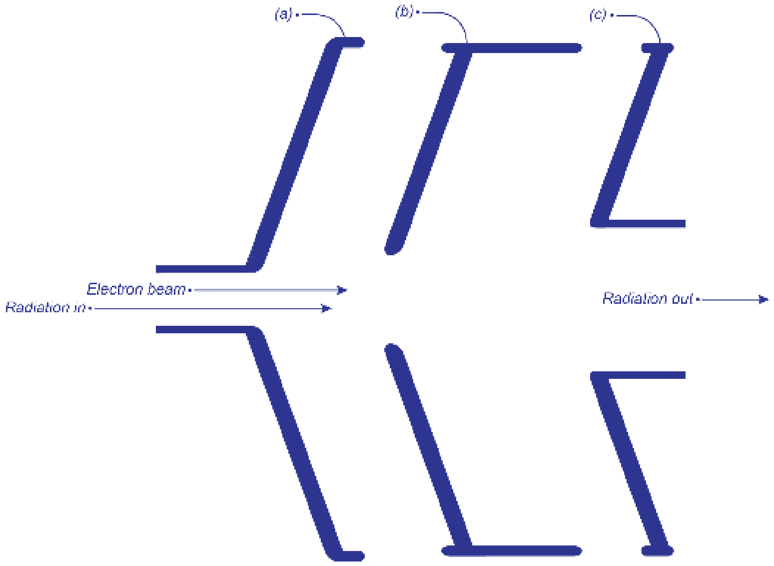

(b) Proposed axial output scheme.

Figure 6.27: Geometry of depressed collector systems.

In this arrangement the electrons and the radiation are decoupled before the electrons enter the collector. The electrodes (b – e) are biased so that the voltage is progressively less than that of the anode. This allows a percentage of the spent electron beams energy to be recovered as it passes through the electric field generated by these electrodes. A multi stage system is capable of recovering a substantial portion of the energy from the beam.

In the scheme proposed for the gyro-TWA (b), the electron beam and the radiation would be decoupled in the collector. The radiation would pass through the system with very little or no interaction with the structure and exit as a Gaussian beam, where a secondary quasi-optical system would re-condition the beam for applications. The initial concept would be a simple single stage design, with only one or two apertures at most.

During the cold testing of the horn an apparatus was constructed that would allow for a proof of concept test of a single stage collector to be carried out using several different sized apertures. The motivation behind this test is to establish a baseline for the reflection produced in a practical situation by an aperture in a waveguide in front of the horn. This situation is analogous to a single stage collector with a window. The apertures for the experiment consisted of a set of machined brass rings of differing inner radii, as shown in Figure 6.28 (a –d). Each ring has the same length of 5 mm.

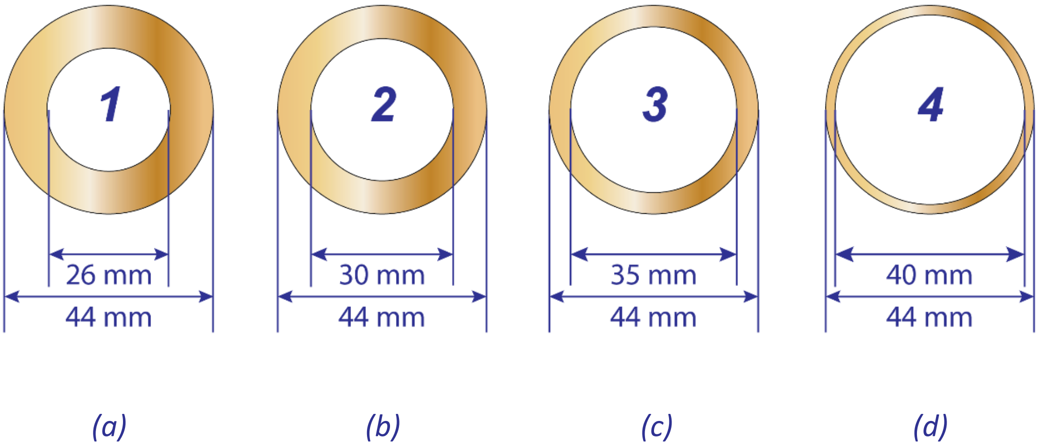

(a) (b) (c) (d)

Figure 6.28: Brass aperture rings for proof of concept.

Each of these rings was placed within a steel waveguide with an inner diameter of 44 mm and located at a certain distance which could be varied from the output end of the corrugated horn. The corrugated horn was inserted at the opposite end of a steel waveguide and held in place by a plastic ring with an outer diameter of 44 mm and an inner diameter of 31.7 mm. The horn was again connected to the W-band VNA head in a similar setup to the original reflection measurement. This apparatus is demonstrated in Figure 6.29.

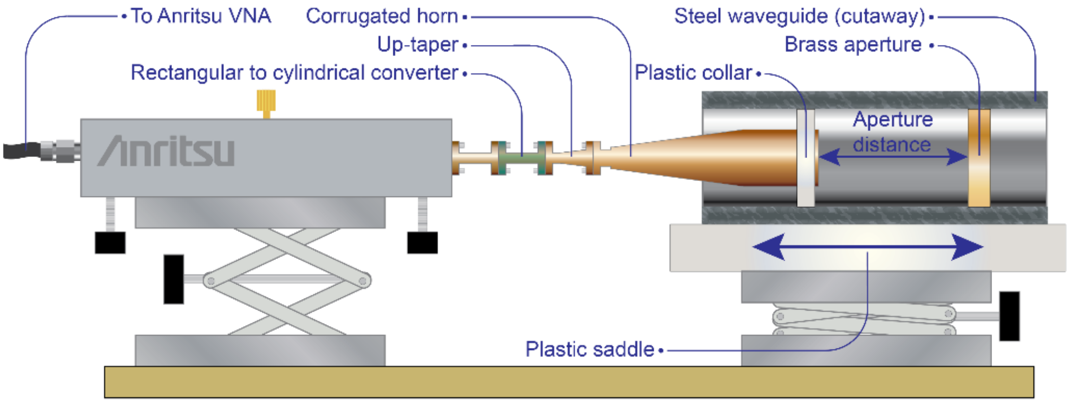

Figure 6.29: Proof of concept apparatus.

Using this apparatus it is possible to measure the reflection from each aperture by moving the horn inside the waveguide. A set of reflection measurements was obtained for each of the apertures over a range of distances from 0 mm to 140 mm and over the frequency range between 90 GHz to 100 GHz.

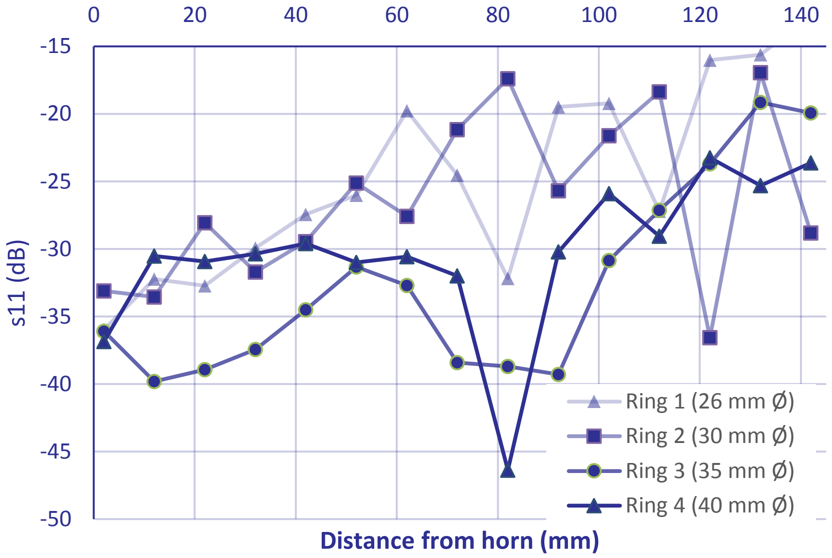

Figure 6.30: Reflection due to brass aperture (95 GHz)

Figure 6.30 shows the results from the centre frequency at 95 GHz. The trend demonstrates clearly that the reflection is increased as the ring aperture moves further from the horn, as would be expected. From this figure a range of possible aperture sizes and collector lengths may be inferred. For example, at a distance from the horn of 80 mm both the 3rd and 4th rings have a refection that is less than -35 dB.

This is not an unreasonable length for a collector with a window of 40 mm in diameter.

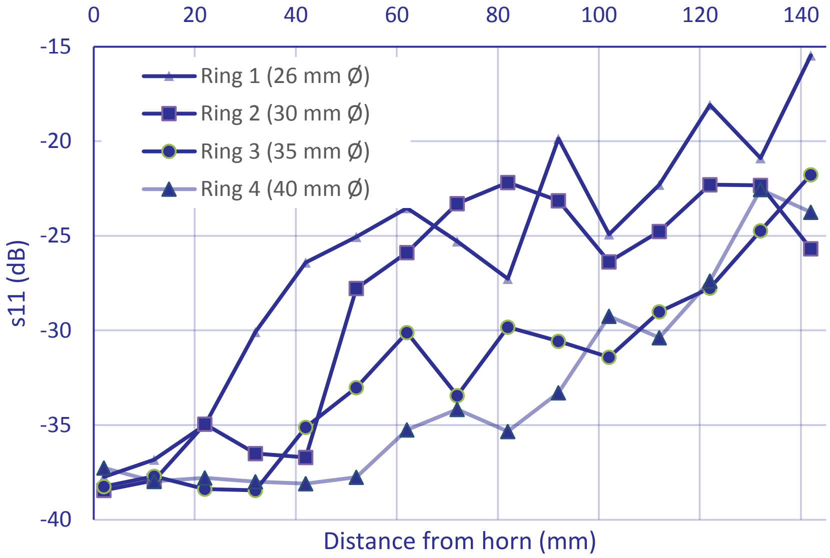

Figure 6.31: Average reflection due to brass aperture (94-96 GHz)

The average reflection from 94 GHz to 96 GHz is also shown in Figure 6.31, which gives a slightly better overview of the trend over the entire bandwidth.

To validate this experiment some simulations were conducted using both µ-wave and CST studio. The geometry of the setup in Figure 6.29 was investigated, with an aperture ring of 26 mm at z = 142.3 mm from the horn (the furthest experimental data point). The results of these simulations are shown in Figure 6.32 for the reflection (s_{11}) over the frequency range from 90 GHz to 100 GHz.

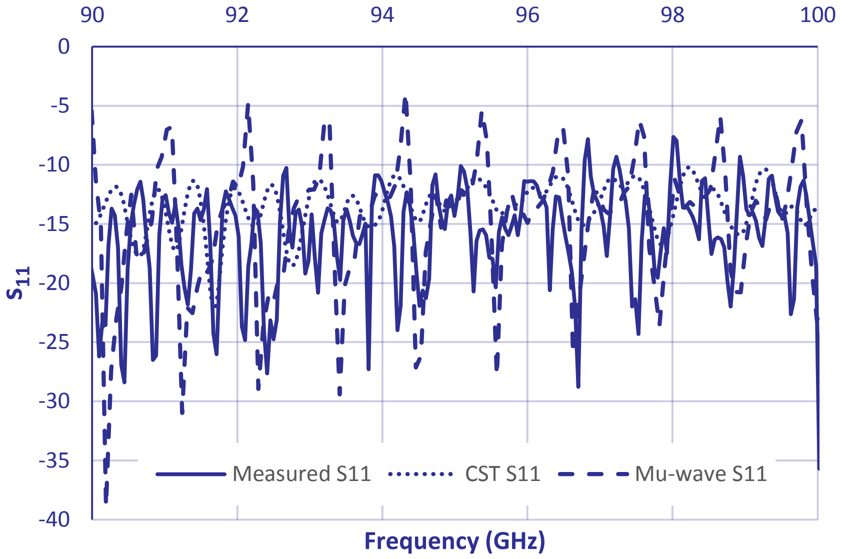

Figure 6.32: Comparison (CST/mu-wave/experiment) between S11 for brass ring aperture at z = 142.3 mm from horn (aperture diameter =26 mm)

A better representation of the trend can be seen in Figure 6.33, where the average reflection is compared. Here there is a general agreement between the simulation and experimental data. However the performance of the physical device is slightly better than would be expected from the simulations.

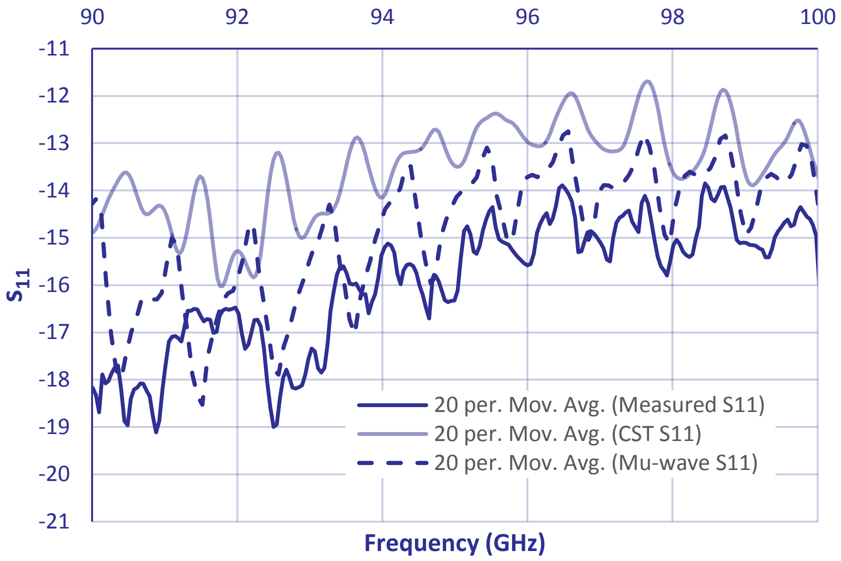

Figure 6.33: Comparison (CST/mu-wave/experiment) between S11 for brass ring aperture at z = 142.3 mm from horn (aperture diameter =26 mm). Data has been smother using a moving average in order to see the trend.

This 'proof of concept' experiment demonstrates the feasibility of using a corrugated horn as a method to decouple an electron beam from the radiation within a gyro-TWA. The results show that even with the inclusion of an aperture after the horn that the reflection can still be kept below the target of -30 dB if a proper length and aperture size of the depressed collector system are chosen.

7 Experimental components and electron beam diagnostics

The following chapter describes the experimental procedure and apparatus used to perform a high power millimetre wave experiments using the corrugated horn as an output for the radiation from the gyro-BWO. The first part provides a brief overview of the gyro-BWO/TWA experimental set up and supporting equipment.

7.1 Experimental Introduction

The corrugated horn was integrated in to the gyro-TWA/BWO experiment to test the performance in high power millimetre wave conditions. The experiment was operated in the oscillator configuration using the TWA helix without the seed signal introduced through the input coupler and with the direction of the magnetic fields in the main coil reversed with the cathode coil used to provide the cusp magnetic field profile. Figure 7.1, gives a schematic overview of the primary experimental setup used in the gyro-BWO, including the corrugated horn, which is attached to the system after the 3-disk window.

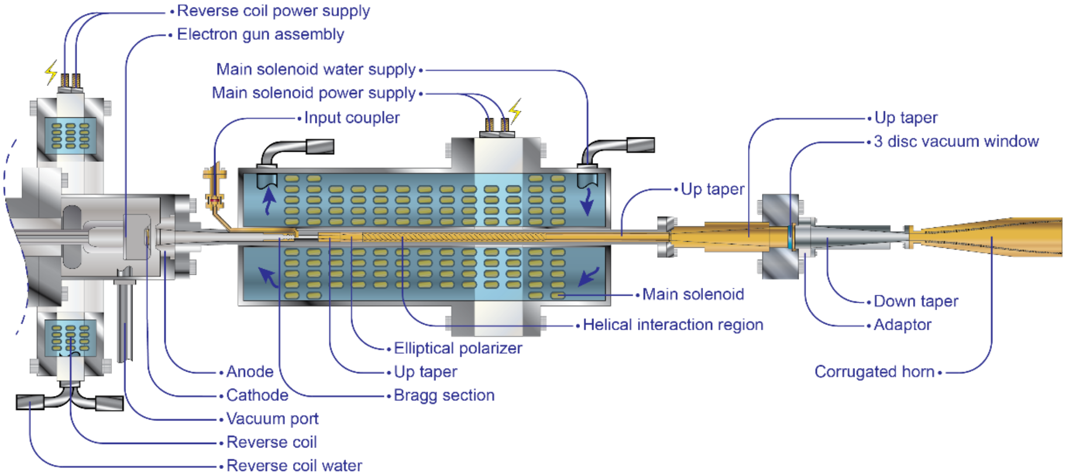

Figure 7.1: Primary experimental schematic (gyro-TWA configuration)

The purpose of operating the experiment in this gyro-BWO configuration enables the testing of the corrugated horn without having to break the vacuum and make major modifications to the setup. This also removes the added complication of the Quinstar solid state W-band amplifier, which is used as the input stage for the gyro-TWA experiment. In this configuration the corrugated horn could simply be connected to the outside of the vacuum window, therefore removing the added expense of constructing a window after the horn. During these tests of the corrugated horn the output mode was measured from the horn as well as the operational frequency of the gyro-TWA/BWO and the output power from the oscillator.

7.2 Experimental Apparatus

The experimental apparatus used to carry out the ‘high power mm-wave testing’ of the horn is summarised in the following sections, providing a brief overview of the individual systems and components of which the gyro-TWA/BWO is comprised. The first section comprises the main body of the gyro-TWA/BWO experiment, including the primary components that make up the gyro-device and the secondary equipment (power supplies etc.). The main body of the gyro-device can be separated into four sub-sections: The cusp-gun, the field coils, the beam tube and the output. Each of these sections will be briefly covered in the following pages.

The second section describing the apparatus contains the equipment and arrangement of the experiment that was performed to measure the performance of the horn in conjunction with the gyro-BWO. This includes the far-field apparatus, the detector and measurement equipment used to record the far-field and carry out the frequency measurements.

7.3 Cusp gun

The electron beam used to generate the millimetre wave signal in this case was provided by a cusp electron gun, which generates an axis encircling annular electron beam. This is an ideal beam for interaction with the cavity modes formed within the helical interaction region. The cusp gun, rather than an individual component is composed of a number of interrelated elements. The primary parts being: the electron gun, the main solenoid and the reverse coil. Each of these components is also dependent on a number of supporting sub-systems including the DC power supplies and pulse forming power supply.

7.3.1 Thermionic Emission

The source of the electron beam for the cusp gun is a thermionic cathode operating in the temperature limited regime. This type of cathode was selected for a long lifetime and high reliability. Appendix 7 gives a description of thermionic emission, space charge and temperature limited operation of a thermionic cathode.

There are several different regimes of operation for a thermionic cathode depending on the magnitude of the electric field on the cathode due to the voltage applied and the temperature of the emitter. Figure 7.2 illustrates the mechanisms dominating current flow in a thermionic diode, with variation in anode voltage.

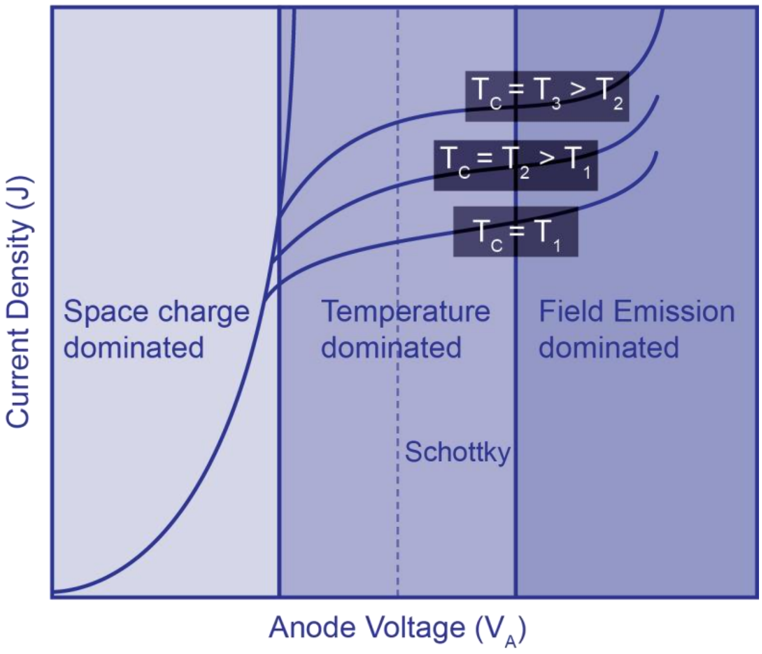

Figure 7.2: Mechanisms dominating current flow through a thermionic diode.

When the voltage is low the cathode can supply sufficient current to satisfy the Child-Langmuir law and the cathode is operated in the space charge limited regime. As the voltage is increased there is a transition region where some parts of the cathode surface are unable to supply the required current and enter the temperature limited regime, while other parts maintain operation in the space charge limited regime. This can be seen in Figure 7.2 as the knee in the curve between space charge dominated and temperature dominated emission. Once this voltage is high enough the diode is fully temperature limited and the current from the cathode increases slowly with an increase in the applied voltage. As the potential difference is increased to much higher voltages (~10^8 Vm^{-1}), the electric field at the cathode surface becomes high enough that the tunnelling of electrons from the surface begins to dominate the total current and the cathode is now operating in the field emission regime.

The fabrication of electrodes is critical when considering the regime of operation. If there are any impurities or irregularities on the emitter surface, which might form microprotrusions then there is a possibility for field enhancement which can reduce the critical electric field for field emission by an order of magnitude (~10^7 Vm^{-1}). These areas will then enter the field emission regime at lower voltages than expected causing degradation of the quality of the electron beam.

7.3.2 Cathode

The thermionic cathode emitter is located at a point between the reverse and main solenoids as shown schematically in Figure 7.3.

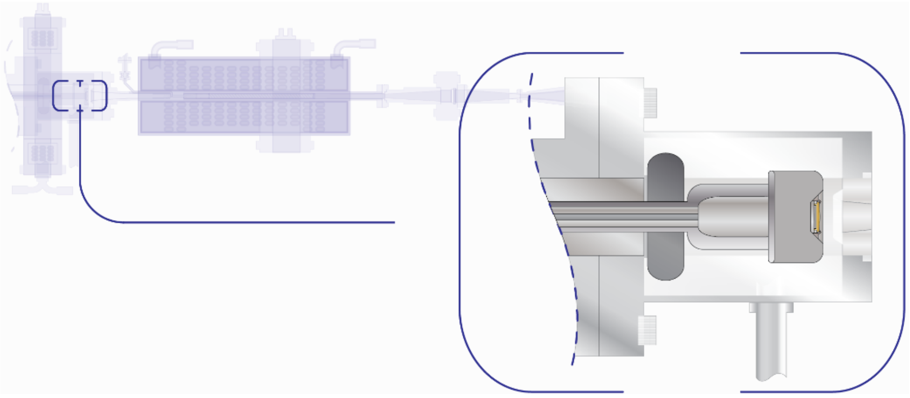

Figure 7.3: Cathode schematic.

The cathode has been constructed to operate at a nominal applied voltage of 40 kV, at an operational temperature of around 1000 °C. This cathode has also been designed with future modification in mind and has been constructed in a modular fashion, for ease of reconfiguration. Figure 7.4 shows the assembled electron gun before installation.

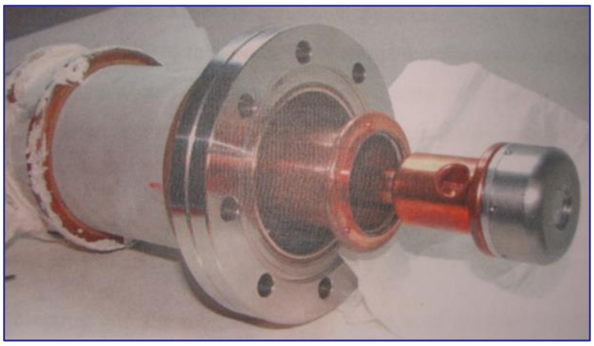

Figure 7.4: Electron gun before assembly and installation.

7.3.3 Anode

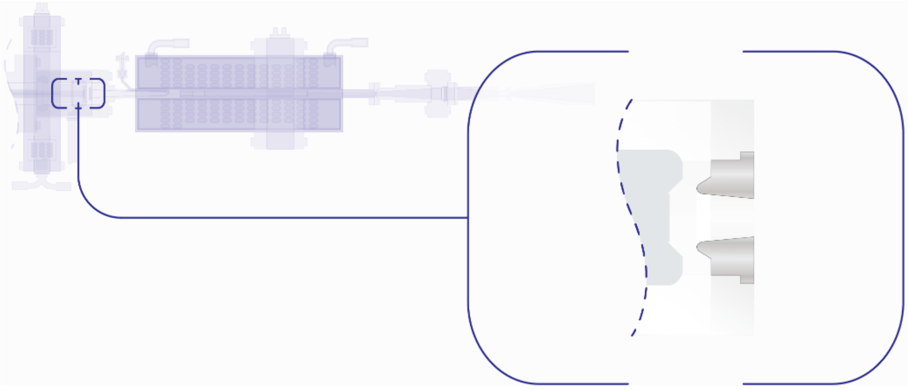

Figure 7.5: Anode schematic.

The anode is constructed from grade 316 stainless steel and was designed and machined in house using a CNC milling machine. Figure 7.5 shows the anode in situ inside the vacuum vessel, which is also the location of the cathode. The anode section is fitted from the opposite side of the cathode and is fixed in position when the main section of the stainless steel beam tube is attached. Each of the stainless sections are bolted together using stainless steel bolts and the high vacuum seals are provided using copper gaskets.

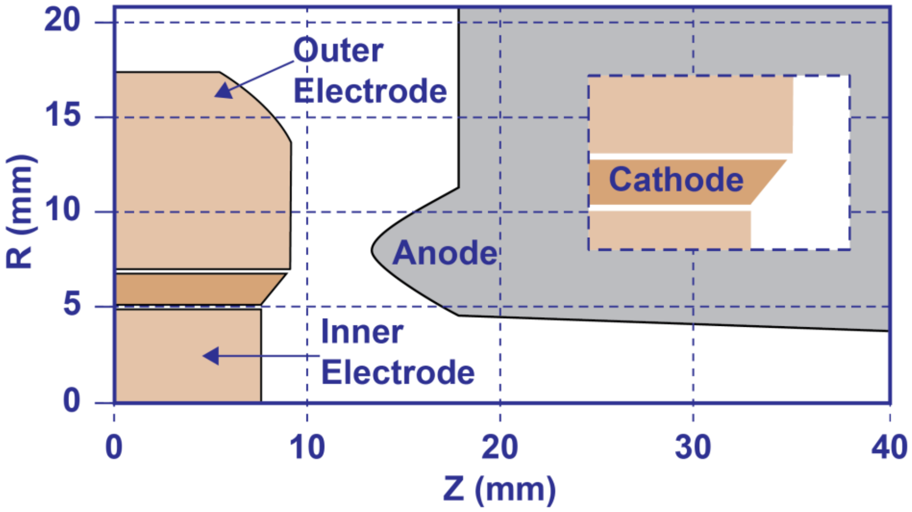

Figure 7.6: Final optimised cathode geometry for the cusp gun.

The final electrode geometry for the cusp gun is illustrated in Figure 7.6. The cathode and focus electrodes can be assembled in a modular fashion so as to allow easy future modification, should this be required. The cathode structure is clearly shown in Figure 7.7, which is a CAD drawing of the cathode showing the electrodes and the emitter[112].

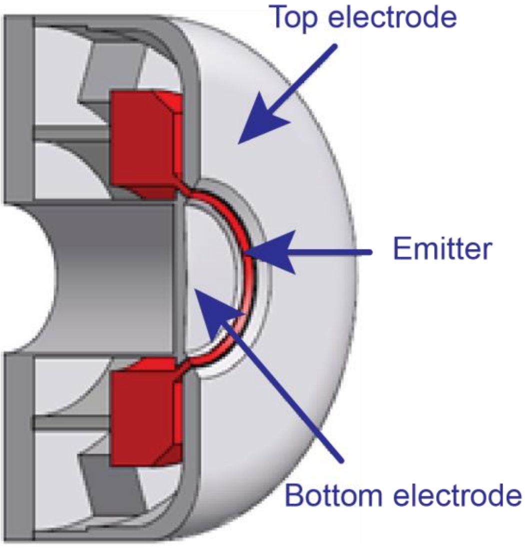

Figure 7.7: Cathode CAD drawing.

In the case of a cusp gun, an axis-encircling beam is formed by passing an annular electron beam through a non-adiabatic magnetic field reversal (cusp), converting part of the electron beam's axial velocity into axis-encircling transverse velocity. A full description of the annular electron beam formation from the cusp electron gun is given in Appendix 8.

7.4 Solenoid system

In the cusp electron gun the magnetic field profile is of primary importance as it is through this that the final beam properties: velocity ratio alpha, axial velocity and radius, of the electron beam are decided. The generation of the magnetic field is one of the more challenging aspects of the construction of this gyro-BWO system due to the very large DC currents required. The final design of both solenoids have to take into consideration cooling of the wires by reducing the output power through the addition of shim coils in the cavity coil and allow a large volume of water to pass through the wires in both coils. This is required due to the large amount of heat produced in a small volume. The design of the solenoids has to overcome the forces produced by two high magnetic field coils and the large heat produced by currents of up to 270A required to produce the B-field. In the previous simulation of the electron gun it was stated that the solenoid wire was 2.2mm by 2.2mm square copper wire that has insulating varnish coating on the surface so that no breakdown will occur between the layers of the coils.

7.4.1 Water cooling

Water cooling for the field coils is provided by a recirculating water system and high pressure pumping system. This system allows the field coils to be maintained at an ambient temperature. The water from this recirculating system is pumped at high pressure through carbon filters before an isolation valve separated the flow. The coolant water is then introduced into the stainless steel jackets surrounding the coils, where the water pressure is 3 bar in the main coil and 1 bar in the reverse coil. The temperature of the water is monitored both before and after passing through the system to ensure that there is adequate cooling of the coils during operation.

7.4.2 Reverse coil

The magnetic fields that are essential to the operation of both the cusp gun and the CRM instability are provided by two sets of conventionally cooled copper wound solenoids: The reverse coil and the main solenoid/coil.

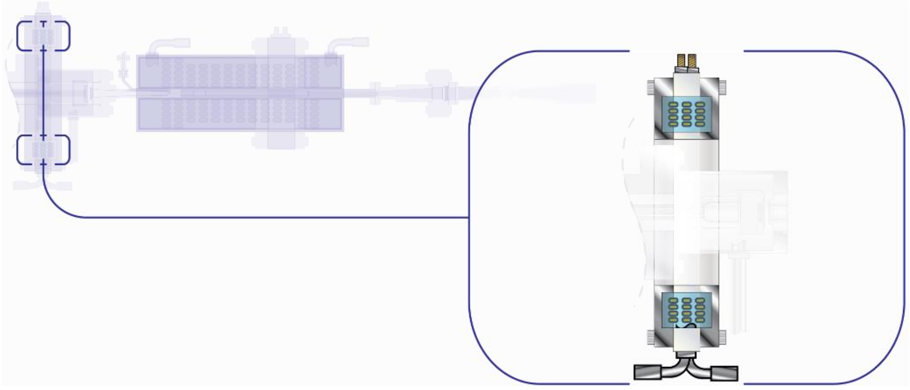

Figure 7.8: Reverse coil schematic.

The reverse coil (Figure 7.8) is used to provide the cathode field in opposition to the main coil, thus providing the required field reversal. The coil is wound using 2.2 mm by 2.2 mm coated copper wire. There are 4 layers with 10 turns per layer. The coil is contained within a stainless steel jacket, wherein a constant flow of high pressure water at 1 Bar provides the cooling for the coils. This jacket is also connected to a set of threaded rods that comprise a system by which the coil may be adjusted in 3 dimensions for optimal alignment of the fields. The reverse coil supply provides a maximum DC current and voltage is shown in Table 7.1.

Field/Parameter	**B_0 = 1.65 T**	**B_0 = 1.82 T**	**B_0 = 2.1 T**
Magnetic Field (mT)	08	6.18	6.79
Magnetic Field at cathode (mT)	47	4.92	3.69
Resistance (Ω)	0.07	0.07	0.07
Current (A)	169.77	180.8	198.9
Voltage (V)	11.85	12.62	13.88
Power (kW)	2.01	2.28	2.76

Table 7.1: Reverse coil performance characteristics.

Figure 7.9 shows the reverse coil in situ with the water cooling hoses in place and the articulation frame for adjusting the geometry. The external components of the cathode and anode can also be seen passing through the coil.

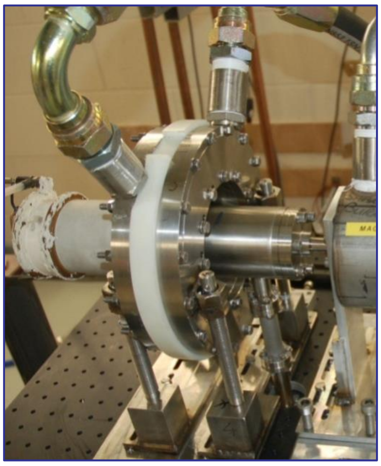

Figure 7.9: Photo of the reverse coil in situ.

7.4.3 Main solenoid

The larger of the two magnetic field coils is the main solenoid (Figure 7.10), which is primarily used as the source for the field in the interaction region. The field strength provided by the main coil is one of the factors that determines the operational frequency of the device, but the interaction with the field reversal at the cusp is also a factor of the main coil field strength and this is also important in determining the beam alpha, (the ratio of the transverse velocity to the axial velocity of the electrons.

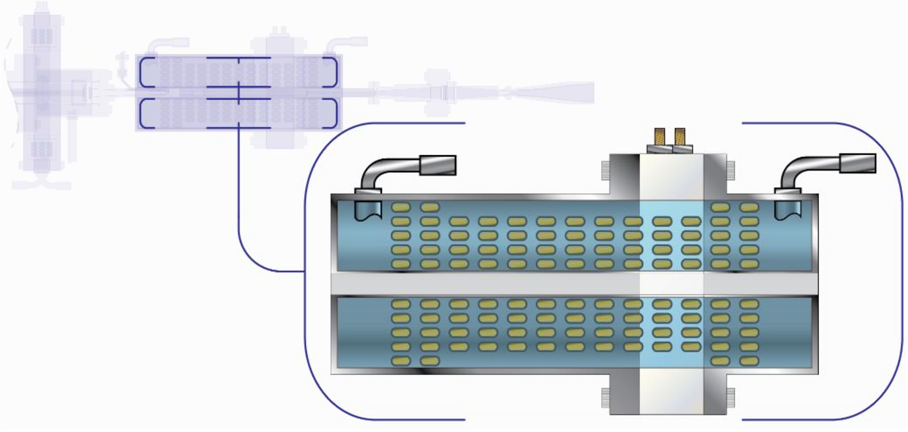

Figure 7.10: Main solenoid schematic.

The coil is wound using the same 2.2 mm by 2.2 mm coated copper wire that is used in the construction of the reverse coil. There are 14 layers with 103 turns per layer and an additional 2 layers with 15 turns at either end of the coil. The main coil is also contained within a stainless steel jacket and connected to a similar articulation frame as the reverse coil for alignment of the field. The main solenoid can be seen in situ with the electrical connections and water cooling hoses in place in Figure 7.11.

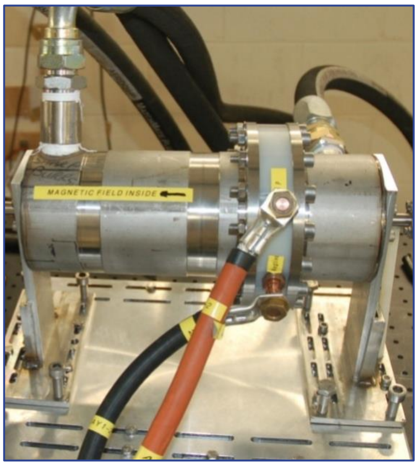

Figure 7.11: Photo of main coil in situ

The magnetic field range of the main coil can be selected from a range between 1.5 and 2.1 Tesla, depending on the desired frequency of the cyclotron interaction. This coil in conjunction with the reverse coil can achieve a tuneable electron beam with an alpha between 1 and 3 and an axial velocity spread of less than 8%. The parameters of the main solenoid are given in Table 7.2.

Field/Parameter	**B_0 = 1.65 T**	**B_0 = 1.82 T**	**B_0 = 2.1 T**
Resistance (Ω)	0.99	0.99	0.99
Current (A)	211.4	228.84	262.60
Voltage (V)	209	226	260
Power (kW)	44.25	51.85	68.28

Table 7.2: Properties of the cavity solenoid.

7.4.4 Solenoid power supply

The power supplies for both the main and reverse coils are controlled directly from outside the experimental bay and connected to the experiment via a conduit running into the bay from the rear ensuring the safety of personnel during live operations. This allows the revere coil to be adjusted over a range of field values up to 68 mT. By varying this magnetic field the location and strength of the cusp may be altered and therefore also the electron beam alpha value. The main coil power supply is capable of providing a maximum DC current of ~265 A at ~260 V, and is therefore capable of providing a maximum power of ~69 kW in to the solenoid.

7.5 Beam Tube and Interaction Region

The next section comprises the main body of the experimental system: The interaction region and interrelated sub-components (Figure 7.12).

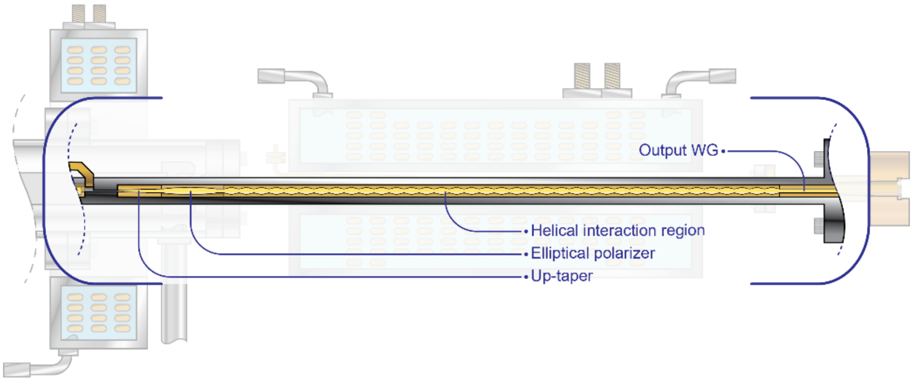

Figure 7.12: Schematic of the beam tube/interaction region.

For the purpose of further discussion it is convenient to classify the interaction region as being all the system that is physically interconnected to the main beam tube, although this is a purely arbitrary construct.

This stainless steel part contains the Bragg section, the input coupler, an up-taper section followed by the elliptical polarizer section, which leads to a further up-taper before terminating at the 3-layer vacuum window. Each of the inner components within the beam tube is designed and manufactured from copper.

Figure 7.13: Beam tube flow chart showing gyro-TWA system.

They are constructed as individual component pieces and as such can be changed out as necessary to provide for modification of the design. These pieces are made with flat edges machined along their outer length to allow for pumping out of the main beam tube. A flow chart describing the relationship between these components is shown in Figure 7.13.

7.6 Pulsed Power Supply

The gyro-TWA and gyro-BWO devices have been designed and constructed with the capability to operate in the CW regime. However for experimental development and design a pulsed power supply system was developed with the capability to provide a stable pulsed output amplitude of 40kV. A double Blumlien pulse generator was chosen to meet this requirement.

This is a type of cable pulse forming line (PFL), is capable of producing square, high power output pulse over a short pulse duration. A simple circuit describing a PFL is shown in Figure 7.14. The transmission line is charged by a DC power supply (V), which has an impedance that is substantially greater than the impedance of the transmission line (R_L). The charged line is then discharged across a load (Z_L).

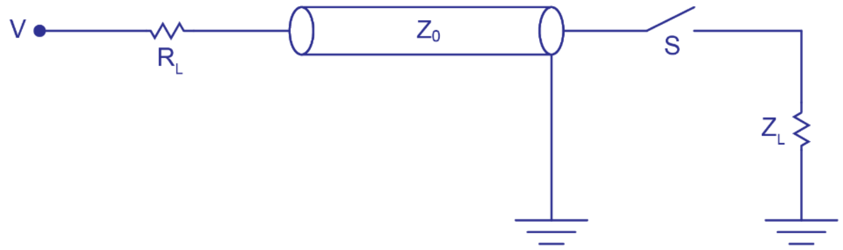

Figure 7.14: Shows a schematic of a pulse forming line.

When the switch is closed a voltage pulse will be formed across the load (Z_L) with a pulse length (τ), which is a function of the cable length (l) as well as the speed of the wave through this cable (v_c), the longer the cable the longer the output voltage pulse. The pulse duration is given by equation 7.1 and the output voltage by equation 7.2.

$$\tau = 2\frac{l}{v_c} \qquad 7.1$$

$$V_{out} = \frac{Z_L}{Z_L + Z_0} V \qquad 7.2$$

The major disadvantage of this type of PFL can be seen from equation 7.2. If the load and the transmission line are matched then the output voltage cannot exceed half of the input voltage. This can lead to increased costs and inefficiencies due to the large input power supply. One solution to this problem is the Blumlien pulse generator. A circuit diagram of a simple Blumlien pulse generator is shown in Figure 7.15.

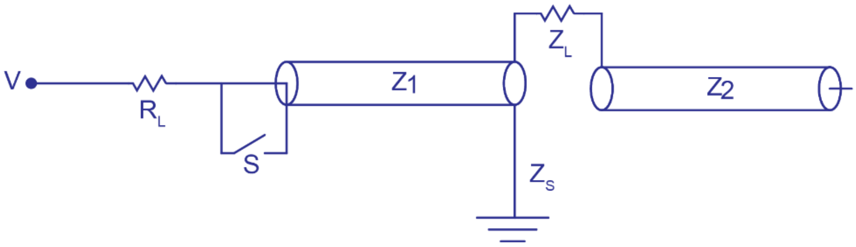

Figure 7.15: Schematic of a single Blumlien pulse generator (unfolded).

In this case two transmission lines of the same length are charged with an applied DC voltage (V). When these lines are discharged into the load resister (Z_L) it is now possible to get almost twice the output voltage compared to the input voltage if

$Z_L \gg Z_1, Z_2$ as shown by equation 7.3. The pulse length remains the same as before (7.4) and is still determined by the overall length and the speed of the signal in the line.

$$V_{out} = \frac{2VZ_L}{Z_1 + Z_2 + Z_L} \qquad 7.3$$

This is a far better arrangement than the simple PFL as the input and output voltage can now be equivalent. However, it still suffers from a loss in efficiency and voltage due to the connection between the second transmission line and the earth, which also has an impedance (Z_s).

The power and voltage can again be increased if a third transmission line is added to make a double cable Blumlein. This is in affect a set of two single cable Blumleins, which can be charged in series and discharged in parallel and therefore the output voltage can now be four times the input voltage. This circuit is demonstrated in Figure 7.16.

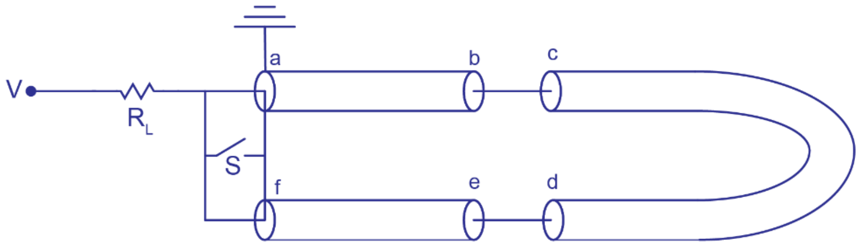

Figure 7.16: Schematic of a diagram of a double-blumlein.

The output from this circuit can either be inverted or non-inverted, depending on the location of the earth and the output. For the inverted Blumlein the earth is at point b and the output at point d while the non-inverting Blumlein has the earth at point d and output at point b. An inverting double cable Blumlein was built and used in this experiment and a schematic is shown in Figure 7.17.

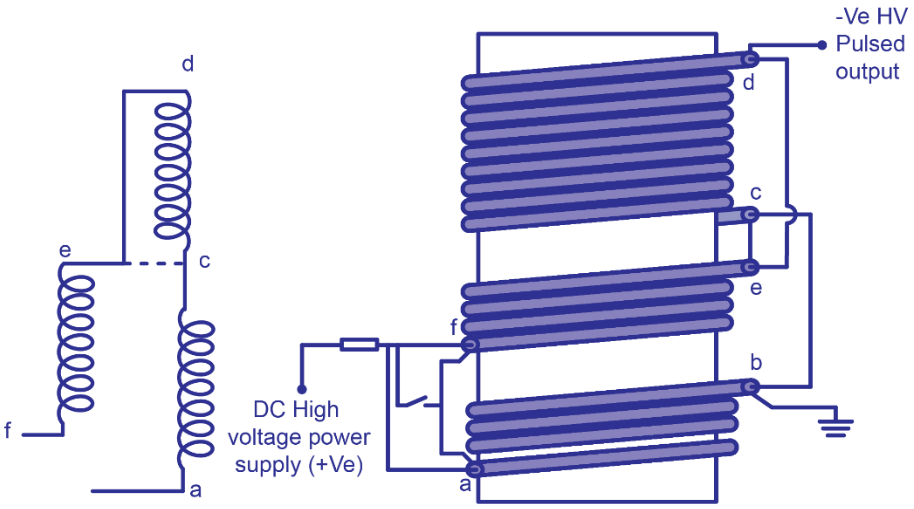

Figure 7.17: A schematic diagram of the double cable Blumlein.

7.7 Electron Beam Diagnostics

7.7.1 Voltage Divider

The diode voltage can be measured on an oscilloscope by using a voltage divider to reduce the signal voltage to the scope. By this method the magnitude of a large voltage pulse is easily evaluated by measuring a much smaller signal

$$V_{out} = \frac{R_2}{R_1 + R_2} V_{in} \qquad 7.4$$

The measured voltage is given in equation 7.4, where V_{in} is the input voltage, V_{out} the output voltage and the values R_1 and R_2 are the series resistances. The voltage divider circuit is given, along with a photograph, in Figure 7.18. This circuit was calibrated against a commercially available probe that is capable of measuring voltages up to a maximum of 15kV.

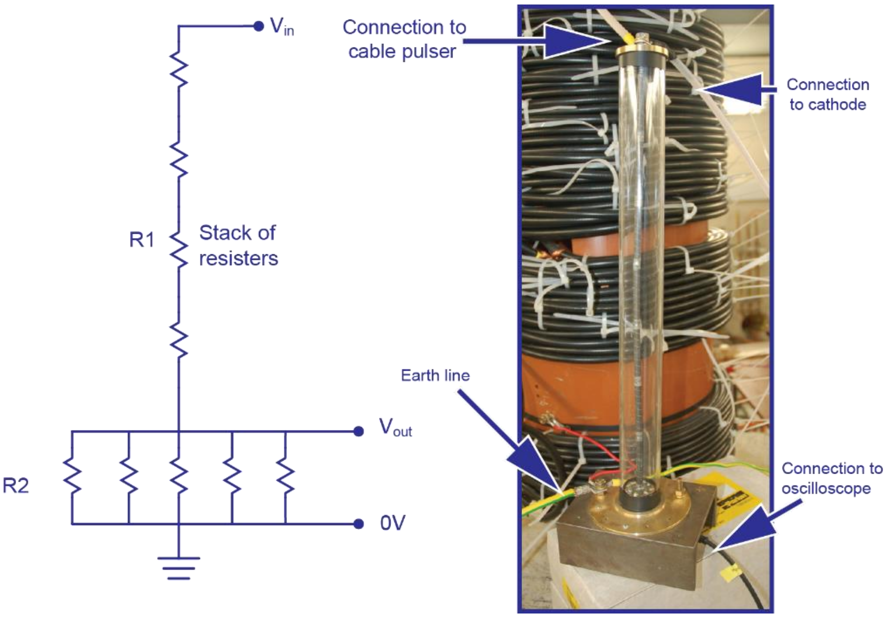

Figure 7.18: The voltage divider – showing the circuit diagram and the constructed voltage divider.

7.7.2 Rogowski Coil

The diode current and beam current can be measured using a Rogowski coil to measure the current on the anode. A Rogowski coil is a relatively simple coil of wire that can be used as a magnetic probe to measure alternating current. In the experiment the Rogowski coil is formed by wrapping a solenoid around a ferrite annulus and passing the earth connection from the anode can through the annulus.

A pulsed current passing through the annulus induces a change in magnetic flux in the coil and therefore a voltage across the terminals. The induced voltage is proportional to the rate of change of the current in the earth connection, so by using a Rogowski coil it is possible to measure the diode current.

The Rogowski coil was calibrated in the experiment by measuring the current with a Faraday cup and the Rogowski coil. The Faraday cup measures the beam current at the end of the beam tube and if there is no interception of the beam then the both the current measured by the Rogowski coil and the Faraday cup should be equal.

Figure 7.19 shows the location of the Rogowski coil in the experimental set-up, as well as some of the components of the vacuum system.

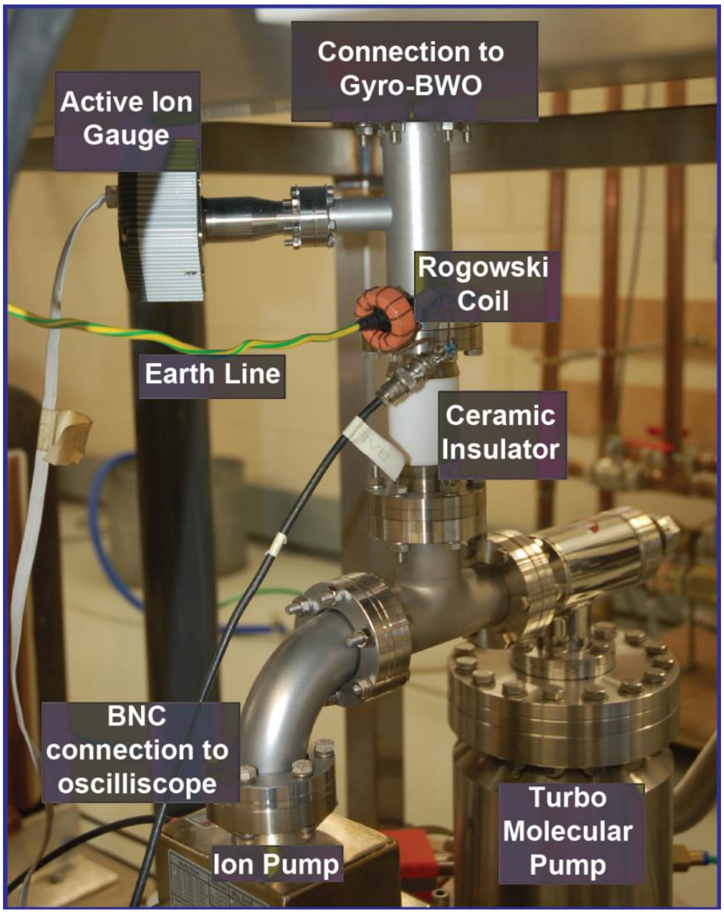

Figure 7.19: The Rogowski coil on the gyro-BWO system.

7.8 Input Coupler

The gyro-TWA design requires a source of radiation to drive the instability and this is provided by an input coupler that is located after a Bragg section. Figure 7.20 gives a cutaway view of the input coupler as well as the Bragg section and pill-box window in relation to the main stainless steel beam tube.

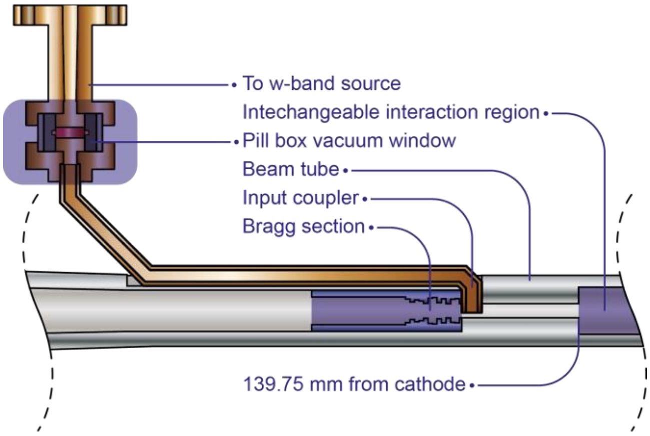

Figure 7.20: Bragg section and input coupler schematic.

This input coupler can also be used for the gyro-BWO, where the backward wave may be extracted from the coupler, rather than being reflected back down the beam tube and out through the window. In this configuration the input couplers role is reversed and it can be used to output the radiation. The coupler is required to be connected with other systems that are not at vacuum (either amplifiers or transmission lines depending on mode of operation). A pill-box window is therefore included in the coupler to maintain the system at ultra-high vacuum while maintaining a broad band capability. The performance of this window is shown Figure 7.21.

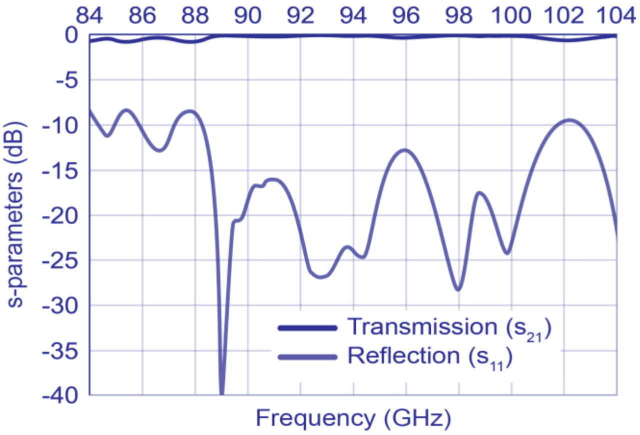

Figure 7.21: Pill box window bandwidth.

The first component, within the beam tube, encountered by the electron beam on its trajectory is the Bragg section. This is designed to allow the electron beam to transit into the main interaction zone while preventing the radiation from penetrating into the cathode region. This solution is used in place of a back-stop filter, which cuts off the travelling waveguide modes by reducing the diameter of the waveguide. Use of a

Bragg filter can, with the correct design, provide a method that allows both for ample clearance for the electron beam and an acceptable reflection for radiation travelling back towards the cathode.

7.8.1 UP taper

The interaction region has a greater diameter than the Bragg section and is oversized as far as the fundamental waveguide mode is concerned. In fact at a mean radius of 1.3 mm instead of the 1.18 mm in standard WR-10 waveguide. Therefore an up-taper section is required to match the input section with the helix.

7.8.2 Elliptical polariser

Before the radiation is transmitted into the helix where it will interact with the electron beam the mode must be converted from the fundamental TE_{11} mode to a rotating TE_{11} mode because the interaction inside the corrugated helical waveguide is requires a rotating mode with the opposite chirality to the helix. This is achieved by introducing an elliptical polariser, which produces a phase shift in the propagating mode and a subsequent rotation in the output polarization before the interaction region, converting the linearly polarised incident waves into circular polarised waves.

To understand the operation of the elliptical polariser it is useful to consider that a linearly polarised wave may be separated into two waves in perpendicular directions, each having the same phase. If the phase is different between these components and is altered then a rotation of the combined wave is produced.

To produce circularly polarised waves a phase shift of $\pi / 2$ is required between the components of the two waves. The wavenumber of the x and y components of a wave travelling in a circular waveguide is equal, but this is not the case in an elliptical waveguide. Each wave will 'see' a different radius of waveguide and therefore have a different cut-off frequency and different phase velocity. A schematic representation of a circular and an elliptical waveguide is shown in Figure 7.22. This shows a linearly polarised wave (Er) travelling through each waveguide at 45 degrees and its resultant components of equal amplitude Ex and Ey.

In the elliptical waveguide these components propagate along the same waveguide with a different inner radius. From the diagram, it can be shown that each of the components in the elliptical waveguide may be propagating through a circular waveguide with a radius equal to the major and semi-major axis of the ellipse and since the apparent radius is different for each component they will have a different cut-off frequency and there will be a phase shift between the two waves when propagating through the elliptical polariser.

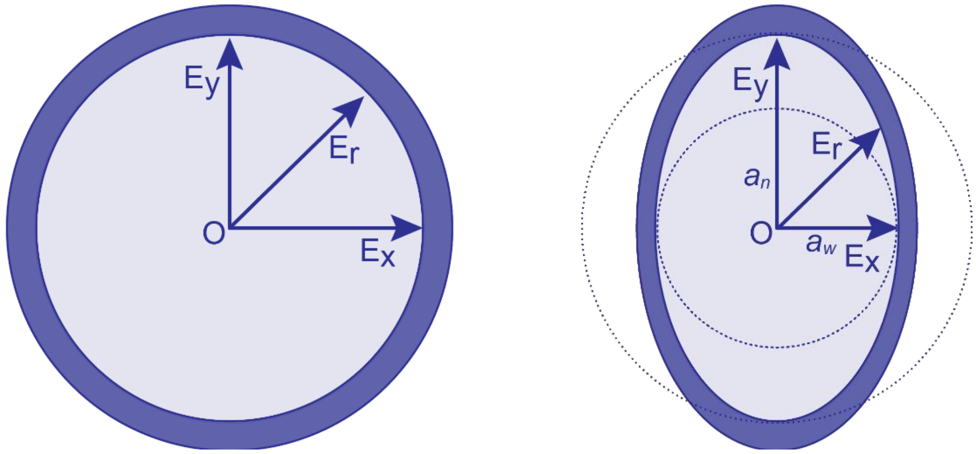

(a)Circular Waveguide *(b)Elliptical Waveguide*

Figure 7.22: Schematic representation of an elliptical polariser using a double circular waveguide model.

This can be expressed mathematically as follows: In the elliptical polariser the fundamental mode is the TE_{11} mode and the wavelength in a waveguide is[113]:

$$\lambda_g = \lambda_0 / \sqrt{1-(\lambda_0 / \lambda_c)^2} \qquad 7.5$$

The cut-off wavelength is $\lambda_c = 3.412a$ for a TE_{11} mode, a is the radius of the waveguide. Therefore equation can be written as:

$$\lambda_g = \lambda_0 \sqrt{1-(\lambda_0 / 3.412a)^2} \qquad 7.6$$

In an elliptical waveguide this wavelength is different for both of the E_x and E_y components. The first component (wave E_1) propagates through the waveguide of radius a_w and has a wavelength given by equation 7.7 and the other (wave E_2) with radius a_n and a wavelength is given by equation 7.8.

$$\lambda_{g1} = \lambda_0 \sqrt{1-\left(\lambda_0 / 3.412 a_w\right)^2} \tag{7.7}$$

$$\lambda_{g2} = \lambda_0 \sqrt{1-\left(\lambda_0 / 3.412 a_n\right)^2} \tag{7.8}$$

The phase shift of a waveguide with a length L is given by equation 7.9:

$$\psi = 360° L / \lambda_g \tag{7.9}$$

The phase shift of the wave E_1 is given by equation 7.10 and the E_2 by equation 7.11.

$$\psi_w = 360° L / \lambda_{gx} \tag{7.10}$$

$$\psi_n = 360° L / \lambda_{gy} \tag{7.11}$$

The phase shift of the elliptical waveguide is then:

$$\psi_e = \psi_w - \psi_n \tag{7.12}$$

Then substituting equations 7.10 and 7.11 for the phase shift of each axis and equations 7.7 and 7.8 for the wavelengths gives a total equation for the phase shift given by 7.13.

$$\psi_e = 360° L \left(\frac{\sqrt{1-\left(\lambda_0 / 3.412 a_w\right)^2} - \sqrt{1-\left(\lambda_0 / 3.412 a_n\right)^2}}{\lambda_0} \right) \tag{7.13}$$

7.9 Helical interaction region

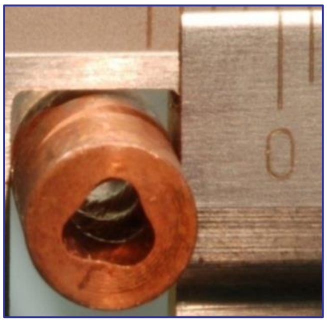

Figure 7.23: Typical helical interaction region

The fundamental and physical core of the system is the interaction region where the electron beam interacts with the RF field to either produce an amplified or stimulated microwave emission, depending on what regime of operation is chosen. The helical interaction region has been designed by Drs He, Donaldson and Zhang**[6.1]** for amplification of a microwave signal and is constructed from oxygen free copper. Figure 7.23 shows a section of the copper helix and its cut-out. The final 3 fold helix is approximately 100 mm in length with a mean radius of 1.3 mm. The helix is located within the beam tube at a position that sees the constant maximum field from the main solenoid. The parameters for the helix are given in Table 7.3.

Parameter	Value
Average radius (mm)	1.3
Corrugation amplitude (mm)	0.24
Corrugation Period (mm)	3.75

Table 7.3: Helix parameters

7.10 2nd Up-taper

A further taper is required after the helix, before the window section is reached, to match the helix with the window. It is also at this position within the beam tube that the electron beam is spent and is dumped on the inner surface of the beam tube.

7.11 Three Disc Vacuum Window

The output section of the gyro-TWA/BWO is a 3-disc vacuum window, which is required to keep the vacuum tube at ultra-high vacuum and maintain a very low reflection. This is achieved by using a system of dielectric windows that are optimized to produce a very low reflection over a broad bandwidth.

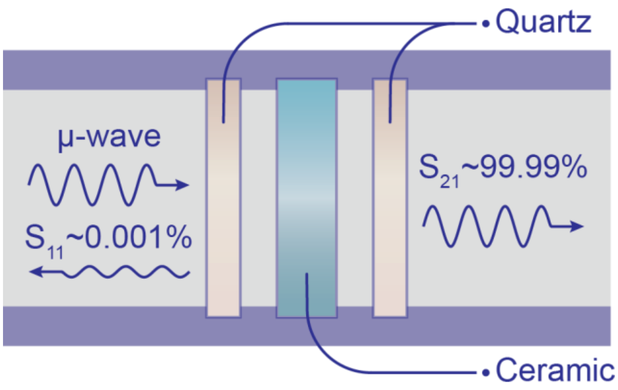

Figure 7.24- 3 disk window schematic

7.12 Vacuum System

The Vacuum system consists of an ion pump, a turbo molecular pump and a scroll rough pump all operating together. This system is designed to allow an electron beam to propagate in a suitably evacuated tube without any collisions with the heavy particles present in air that would otherwise prevent such propagation. The system is evacuated at the diode and kept sealed using ConFlat flanges with copper gaskets. The Scroll pump is used first to rough pump the system to a pressure of ~10^{-3} mBar. This pressure is within the operational limits of the turbo molecular pump, which can then reduce the pressure to the 10^{-9} mBar range required for operation of the experiment. The turbo molecular pump is sensitive to voltage fluctuations and it is therefore desirable to maintain the operational vacuum using an ion pump.

Figure 7.25:-Vacuum system schematic.

Figure 7.25 provides a simplified schematic of the vacuum system. The valves and diagnostic systems have been omitted for clarity.

8 Electron Beam and High Power MM-wave Measurements

In this chapter a description of the experimental methods and results of a far-field scan and a frequency measurement with and without the corrugated horn in place are discussed. Measurement of the electron beam accelerating potential, beam current, rectified millimetre wave pulse, power and the output from a 94GHz harmonic mixer from a gyro-BWO are presented. The tunability of the gyro-BWO is demonstrated in a graph plotting the output power and frequency as a function of the axial guide magnetic field.

8.1 Experimental Bay

The experimental apparatus, which comprises the gyro-TWA/BWO and its primary support components is located within a lead lined, reinforced concrete bay. This experimental bay provides screening from the X-ray radiation produced during the operation of the gyro-device as well as isolating the high power components from the user side. The experimental bay is accessed via a lead lined door and cannot be operated without enabling a series of safety interlocks, which ensure both the safety of users and that of the apparatus. A schematic representation of the experimental bay and set-up for the far-field experiment is shown in Figure 8.1.

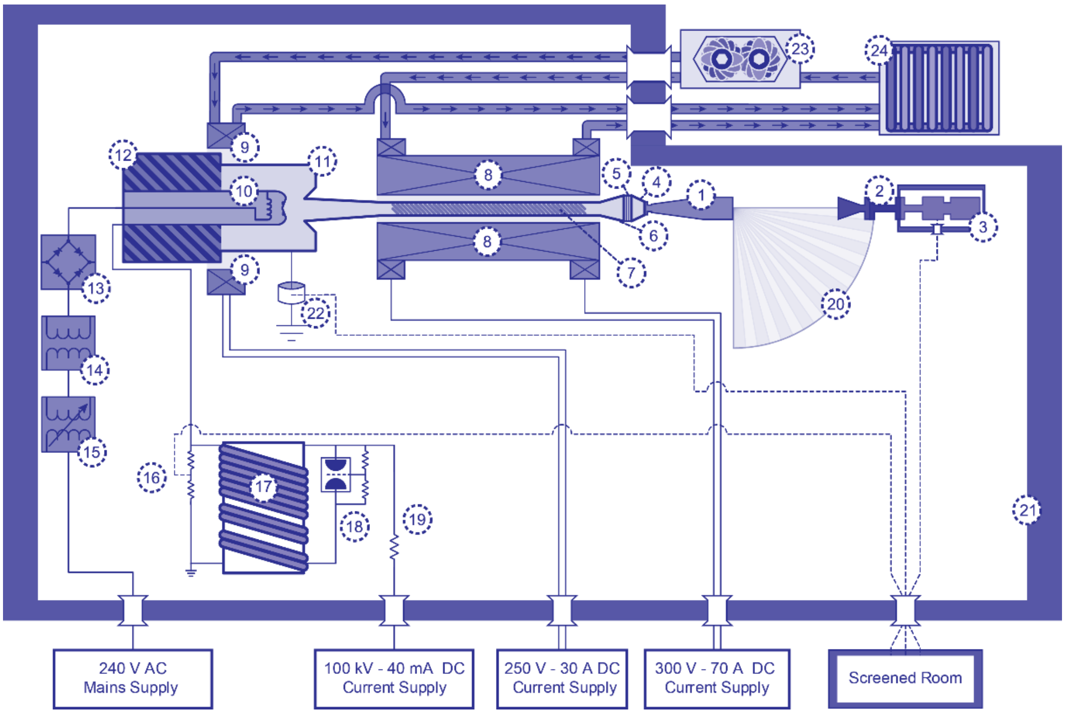

Figure 8.1: Experimental bay schematic (not to scale).

(1) Microwave horn. (2) WR-10 receiving horn. (3) Detector/mixer in a screened box. (4) Down taper and adapter. (5) 3-disk window. (6) Up-taper. (7) Helically corrugated waveguide. (8) Cavity solenoid. (9) Reverse coil. (10) Thermionic cathode. (11) Anode. (12) Insulating ceramics. (13) AC-DC converter. (14) Isolating transformer. (15) Variable transformer. (16) Voltage divider. (17) Double Blumlein cable pulser. (18) Spark gap switch. (19) Current limiting resistors. (20) Far-field scanning platform. (21)

Lead walls (22) Rogowski coil. (23) 4 Bar - 1200 litres/min water pump. (24) 120kW cooling radiators.

8.2 Far Field Apparatus

For the far-field and measurements of the horn on the gyro-BWO a similar apparatus was constructed to that used during the VNA far-field scan. Due to the limitations on the physical space available the scanning table could not be used, but the optical rail and car assembly that was used in the previous experiment was moved to the bay and fixed to a smaller scanning platform with the detector affixed to the optical rail as before using the same methods to align the transmitting and receiving horns.

The far field signal was detected using a diode microwave detector connected to a standard WR-10 rectangular horn and a matched load. This assembly was housed within a screened box that was connected via a screened cable to the oscilloscope outside the experimental bay. This arrangement of the box is shown schematically in Figure 8.2 (a) and a photograph of the horn and detector is seen in Figure 8.2 (b-c).

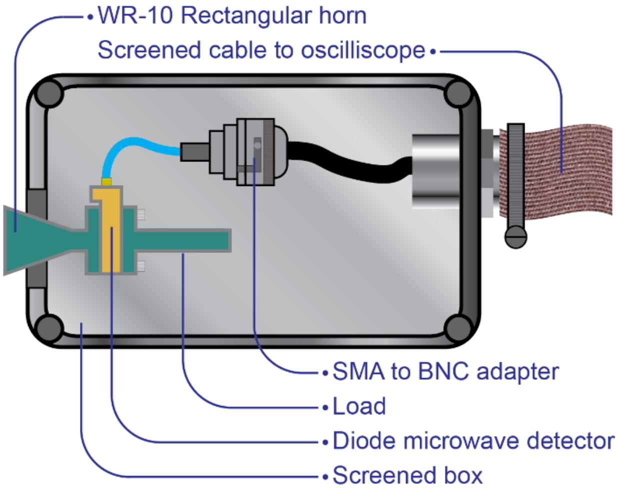

(a) Microwave detector schematic.

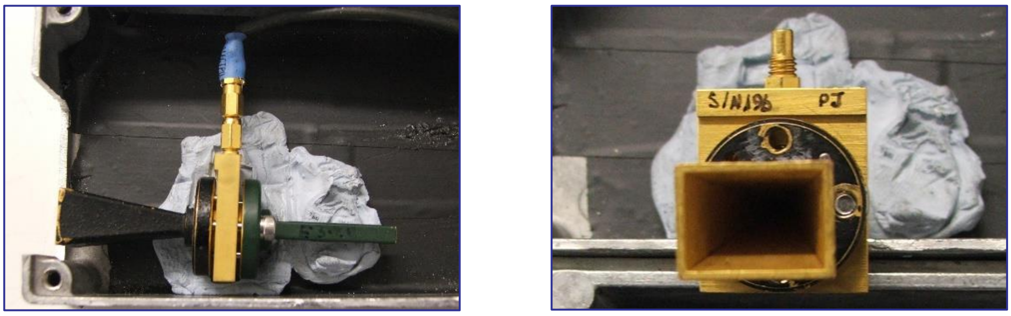

(b) Microwave detector.

(c) Horn (end on)

Figure 8.2-Detector assembly.

Before the detector could be used it was calibrated using a known mm source. Figure 8.3 is the calibration curve that was generated for the microwave detector used in the experiment. The detector was measured over the range between 0 – 60 mV corresponding to the known output power from the solid state amplifier.

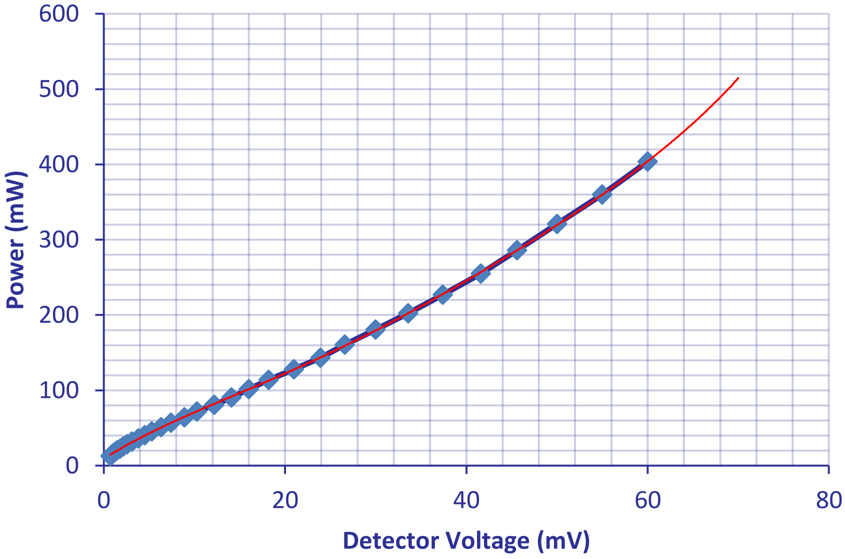

Figure 8.3: Calibration curve for microwave detector

The diagnostic equipment was contained within an electromagnetically screened room (Figure 8.4) located outside of the main experimental bay. To reduce parasitic radiated noise due to the switching of the spark gap all the diagnostic lines were shielded with copper braiding connected to the screened room with the inner coaxial cable connected to the digital storage oscilloscopes (DSO) located in the screened room. The DSOs were used to record the signals from the electron beam and microwave diagnostics.

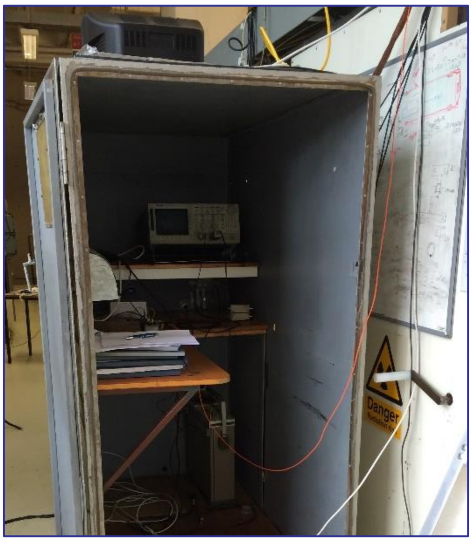

Figure 8.4: Electromagnetically screened room

8.3 Mode Scan

The investigation of the corrugated horn “prototype 1” was advanced by integration of the component with the gyro-BWO in a “hot test” (electron beam present) environment. Using the gyro-TWA helix with the system re-configured, by changing the direction of the main coil, to operate as an oscillator. In this configuration the input coupler becomes redundant and is blanked off by placing solid metal flange to act as an electrical short on the input waveguide. The radiation produced is therefore reflected by the Bragg section (and the short as well) and transmitted into the horn via the 3-disk window. The second path that the radiation takes as it passes once more through the helix does not cause any problems due to the dependence of the interaction with the chirality of the helix.

Figure 8.5: Corrugated horn fitted to adapter and down taper.

The corrugated horn was connected to the output of the three disk window by means of a short aluminium down-taper section and an adapter section, which connects to the window. In this way a far field mode scan of the radiation pattern produced by the horn under operational conditions could be undertaken. The adaptor and taper attached to the horn is shown in Figure 8.5 and the assembled horn with taper can be seen on the experiment in Figure 8.6.

A series of microwave pulses were generated in the gyro-BWO system and transmitted via the corrugated horn into the receiving horn and detector, where the microwave signal pulse could be measured and recorded. The cavity coil and the reverse coil field were set at 244 and 193 Amps respectively, for the duration of this experiment and the cathode heating voltage and current were set at 9.55 V and 8.04 A respectively. These values have been demonstrated to provide an output microwave pulse with a frequency of ~94 GHz, which was later confirmed in a heterodyne mixer experiment allowing the frequency of the pulse to be measured directly.

The microwave signal was measured at one degree increments starting at the zero degree point aligned to correspond with the boresight of the horn. The detector was placed at 440 mm from the horn aperture in correspondence with the 'VNA millimetre wave' measurements of the corrugated horn. At each point a number of measurement pulses were recorded to find a stable signal and to remove the possibility of any extreme random fluctuations in the signal measurements. This method was used in place of the more desirable method, whereby two detectors would be used to produce a normalized set of data by keeping one detector fixed in position and scanning the second. Unfortunately, due to the narrow beam profile that is generated using the corrugated horn, this method could not be practicably employed as the power measured was seen to fall off quickly at even reasonably small angles of axis therefore there was no physical room for both detectors (and screened boxes) in the region of interest for the mode scan.

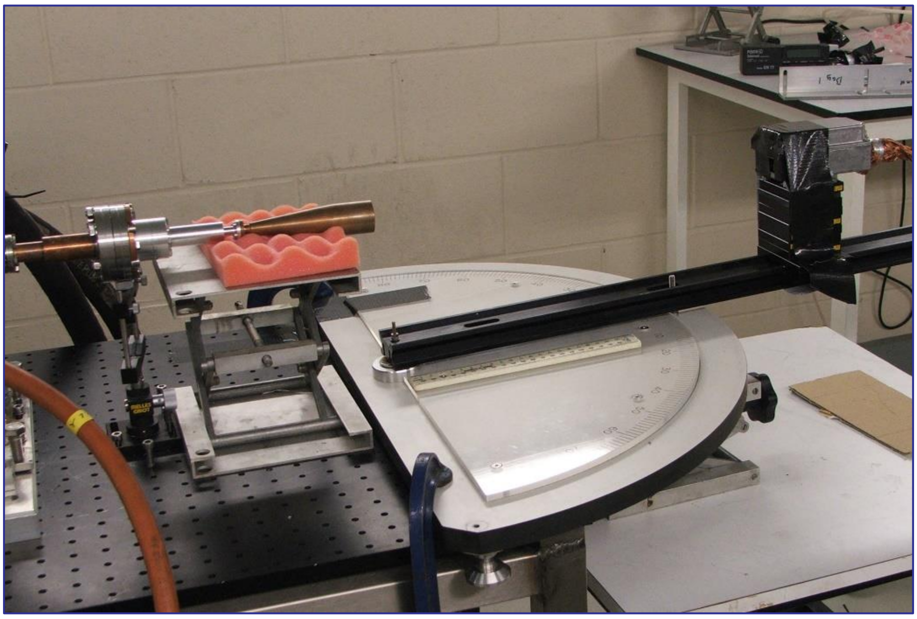

Figure 8.6: Corrugated horn attached to the 3 –disc window for the far-field scan.

A series of measurements for the E-plane polarization was thus commenced starting with the right quadrant (facing into the boresight) and continuing at 1 degree increments until the signal was almost indistinguishable from the system noise, and then at 2 degree increments, then 5, until the detector was at a 30 degree angle. The apparatus is shown in Figure 8.6. This approach was mirrored for the measurements in the left quadrant. This method was repeated for the H-plane polarisation, where the only significant difference was the smaller angle that the signal was seen to drop into the noise region. So for these data points fewer measurements were required, as was to be expected.

The results obtained are presented in the following series of charts and compared to the results that I obtained previously for the gyro-BWO experiment[114] without the corrugated horn in place. For these experiments a conical small taper was attached to the output of the window and a series of mode scans were carried out in the same manner as was detailed in the previous paragraph.

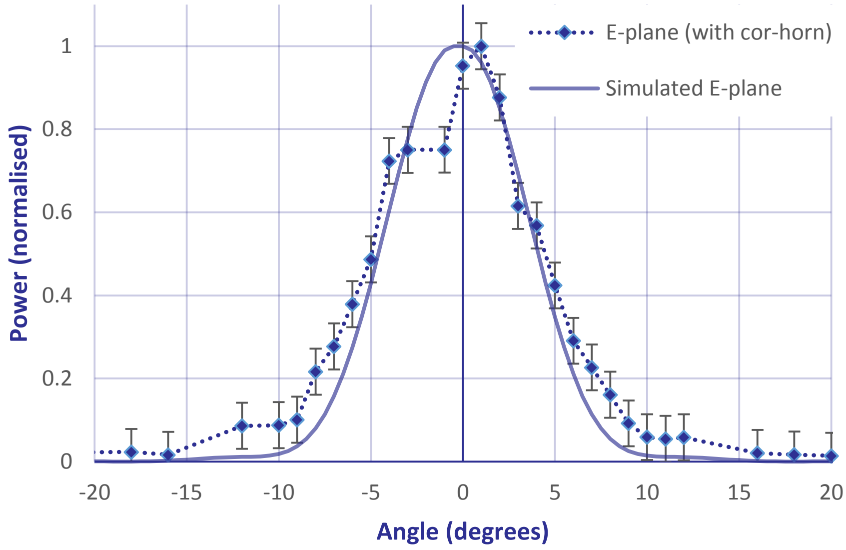

Figure 8.7: Normalised E-plane Vs. Simulation Data.

Using the calibration curve derived for the W-band detector, a plot of the far fields for the E and H-planes were derived showing the power as a function of angle. This data is shown in Figure 8.7 and Figure 8.8 plotted in conjunction with the mode scan data derived from the simulations.

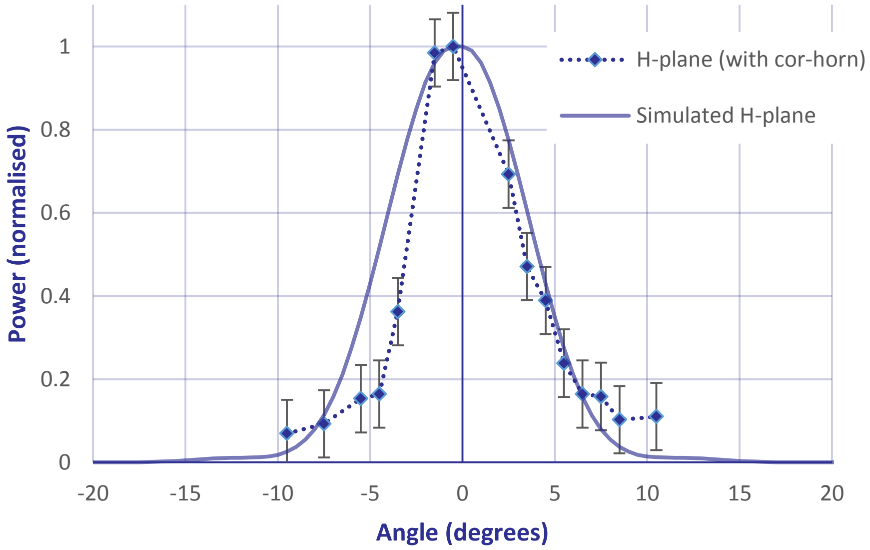

Figure 8.8: Normalised H-plane Vs. Simulation Data.

From the data analysis of the 'electron beam' experiment far field it is evident that the performance of the horn is comparable with that of the simulation. The power is deployed over a small central angle, which is similar to the distribution seen in simulations. However, the sensitivity of the measuring equipment limits the comparability between the experimental data and simulation for the side-lobes at higher angles, therefore the comparison is only justifiable at small angles (less than 10 degrees). The variability of the power produced by the gyro-BWO is a further limiting factor that reduces the possible resolution of the far-field pattern as evicened from the error bars on the measurement. These plots can be compared to the far-field results, which were obtained without the corrugated horn and are shown in Figure 8.9.

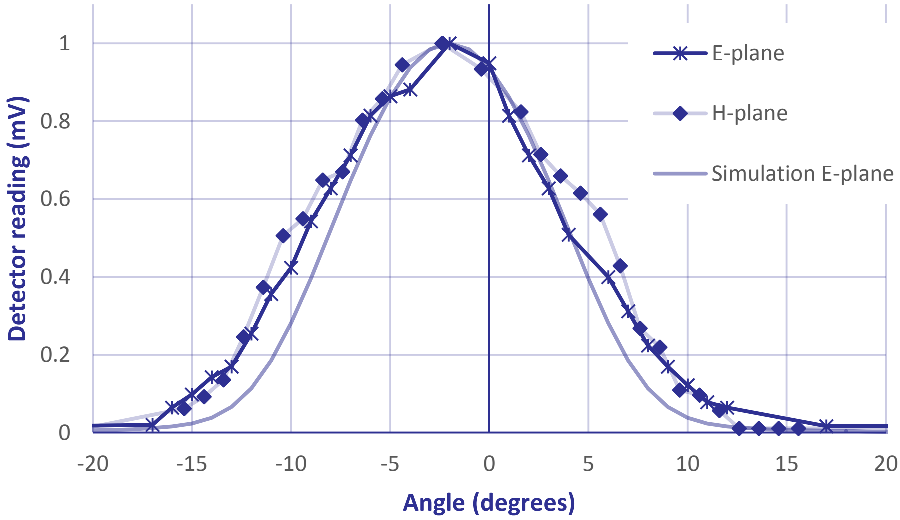

Figure 8.9: Gyro-BWO far-field patterns without the corrugated horn (window and taper only)

Here the E-plane and H-plane scan has been plotted along with a simulated far field, which has been generated from a model of the conical output taper in CST Microwave Studio. The excitation signal is a rotating TE_{11} mode to match the output from the gyro-BWO.

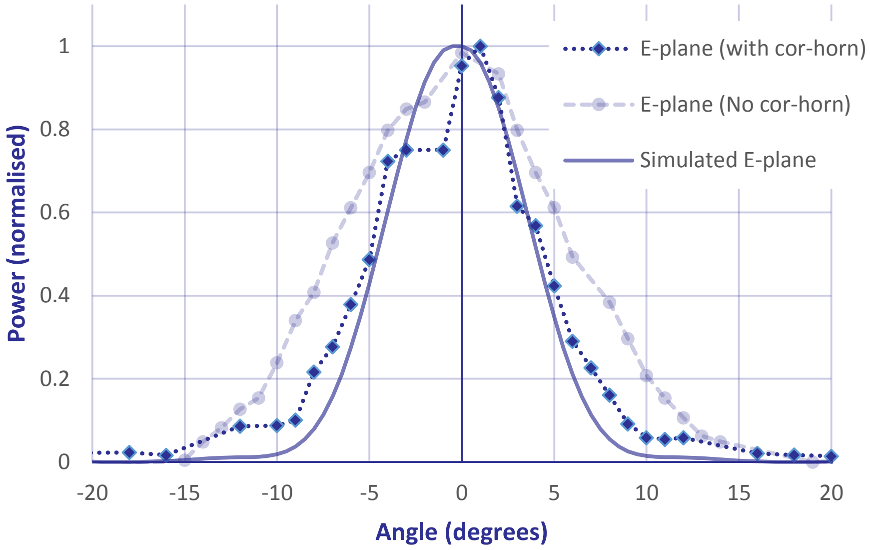

Figure 8.10: Gyro-BWO far-field comparison E-plane.

A combination of the above plots is best used to demonstrate the effectiveness of the corrugated horn. Figure 8.10 and Figure 8.11 show the E-plane and H-plane far-field scans from the gyro-BWO with and without the corrugated horn.

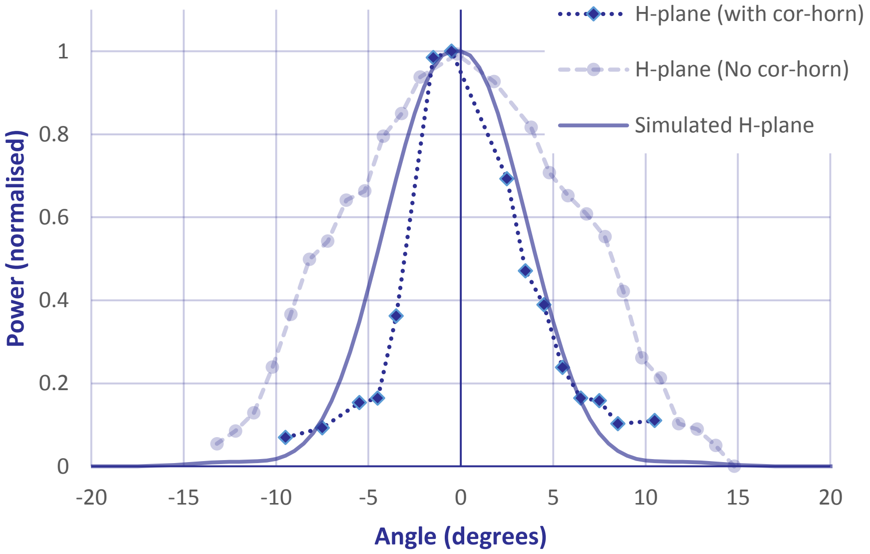

Figure 8.11: Gyro-BWO far-field comparison H-plane.

8.4 Power Measurement

In order to measure the absolute power of the terahertz radiation pulse from the gyro-BWO a 1.5 W, 90 – 97 GHz tunable signal was propagated into the gyro-BWO as a calibration source using the coupler. The radiation was then measured by a detector at a far-field point at the downstream window end. The whole transmission loss of the system was carefully measured by the VNA to be ~6 dB. By comparison of the detector outputs from the gyro-BWO experiment and the calibration signal the output power of the gyro-BWO could be measured accurately.

8.5 Frequency Measurement

The output frequency generated when operating the device in the oscillator configuration was also experimentally measured to confirm what frequency was transmitted through the corrugated horn during the mode scan measurements. The frequency range of the measuring equipment available was below the predicted W-band frequency of the oscillator, with the highest measurement frequency of the high speed digital oscilloscope at 20 GHz. The most efficacious method for determining the output frequency was therefore a heterodyne measurement using a mixer. This method allows the measurement of the difference frequency between a known reference signal and the unknown output signal from the oscillator.

A heterodyne frequency diagnostic was used to measure the frequency of the output radiation of the gyro-BWO. An in-band fundamental mixer (Millitech MXP-10-R) and a local oscillator signal produced from a 95 GHz Gunn diode (Millitech GDM-10-1013IR) were used and the resultant intermediate frequency (IF) signal was recorded by using a 20 GHz, deep memory digitising oscilloscope (Agilent DSX-X 92004A).

The frequency range of interest here is between ~90 – 100 GHz, therefore the reference signal should also be within this range to simplify the measurement of the difference frequency. In this case a Gunn diode was used to produce the reference signal. The diode was previously calibrated to produce a stable signal at 95 GHz. This signal was combined in an mm-wavelength mixer with the oscillator output, which was received and passed to the mixer by means of a horn and detector also connected to the mixer. The mixer output was analysed on the high frequency digital oscilloscope. The data from the scope was exported for analysis and a typical signal is shown in Figure 8.12.

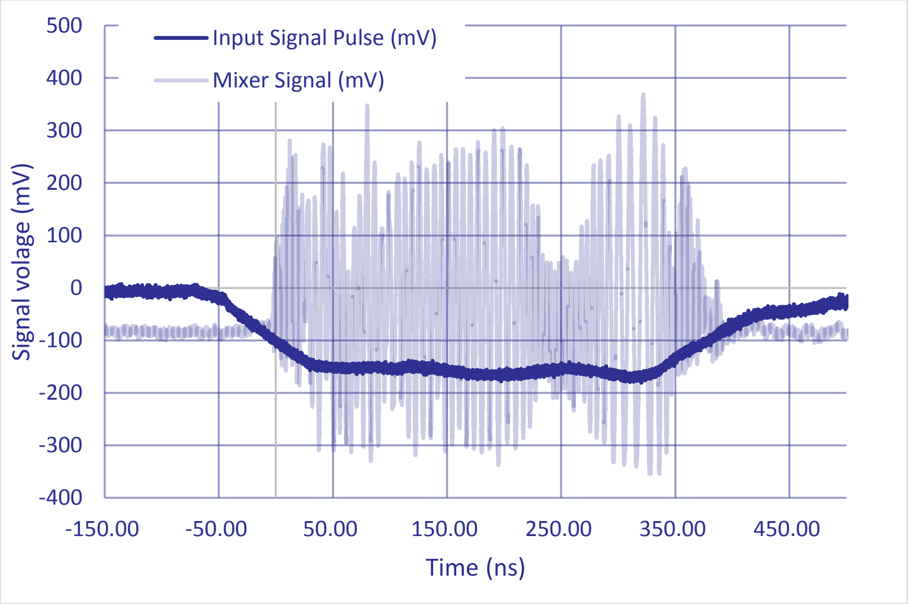

Figure 8.12: Input signal and mixer output signal at 235 V (main coil) and 180 V (reverse coil).

The mixer signal from the scope contained unwanted noise from outside the signal pulse. This data was removed before the mixer signal data were imported into Matlab, where a fast Fourier transform was carried out. A portion of this window is seen in Figure 8.13.

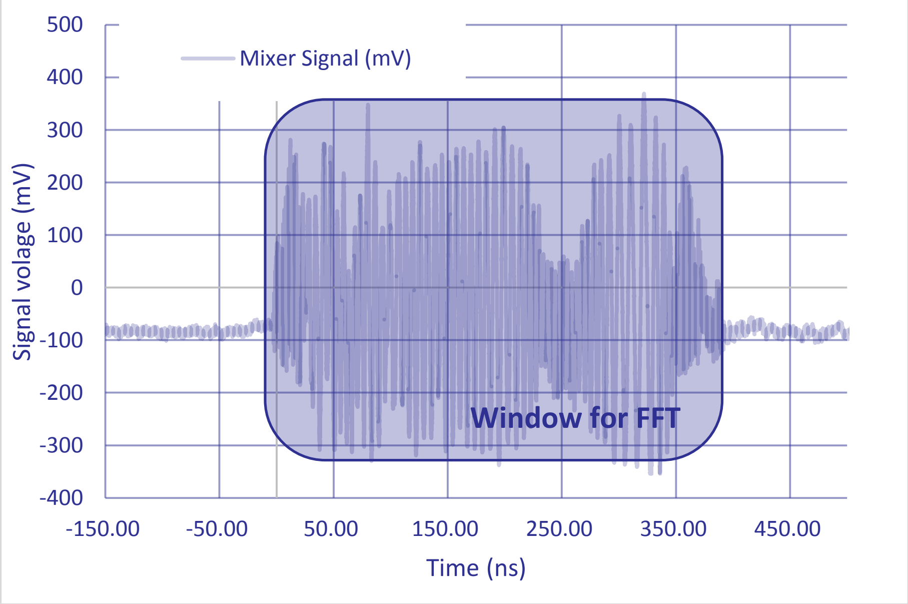

(a) Mixer signal showinng FFT window.

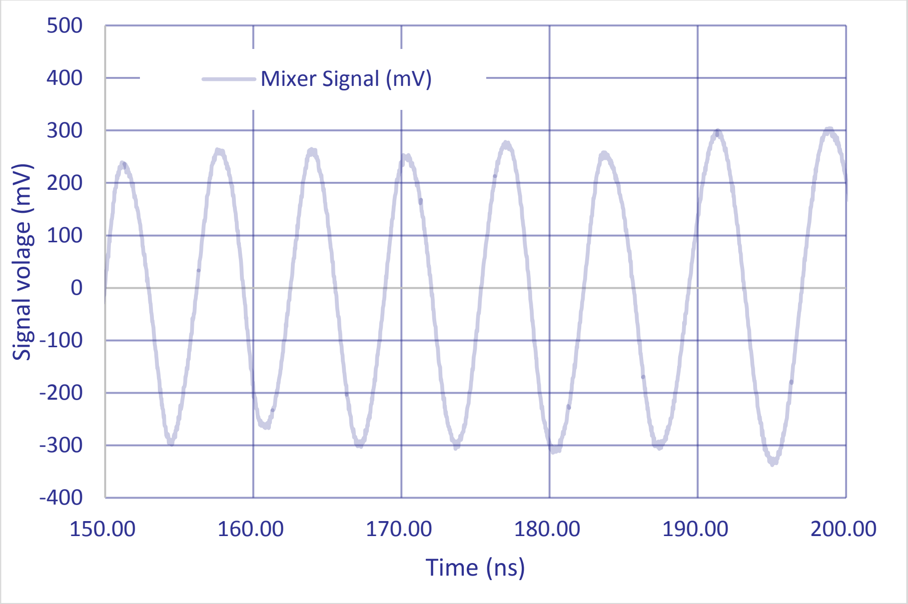

(b) Detail view of mixer signal.

Figure 8.13: Mixer signal showing region of interest for FFT.

Figure 8.14 shows a comparison between the FFT of the mixer signal as compared to that directly observed from the FFT analysis on the digital scope and the FFT calculated from the mixer signal exported from the scope and analysed using a Matlab script. The FFT shown in Figure 8.14 is derived from one of the measurements of the output pulse at 235 A on the main solenoid and 180 A on the reverse coil corresponding to a cavity magnetic field of 1.867 T.

The Matlab trace (red) has less noise than the scope trace (blue) due to the 'windowing' of the mixer output signal, but the peak frequency response is clearly shown in the same location. The Matlab signal was also converted to dBm for this comparison only. Subsequent analysis only required the location of the peak frequency, therefore this additional step was unnecessary.

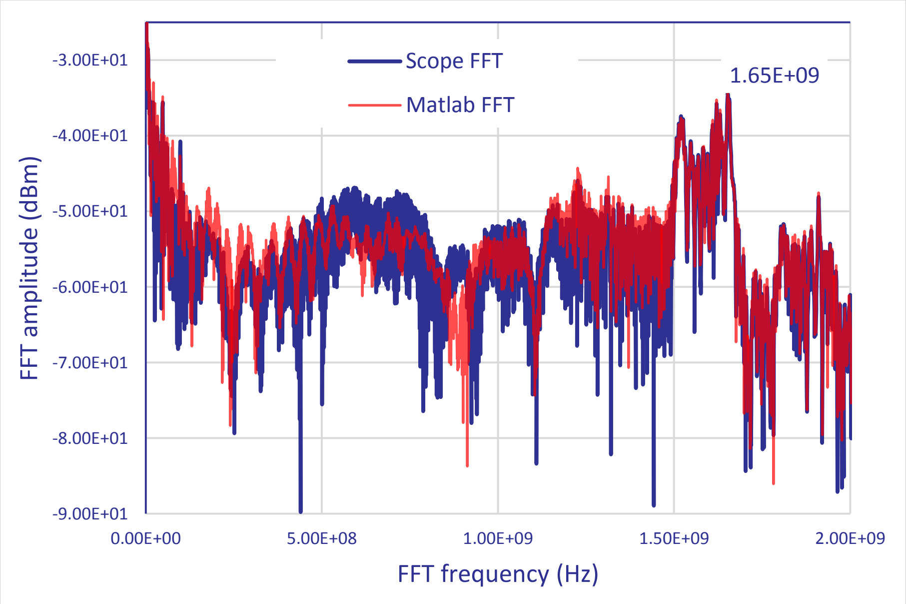

Figure 8.14: FFT of mixer signal (scope and Matlab).

Typical frequency measurements are plotted in Figure 8.15 for the difference between the mixer frequency and the known frequency produced by the Gunn diode as a function of the magnetic field in the cavity.

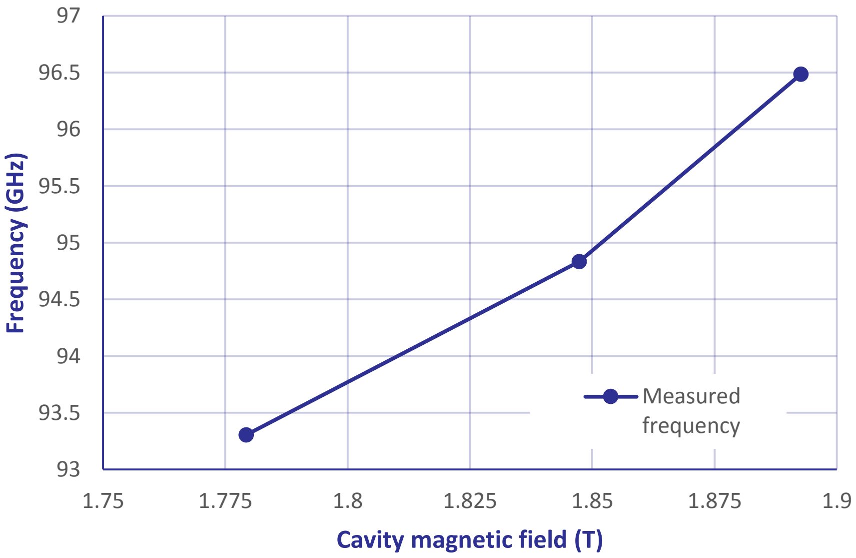

Figure 8.15: Heterodyne frequency measurements with corrugated horn

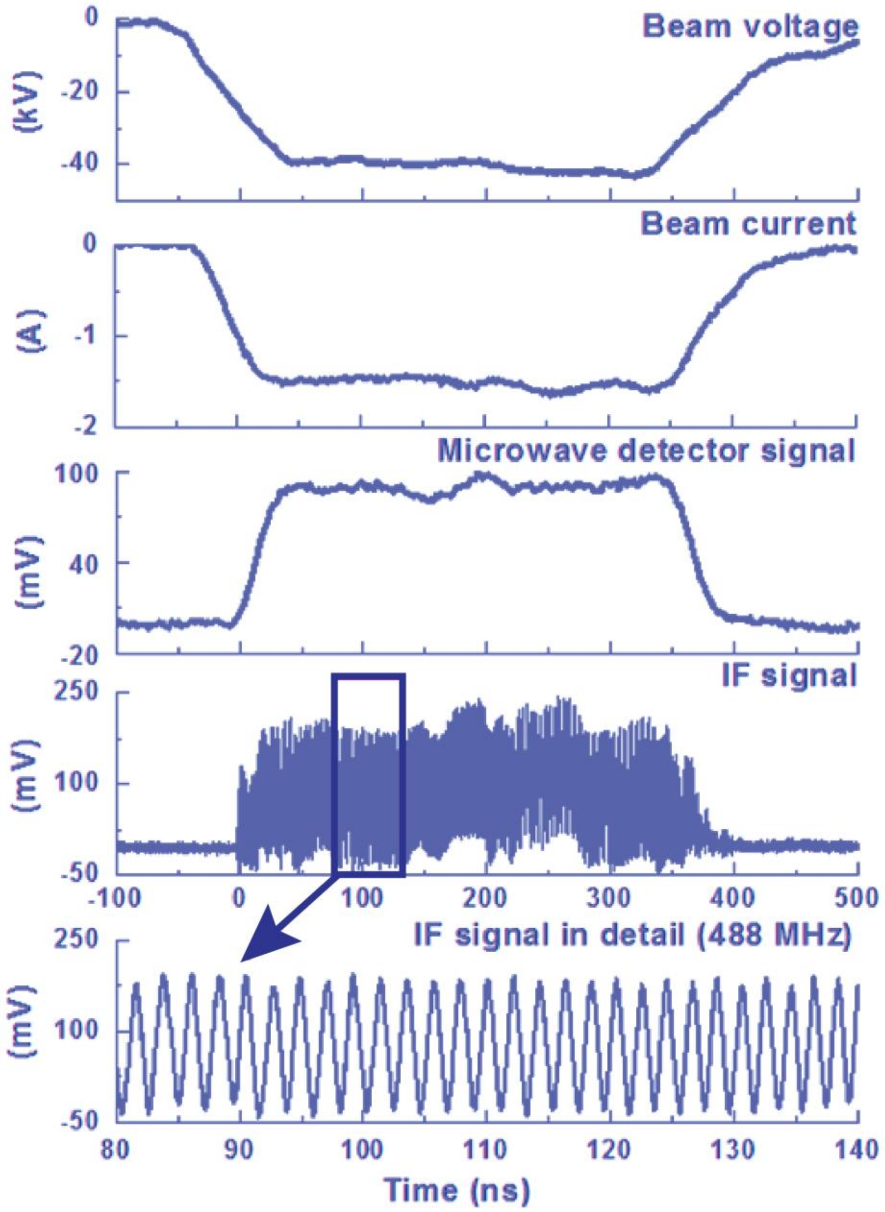

Figure 8.16: Recorded beam accelerating potential, current and millimetre wave signal and heterodyne IF signal from the gyro-BWO without the corrugated horn.

The results are summarized in Figure 8.17. The gyro-BWO generated a maximum output power of 12 kW when driven by a 40 kV, 1.5 Amp annular-shaped large-orbit electron beam and achieved a frequency tuning band of 88-102.5 GHz by adjusting the cavity magnetic field.

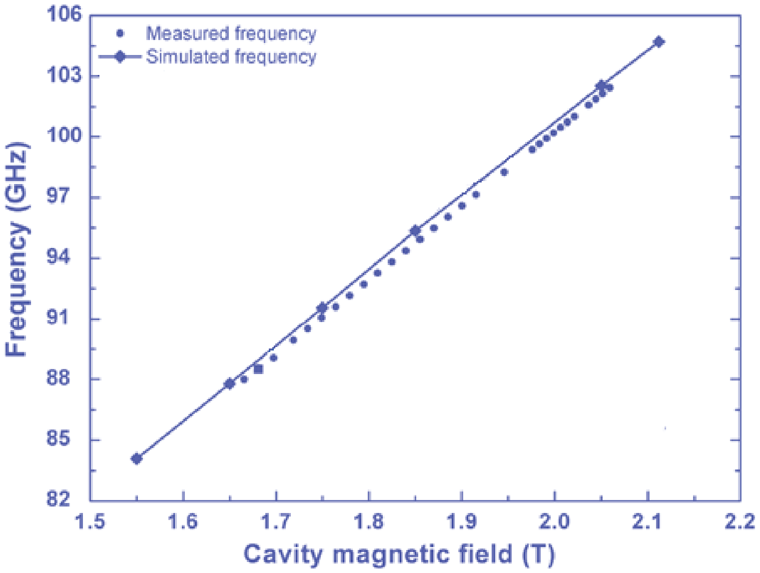

(a) Frequency measurements compared with simulation.

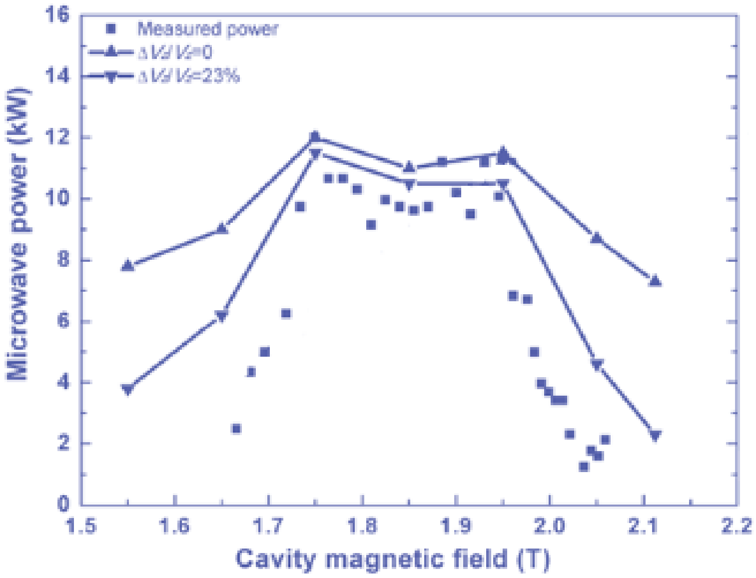

(b)Power measurements compared with simulation showing 0 and 23% velocity spread.

Figure 8.17: Heterodyne frequency measurements from gyro-BWO experiment without corrugated horn.

The above results clearly demonstrate the applicability for the corrugated horn to be implemented into the Strathclyde gyro-devices. The far-field measurements are narrower than the results shown for a conical taper on the window alone. The frequency measurements agree very well with the measured results, without the horn, therefore the inclusion of the horn in the system had no detrimental effect on the overall performance with the Gaussian profile easier to be applied to transmission line systems.

9 Conclusions and Future Work

This chapter provides a brief summation of the results and work undertaken during the course of this thesis. The future of this research is also discussed.

9.1 Overview

The work carried out in this thesis was primarily concerned with investigating the feasibility of using a hybrid-mode corrugated feed horn as a broadband quasi-optical output coupler in a W-band gyro device. Simulations of several types of corrugated feed were carried out using mode matching and finite element time domain software as well as numerical analysis. Optimisation and design of a final broadband prototype using these methods resulted in a 100 step corrugated horn that was integrated with the Strathclyde W-band gyro-BWO.

9.2 Review of Results

At the outset of the thesis a number of outcomes were defined. These are summarised in the following, with a brief synopsis detailing the results that were achieved.

- **Component to allow the design and construction of a gyro-TWA.**

  The prototype horn that was constructed was successfully integrated into the Strathclyde W-band gyro-BWO experiment.
- **Operational bandwidth between 90 and 100 GHz.**

  The prototype horn was measured and its performance calculated by simulations to have a broadband reflection of less than -35 dB and a narrow main beam and low cross-polar radiation pattern over the bandwidth. This is consistent with a continuously tuneable component that will not compromise the performance of the system.
- **Allow for the incorporation of a depressed collector**.

  The design of this horn does allow for the possibility of a future implementation as part of an energy recovery system in the form of a depressed collector. This was validated in simulations and ‘cold testing.’
- **Produce a quasi-optical output mode.**

  The hybrid mode at the aperture of the horn was calculated to be coupled with the fundamental free space Gaussian mode with a 98% coupling coefficient.

- **Radiation must propagate across an insulating gap.**

  The coupling to the fundamental free space Gaussian mode allows the radiated beam to pass into free space and across a break in the waveguide structure without interference.
- **Consider the electron beam in the design.**

  The design and simulation of the horn was carried out at all times with careful consideration of the results obtained from electron beam simulations and the final design was constructed to take the beam spread into account and should not interfere with the electron beam in the gyro-TWA experiment.
- **Radiation primary lobe (beam width) must be well defined with a narrow beam waist at the window.**
  - From simulations and cold tests the diameter of a window after a length of 100 mm outside of the horn is between 40 mm and 60 mm, where the worst case (60 mm) is from simulation. Therefore, it seems viable to assume that a collector could be fabricated

9.3 Simulation

A series of computational simulations using mode matching (μ-wave) and finite-difference time-domain simulation (CST-studio), as well as analytical studies (Matlab and MathCAD) were carried out on a variety of different design variants to determine an optimal prototype for construction and integration in the experiment. These simulations were used to optimize the final prototype and to validate the design by cross checking between the different simulation methods and software packages.

From these simulations the final design for the corrugated horn with a linearly varying corrugation depth, which is tapered over the length of the horn from $\lambda/2$ to $\lambda/4$ to better the reflection performance over the bandwidth was finalised. This design had 100 corrugations with an output diameter of 224 mm and an input diameter of 6 mm and a gap and vane width of 0.6 and 0.5 mm respectively.

The prototype simulation showed a highly symmetric radiation pattern with 99.9 % of the radiated power is contained within an angle of 25 degrees at 95 GHz. The far-field radiation pattern remained consistent over the bandwidth, with the first side lobe at ~10 degrees and -18 dB and a cross-polar component less than -40 dB.

9.4 Cold Testing

The microwave properties of the horn prototype were measured using a W-band vector network analyser. The reflection performance and Far-field scans over the frequency range from 90 GHz to 100 GHz were carried out for the E-plane co-polar component, the H-plane co-polar component and for the 45 degree cross-polar component of the far-field radiation pattern. The reflection performance of the horn over the bandwidth of less than -30 dB meets the requirements for a gyro-amplifier design. The far-field measurement allowed the performance of the horn to be evaluated over the entire frequency range. At 95 GHz the first measured side-lobe is at 15 degrees at -22 dB, showing more than 99% of the output power is within a 30 degree angle.

There is a slight difference between the measurement and simulation, which is possibly due to manufacturing tolerances that can result in variations in the dimensions of some of the corrugations in the throat region. This is manifest by the results shown in the offset between the simulated and measured nulls as well as broadening of the secondary lobe in the E-plane scan. This situation has been simulated using both the mode matching method as well as CST Microwave Studio and the results demonstrate that if the corrugation dimensions of the throat region are altered by 50 microns similar results are obtained. The measured far-field shows a rotationally symmetric radiation pattern that demonstrates a Gaussian profile. The experimental ‘cold test’ results agree well with the simulations, demonstrating the potential for this horn to be used successfully to launch a Gaussian radiation beam through a depressed collector system.

9.5 Hot Testing

As part of the experiments on the Strathclyde Gyro-BWO, the corrugated horn was integrated with the system after the broadband window where it underwent testing in a ‘hot’ experiment at high power. This allowed the horn to be evaluated in the far-field and over the frequency band under gyro-BWO operational conditions. Frequency measurements of the horn on the gyro-BWO determined that the operation of the device was not compromised by its addition and a comparison between the far-field measured with and without the horn in place showed a substantial improvement in the width of the main beam. This is consistent with a Gaussian mode and demonstrates the viability of the horn in future generations of the amplifier and oscillator.

9.6 Future work

The future of this work at the University of Strathclyde will continue the development of the corrugated horn as a method by which the beam and EM-wave may be decoupled for use in energy recovery. Work is also continuing on the development of broadband windows to be included in the structure of the horn as well as further designs and refinement of the technology for higher frequencies in the sub-mm and terahertz bands.

9.6.1 Energy recovery at w-band

Cold testing and simulations have demonstrated the possible application of the prototype horn for use in an energy recovery system with a quasi-optical output. The challenge remaining for this system to be viable is to design and test an electron beam collector system that is compatible with the horn. The simplest method is the axial output, where the horn and window are co-axial and the electron beam is collected in the gap between the two. This presents a challenge in the fabrication of a window with a diameter large enough for the quasi-optical mode to pass while allowing a gap that is wide enough to collect the electrons.

A second possible solution would be to design a system of mirrors to steer the quasi-optical beam to a radial window in a manner analogous to the Vlasov type of system.

This would enable the reduction in the diameter of the output window, but has the added complexity of the design and manufacture of a system of mirrors within the depressed collector system itself.

9.6.2 New-window designs at W-band

The initial goal of this project was concerned with the design of a launcher for a depressed collector system, but the corrugated horn designed has also application as an interface between the amplifier and any device requiring a W-band source. The HE_{11} mode is highly advantageous for use in corrugated transmission lines and in electron spin resonance spectroscopy.

For such systems the quality of the mode and the coupling to the Gaussian must be extremely high, therefore the window and horn must be considered as a single entity and modelling is now in progress towards building new improved designs, which include the window in the structure of the horn and also improve on the coupling between the Gaussian mode and the HE_{11} mode at the aperture.

9.6.3 Next generation gyro-devices

The next generation of gyro-amplifier under development at the University of Strathclyde will operate around 263GHz and 375 GHz, with future plans to push the technology further into the terahertz range. The application of the corrugated horn to this research is currently underway. The basic requirements and design of such a horn are very similar to the case for the W-band design, therefore this design should be quite capable of serving devices with higher frequencies just as well. The major challenge will be in producing viable designs, which are high performance while still being within the capabilities for manufacture at such high frequencies. Early results from this work have proven encouraging with horn designs at 375 GHz returning a performance well within the desired range.

9.7 Conclusion

In conclusion, the work presented here, lays out the foundations for the implementation of a new method for extracting the radiation from the Strathclyde class of gyro-devices. This quasi-optical mode converter can be demonstrated to have the required properties that would make it an attractive device for use to enable the decoupling of the electron beam and the electromagnetic wave in an energy recovery system. The beam width has been shown in ‘cold’ and ‘hot’ testing to match simulations and the beam width, directivity and the reflection are all within an acceptable range for the design of a depressed collector system incorporating the horn. The design methodology was successful and has been carried on into future designs of corrugated horns for gyro-amplifiers at Strathclyde. The former for prototype horn was constructed in-house at the University of Strathclyde with copper deposition carried out by Waveform (Thomas Keating Ltd) and tested using a vector network analyser and also in the ‘hot’ gyro-BWO experiment, where it met the design and simulation criteria and proved the concept was sound for use in high power and mm and sub-mm gyro-devices.

A.1 Major milestones in high power microwave 1885 to 1965

Summarised below are the milestones in the research and development of high frequency and power sub microwave devices from 1885 to 965, which are pertinent to this work.

- **1885-97:** Hertz demonstrates the first experimental evidence of the propagation of electromagnetic waves[115].
- **1893:** Hertz produces 30–60-cm signals using a spark gap generator[116].
- **1895**: Bose and Lebedew produce 5–6-mm signals using a spark gap[117].
- **1894-1896**: Marconi demonstrates wireless telegraphy, transmitting signals over a two-mile range[118].
- **1897:** Righi opened the field of microwave optics at 3 GHz and 10 GHz using small parabolic reflectors[119].
- **1919**: Barkhausen and Kurz develop a triode-type tube and generate 3cm signals[120].
- **1920**: The magnetron is invented by Hull and produces a low-power signal at 1cm[121].
- **1927**: Okabe invents a split-anode magnetron in Japan[122].
- **1935**: The principle of electron velocity modulation is published by Heil and Heil[123].
- **1937**: The klystron is invented by the Varian brothers[124].
- **1938**: The high-Q re-entrant cavity is developed by Hansen[125].
- **1939**: The cavity magnetron is invented by Boot and Randall, which operated at 10-cm. This was possibly one of the most important developments in high power microwaves and was a major factor in the supremacy of the Allied radar during World War II[126].
- **1945**: The wartime development of the TWT revealed by Kompfner[127].
- **1947**: The theoretical basis of TWT operation published by Pierce[128].
- **1950**: Warnecke, Kleen, Lerbs, Doehler, and Huber develop a crossed field amplifier[129].

- **1953**: The backward wave oscillator (BWO) is developed by Kompfner and Williams[130].
- **1955**: The O-type BWO is demonstrated by Warnecke, Guenard, Doehler, and Epsztein[131].
- **1958**: The first theoretical basis for the operation of a gyrotron is laid out by Twiss in Australia[132].
- **1959** Gaponov[133] (CCCP) and Schneider[134] (US) develop the same concept of the electron cyclotron maser (ECM) or gyrotron.
- **1965** ECM theory was followed up by experimentalists such as Bott[135] who used low voltage (~20kV) low current (~1mA) electron beams with total power in the 10Ws

A.2 Reflex Klystrons IOTs Triodes and Magnetrons

The Barkhausen–Kurz Tube

Perhaps the earliest attempt to produce a device that exploits this type of electron velocity modulation is the Barkhausen–Kurz tube, or reflex triode.

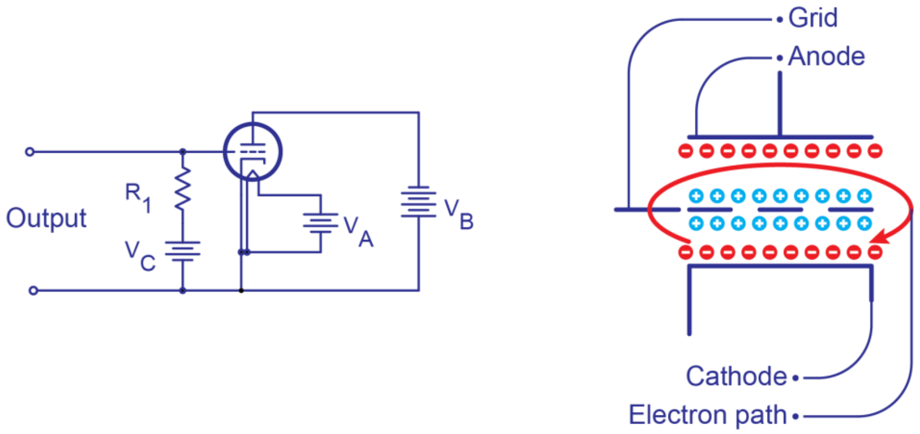

Figure A.2.1: Barkhausen–Kurz tube circuit.

Early investigations into the production of higher frequencies using triode devices of the time were unsuccessful due to the limits on electron transit time between the internal components. Even with the smallest possible structures, which could be manufactured at the time devices were limited to megahertz operation, but the possibility of increasing this limit came with the idea that a velocity modulated electron beam could overcome the problem. It was in Germany in 1920 that Heinrich Barkhausen and Karl Kurz[136] developed a new type of triode that used a velocity modulated electron beam to extend the range of vacuum tube sources into the UHF band.

The operational principle of the Barkhausen–Kurz tube is similar to that of a conventional triode, but both the anode and cathode are held at a negative potential relative to a positive grid. The electrons are expelled from the cathode and accelerated through this grid, where they see a repulsive force from the negative anode and are therefore accelerated back towards the grid. This electron motion sets up an oscillation of an electron bunch between the cathode and anode and a subsequent generation of an output signal with a frequency that is determined by the period of the cycle.

Magnetron

The magnetron is a ubiquitous and possibly the most important microwave device ever produced. It was invented by Albert Hull in 1920[137] in the General Electric research labs in the United States, but this initial design was a simple device that was incapable of high frequency operation. It was not until the invention of the cavity magnetron by Boot and Randall during World War II that the true importance of this device was to be realised.

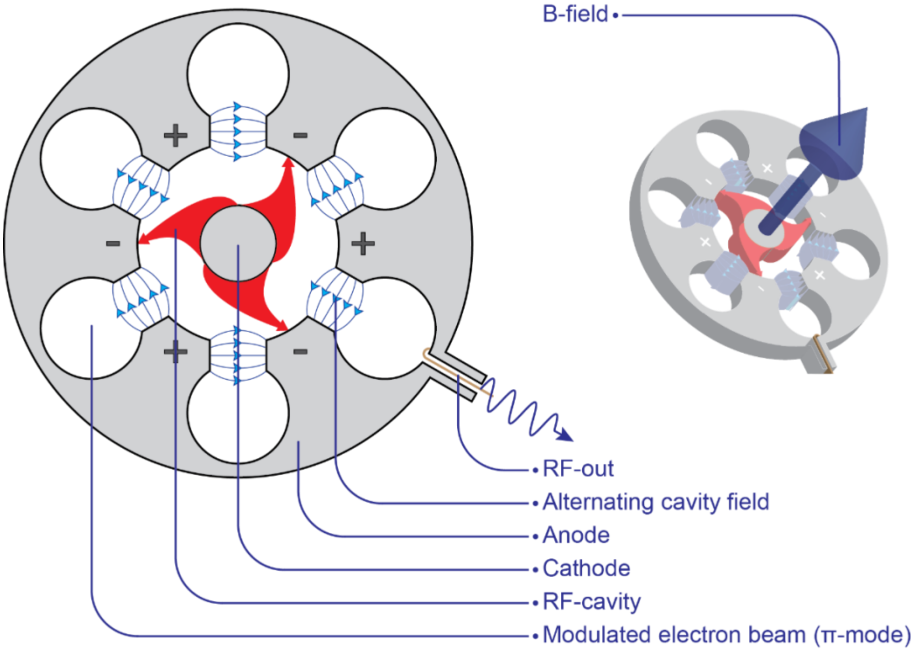

Figure A.2.2: Typical magnetron design schematic.

The basic premise for magnetron operation (Figure A.2.2) is that of a central cylindrical cathode enclosed by a hollow anode. When emitted electrons are released from the cathode, they will tend to stream radially outwards towards the anode. If there is a constant and homogeneous magnetic field in place, perpendicular to the elections path then there will be a force on the electrons ($e \times \boldsymbol{B}$) proportional to the magnitude of the field that will tend to bend the electron trajectory back towards the cathode. If the anode is then formed in such a way as to form a resonant periodic structure then the system can be tuned in such a way that a rotating electron cloud passes from cathode to anode while exiting currents on and around the resonant features. This field is subsequently responsible for generating an RF oscillation within the structure with a frequency determined by the geometrical and electrical parameters. This modus of operation clearly defines the magnetron in the category of crossed-field, or m-type tubes. There are several variants of cavity magnetron design, utilising a variety of cavity types and operational modes including the rising sun-type, vane-type, slot type, hole and slot-type as shown in Figure A.2.3.

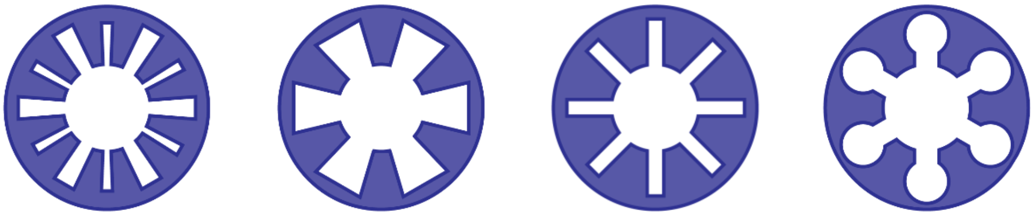

(a) rising sun-type *(b) vane-type* *(c) slot type* *(d) hole and slot-type*

Figure A.2.3: Magnetron variants.

Extraction of RF power may be achieved by introducing a coupling loop or waveguide into one of the resonant cavities. The magnetron will surely have an enduring legacy, not least as one of the key enabling technologies for radar, but also in the humbler guise of the microwave oven in the home.

Crossed-field amplifier

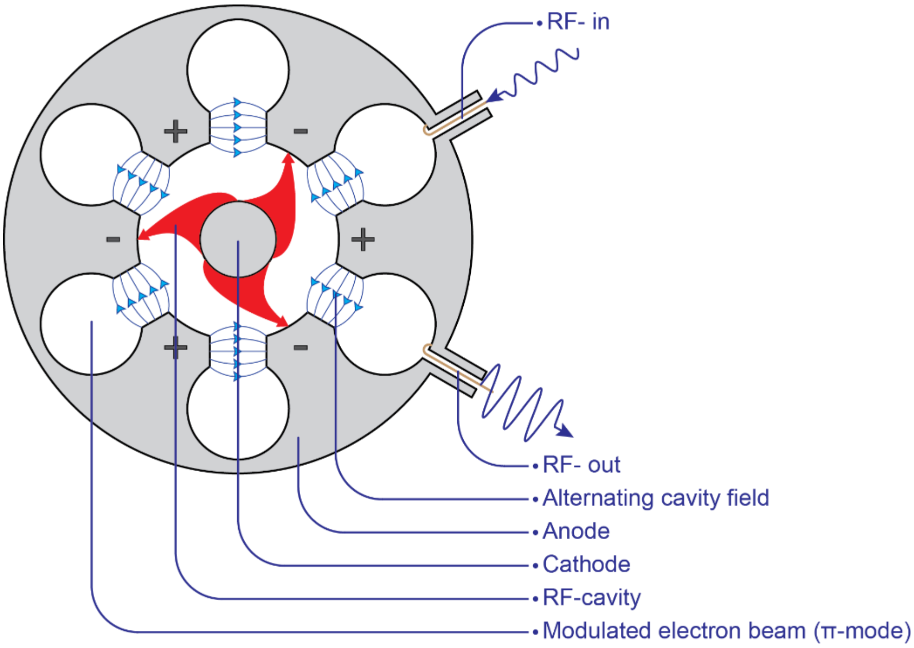

Figure A.2.4: Crossed field amplifier schematic

The crossed field amplifier was first developed in the mid-1950's, as a development on the magnetron for use in very-high-power transmitters. Raytheon engineer William C. Brown developed the technology while looking for a new broadband microwave amplifier. These devices are capable of powers in the megawatt range and high operational efficiencies (~70%). They are however limited in their gain and bandwidth when compared with other high power slow wave tubes (klystrons and TWT's).

Inductive output tube

The inductive output tube (IOT) or Klystrode is somewhat similar to both the klystron and triode. Invented in 1938 by Andrew V. Haeff at RCA[138] the IOT was one of the first power sources used for television broadcast, but later developments, especially the klystron, left the IOT as a footnote in the history of microwave devices. The re-development of this technology was spurred by new technical challenges in the television industry, where the IOT has proved to provide the ideal broadband source for high definition digital broadcasts. Modern IOT's have benefited from the advancement in both materials and design technologies (computer modelling) and are therefore capable of much higher output powers that was achievable in the 1940's. They are however still fundamentally limited by the inclusion of the triode-like control grid in front of the cathode, which prevents true high frequency operation.

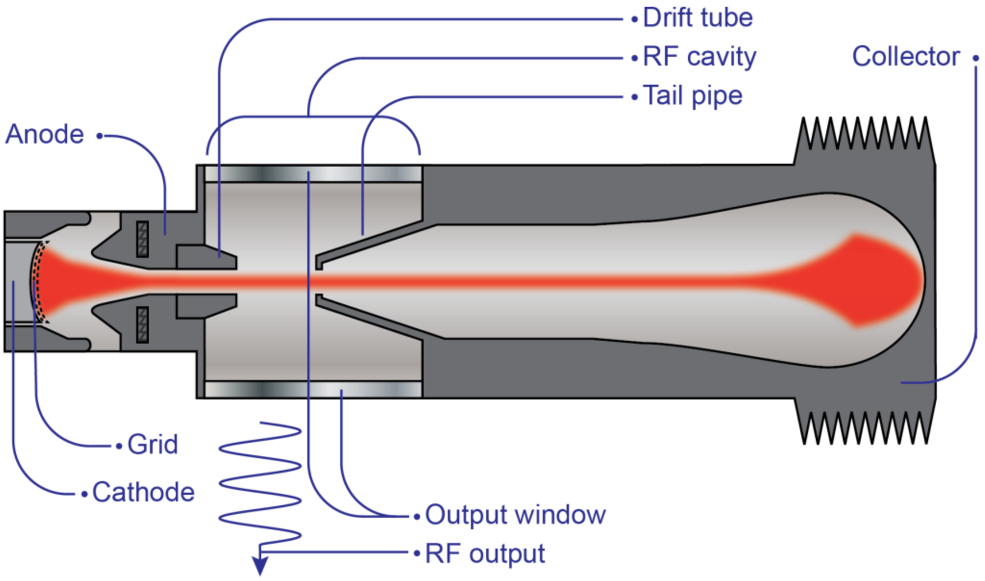

Figure A.2.5: A schematic of an IOT (note inclusion of control grid).

In principle, the operation of an IOT is similar to the triode, where electrons accelerated from a cathode by a control grid are focussed into a modulated beam. This beam passes into a drift tube, preventing back-streaming and into a resonant cavity where the cavity modes are excited. The generated signal can then be extracted from the cavity by a coupler and the beam dumped into a collector system.

A.3 Free Electron Laser

The most common devices, which produce radiation from electrons oscillating in periodic external fields are free-electron lasers (FELs). These devices are different from the other high-power microwave sources that have been discussed, in that FEL's can generate output over a very large range of frequencies, which extend far beyond the microwave region of the electromagnetic spectrum and well into the visible and ultraviolet range.

The term free electron laser or FEL is generally used to describe devices that generate coherent radiation (light) by means of a fast-wave interaction in which a beam of relativistic free electrons is induced to radiate coherently by passage through a periodic wiggler field. Perhaps another name by R. M. Phillips is more descriptive: UBIRTON (Undulated Beam Interaction electron)[139] there is another type of wiggler using an electrostatic instead of magnetostatic fields to provide electron undulation, which is called the scattron. In 1971, Madey initiated an important step by proposing that an undulator structure working as an amplifier at optical wavelengths could replace the active medium between the mirrors of a laser optical cavity, he called such a device a free-electron laser[140]. While some researchers seek to extend the operation of modern descendants of the undulator called free-electron lasers to lower and lower wavelengths, other modern descendants of the ubitron (which are also called free electron lasers) can produce higher and higher microwave power outputs from mildly relativistic electron beams.

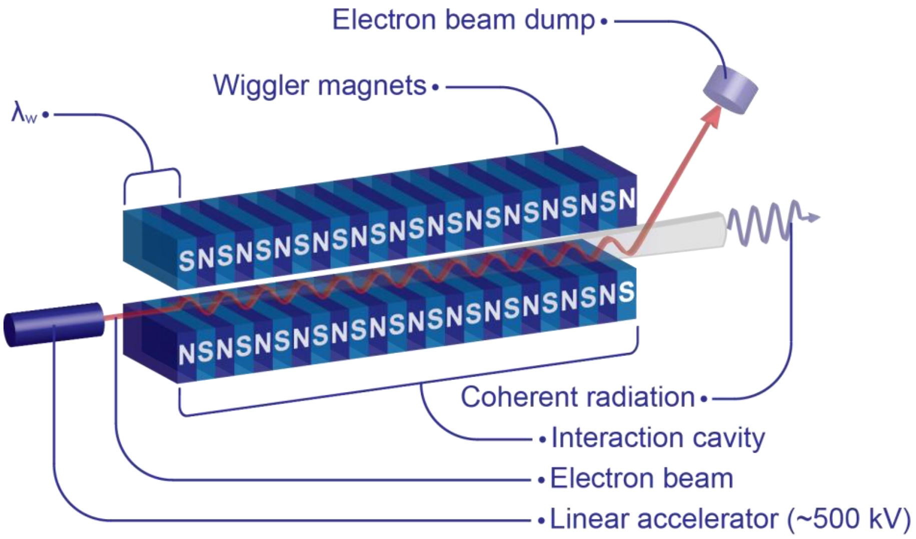

Figure A.3.1: Schematic of a basic FEL configuration.

As the electrons vibrating by the spatially periodic wiggler field they will radiate, if the electron beam is highly relativistic then the radiation will have a much shorter wavelength than in the laboratory frame. Therefore, FEMs are capable of generating electromagnetic waves of very short wavelength determined by the relativistic Doppler Effect. The bunching of the electrons in the FEM is due to the perturbation of the beam electrons by the ponderomotive potential well which is caused by beating of the electromagnetic wave with the spatially periodic wiggler field. It is this bunching that enforces the coherence of the emitted radiation. As the radiation wavelength is not determined by the characteristic size of the interaction region, such fast-wave devices require no periodically rippled walls or dielectric loading and can instead use a simple hollow-pipe oversized waveguide as the circuit. These devices are capable of producing very high power radiation at cm, mm, and submillimetre wavelengths since the use of a large waveguide or cavity cross sections reduces wall losses and breakdown restrictions, as well as permitting the passage of larger size, higher power electron beams. It also relaxes the constraint that the electron beam in a single cavity can only remain in a favourable RF phase for half of a RF period (as in klystrons and other devices employing transition radiation).

Free electron lasers appear to be potentially capable of fulfilling all the requirements for a frequency tunable high-power mm-wave source. It has achieved more than 1 MW output power in the entire frequency range of 130-260 GHz, and even higher frequencies are quite feasible. A disadvantage of FELs is that they often require high energy ~(500keV and above) electron beams for optimum operation which results in a large size electrode beam source to ensure adequate voltage hold off as well as the generation of high energy X-rays which needs to be adequately shielded.

A.4 Mode converter Variants

Waveguide-launcher

Waveguide-launcher – Type 1

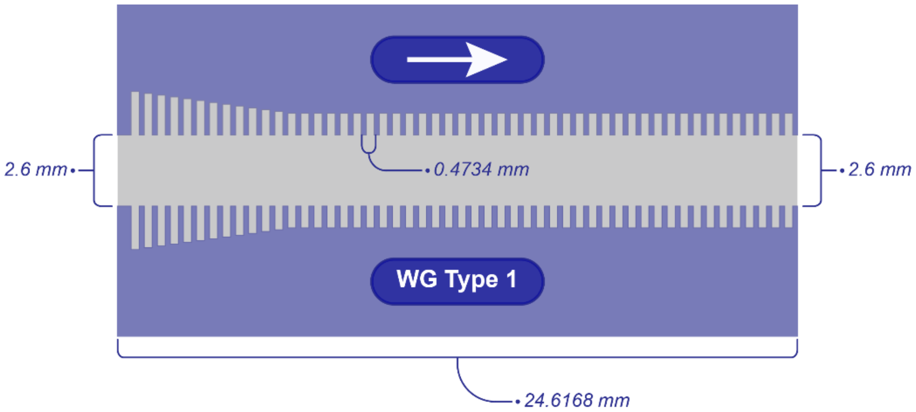

Figure A.4.1: Waveguide with a mode converting input (outer corrugations tapered)

The first design to be simulated using the mode matching method was a simple corrugated waveguide (Figure A.4.1) with an impedance matching section wherein the depth of the corrugations are tapered from $\lambda_c/2$ at the input to $\lambda_c/4$ at the output of the mode converter while keeping the inner radius constant, before a section of constant corrugation depths at $\lambda_c/4$. Here λ_c is the wavelength at the centre of the operational bandwidth. For the purpose of these simulations a value for λ_c was chosen to be 3.156 mm, which is the centre wavelength of the frequency range at 95 GHz. The input diameter of these simulations is 2.6 mm. This is the radius of the current smooth waveguide in the gyro-BWO experiment. The gap and vane thickness were set at 3.156 mm $(0.1\ \lambda)$ and 1.578 mm $(Gap/2)$ and remain the same for all the preliminary simulations.

This design was rapidly discounted as a viable design and disqualified from any future analysis due to the extremely wide radiation pattern that was produced in the far field as is seen in Figure A.4.2.

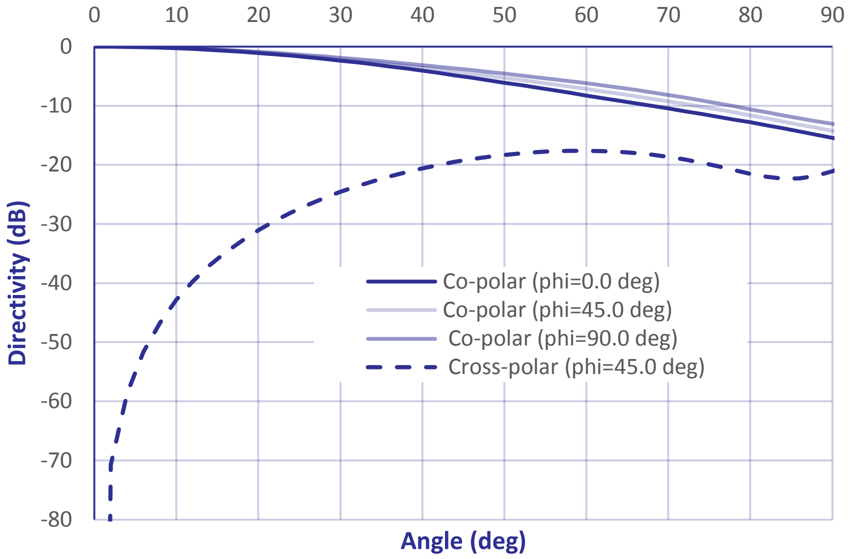

Figure A.4.2: WG Type 1 far field

Figure A.4.3 shows that this type of launcher has problems with meeting the reflection targets and Figure A.4.4 demonstrates that the transmission profile of this design is also unacceptable for our design bandwidth. However, this was an initial un-optimized design, so with careful adjustment of the gap and vane parameters a better performing design may be achievable.

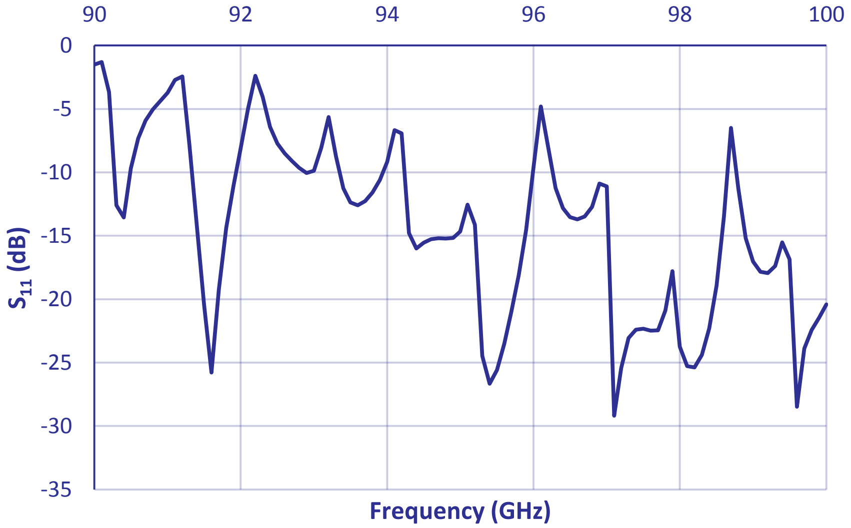

Figure A.4.3: WG Type 1 S_{11} performance over 90-100 GHz bandwidth

The transmission and reflection profile of this type of launcher also demonstrates that such a corrugated structure, with an inner radius smaller than the cut off diameter of the TM_{11} mode at 90 GHz (~4.06 mm) presents a structure that performs very much like a Bragg reflector.

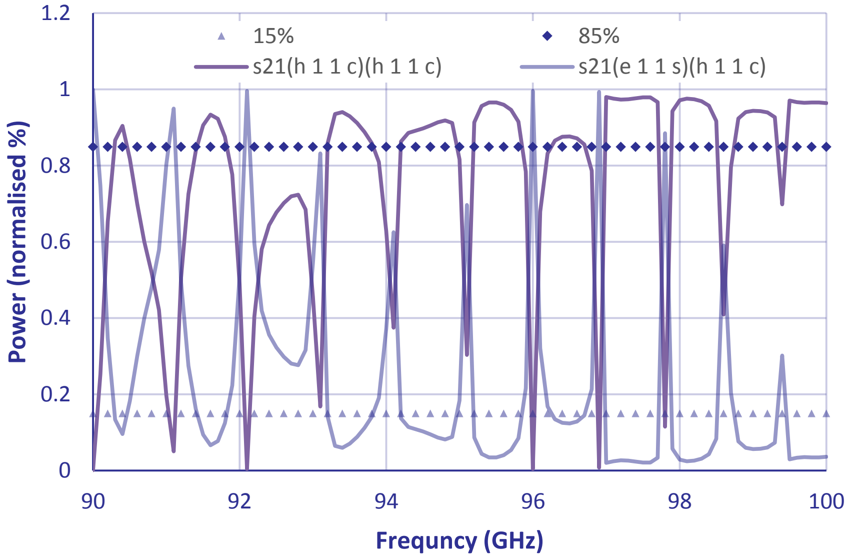

Figure 4.4: WG Type 1 S_{21} performance over 90-100 GHz bandwidth (TM_{21} is $e_{11}s$ and $TE_{21}$is h_{11}).

Waveguide-launcher – Type 2

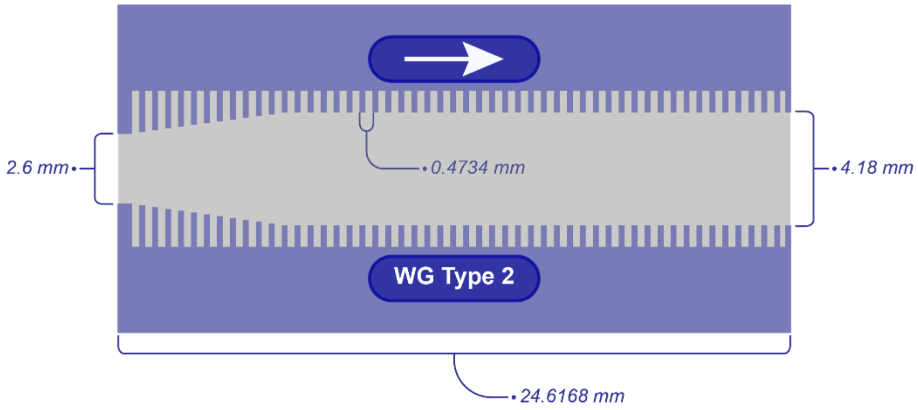

Figure A.4.5: Waveguide with a mode converting input (inner corrugations tapered)

A second possibility for a corrugated waveguide launcher is seen in Figure A.4.5. Here the inner waveguide corrugations are tapered from $\lambda_c/2$ at the input to $\lambda_c/4$ at the output of the mode converter while keeping the outer radius constant.

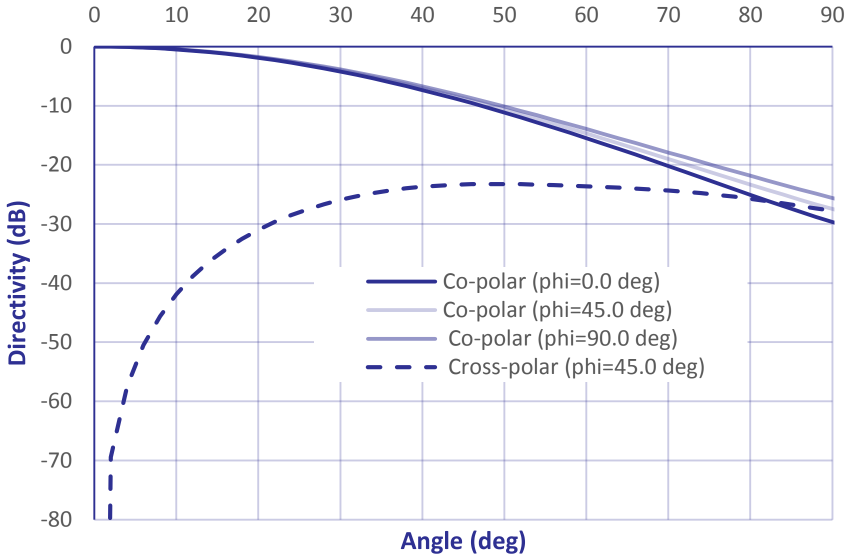

Figure A.4.6: WG Type 2 far field

Figure A.4.6 shows that the increase in the aperture from 2.6 mm to 4.18 mm has reduced the angular spread of the main far-field beam-lobe, although this reduction is still not suitable for our design.

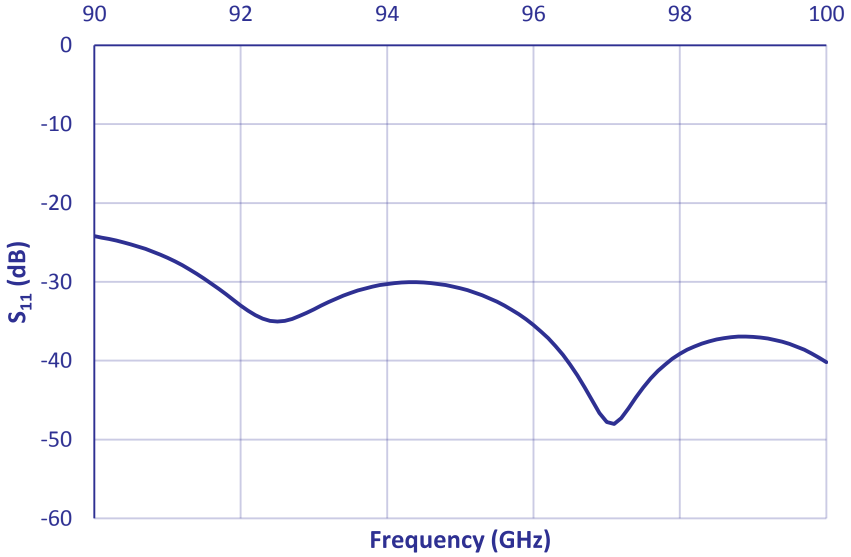

Figure A.4.7: WG Type 2 S_{11} performance over 90-100 GHz bandwidth

Increasing the aperture and tapering up to a larger inner diameter of 4.18 mm had an effect on both the transmission and reflection, as can be seen in Figure A.4.7 and Figure A.4.8. The reflection is closer to the desired value of -35 dB over the bandwidth and the transmission becomes much closer to the 85/15% ratio of interest.

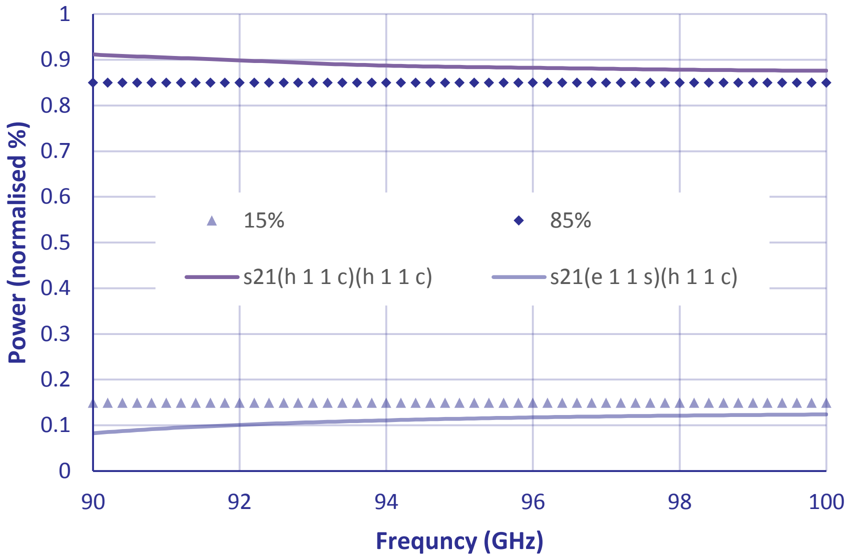

Figure A.4.8: WG Type 2 S_{21} performance over 90-100 GHz bandwidth

Waveguide-launcher – Type 3

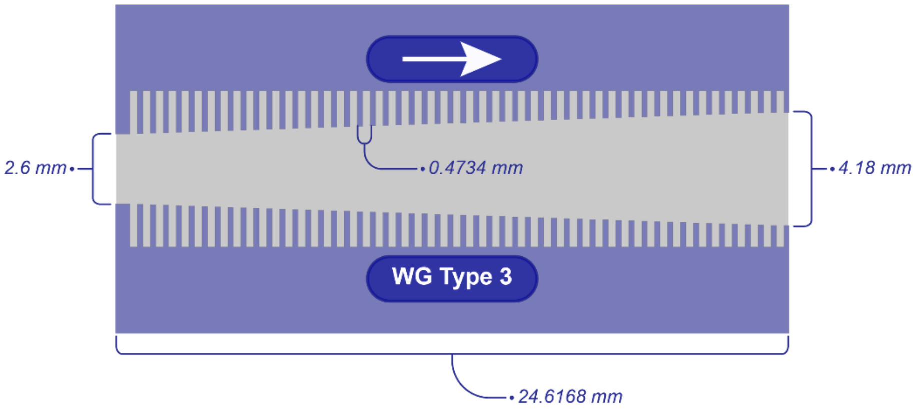

Figure A.4.9: Waveguide with a constant linear tapered mode converter.

A third possibility for a corrugated waveguide launcher where the depth of the corrugations are tapered from $\lambda_c/2$ at the input to $\lambda_c/4$ at the output of the launcher. This profile can be seen clearly in Figure A.4.9.

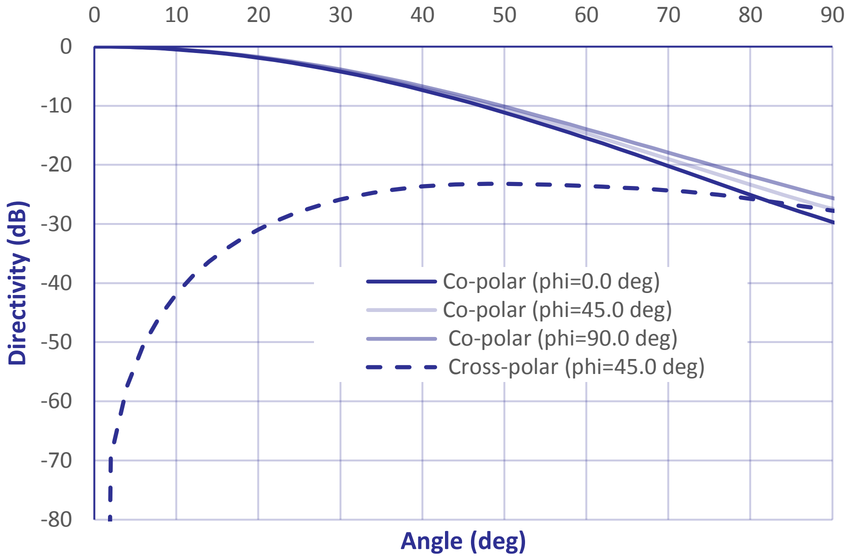

Figure A.4.10: WG Type 3 far field

The output in this design retains the larger diameter from the second design and the far-field has a very similar performance (Figure A.4.10).

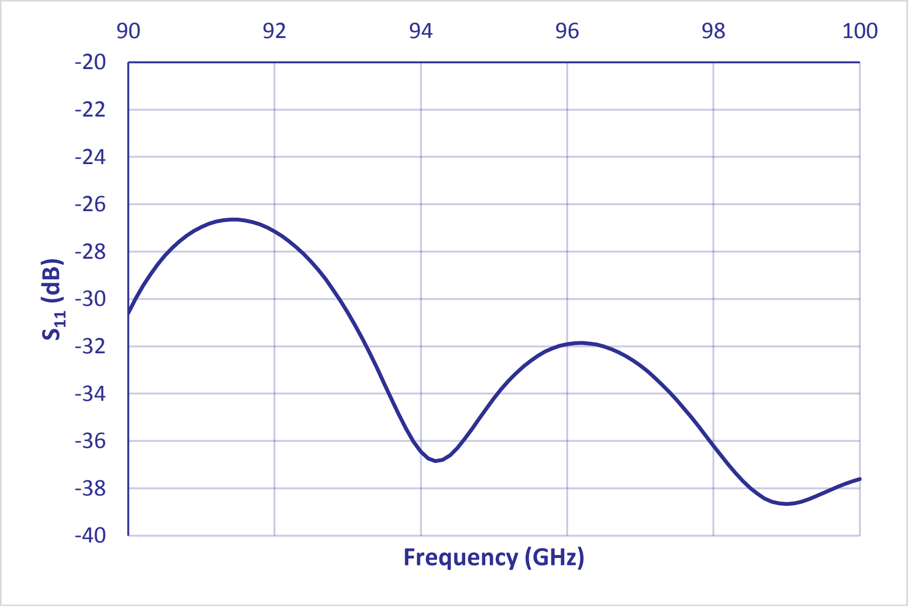

Figure A.4.11: WG Type 3 S_{11} performance over 90-100 GHz bandwidth

The transmission and reflection are also very similar to the second design type, the S_{11} is slightly different (Figure A.4.11). This difference in the reflection between type 2 and 3 is not great and the overall trend seems to suggest that this profile may also be suitable.

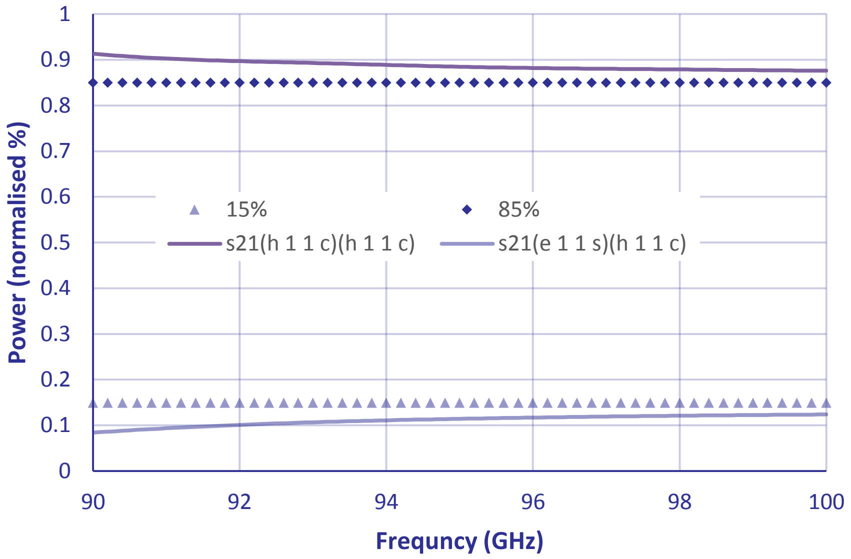

Figure A.4.12: WG Type 3 S_{21} performance over 90-100 GHz bandwidth

It is also clear that the S_{21} has no discernible change between types 2 and 3 (Figure A.4.15).

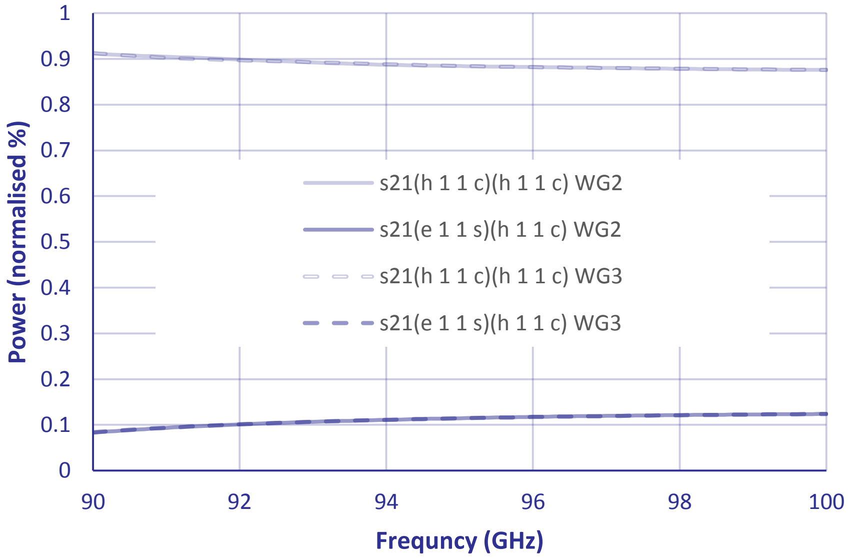

Figure A.4.13: Comparison between WG Type 2 and 3 showing S_{21} performance over 90-100 GHz bandwidth

Figure A.4.13 shows how closely the transmission performance of the waveguide Type 2 and 3 are matched.

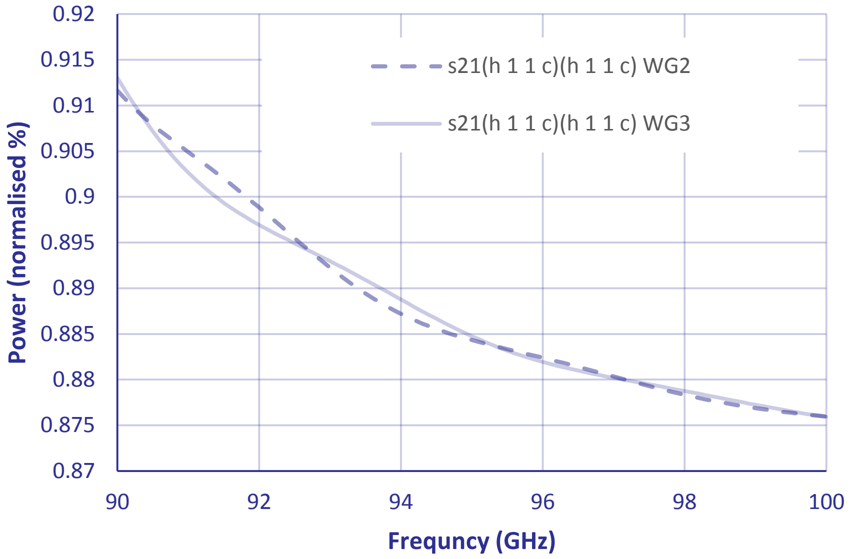

Figure A.4.14: Detail from Figure A.4.13

A more detailed view (Figure A.4.14) shows that there are some slight differences in the S_{21} for the TE_{11} modes, but these differences are very small and if the far-field patterns of the two types are superimposed (Figure A.4.15) it is clear that the performance in both cases is nearly identical.

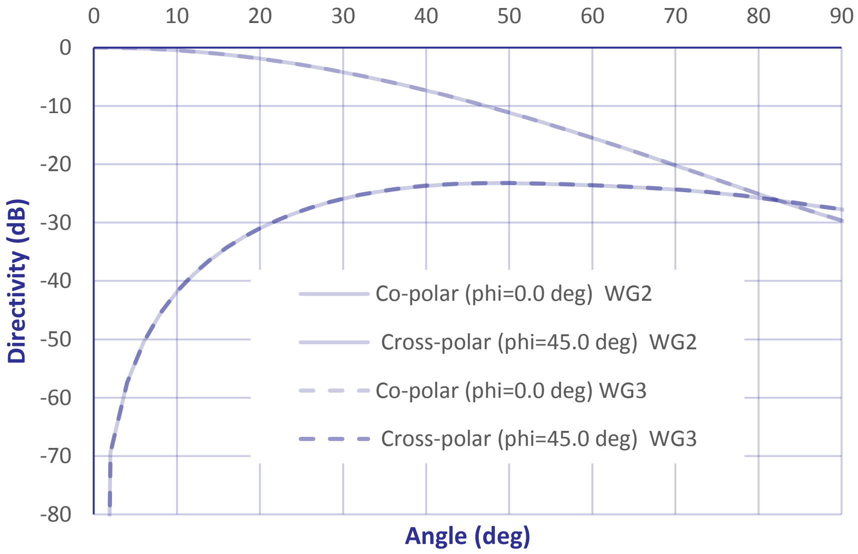

Figure A.4.15: Comparison between WG Type 2 and WG Type 3 far fields.

These initial simulations remove the possibility of using this waveguide type of launcher due to the angular spread of the radiated fields. Our design calls for a radiation beam that can be transmitted through a collector system and vacuum window, therefore a better design with a smaller central lobe in the far-field was sought.

The next stage in the design process called for the testing of a number of alternative profiles. Because the variation in parameters was greatly increased over which a design could be formulated a baseline was determined for several of the profiles, as far as was practicable for the process. Each design was kept as similar as possible: The input and output diameters were kept constant, as were the corrugation depths and the number of corrugations. The impedance matching was achieved in each case by allowing a linear taper of the corrugation depth at the input to the output.

Linear horn

To decrease the main beam lobe in the far-field the simplest approach is to linearly flare the profile of the waveguide and thereby increase the aperture dimension by tapering up in a horn. In this case a linear profile was derived from the desired input and output radii (equation A4.1)

$$r(z) = r_{in} + (r_{out} - r_{in})\left(\frac{Z}{L}\right) \tag{A4.1}$$

Linear Horn – Type 1

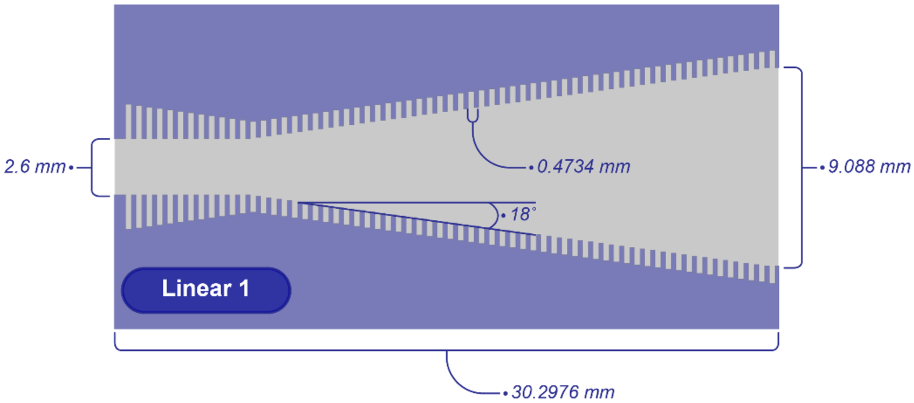

Figure A.4.16: Linear profiled horn – Type 1

The first linear horn incorporated the same mode converter as the first waveguide type, where the depth of the corrugations are again tapered from $\lambda_c/2$ at the input to $\lambda_c/4$ at the output of the mode converter while keeping the inner radius constant. The period and corrugations are kept the same as well as the input. The output is increased to 9.088 mm ($2.88\,\lambda$). The profile for this simulation is shown in Figure A.4.16

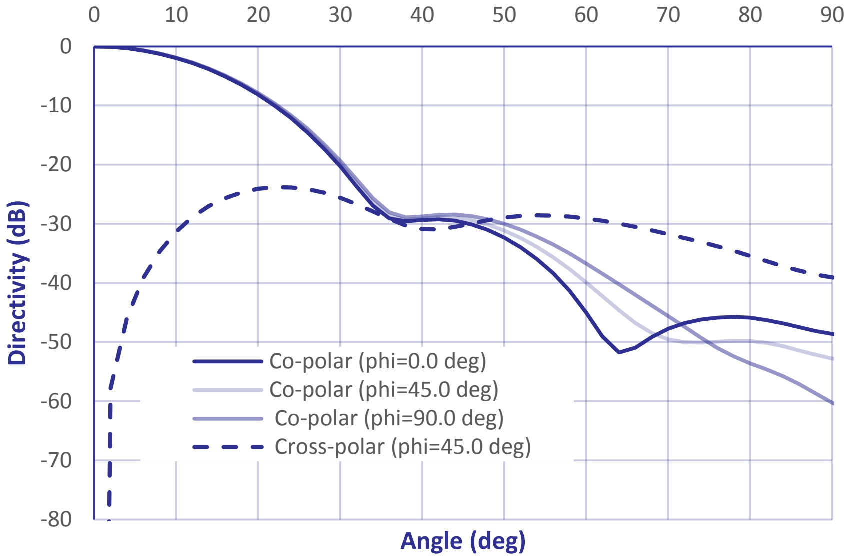

Figure A.4.17: Linear profiled horn – Type 1 far field

The far-field performance of the first linear profile can be seen in Figure A.4.17. The main lobe has been reduced from a value of -20 dB at 70 degrees in the waveguide type to -20 dB at 30 degrees with an increase of diameter of ~100%.

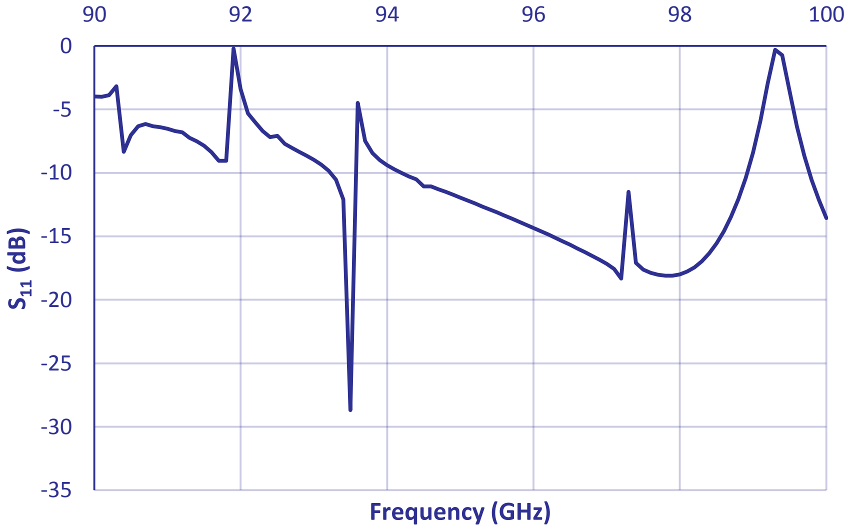

Figure A.4.18: Linear profiled horn – Type 1 S11

The S_{11} performance of this design is not acceptable (Figure A.4.18), with only a single point at 93.5 GHz even coming close to the design goal reaching only -28.7 dB. The transmission performance is also well outside the desired gaols. Figure A.4.23 shows that this type of design is at best only able to perform over a very narrow frequency band around 98 GHz.

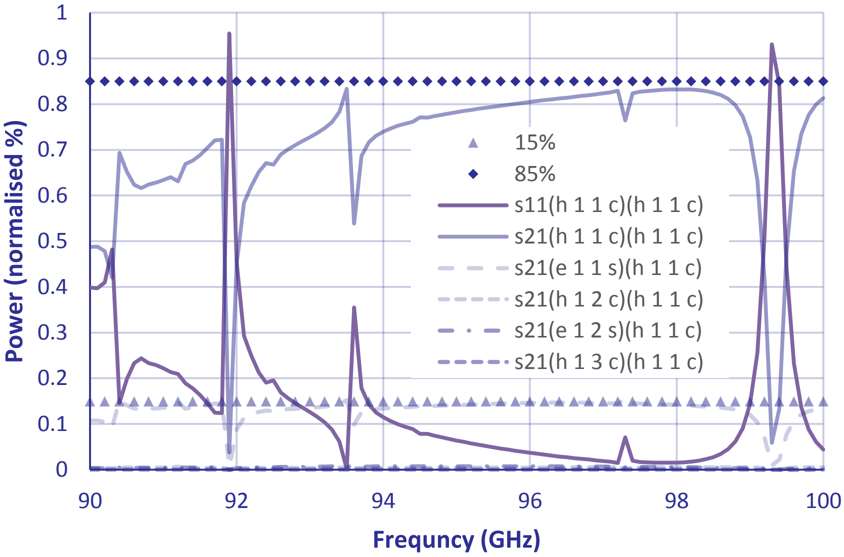

Figure A.4.19: Linear profiled horn – Type 1 S_{21}

This type of mode converter seems unsuited to the design at the diameter of our design and so is rejected from further analysis.

Linear Horn – Type 2

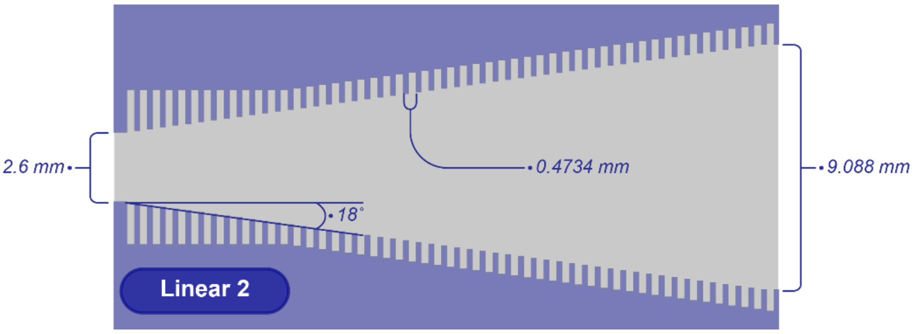

Figure A.4.20: Linear profiled horn – Type 2

The second type of linear horn under consideration uses the same mode converter profile as the waveguide type-2. The inner diameter of the horn is increased from the input to the output and the mode converter region only alters the outside waveguide diameters on the first 12 corrugations, with the remainder kept at a constant $\lambda_c/4$ until the output aperture, which is once again 9.088 mm.

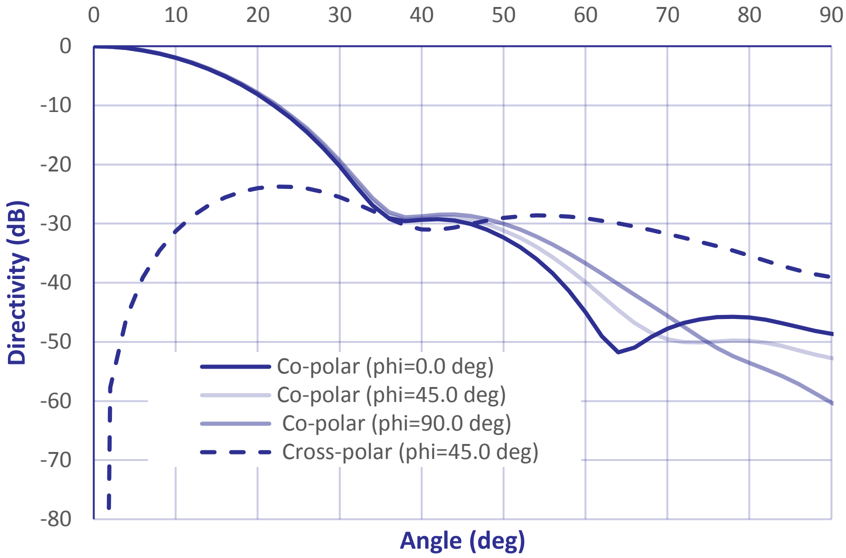

Figure A.4.21: Linear profiled horn – Type 2 far field

Figure A.4.21 demonstrates that the far-field performance of the second type of linear horn is similar to that of the previous design.

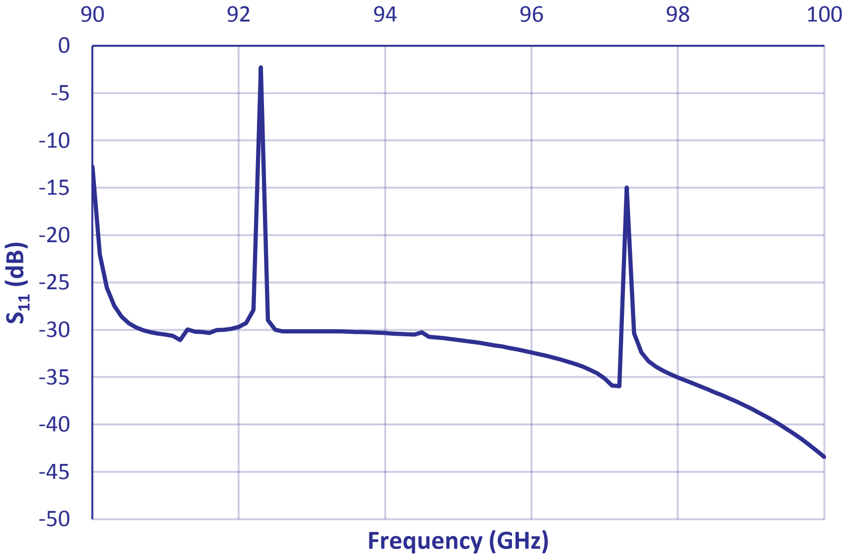

Figure A.4.22: Linear profiled horn – Type 2 S_{11}

The S_{11} and S_{21} of the second type are clearly different as seen in Figure A.4.22 and Figure A.4.23. While the performance in both reflection and transmission are far superior to the previous design there are a couple of regions where this design does not perform at all. This could be addressed by optimisation, but that is not part of this design iteration.

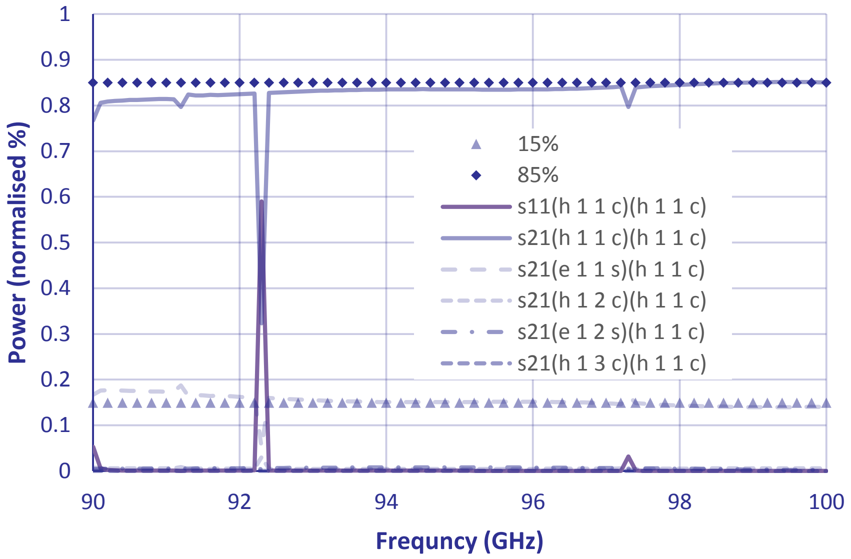

Figure A.4.23: Linear profiled horn – Type 2 S_{21}

Linear Horn – Type 3

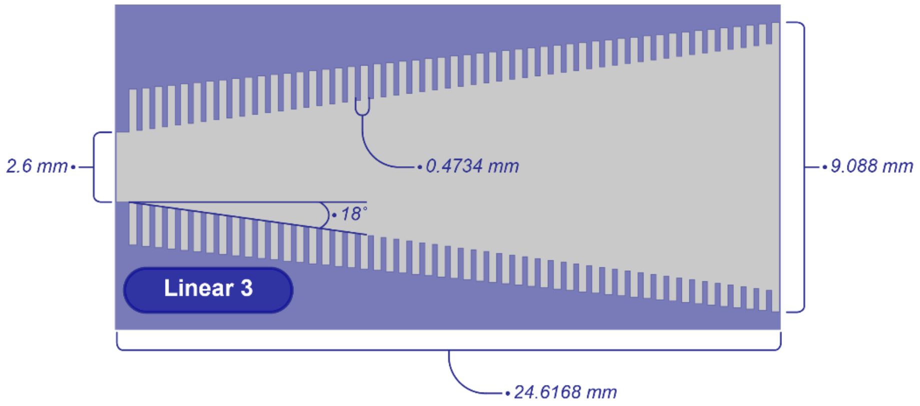

Figure A.4.24: Linear profiled horn – Type 3

The third type of linear horn was designed to have impedance matching achieved by a gradual (linear) change in the corrugation depth from $\lambda/2$ to $\lambda/4$ over the length of the horn. Once again the other design parameters remain the same.

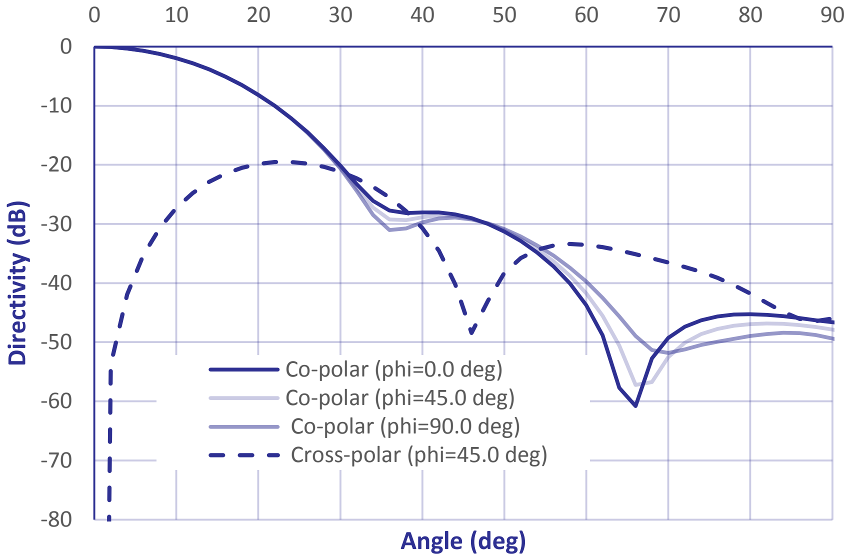

Figure A.4.25: Linear profiled horn – Type 3 far field pattern

The far-field performance of the third type of linear profiled horn is shown in Figure A.4.25. There is a slight difference between the cross-polar plots of this and type 1 and 2, the former being ~3db lower, but the main lobes of the co-polar pattern in the latter case exhibits a better overall angular symmetry to 30 degrees.

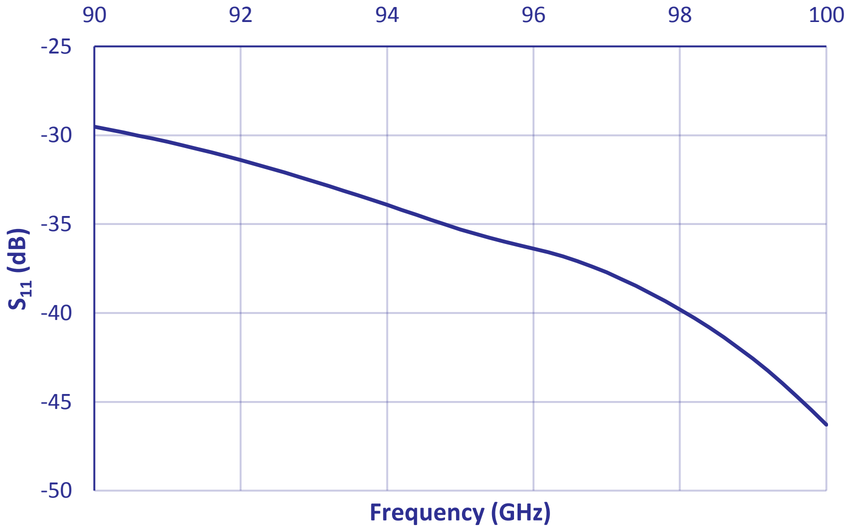

Figure A.4.26: Linear profiled horn – Type 3 S_{11}

This third design also shows at least half the bandwidth is within the target for reflection. Figure A.4.26 shows that the S_{11} for 95 to 100 GHz is well under -35 dB.

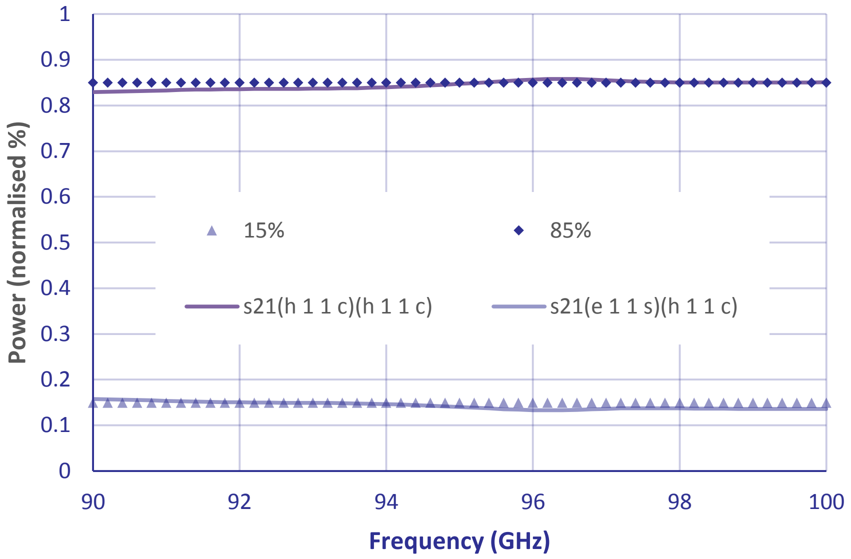

Figure A.4.27: Linear profiled horn – Type 3 S_{21}

Figure A.4.27 clearly indicates that the third linear profile has achieved a superior transmission profile than the previous two, with the TE_{11} and TM_{11} modes both very close to the 85% and 15% transmitted power mixture that is desired.

Gaussian Horn

Another type of profile that has promising characteristics is the Gaussian profiled mode converting horn. Recent results from the University of Navarra in Spain**[141]** have shown that this profile can achieve promising results over a shorter, more compact length. This shorter design would prove ideal in a situation where there is an electron beam expanding as it travels along the horn. The following simulation results are from a profile derived from a modified Gaussian function (equation A4.2).

$$\begin{gathered}\omega(z) = \omega_0 \sqrt{1 + \left(\frac{\lambda z}{\pi \omega_0^2}\right)^2} \\ r(z) = \omega(z)\ if\ z \leq \frac{L}{2} \\ or\ r(z) = -\omega(L - z) + 2\omega\left(\frac{L}{2}\right)\ if\ z \geq \frac{L}{2}\end{gathered} \qquad \text{A4.2}$$

Gaussian Horn – Type 1

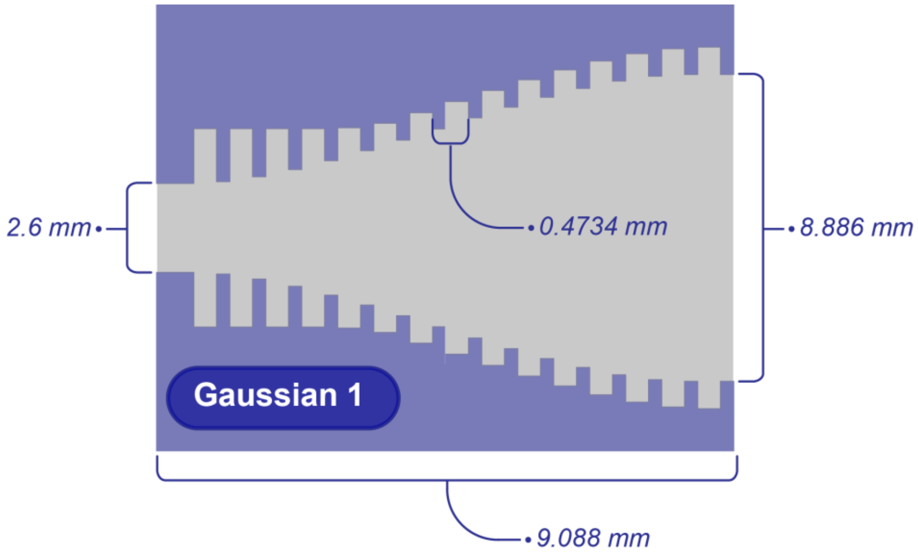

Figure A.4.28: Gaussian profiled horn – Type 1

Two types of Gaussian profiles where investigated. In the first case the initial waveguide diameter was once again set 2.6 mm and the other parameters, except the output and length, were kept the same as before. The first type of Gaussian profile retained the mode converting section where the outer radius was kept constant, but the inner radius was allowed to follow the Gaussian profile, changing from $\lambda_c/2$ at the input to $\lambda_c/4$ over 5 periods. The profile for this type of Gaussian horn required a shorter length with less periods. The output diameter was also changed very slightly from 9.088 mm to 8.886 mm to accommodate this new profile.

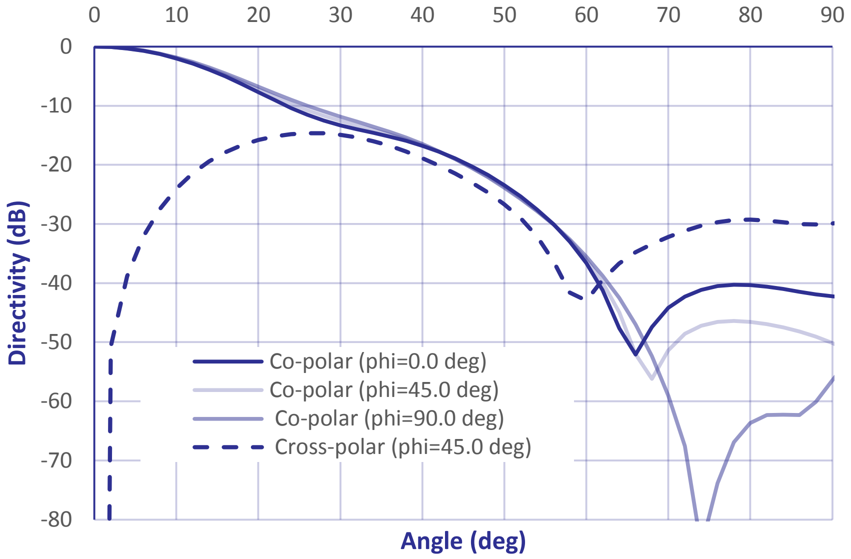

Figure A.4.29: Gaussian profiled horn – Type 1 far field pattern

The far-field performance of this first Gaussian profile is shown in Figure A.4.29. This pattern does not retain the narrow central lobe as was seen in the linear horns even though the aperture diameter is almost identical. The -20 dB level is now at ~45 degrees rather than 30 degrees as before.

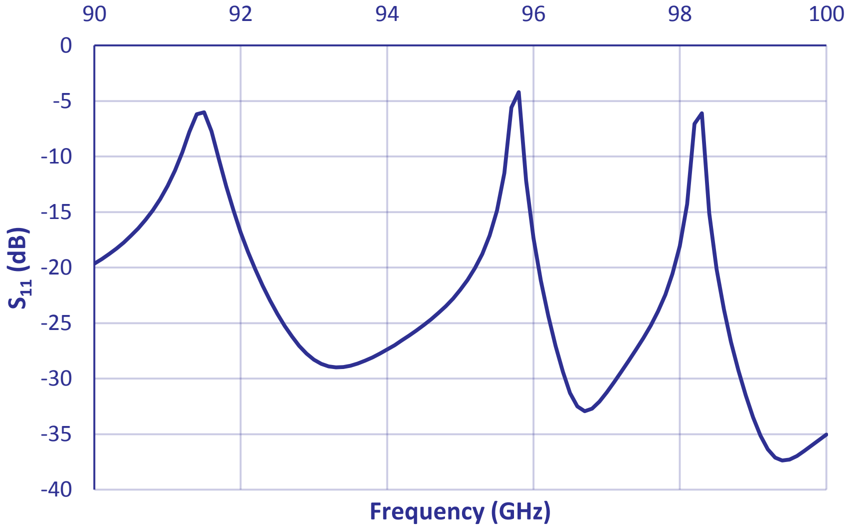

Figure A.4.30: Gaussian profiled horn – Type 1 S_{11}

Figure A.4.30 demonstrates that the first type of Gaussian profiled design the S_{11} for 95 to 100 GHz is not suited for our needs with a number of regions where the reflection would be too high. This may be a result of the shorter length of this profile and an imperfect impedance matching between the input waveguide and the launcher. This is also clear from Figure A.4.31, which shows that the target ratio of TE_{11}/TM_{11} has not been achieved.

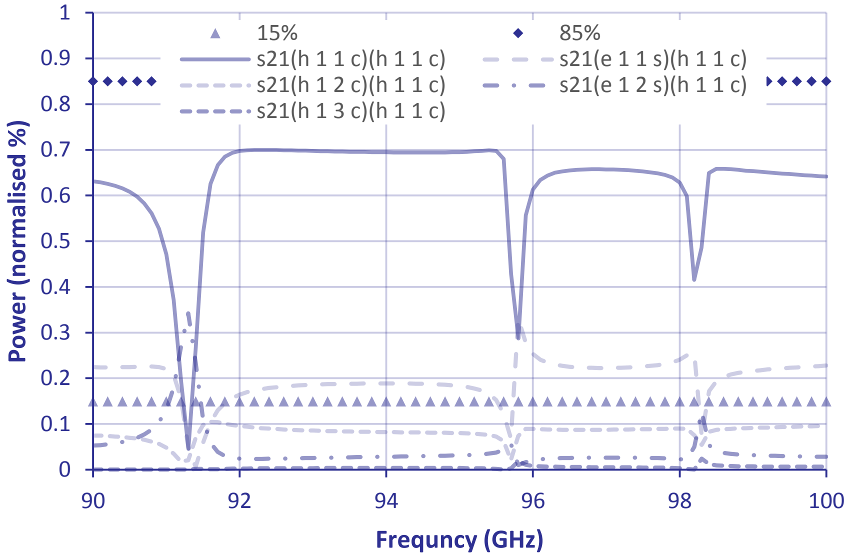

Figure A.4.31: Gaussian profiled horn – Type 1 S_{21}

Gaussian Horn – Type 2

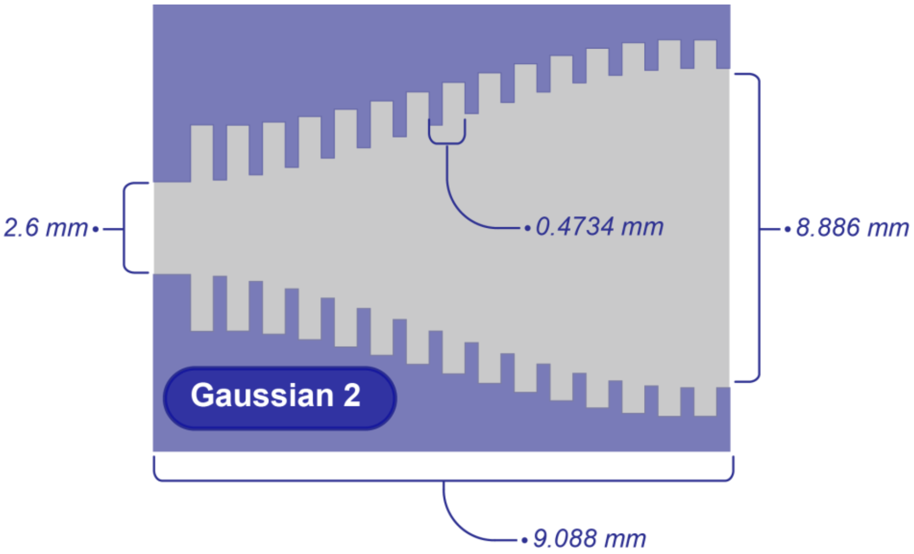

Figure A.4.32: Gaussian profiled horn – Type 2

The second Gaussian profile to be simulated used the profile where the corrugation depths were changed from $\lambda_c/2$ at the input to $\lambda_c/4$ over the length of the horn. All other parameters remained the same as the first Gaussian profile.

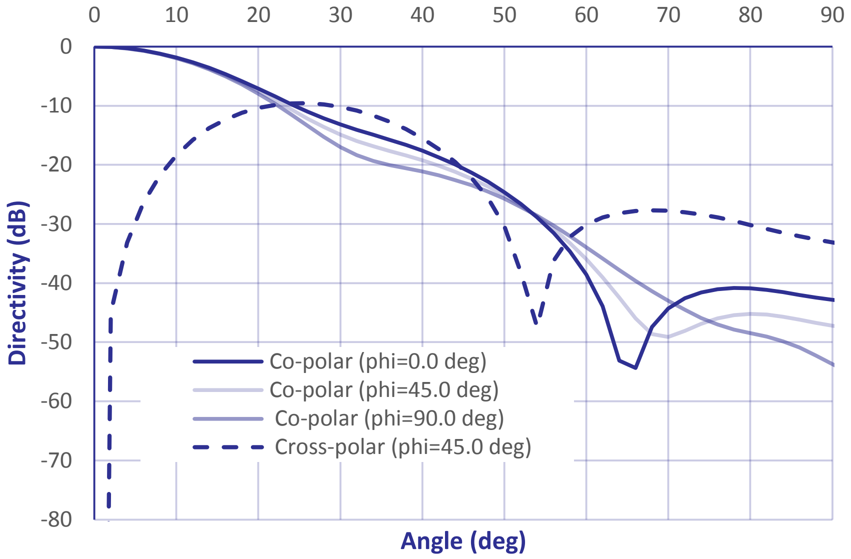

Figure A.4.33: Gaussian profiled horn – Type 2 far field pattern

In this case, the far-field performance (Figure A.4.33) of the second Gaussian profile remains close to that of the first with the one notable exception in that the cross-polar pattern maximum has increased from -15 dB to -10 dB.

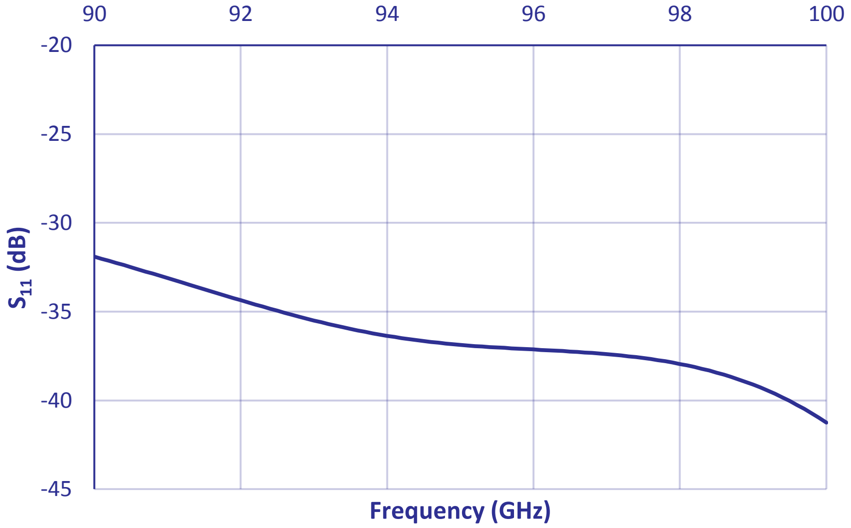

Figure A.4.34: Gaussian profiled horn – Type 2 S_{11}

There is a marked difference in the reflected (Figure A.4.34) and transmitted (Figure A.4.35) power in this case, with almost 80% of the bandwidth falling below the -35 dB reflection target. The TE_{11}/TM_{11} ratio has however not been met the design criteria.

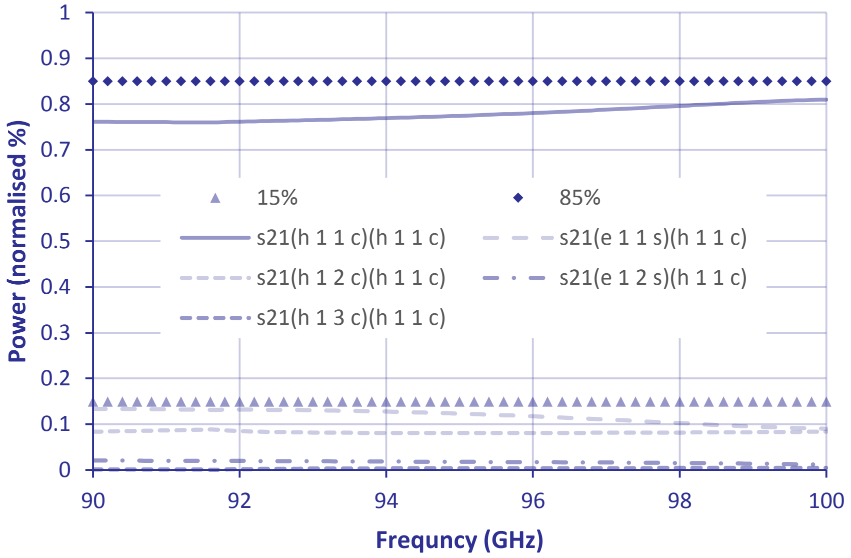

Figure A.4.35: Gaussian profiled horn – Type 2 S_{21}

A.5 CST Microwave Studio

CST Microwave Studio (MWS) is a specialist 3-D electromagnetic simulation tool, which is a component of CST Studio Suite (CST 2012). Unlike the majority of EM solvers, MWS employs a finite integration technique (FIT) for solving Maxwell's equations. The package comprises dedicated eigenmode, transient and frequency domain solvers, with an eye to high frequency problems. A similar package within the Suite, EM Studio, targets low frequency problems. Computer Simulation Technology – the publishers of MWS – develop and market high performance software for simulating EM fields across all frequency bands. As a result, MWS finds applications in such diverse fields as telecommunications, defence and electronics. In contrast to Magic, MWS is a predominantly menu-driven package, with simple on screen options for the creation of structures, ports, incoming waves, and a variety of other tools. That being said, there exists the potential for importing macros which have been created using Visual Basic.

One of the advantages of the MWS package lies with the use of advanced meshing strategies. While typical electromagnetic and PIC codes utilise cube-like hexahedron cells for their meshes, MWS also offers a pyramid-like tetrahedron meshing style. While the standard hexahedral mesh is robust in dealing with complex geometries, and provides a faster simulation of the problem, the cells in such a mesh do not always conform to the geometries associated with changes in material. However, MWS makes use of a perfect boundary approximation – whereby even curved boundaries can be approximated within a Cartesian mesh (i.e. a hexahedral mesh) and as such, CST claim this does not pose a problem. In comparison, the tetrahedral mesh does conform more accurately to boundaries and changes in the material – therefore, it can be used to more accurately represent a complex structure. However, as a result of the tetrahedral mesh cells, more of them are required, and thus, the simulation time can increase dramatically. In addition, although they can afford improved meshing of boundaries, complex structures will require the use of anisotropic tetrahedral shapes, resulting in a non-uniform mesh and therefore, reduced computational accuracy.

The transient solver focuses on solving in the time domain, evaluating the Sparameters of a structure, across a broadband frequency range, in a single computation run. There also exists the ability to only examine certain electromagnetic modes of interest. Additionally, the spatial distribution of the electromagnetic fields at desired frequencies can be displayed.

The eigenmode solver is dedicated for examining closed, lossy, resonant structures, such as cavities. The primary function is the calculation of a defined number of modes within the structure, supplying the resonant frequency and field structure of the mode.

The Finite Integration Technique

The finite integration method examines the integral form of Maxwell's equations[142, 143, 144]. A finite domain for the calculation is defined. MWS creates a mesh grid by splitting the geometry into a series of small cuboids, known as grid cells. The cells can be viewed within MWS, as a so-called primary mesh; however, an additional second mesh is generated, which is offset to that of the initial mesh. Maxwell's equations are discretised on these two grids. As can be seen in the Figure A.5.1, the electric grid voltage, e, and the magnetic facet flux, b, are located on the primary grid. Similarly, the magnetic grid voltage, h, and the electric facet flux, d, are on the secondary grid.

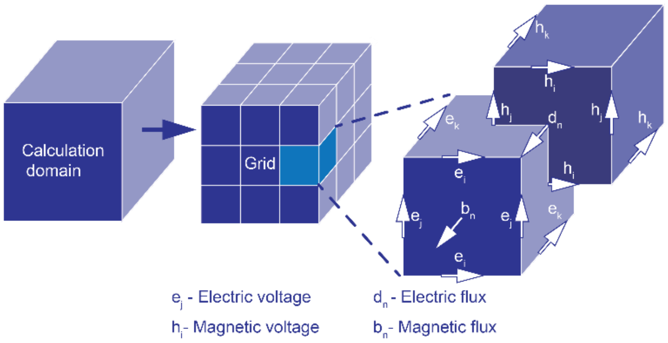

Figure A5.1: Example of the meshing structure used in the finite integration technique (CST MS)

Once the grid is established, Maxwell's equations can be solved for each cell face individually. By considering Faraday's law, the closed line integral of the surface can be equated as the sum of the four grid voltages. This can be done without the introduction of any further errors. If this is repeated for all cell faces within the simulation, the calculation can be summarised using a matrix. Ampere’s law can be considered in the same way, resulting in a similar matrix. As a result, a complete discretised set of matrix equations, referred to as Maxwell’s grid equations are obtained. As well as retaining the information described in the differential form of Maxwell’s equations, the grid equations also contain information on the size of the mesh utilised.

However, numerical inaccuracy is introduced when the equations representing the material properties are considered. After defining the relationship between the voltages and fluxes, their integrals have to be approximated over both the edges of the grid, and areas of the cells. Therefore, the resulting coefficients depend on the averaged parameters, along with the spatial resolution of the mesh

A.6 Vector Network Analyser

Network analysers are instruments capable of measuring characteristics of transmitted and reflected signals within a transmission line, relative to some reference signal[145]. A VNA is capable of providing both amplitude and phase information of the signal.

Network analysers consist of several individual components which comprise the entire instrument. Common elements in all analysers are the detectors, computer and display. Additional components include the microwave source and test sets; however, depending on the particular analyser in question, these may be an integrated component or may be external. Frequency multiplication is typically used within the test set, in order to provide operation over a wide range of frequencies using a single, highly stable, low frequency source.

In order to provide accurate information, calibration of the network analyser is necessary before each individual measurement is performed. A number of differing calibration schemes exist, with more involved calibrations resulting in more complex error calculations being performed by the analyser, and as a result, potentially increased accuracy in the measurements, due to the elimination of systematic error. Pre-made calibration standards are available for standard types of transmission line, allowing the user to calibrate the system without manufacturing their own calibration pieces. Typical calibration standards include lengths of transmission lines, “perfect” matched loads, and short circuits.

In this investigation, amplitude measurements are presented in the form of S-parameter plots. Such plots display the amplitude and phase response of the system under examination as a function of frequency. For a two port system, the signal detected at a given port, p_1, based on an input from the other port, p_2, a phasor, S_{p1p2}, can be written. For example, S_{21} refers to the response observed at port 2, given an input at port 1, i.e. a transmitted signal. Conversely, S_{11} would show the signal received at port 1 due to a signal from the same port, i.e. a reflected signal. For a linear, 2 port device, the measurement of the four scattering parameters completely characterises its response to an arbitrary excitation. This can be shown by the scattering matrix in equation (A6.1), where the subscripts i and o refer to incoming and outgoing signals, respectively.

$$\begin{bmatrix} \mathrm{p}_{1o} \\ p_{2o} \end{bmatrix} = \begin{bmatrix} s_{11} & s_{12} \\ s_{21} & s_{22} \end{bmatrix} \begin{bmatrix} \mathrm{p}_{1i} \\ p_{2i} \end{bmatrix} \quad \text{A6.1}$$

A.7 Thermionic Emission

The free electron theory of metals (developed by Sommerfield) models the forces on electrons in conductive solids by the application of quantum mechanics to the problem of electron thermionic emission. At temperatures above absolute zero, some electrons have sufficient energy to escape the cathode surface. As the temperature rises, an increasing number of electrons have sufficient velocity to escape. Electron emission achieved through surface heating is referred to as thermionic emission. The emission process is best illustrated through the use of an energy level diagram.

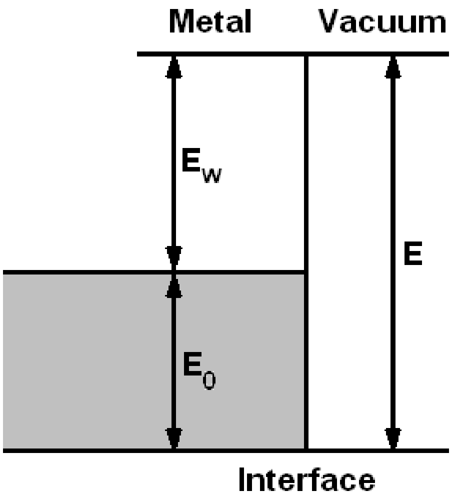

Figure A.7.1: Energy level diagram illustrating the origins of work function.

The energy levels of adjacent atoms in the cathode material merge to form the conduction band, the top of which is at the Fermi level (E_0), the limit of electron energies at 0K. The energy difference between the Fermi level and the energy level of the vacuum is known as the work function (E_W or eϕ). Electrons are emitted when the temperature is raised such that the component of their energy in a direction perpendicular to the cathode surface is E_0 **+** eϕ or greater. This gives rise to a critical momentum required for an electron to overcome the material work function.

$$\frac{P_{xc}^2}{2m} = \frac{1}{2} m u_x^2 = E_0 + e\phi \qquad \text{A7.1}$$

If the number of electrons per unit volume, n_e, having momentum $P_z > P_{zc}$ can be found then the emission current density, J, can is given by:

$$J = \rho u_x = e n_e u_x \qquad \text{A7.2}$$

The value of n_e may be determined density of energy states and the Fermi-Dirac distribution function (the probability that the states are occupied). Using this method it is relatively simple to prove that the current density is given by:

$$J = A_0 T^2 e^{-\frac{e\phi}{kT}} \qquad \text{A7.3}$$

This is the well-known Richardson-Dushman equation for thermionic emission. The universal constant A_0 has the value:

$$A_0 = 1.2 \times 10^6 \quad \text{Am}^{-2}\text{deg}^{2} \qquad \text{A7.4}$$

The most notable feature of this result is that the current varies exponentially with both work function and temperature. The T^2 term is, by comparison, negligible. Experimentally, the value of A_0 is found to be significantly lower than predicted (about a quarter to a half the value). Firstly, this is because the work function was assumed to be independent of temperature, when in reality it normally varies approximately linearly. The Richardson-Dushman can be rewritten in an attempt to account for this variation:

$$J = \left(A_0 e^{-\frac{e\alpha\phi}{kT}} \right) T^2 e^{-e\phi_R / kT} \qquad \text{A7.5}$$

Secondly, it is assumed that the work function is constant across the entire surface of the emitter. If this is not the case then the vast majority of the emission will be from the lower work function region, reducing the effective area of the cathode.

Cathodes may be either directly or indirectly heated. In a directly heated cathode, the filament described in the Edison effect forms the cathode. Directly heated cathodes are fairly efficient and are capable of emitting a large number of electrons. An added advantage of this type of filament is the speed at which it reaches electron-emitting temperature. Being almost instantaneous, pieces of electronic equipment that must be turned on at infrequent intervals and be instantly ready use tubes with directly heated cathodes. However, because of its construction, some parts of the filament are closer to the plate than others, giving rise to non-uniform emission and, hence, a loss of efficiency.

Another disadvantage occurs when DC is used to heat the filament. The filament has a resistance and so, when current flows through it, a voltage drop occurs. The result of this is that one side of the filament is at a lower voltage than the other side and so one side of the filament will emit more electrons than the other. Again, this reduces the efficiency. Using AC on the other hand, causes small undulations in temperature as the current rises and falls. In turn, this causes a small, but still highly undesirable, undulation in the emission of electrons. In other words, there is noise.

Indirectly heated cathodes are invariably constructed using a barium aluminate impregnated tungsten cathode or an oxide-coated material. The cathode encloses the twisted wire filament and the only function of the filament is to act as a heater for the cathode.

Indirectly heated cathodes are relatively large and so, when heated, they take longer to reach electron-emitting temperatures. Once up to operating temperature, however, they do not respond to the small variations in heater temperature caused by AC fluctuations. These advantages have led to most tubes in use today using indirectly heated cathodes.

Space Charge Limitation

Once electron emission has started, the presence of the negative charge will reduce the potential that was present in its absence. In the region close to the surface of an emitting cathode, where many electrons are present, the reduction has a significant effect on the emission process. The initial potential in the electron gun increases linearly from cathode to anode. However, in the presence of an electron beam, this potential profile is depressed, the depression growing deeper as the emission is increased. The equilibrium, or space charge limit, occurs when the electron beam is sufficiently dense so as to reduce the potential at the cathode surface to zero (were the potential to become negative, electrons would be forced back to the cathode). Should the potential deviate in either the positive or negative direction, more or less electrons will flow from the cathode, re-establishing the equilibrium.

Once the space charge limit has been reached, parameters such as cathode temperature or surface quality have no effect on emission. This property proves highly useful as it eliminates the necessity for extreme uniformity in cathode temperature. Should the diode voltage be increased, the potential at all points is raised and additional current will flow to suppress the cathode surface potential to zero. Diode current in this regime is, therefore, dependant only on diode voltage. In the case of a parallel plane diode it is again rather straightforward to the following expression for current density in the space charge limited regime:

$$J = \frac{4}{9}\varepsilon_0 (2\eta)^{\frac{1}{2}} \frac{V^{\frac{3}{2}}}{x^2} \qquad \text{A7.6}$$

This is the Child-Langmuir law for the flow of electrons in a parallel-plane, space charge limited diode and is commonly written in the simplified form:

$$J = 2.33\times10^{-6} \frac{V^{\frac{3}{2}}}{x^2} \qquad \text{A7.7}$$

where I=JA, with A being the area of the cathode. P is known as the diode perveance and for a parallel plane diode is given by:

$$P = IV^{\frac{3}{2}} \qquad \text{A7.8}$$

Importantly, perveance is a function only of diode geometry. Whilst the perveance varies from one geometry to the next, all geometries obey the equation I = $PV^{3/2}$.

A.8 Cusp Gun Theory

For applications in plasma physics, investigations of charged particle orbits in highly non-adiabatic electromagnetic fields were carried out in the 1950s[146, 147]. These studies were primarily conducted for comparison with experimental data from a θ-pinch under field reversal; however, the work of Schmidt [148] gives brief consideration to the formation of a rotating electron ring. Similar investigations were carried out by Sinelnikov et al[149] for the production of a dense cloud of relativistic electrons gyrating in a magnetic field with a small ratio of translational to rotational electron energies, primarily for nuclear fusion and particle accelerator applications.

Non-adiabatic orbit calculations show that charged particles injected into a magnetic field with a cusp along its axis will pass through the magnetic trap provided that:

$$r_L = \frac{v_z}{\omega_{ce}} \geq r \qquad \text{A8.1}$$

where v_z is the axial velocity and r the radial distance of the injected particles from the axis of the cusp.

Charged Particle Motion through a Magnetic Cusp

The motion of a particle in an axially symmetric system in which the magnetic field is represented by a solenoid vector potential A_θ can be described by the Hamiltonian:

$$H = \frac{P_r^2}{2m} + \frac{P_z^2}{2m} + \frac{1}{2m}\left(\frac{P_\theta - qrA_\theta}{r}\right)^2 + qV \qquad \text{A8.2}$$

where P_θ is the canonical angular momentum and V is the scalar potential. Busch's theorem states that the canonical angular momentum of an electron is a constant of its motion. Additionally, due to the axial symmetry, $\partial A_\theta/\partial\theta = \partial V/\partial\theta = 0$. Hence, equation 2 can be rewritten as:

$$H = \frac{P_r^2}{2m} + \frac{P_z^2}{2m} + \psi \qquad \text{A8.3}$$

where

$$\Psi = \frac{1}{2m}\left(\frac{P_\theta - qrA_\theta}{r}\right)^2 + qV \qquad \text{A8.4}$$

is an effective potential. Equation 2 now represents particle motion in the r-z plane under the influence of this effective potential. If the effect of the accelerating potential, V, is ignored and instead only the effects of the magnetic field are considered then, for confined particles, Ψ is a function only of r and it must have at least one minimum. Hence, there must exist at least one point where:

$$\frac{d\psi}{dr} = -\frac{P_\theta - qrA_\theta}{mr}\left(\frac{P_\theta}{r^2} + q\frac{\partial A_\theta}{\partial r}\right) = 0 \qquad \text{A8.5}$$

This implies either:

$$\frac{P_\theta - qrA_\theta}{r} = 0 \quad \text{or,} \qquad \text{A8.6}$$

$$\frac{P_\theta}{r^2} + q\frac{\partial A_\theta}{\partial r} = 0 \qquad \text{A8.7}$$

It is important to note that the angular momentum of the particle relative to the system axis is given by:

$$P_\theta - qrA_\theta = mv_\theta r \qquad \text{A8.8}$$

Hence, it can be seen that equation A8.6 represents the case where individual particle trajectories do not encircle the axis. If it is assumed that the particles enter the system in this state (the most probable scenario) then, from equation A8.6:

$$P_\theta = qrA_\theta \quad \text{A8.9}$$

For a particle in orbit at radius r:

$$A_\theta = \frac{1}{2} r \overline{B}_z \quad \text{A8.10}$$

where

$$\overline{B}_z = \frac{1}{\pi r^2} \int_0^r B_z 2\pi r' dr' \quad \text{A8.11}$$

As the particles traverse the magnetic cusp, the sign of B_z (and, therefore, of A_θ) is reversed non-adiabatically (the length of the cusp transition must be short compared to the Larmour step) and equation A8.6 no longer holds. Assuming the particles remain confined they must now encircle the axis and equation A8.7 must now be true – the beam is axis-encircling.

Description of Emerging Beam

One of the interesting features of a cusp gun is the dependence of pitch factor on clearly defined parameters that can be predicted by the conservation of canonical angular momentum. The general form of Busch's theorem can be written as:

$$\dot{\theta} = \frac{\eta}{2\gamma c}\left(B_z - B_{z0} \frac{r_0^2}{r^2} \right) \quad \text{A8.12}$$

where θ' is the angular velocity, η is the charge to mass ratio of an electron, γ is the relativistic factor and B_{z0} and r_0 are the axial magnetic field amplitude and the radius where the angular velocity is zero. In the case of the cusp gun, B_{z0} is the axial field amplitude at the cathode surface and r_0 is the cathode radius. B_z and r are the axial magnetic flux and the Larmour radius at any given position. In the case of the cusp gun, Busch's theorem can be written as:

$$\frac{v_\perp}{r_L} = \frac{\eta}{2\gamma c}\left(B_{cavity} - B_{cathode}\frac{r_{cathode}^2}{r_L^2} \right) \qquad \text{A8.13}$$

Substituting:

$$r_L = \frac{v_\perp \gamma c}{\eta B_{cavity}} \quad \text{and} \quad v_\perp = v\sqrt{\frac{\alpha^2}{1+\alpha^2}} \qquad \text{A8.14}$$

Solving for the pitch factor gives:

$$\alpha = \sqrt{\frac{-r_0^2\eta^2 B_{cathode}B_{cavity}}{\gamma^2 v^2 c^2 + r_{cathode}^2\eta^2 B_{cathode}B_{cavity}}} \qquad \text{A8.15}$$

The closer the radius of the beam to the Larmour radius on traversing the cusp, the better the guiding centre alignment and the tighter the helical trajectories will be. In practice, the emitter strip has finite width and so the injected electrons have a spread in initial radius. The associated spread in canonical angular momentum results in a perpendicular velocity spread post-cusp as given by the equation:

$$\left(\frac{\Delta v_\perp}{v_\perp}\right)_{RMS} = \frac{\Delta r}{\sqrt{3}r_0} \qquad \text{A8.16}$$

where r_{ce} is the average radius of the emitting annulus and 2Δr is its width. The corresponding axial velocity spread is then approximately given by:

$$\frac{\Delta v_z}{v_z} \approx \alpha^2 \frac{\Delta v_\perp}{v_\perp} \qquad \text{A8.17}$$

This inherent spread limits efficiency and so for good performance requires a thin emitting annulus. In order to maintain a large emitting surface and, hence, reduce cathode loading, beam power can be increased by using adiabatic compression and electrostatic focusing in the pre-cusp region. In addition to the initial radial spread, initial velocity spread must also be considered. In the relativistic case, for a small incident velocity spread Δv, the approximate post-cusp velocity spread is given by:

$$\frac{\Delta v_z}{v_z} = \left[1 + \alpha^2 + \alpha^2\left(\gamma_0^2 - 1\right)\right]\frac{\Delta v_0}{v_0} \qquad \text{A8.18}$$

$$\frac{\Delta v_\perp}{v_\perp} = -\left(\gamma_0^2 - 1\right)\frac{\Delta v_0}{v_0} \qquad \text{A8.19}$$

Previous studies [150] of charged particle motion through a cusped magnetic field have reported that the magnetic field in the final cavity typically modifies the canonical angular momentum of each particle in such a way as to decrease Δv_z significantly whilst increasing $\Delta v_\perp$ only moderately.

Early experiments on the passage of an intense relativistic electron beam through a cusped magnetic field were carried out by Friedman [151]. This work provided much evidence – though no conclusive proof – of helical electron trajectories. A number of further studies were carried out over the ensuing decades, encompassing a variety of applications[152] before work was started to design cusp guns as an electron beam source for microwave devices. Groups in Russia, the United States[153, 154] and Korea[155, 156] have all published experimental results relating to cusp guns for microwave devices.

References

1 W. He, C. R. Donaldson, F. Li, L. Zhang, A. W. Cross, A. D. R. Phelps, K. Ronald, C. W. Robertson, C. G. Whyte, and A. R. Young, “W-band gyro-devices using helically corrugated waveguide and cusp gun: Design, simulation and experiment,” TST, vol. 4, no. 1, pp. 9–19, 2011.

2 W. He, C.R. Donaldson, L. Zhang, K. Ronald, P. McElhinney and A.W. Cross, "High power wide-band gyro-BWO operating towards the terahertz region", Phys. Rev. Lett., 110, 165101, 2013.

3 *521-2002 - IEEE Standard Letter Designations for Radar-Frequency Bands.*

4 *Hertz, H.: ‘On electric radiation’. Wiedemann’s Annalen*, 1888, Vol. 36, pp. 769

5 Bose, J.C.: ‘On a complete apparatus for the study of the properties of electric waves’, Elec. Eng., Oct. 2, 1896.

6 Bose, J.C.: ‘Collected physical papers’, Longmans, Green and Co., New York, 1927.

7 Lebedew, P., "Ueber die Dopplbrechung der Strahlen electrischer Kraft," Annalen der Physik und Chemie, series 3, vol.56, no.9, pp.1-17, 1895

8 Clerk Maxwell, J, "A Dynamical Theory of the Electromagnetic Field", Royal Society of London Philosophical Transactions Series I, 155, 459-512, 1865

9 Marconi, G., "Wireless telegraphy," Electrical Engineers, Journal of the Institution of, vol.28, no.139, pp.273, 290, April 1899

10 DÖRing, H., Review article: Microwave tube development in Germany from 1920–1945†. International Journal of Electronics, 1991. 70(5): p. 955-978

11 A.W. Hull, “The Effect of a Uniform Magnetic Field on the Motion of Electrons between Coaxial Cylinders”, Phys. Rev., 18, 31 (1921)

12 Varian, R. H.; Varian, S. F. (1939). "A High Frequency Oscillator and Amplifier". Journal of Applied Physics 10 (5): 321.

13 Rees, D., M. Lynch and P. Tallerico (1998). Accelerator production of tritium 700 MHz and 350 MHz klystron test results. Conference: 19. international

linac conference, Chicago, IL (United States), 23-28 Aug 1998; Other Information: PBD: [1998]: Medium: ED; Size: 4 p.

14 Steer, B., A. Roitman, P. Horoyski, M. Hyttinen, R. Dobbs and D. Berry (2007). Advantages of extended interaction klystron technology at millimeter and sub-millimeter frequencies. Pulsed Power Conference, 2007 16th IEEE International.

15 Alexander N. Korolev, Sergei A. Zaitsev, Ivan I. Golenitskij, etc. Traditional and Novel Vacuum Electron Devices, IEEE Trans. On Electron Devices, Vol. 48, No. 12, Dec. 2001.

16 Steven H. Gold, Review of High-power microwave source research, Rev. Sci. Instrum. 68(11), 1997.

17 V.A. Flyagin, A.V. Gaponov-Grekhov, M.I. Petelin, B.K. Ylpatov, “The Gyrotron,” IEEE Trans. Microwave theory Tech., 25, pp. 514-521, (1977).

18 Chu, K. R., 2002, ‘‘Overview of research on the gyrotron traveling-wave amplifier,’’ IEEE Trans. Plasma Sci. 30, 903–908.

19 K. R. Chu, “The electron cyclotron maser,” REVIEWS OF MODERN PHYSICS, p. 492, 2004.

20 G. A.V., “Interaction between electron fluxes and electromagnetic waves in waveguides,” Izv. Vyssh. Uchebn. Zaved. Radiofiz., vol. 2, pp. 450-463, 1959.

21 Twiss, R.Q., "On Negative Absorption in an Electron-Ion Plasma when Radiation Takes Place by Free-Free Transitions.", Astrophysical Journal, vol. 136, p.438 Sep. 1962.

22 J. Schneider, “Stimulated Emission of Radiation by Relativistic Electrons in a Magnetic Field,” Phys. Rev. Lett, vol. 2, no. 12, pp. 504-505, 1959.

23 C. Sirtori, “Applied physics: Bridge for the terahertz gap,” NATURE, no. 6885, pp. 132-133, 2002

24 Special Technology Area Review on Vacuum Electronics Technology for RF Applications, Department of Defence advisory group on electron devices report, USA, (2005). .

25 K.K. Chow and R.H. Pantell, “Backward Wave Oscillators in Unloaded Waveguides”, Proc IEEE, Vol 48, 1960

26 Bott I.B. “Tuneable Source of Millimetre and Submillimetre Wave Radiation” Proc. IEEE, vol 52, 1964

27 J. Feinstien, “Research on Electronic Interation with Fields of Mirror Resonators”, Proc. Int.

28 Flyagin, V.A.; Gaponov, A. V.; Petelin, M.I.; Yulpatov, V. K., "The Gyrotron," Microwave Theory and Techniques, IEEE Transactions on , vol.25, no.6, pp.514,521, Jun 1977.

29 A.A. Andronov, V.A. Flyagin, A.V. Gaponov, A.L. Gol'denberg, M.I. Petelin, V.G. Usov, V.K. Yulpatov, The gyrotron: High-power source of millimetre and submillimetre waves, Infrared Physics, Volume 18, Issues 5–6, December 1978, Pages 385-393.

30 M. Petelin, “Physics of advanced gyrotrons,” Plasma Phys. and Contr. Nucl. Fusion, no. Supplement B, pp. 343-351, 1993.

31 Flyagin, V.A.; Goldenberg, A.L.; Ginzburg, N. S.; Kovaljov, N. F.; Petelin, M. I., "Investigations of Powerful Gyrotrons," Microwave Conference, 1982. 12th European , vol., no., pp.513,513, 13-17 Sept. 1982.

32 Flyagin, V.A.; Nusinovich, G.S., "Gyrotron oscillators," Proceedings of the IEEE , vol.76, no.6, pp.644,656, June 1988.

33 A. A. Tolkachev, B. A. Levitan, G. K. Solovjev, V. V. Veytsel, and V. E. Farber, “A megawatt ower mullimeter-wave phased-array radar,” IEEE Aerosp. Electron. Syst. Mag., 15, pp. 25-31, (2000).

34 http://www.iapras.ru/english/science/m_el/m_el1_2.html

35 S.J. Cooke, A.W. Cross, W. He and A.D.R. Phelps, ‘Experimental operation of a cyclotron autoresonance maser oscillator at the second harmonic’, Phys. Rev. Letts, 77, No 23, pp4836-4839, 1996.

36 V. K. Yulptov, “Nonlinear theory of interaction between a periodic electron beam and an electromagnetic wave,” Radiophy. Quantum Electron., 10, pp. 471-476, (1967).

37 N. S. Ginzburg, I. G. Zarnitsyna, and G. S. Nusinovich, “Theory of relativistic cyclotron autroresonace maser with opposite wave,” Radio Eng. Electron. Phys., 24, pp. 113-118, (1979).

38 A. K. Ganguly and S. Ahn, “Non-linear analysis of the gyro-BWO in three dimensions,” Int. J. Electron, 67, pp. 261-276, (1989).

39 G. S. Nusinovich and O. Dumbrajs, “Theory of gyro-backward wave oscillator with tapered magnetic field with waveguide cross section,” IEEE Trans. on Plasma Sci., 24, pp. 620-629, (1996).

40 V.L. Granatstein, M. E. Read and L. R. Barnett “Measured performance of Gyrotron oscillators and amplifers,” Int. J. Infrared Millimeter Waves, 5, pp. 267-302, (1982).

41 Kane Yee, "Numerical solution of initial boundary value problems involving maxwell's equations in isotropic media," Antennas and Propagation, IEEE Transactions on , vol.14, no.3, pp.302,307, May 1966

42 Haeff, A.V.; Nergaard, L.S., "A Wide-Band Inductive-Output Amplifier," Proceedings of the IRE , vol.28, no.3, pp.126,130, March 1940

43 S. N. Vlasov and I. M. Orlova, “Quasi-optical transformer which transforms the waves in a waveguide having circular cross-section into highly-direction wave beam,” Radiophysics Quantum Electron., vol. 17, pp. 148–154, 1974.

44 M. Skolnik, “Role of Radar in Microwaves,” IEEE TRANSACTIONS ON MICROWAVE THEORY AND TECHNIQUES, vol. 50, no. 3, pp. 625-632 , 2002.

45 T. Nakamura , K. Kaiya , N. Takahashia , T. Matsuzawa , M. Ohtac , C. C. Rowlands , G. M. Smith and P. C. Riedi, "“High frequency EPR investigations of gadolinium(III)-doped strontium aluminates”,", Physical Chemistry Chemical Physics, 3, pp 1721, 2001

46 D.J. Keeble, R. M. Robb, G. M. Smith, H. EL Mkami, S.E. Rodil and J. Roberston, "“Paramagnetic defects in hydrogenated amorphous carbon powders”", J. Phys: Condens. Matter, 15, pp 7463-7468, 2003

47 M. Blank, “Designofa 50-MW 30-GHz gyroklystron amplifier for accelerator applications,” in in Proceedings IEEE International Vacuum Electronics Conference, new York, 2002.

48 R. Pantell, “Backward-wave oscillations in an un-loaded waveguide,” in Proc. IRE 47.

49 C. J. RL Schriever, “A rotating beam waveguide oscillator,” in Proceedings of the IEEE, 1966.

50 T. P. M. P. V. F. NI Zaytsev, “Millimeter-and submillimeter-wave gyrotrons,” Radio Eng. Electron. Phys, vol. 21, pp. 103-107, 1974.

51 D. V. Kisel, G. S. Korablev, V. G. Pavelev, M. I. Petelin and S. E. Tsimring, “An experimental study of a gyrotron, operating at the second harmonic of the cyclotron frequency, with optimized distribution of the high-frequency field,” Radio Engineering and Electronic Physics, vol. 19, pp. 95-100, April 1974.

52 T. C. Luce, “Applications of High-Power Millimeter Waves in Fusion Energy Research,” IEEE TRANSACTIONS ON PLASMA SCIENCE, vol. 30, pp. 734-754, 2002.

53 Felch, K.L.; Danly, B.G.; Jory, H.R.; Kreischer, K.E.; Lawson, W.; Levush, B.; Temkin, R.J., "Characteristics and applications of fast-wave gyrodevices," Proceedings of the IEEE , vol.87, no.5, pp.752,781, May 1999.

54 Steer, B., A. Roitman, P. Horoyski, M. Hyttinen, R. Dobbs and D. Berry (2007). Advantages of extended interaction klystron technology at millimeter and sub-millimeter frequencies. Pulsed Power Conference, 2007 16th IEEE International.

55 Luhmann, N.C., Jr.; Barnett, L.R.; Pao, K.F.; Tsai, W.C.; Chu, K.R., "UC Davis 94 GHz gyrotron traveling-wave amplifier developments," Infrared and Millimeter Waves and 13th International Conference on Terahertz Electronics, 200 IRMMW-THz 200 The Joint 30th International Conference on , vol.2, no., pp.654 vol. 2,, 19-23 Sept. 200

56 Luhmann, N.C., Jr.; Barnett, L.R.; Pao, K.F.; Tsai, W.C.; Chu, K.R., "UC Davis 94 GHz gyrotron traveling-wave amplifier developments," Infrared and

Millimeter Waves and 13th International Conference on Terahertz Electronics, 200 IRMMW-THz 200 The Joint 30th International Conference on , vol.2, no., pp.654 vol. 2,, 19-23 Sept. 200

57 H. H. Song, D. B. McDermott, Y. Hirata, L. R. Barnett, C. W. Domier, H. L. Hsu, T. H. Chang, W. C. Tsai, K. R. Chu, and N. C. Luhmann, Jr., “Theory and experiment of a 94 GHz gyrotron traveling-wave amplifier,” Phys. Plasmas, vol. 11, no. 2935 , 2004.

58 Y. S. Yeh, C. L. Hung, C.-W. Su, T.-S. Wu, Y.-Y. Shin and Y.-T. Lo, “W-band second-harmonic gyrotron traveling wave amplifier with distributed-loss and severed structures,” International Journal of Infrared and Millimeter Waves, vol. 1, no. 25, pp. 29-42, January 2004.

59 M. Blank, “Demonstration of a Broadband W-Band Gyro-TWT Amplifier,” in Plasma Science, 200 ICOPS '0 IEEE Conference Record - Abstracts. IEEE International Conference on, 200

60 J. R. Sirigiri, K.E. Kreischer, M. A. Shapiro and R. J. Temkin, “Novel quasioptical W-band gyro-TWT,” in Vacuum Electronics Conference, 2000. Abstracts., 2000.

61 Blank, M.; Felch, K.; James, B.G.; Borchard, P.; Cahalan, P.; Chu, T.S.; Jory, H.; Danly, B.G.; Levush, B.; Calame, J.P.; Nguyen, K.T.; Pershing, D.E., "Development and demonstration of high-average power W-band gyro-amplifiers for radar applications," Plasma Science, IEEE Transactions on , vol.30, no.3, pp.865,875, Jun 2002

62 McDermott, D.B.; Song, H.H.; Hirata, Y.; Lin, A.T.; Barnett, L.R.; Chang, T.H.; Hsin-Lu Hsu; Marandos, P.S.; Lee, J.S.; Kwo Ray Chu; Luhmann, N.C., Jr., "Design of a W-band TE01 mode gyrotron traveling-wave amplifier with high power and broad-band capabilities," Plasma Science, IEEE Transactions on , vol.30, no.3, pp.894,902, Jun 2002

63 Maxwell, J. C. (1865). A Dynamical Theory of the Electromagnetic Field. Philosophical Transactions of the Royal Society of London 155, 459-512.

64 Heaviside, O. (1880). Electromagnetic waves, the propagation of potential, and the electromagnetic effects of a moving charge. The Electrician, Part I, Nov. 9, 1888, p. 23; Part II, Nov. 23, 1888, p. 83; Part III, Dec. 7, 1888, p. 147; Part IV, Sept. 6, 1889, p. 458.

65 Pozar, D. M. (1997). Microwave engineering. Wiley.

66 Jackson, John David, “Classical Electrodynamics,” Wiley, 1998

67 Lorrain, Paul, Corson, Dale R., Lorrain, François, “Electromagnetic Fields and Waves: Including Electric Circuits,”Freeman, 1988

68 Nathan Marcuvitz, Waveguide Handbook, IET, 1951

69 Schelkunoff, S. A. (1939). "On Diffraction and Radiation of Electromagnetic Waves." Physical Review 56(4): 308-316.

70 Pozar, D. M. (1997). Microwave engineering. Wiley.

71 Mahmoud, S. F., “Electromagnetic waveguides : theory and applications,” Peregrinus 1991

72 Clarricoats, P. J B; Saha, P.K., "Propagation and radiation behaviour of corrugated feeds. Part 1: Corrugated-waveguide feed," Electrical Engineers, Proceedings of the Institution of, vol.118, no.9, pp.1167, 1176, September 1971.

73 A.D. Olver, P.J.B. Clarricoats, A.A. Kishk and L. Shafai, “Microwave Horns and Feeds”, IEE Electromagnetic waves series 39, The Institution of Electrical Engineers, 1994.

74 Clarricoats, P.J.B. and Olver, A.D., “Corrugated Horns for Microwave Antennas”, IEE Electromagnetic waves series 39, The Institution of Electrical Engineers, 1984.

75 Birch, J.R., et al., *An intercomparison of measurement techniques for the determination of the dielectric properties of solids at near millimetre wavelengths.* Microwave Theory and Techniques, IEEE Transactions on, 1994. 42(6): p. 956-96

76 Simonis, G.J., et al., *Characterization of near-millimeter wave materials by means of non-dispersive fourier transform spectroscopy.* International Journal of Infrared and Millimeter Waves, 1984. 5(1): p. 57-72.

77 Tsuji, M., H. Shigesawa, and K. Takiyama, *Submillimeter-wave dielectric measurements using an open-resonator.* International Journal of Infrared and Millimeter Waves, 1982. 3(6): p. 801-81

78 J.F. Ramsey “tubular beams from radiating apertures”, Advanced in microwaves, vol 3, 1968.

79 Silver S., 1949, Microwave Antenna Theory and Design. New York: McGraw-Hill Book Company, Inc.

80 Goldsmith, P., *Gaussian Beam Quasioptical Propogation and Applications*. Quasioptical Systems. 1998.

81 Zauderer, E., *Complex argument Hermite-Gaussian and Laguerre-Gaussian beams.* J. Opt. Soc. Am. A, 1986. 3(4)

82 Pedrotti, F.L. and L.S. Pedrotti, *Introduction to optics*. 2nd ed. 1993, Englewood Cliffs, N.J.: Prentice Hall.

83 Goldsmith, P.F., *Quasi-Optical Techniques.* Proceedings of the IEEE, 1992. 80(11): p. 1729-1747.

84 Shapiro, M. A. and R. J. Temkin (2011). "Calculation of a Hyperbolic Corrugated Horn Converting the TEM00 Mode to the HE11 Mode." Journal of Infrared, Millimeter, and Terahertz Waves 32(3): 283-294.

85 McElhinney, P., C. R. Donaldson, Z. Liang and H. Wenlong (2013). "A high directivity broadband corrugated horn for W-band gyro-devices." Antennas and Propagation, IEEE Transactions on 61(3): 1453-1456.

86 P. A. S. Cruickshank , D. R. Bolton , D. A. Robertson , R. J. Wylde and G. M. Smith "Reducing standing waves inquasi-optical systems by optimal feedhorn design", Proc.Joint 32nd Int. Conf. Infrared Millimeter Waves 15th Int. Conf. TerahertzElectronics, pp.922 -923 2007

87 McKay, J. E., D. A. Robertson, P. A. S. Cruickshank, R. I. Hunter, D. R. Bolton, R. J. Wylde and G. M. Smith (2013). "Compact Wideband Corrugated Feedhorns

With Ultra-Low Sidelobes for Very High Performance Antennas and Quasi-Optical Systems." Antennas and Propagation, IEEE Transactions on 61(4): 1714-1721.

88 Liang, Z., H. Wenlong, A. W. Cross, A. Phelps, K. Ronald and C. G. Whyte (2009). "Design of an Energy Recovery System for a Gyrotron Backward-Wave Oscillator." Plasma Science, IEEE Transactions on 37(3): 390-394.

89 Liang, Z., H. Wenlong, A. W. Cross, A. Phelps, K. Ronald and C. G. Whyte (2009). "Numerical Optimization of a Multistage Depressed Collector With Secondary Electron Emission for an X-band Gyro-BWO." Plasma Science, IEEE Transactions on 37(12): 2328-2334.

90 Donaldson, C.R., et al., Design and numerical optimization of a cusp-gun-based electron beam for millimetre wave gyro-devices. IEEE Trans. Plasma Sci., 2009: p. 2153-2157

91 Donaldson, C.R., et al., A cusp electron gun for millimetre wave gyrodevices. Appl. Phys. Lett., 2010(96): p. 141501.

92 He, W., C. R. Donaldson, L. Zhang, K. Ronald, P. McElhinney and A. W. Cross (2013). "High Power Wideband Gyrotron Backward Wave Oscillator Operating towards the Terahertz Region." Physical Review Letters 110(16): 165101.

93 S. N. Vlasov and I. M. Orlova, “Quasi-optical transformer which transforms the waves in a waveguide having circular cross-section into highly-direction wave beam,” Radiophysics Quantum Electron., vol. 17,pp. 148–154, 1974

94 Potter, P. D. "A new horn antenna with suppressed sidelobes and equal beamwidths.” Microwave J., 6 pp. 71-78, 1963.

95 Thomas, B., "Design of corrugated conical horns," Antennas and Propagation, IEEE Transactions on , vol.26, no.2, pp.367,372, Mar 1978

96 Granet, C.; James, Graeme L., "Design of corrugated horns: a primer," Antennas and Propagation Magazine, IEEE , vol.47, no.2, pp.76,84, April 2005

97 Jamnejad, V.; Hoorfar, A., "Design of corrugated horn antennas by evolutionary optimization techniques," Antennas and Wireless Propagation Letters, IEEE , vol.3, no.1, pp.276,279, Dec. 2004.

98 Robinson, J.; Sinton, S.; Rahmat-Samii, Y., "Particle swarm, genetic algorithm, and their hybrids: optimization of a profiled corrugated horn antenna," Antennas and Propagation Society International Symposium, 2002. IEEE , vol.1, no., pp.314,317 vol.1, 2002

99 Thomas, B.; James, Graeme L.; Greene, K.J., "Design of wide-band corrugated conical horns for Cassegrain antennas," Antennas and Propagation, IEEE Transactions on , vol.34, no.6, pp.750,757, Jun 1986

100 Clarricoats, P.J.B.; Saha, P.K.: 'Propagation and radiation behaviour of corrugated feeds. Part 1: Corrugated-waveguide feed', Proceedings of the Institution of Electrical Engineers, 1971, 118, (9), p. 1167-1176.

101 Clarricoats, P.J.B.; Elliot, R.D.: 'Multimode corrugated waveguide feed for monopulse radar', IEE Proceedings H (Microwaves, Optics and Antennas), 1981, 128, (2), p. 102-110.

102 James, Graeme L., "Analysis and Design of TE11-to-HE11 Corrugated Cylindrical Waveguide Mode Converters," Microwave Theory and Techniques, IEEE Transactions on , vol.29, no.10, pp.1059,1066, Oct 1981

103 Clarricoats, P.J.B.; Saha, P.K.: 'Propagation and radiation behaviour of corrugated feeds. Part 2: Corrugated-conical-horn feed', Proceedings of the Institution of Electrical Engineers, 1971, 118, (9), p. 1177-1186.

104 Gentili, G.G.; Martini, E.; Nesti, R.; Pelosi, G., "Performance analysis of dual profile corrugated circular waveguide horns for radioastronomy applications," Microwaves, Antennas and Propagation, IEE Proceedings , vol.148, no.2, pp.119,122, 2 Apr 2001

105 Gupta,Ramesh Chandra and Pandya,Jigar and Sood,Khagindra K. and Jyoti,Rajeev, Compact dual-band axially corrugated profiled horn for prime-focus reflector antenna, International Journal of Microwave and Wireless Technologies, volume 3,August, 2011.

106 R Coccioli, G Pelosi, R Ravanelli, A mode matching-integral equation technique for the analysis and design of corrugated horns, Aerospace Science and Technology, Volume 2, Issue 2, February 1998, Pages 121-128.

107 Olver, A.D.; Xiang, J., "Design of profiled corrugated horns," Antennas and Propagation, IEEE Transactions on , vol.36, no.7, pp.936,940, July 1988

108 Liang Zhang, University of Strathclyde, Glasgow, Numerical and Particle in cell simulations.

109 www.electroform.com

110 P. Fürholz and A. Murk, “The impact of slow-wave modes on the radiationperformance of a corrugated horn antenna,” J. Infrared Milli. THz. Waves, vol. 31, no. 2, pp. 169–180, 2009.

111 J.McKay, D.A.Robertson, P.A.S.Cruickshank, R.I.Hunter, D.R.Bolton, R.J.Wylde and G.M.Smith, "Ultra-low sidelobe corrugated feedhorns for high performance antennas and quasi-optical systems", IEEE Antennas and Propagation, Accepted for Publication in Special Issue, 2013

112 Donaldson, Craig, “A W-band Gyrotron Backward Wave Oscillator with Helically Corrugated Waveguide,” University of Strathclyde, 2009.

113 Balanis, Constantine A, Advanced engineering electromagnetics, John Wiley & Sons, 1989

114 He, W., C. R. Donaldson, L. Zhang, K. Ronald, P. McElhinney and A. W. Cross (2013). "High Power Wideband Gyrotron Backward Wave Oscillator Operating towards the Terahertz Region." Physical Review Letters 110(16): 165101.

115 J. D. Kraus, “Heinrich Hertz—Theorist and experimenter,”IEEE Trans. Microwave Theory Tech., vol. 36, pp. 824–829, May 1988

116 J. H. Bryant, “The first century of microwaves—1886 to 1986: Parts I and II,”IEEE Trans. Microwave Theory Tech., vol. 36, pp. 830–858, May 1988

117 J. C. Wiltse, “History of millimeter and submillimeter waves,” IEEE Trans. Microwave Theory Tech., vol. MTT-32, pp. 1118–1126, Sept. 1984.

118 H. Sobol, “Microwave communications—An historical perspective,” IEEE Trans. Microwave Theory Tech., vol. MTT-32, pp. 1170–1181, Sept. 1984

119 RIGHI, A.: ‘L‘ottica delle oscillazioni elettriche’ (N. Zanichelli, Bologna, Italy, 1897)

120 J. H. Bryant, “The first century of microwaves—1886 to 1986, Part II: The Hertzians and their work,”IEEE Trans. Microwave Theory Tech., vol. 36, pp. 847–858, May 1988

121 G. B. Collins, Microwave Magnetrons, ser. Radiat. Lab.. New York: McGraw-Hill, 1948, vol. 6.

122 H. Yagi, “Beam transmission of ultra-short waves,” Proc. IRE, vol. 16, pp. 715–741, June 1928.

123 Arsenjewa-Heil, A. and O. Hell, Eine neue Methode zur Erzeugung kurzer, ungedämpfter, elektromagnetischer Wellen großer Intensität. Zeitschrift für Physik, 1935. 95(11-12): p. 752-762

124 Varian, R. H.; Varian, S. F. (1939). "A High Frequency Oscillator and Amplifier". Journal of Applied Physics 10 (5): 321.

125 J. H. Bryant, “The first century of microwaves—1886 to 1986, Part II: The Hertzians and their work,”IEEE Trans. Microwave Theory Tech., vol. 36, pp. 847–858, May 1988

126 H.A.H. Boot; J.T. Randall, Journal of the Institution of Electrical Engineers - Part IIIA: Radiolocation, Volume 93, Issue 5, 1946, p. 928 – 938.

127 R. Kompfner, “The traveling-wave valve,” Wireless World, vol. 52, pp. 369–379, 1946.

128 J. R. Pierce, “Theory of the beam-type traveling-wave tube,” Proc. IRE, vol. 35, pp. 111–123, Feb. 1947.

129 R.Warnecke,W. Kleen, A. Lerbs, O. Doehler, and H. Huber, “The magnetron-type traveling-wave amplifier,” Proc. IRE, vol. 38, pp. 486–495, May 1950.

130 R. Kompfner and N. T. Williams, “Backward wave tubes,” Proc. IRE, vol. 41, pp. 1602–1611, Nov. 1953.

131 R. Warnecke, P. Guenard, O. Doehler, and B. Epsztein, “The M-type carcinotron tube,” Proc. IRE, vol. 43, pp. 413–424, Apr. 1955.

132 Twiss, R.Q., "On Negative Absorption in an Electron-Ion Plasma when Radiation Takes Place by Free-Free Transitions.", Astrophysical Journal, vol. 136, p.438 Sep. 1962.

133 J. L. Hirshfield and V. L. Granatstein, “The electron cyclotron maser, an historical survey,” IEEE Trans. Microwave Theory Tech., vol. MTT-25, pp. 522–527, June 1977.

134 V. A. Flyagin, A. V. Gaponov, M. I. Petelin, and V. K. Yulpatov, “The gyrotron,” IEEE Trans. Microwave Theory Tech., vol. MTT-25, pp. 514–521, June 1977.

135 I.B. Bott, “Tuneable source of millimeteer and submillimeter radiation”, Phys. Letts., col 14, no 4., 1965.

136 H. Barkhausen and K. Kurz, Physikalische Zeitung 21 (1920) 1

137 A.W. Hull, “The Effect of a Uniform Magnetic Field on the Motion of Electrons between Coaxial Cylinders”, Phys. Rev., 18, 31 (1921)

138 "Haeff, Andrew V.", "Electron discharge device employing resonators", United States, RCA CORP, 2432571, Dec. 1947.

139 Luchini, H. Mots, Undulators and Frree-Electron Lasers, Clarendon Press, Oxford, 1990

140 Madey, J.M.J.:“Stimulated emission of bremsstrahlung in a periodic magnetic field”. J. Appl. Phys. 42, 1906 (1971)

141 Gonzalo, R., J. Teniente and C. del Rio (2002). "Improved radiation pattern performance of Gaussian profiled horn antennas." Antennas and Propagation, IEEE Transactions on 50(11): 1505-1513.

142 Weiland T., 1977, "A discretization model for the solution of Maxwell's equations for six-component fields", Archiv Elektronik und Uebertragungstechnik, 31, pp. 116-120.

143 Weiland T., 1996, "Time domain electromagnetic field computation with finite difference methods", International Journal of Numerical Modelling-Electronic Networks Devices and Fields, 9(4), pp. 295-319.

144 Weiland T., Timm M. and Munteanu I., 2008, "A Practical Guide to 3-D Simulation", IEEE Microwave Magazine, 9(6), pp. 62-75.

145 Bryant G.H., 1993, Principles of microwave measurements. London, United Kingdom: Peter Peregrinus.

146 J.L. Tuck, Phys. Rev. Letters 3, 313 (1959).

147 H. Grad, Phys. Rev. Letters 4, 222 (1960).

148 G. Schmidt, Phys. Fluids 5, 994 (1962).

149 K.D. Sinelnikov, N.A. Kizhnyak, N.S. Repalov, R.M. Zeidlits, V.A. Yamanitski and Z.A. Azovskaya, Proceedings of the Fourth Conference on Plasma Physics and Controlled Thermonuclear Fusion, Kharkov, U.S.S.R. (1963), edited by K.D. Sinelnikov (Israel Program for Scientific Translation, Jerusalem, Israel, 1966).

150 W. Lawson, W.W. Destler, IEEE Trans. Plasma Sci. 22, 895 (1994).

151 M. Friedman, Phys. Rev. Letters 24, 1098 (1970).

152 J.G. Kalnins, H. Kim, D.L. Nelson, „On the Formation of an Electron Ring in a Cusped Magnetic Field, University of Maryland (1971).

153 D.A. Gallagher, M. Barsanti, F. Scafuri, C. Armstrong, IEEE Trans. Plasma Sci. 28, 695 (2000).

154 S.B. Harriet, D.B. McDermott, D.A. Gallagher, N.C. Luhmann, Jr., IEEE Trans. Plasma Sci. 30, 909 (2002).

155 S.G. Jeon, C.W. Baik, D.H. Kim, G.S. Park, N. Sato, K. Yokoo, Jpn. J. Appl. Phys. 41, 5404 (2002).

156 S.G. Jeon, C.W. Baik, D.H. Kim, G.S. Park, Appl. Phys. Lett. 80, 3703 (2002).